Mid-water Localisation for Autonomous Underwater Vehicles

Lashika Janith Bandara Medagoda

A thesis submitted in fulfillment
of the requirements of the degree of
Doctor of Philosophy

THE UNIVERSITY OF
SYDNEY

Australian Centre for Field Robotics
School of Aerospace, Mechanical and Mechatronic Engineering
The University of Sydney

March 2012

Declaration

I hereby declare that this submission is my own work and that, to the best of my knowledge and belief, it contains no material previously published or written by another person nor material which to a substantial extent has been accepted for the award of any other degree or diploma of the University or other institute of higher learning, except where due acknowledgement has been made in the text.

Lashika Janith Bandara Medagoda

31 March 2012

Abstract

Lashika Janith Bandara Medagoda
The University of Sydney

Doctor of Philosophy
March 2012

Mid-water Localisation for Autonomous Underwater Vehicles

Survey-class Autonomous Underwater Vehicles (AUVs) rely on Doppler Velocity Logs (DVL) for precise localisation and navigation near the seafloor. In cases where the seafloor depth is greater than the DVL bottom-lock range, localising between the surface, where GPS is available, and the seafloor presents a localisation problem since both GPS and DVL are unavailable in the mid-water column.

Reliance on acoustic tracking methods such as Ultra Short Base Line (USBL) requires a ship to track the vehicle, while Long Base Line (LBL) requires the setting up of an acoustic transponder network. These methods provide bounded error position localisation ($\mathcal{O}(10m)$) of the underwater vehicle, but inhibits the flexibility and autonomy of the vehicle due to tending or set-up requirements. Proposed alternatives to these include combining GPS on the surface, navigation-grade IMU, the DVL water-track mode and a vehicle model to reduce the dead-reckoning error, although results show that this error is still not competitive with acoustic tracking methods after approximately 10 minutes of descent. Often ocean depth requires hours of descent without GPS or DVL, thus acoustic tracking methods are preferred.

This work proposes a solution to localisation in the mid-water column that exploits the fact that current profile layers of water columns are stable over short periods of time (in the scale of minutes). As demonstrated in simulation, using observations of these currents with the ADCP (Acoustic Doppler Current Profiler) mode of the DVL during descent, along with sensor fusion of other low cost sensors, position error growth can be constrained to near the initial velocity uncertainty of the vehicle at

the sea surface during a vertical dive. Following DVL bottom-lock, the entire velocity history is constrained to an error similar to the DVL velocity uncertainty. When coupled with a tactical-grade IMU and Time Differenced Carrier Phase (TDCP) GPS measurements, approximately 15 m/hr (2σ) position error growth is possible prior to DVL bottom-lock, and 6.5 m/hr (2σ) position error growth is possible following DVL bottom-lock. The method is demonstrated using real data from the *Sirius* AUV coupled with on-bottom view-based SLAM (Simultaneous Localisation and Mapping), without the use of an IMU.

Horizontal localisation in the mid-water zone is also explored using an extension to the water-layer framework. The layered water currents are extended to include horizontal gridding, while the ADCP sensor is remodelled to use beam coordinates to exploit horizontal observation. The water current vector field is modelled as correlated spatially through neighbourhood least-squared constraints. Simulations illustrate the performance possible with this method, and results from real data validate this approach.

In order to minimize the dead-reckoning error during mid-water zone transits, a novel method to incorporate Inertial Measurements and the constraints of a drag-based vehicle model is outlined. The drag-based Vehicle model uses the water current velocity estimates from the ADCP aiding method, while also accounting for the error from the Vehicle parameters given a prior system identification. Due to the redundant observations of motion from the IMU and DVL when available, there is potential for further improvement in estimates of the Vehicle parameters. Simulations are undertaken to assess the advantage of incorporating a vehicle model, and application on real data from the Sirius AUV validates this method.

Acknowledgements

I would like to first thank my supervisor Stefan Williams and my co-supervisors Oscar Pizarro and Michael Jakuba, whose knowledge, insight and feedback have been invaluable.

I would like to thank the AUV group and all who have enabled the successful operation of the AUV, including Matthew Johson-Roberson, Ritesh Lal, Paul Rigby, Stephen Barkby, Nasir Ahsan, Daniel Steinberg, Ariel Freidman, Asher Bender, Donald Dansereau, Lachlan Toohey, Jeremy Randle, Bruce Crundwell, Christian Lees, Andrew Durrant, and the later Duncan Mercer, George Powell and Alan Trinder.

Also, I would like to thank the rest of the ACFR for various discussions and events pertaining and not pertaining to my research here. It has all been a very enjoyable experience.

Special thanks goes to Anh, who has supported me through tireslessly proof-reading my thesis and giving moral support. Finally, I would like to thank my family and friends, who have supported me in all my endeavours.

Contents

List of Figures

List of Tables

List of Algorithms

Nomenclature

Convention

Scalars are represented by regular symbols e.g. x or X.

Vectors are represented by bold lowercase symbols e.g. $\mathbf{v}$.

Matrices are represented by bold uppercase symbols e.g. $\mathbf{P}$.

Notation

General

τ	The time constant for a first order Markov process
ν	A normally distributed random variable
t_k	Time at the k^{th} time step
x_{t_k}	State x at time t_k
$x(t_k)$	Alternative notation for state x at time t_k
$\mathbf{b}$	Bias vector
σ	Standard deviation

Reference frames

$\mathbf{C}_n^b$	Coordinate transform matrix from navigation frame to body frame
$\mathbf{C}_b^n$	Coordinate transform matrix from body frame to navigation frame
$_{MatrixToEuler(\mathbf{C}_{k1}^{k2})}$	The matrix to Euler angle conversion of the Coordinate transform matrix from frame k_1 to frame k_2
$\mathbf{p}_v^b$	Position of the vehicle in the body frame
$\mathbf{p}_v^n$	Position of the vehicle in the navigation frame
$\mathbf{v}_v^b$	Velocity of the vehicle in the body frame
$\mathbf{v}_v^n$	Velocity of the vehicle in the navigation frame
$\boldsymbol{\phi}_v^b$	Attitude of the vehicle in the body frame

$\boldsymbol{\phi}_v^n$	Attitude of the vehicle in the navigation frame

Doppler Velocity Log

v_{DVL}^b	Velocity of the DVL in the body frame
v_{DVL}^n	Velocity of the DVL in the navigation frame
$\hat{\mathbf{r}}_k^b$	Unit vector in the direction of the k$^t h$ DVL/ADCP beam in the body frame
v_k	Radial velocity along the k$^t h$ DVL beam
$\mathbf{z}_{DVL}$	DVL measurement
$\mathbf{v}_c^n$	Velocity of the water current sampled by DVL water-track

Inertial Measurement Unit

$\mathbf{f}_t^b$	Specific force (the IMU accelerometer output) in the body frame at time t
$\mathbf{g}^n$	Gravity vector in the navigation frame
$\mathbf{E}_{b,t}^n$	Rotation rates transformation matrix from body to navigation frame at time t
$\boldsymbol{\omega}_t^b$	Rotation rates (the IMU gyroscope output) in the body frame at time t
$\mathbf{C}_n^{b,t}$	Coordinate transformation matrix from navigation to body frame at time t
$\boldsymbol{\Omega}_e^n$	Rotation rate vector of the Earth in the navigation frame

Estimation

$\mathbf{x}(t_k)$	State vector $\mathbf{x}$ at time t_k
$\mathbf{h}_s[\mathbf{x}(t_k)]$	Predicted observation for constraint or sensor s given the state vector $\mathbf{x}(t_k)$
$\boldsymbol{\nabla}_x$	Jacobian of the observation model with respect to all estimates states
$p(\boldsymbol{\alpha}, \boldsymbol{\beta})$	Joint probability of $\boldsymbol{\alpha}$ and $\boldsymbol{\beta}$
$p(\boldsymbol{\alpha})$	Marginal probability of $\boldsymbol{\alpha}$
$p(\boldsymbol{\alpha}\|\boldsymbol{\beta})$	Conditional probability of $\boldsymbol{\alpha}$ given $\boldsymbol{\beta}$
$\hat{\mathbf{x}}$	State vector
$\hat{\hat{x}}$	Estimate of the state vector
$\hat{\mathbf{P}}$	Covariance matrix
$\hat{\mathbf{y}}$	Information vector
$\hat{\mathbf{Y}}$	Information matrix

Acoustic Doppler Current Profiler

$\mathbf{z}_{ADCP,i}$	ADCP measured current vector in the ith measurement cell
$\mathbf{W}_j$	Weighting function for each water current velocity from depth cell j
$\mathbf{v}^n_{c,j}$	Water current velocity from depth cell j
$\mathbf{b}_{c,i}$	Bias in the ith measurement cell in the body frame
$z_{adcp,i,k}$	ADCP measured radial current velocity in measurement cell i for beam k
$\mathbf{v}^n_{c,j}$	Water current velocity from IWVE j
$\mathbf{b}_{c,i,k}$	Bias in the measurement cell i for beam k
$v_{i,k}$	Radial velocity measurement in the i^{th} measurement cell, along the k^{th} beam
$\mathbf{v}^n_{c,j}$	Water current velocity in the navigation frame of the j^{th} depth cell

Hydrodynamic Vehicle Model

$\dot{x}_b$, $\dot{y}_b$ and $\dot{z}_b$	Water relative velocities of the vehicle in the body frame in the forward, starboard and down directions respectively
$\dot{\psi}$	Yaw rotational velocity of the vehicle
$\mathbf{M}$	Inertia matrix (including added mass)
$\mathbf{C}(\mathbf{v})$	Matrix of Coriolis and centripetal terms (including added mass)
$\mathbf{D}(\mathbf{v})$	Damping matrix
$\boldsymbol{\tau}$	Vector of control inputs
m	True mass of the vehicle
$\mathbf{b}^n$	Buoyancy force in the navigation frame
ρ	Density of water
d	Diameter of the propellor
n	Revolution speed of the thruster
v_T	Velocity of the water going into the propellor
$\mathbf{R}^{k_2}_{k_1}$	Coordinate transform matrix from frame k_1 to frame k_2 in 2 dimensions (only heading)

Abbreviations

AUV	Autonomous Underwater Vehicle
ADCP	Acoustic Doppler Current Profiler
AHRS	Attitude Heading Reference System
DVL	Doppler Velocity Log

EIF	Extended Information Filter
EKF	Extended Kalman Filter
IWVE	Isocurrent Water Volume Element
GPS	Global Positioning System
NED	North East Down
IMU	Inertial Measurement Unit
LBL	Long Base Line
SLAM	Simultaneous Localisation and Mapping
USBL	Ultra Short Base Line

Chapter 1

Introduction

1.1 Background

Autonomous Underwater Vehicles (AUVs) have found application in general underwater exploration and monitoring. This includes high-resolution, georeferenced optical/acoustic oceanfloor mapping, along with providing measurements of water column properties including currents, temperature and salinity. This data collection aids scientific research in areas such as climate change and oceanography. An advantage of AUVs over other methods of ocean observation is that as a self-contained vehicle, an AUV provides autonomy and decoupling from the sea surface.

Georeferencing, or the correct positioning in a global reference frame, is important for AUVs for path planning according to mission requirements, for registering independently navigated information, and for being able to revisit previous missions. Pictured in Figure 1.1 are AUV transects superimposed on large-scale ship-based bathymetry. This task could only have been achieved with georeferencing of the vehicle to fulfil the mission plan. The registration of the data collected during these dives with the large-scale bathymetry is also reliant on accurate georeferencing.

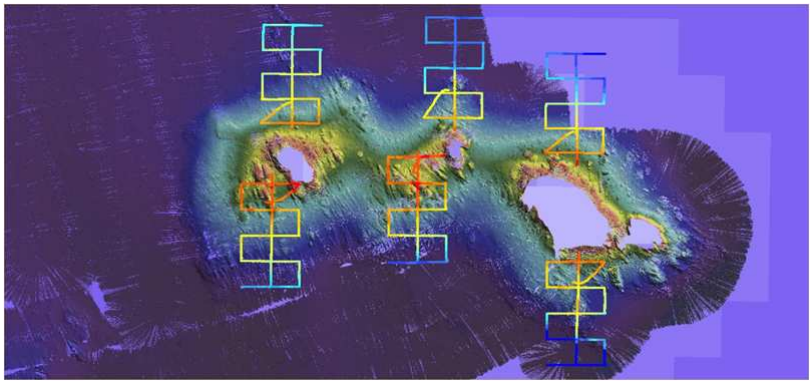

Figure 1.1 – AUV transects in the context of ship based bathymetry from South East Tasmania [59].

Revisitation requires georeferencing accuracy which is a function of the size of the area to be revisited, and the area of the sensor footprint. Pictured in Figure 1.2 is the same patch of rocks of the coast of Tasmania visited in the day, and then again at night, which is only possible with accurate georeferencing [61].

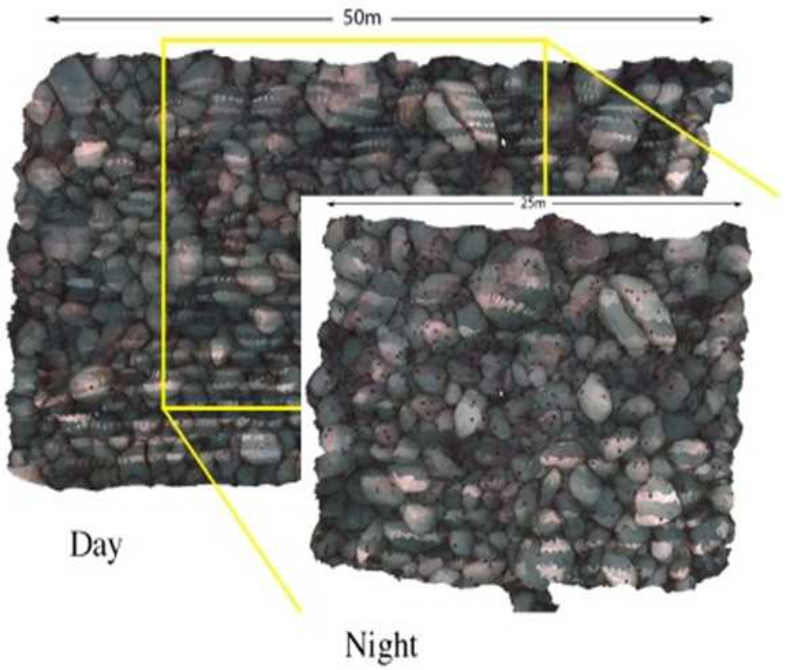

Figure 1.2 – A day and night revistation of the same patch of rocks, showing nocturnal urchin feeding [61].

AUV georeferencing is typically achieved in the following manner. The Global Positioning System (GPS) is available on the surface, but when underwater, the radio signals required for GPS do not penetrate the water. Instead, dead reckoning with Doppler Velocity Log (DVL) when underwater gives velocity-over-ground information when coupled with an attitude sensor, such as a magnetic compass or Inertial Measurement Unit (IMU) based Attitude Heading Reference System (AHRS). Pressure measurements are available for accurate absolute depth information. The *Sirius* AUV onboard devices are shown in Figure 1.3, which is a typical sensor suite for survey-class AUVs.

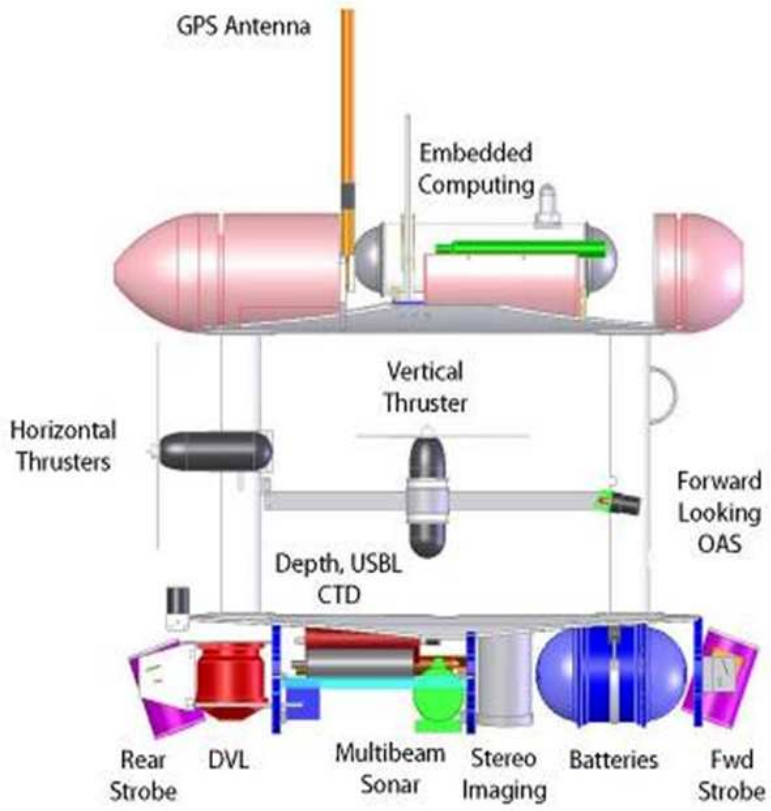

Figure 1.3 – The devices onboard the Sirius AUV.

Combined with Simultaneous Localisation and Mapping (SLAM), the relative seafloor map can be tightly constrained. However, the DVL has a limited range, therefore there are sections of a deeper dive which may not have DVL bottom-lock, and thus

other solutions are required in this situation.

Figure 1.4 illustrates present localisation options and their applicability at certain sections of the water column. On the surface we have GPS. Below the surface, but away from DVL bottom-lock, we rely on acoustic methods such as Ultra Short Base Line (USBL), which requires a ship to track the vehicle acoustically, or Long Base Line (LBL), which necessitates the setting up of an acoustic transponder network.

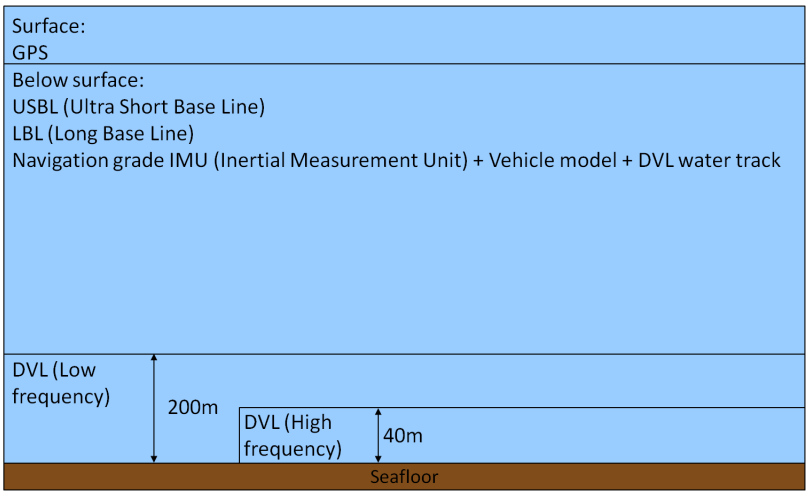

Figure 1.4 – Various present localisation options for AUVs at certain sections of the water column (excluding SLAM).

Alternatively, we may attempt localisation combining a navigation-grade IMU with a vehicle model and the water-track mode of the DVL, which measures the velocity of the sensor relative to a volume of water [17]. The accuracy of this method, however, is limited, as will be shown in the Literature review in the following chapter.

Once near the seafloor, low-frequency, high-power and lower-accuracy DVL will be within bottom-lock range at ∼200m altitude, and at ∼40m we have DVL bottom-lock with the high-frequency, low-power, high-accuracy DVL.

With the majority of the world's ocean floor significantly deeper than the 200m where DVL can be relied for underwater localisation, many missions will rely on USBL or LBL methods to achieve the desired accuracy for their mission. A depth map of the Ocean is illustrated in Figure 1.5. This requirement for using USBL or

establishing LBL infrastructure motivates the need for an alternative high-accuracy solution using only onboard instruments. A method which allows this provides AUVs with the potential for true autonomy, which would be valuable for AUV operations.

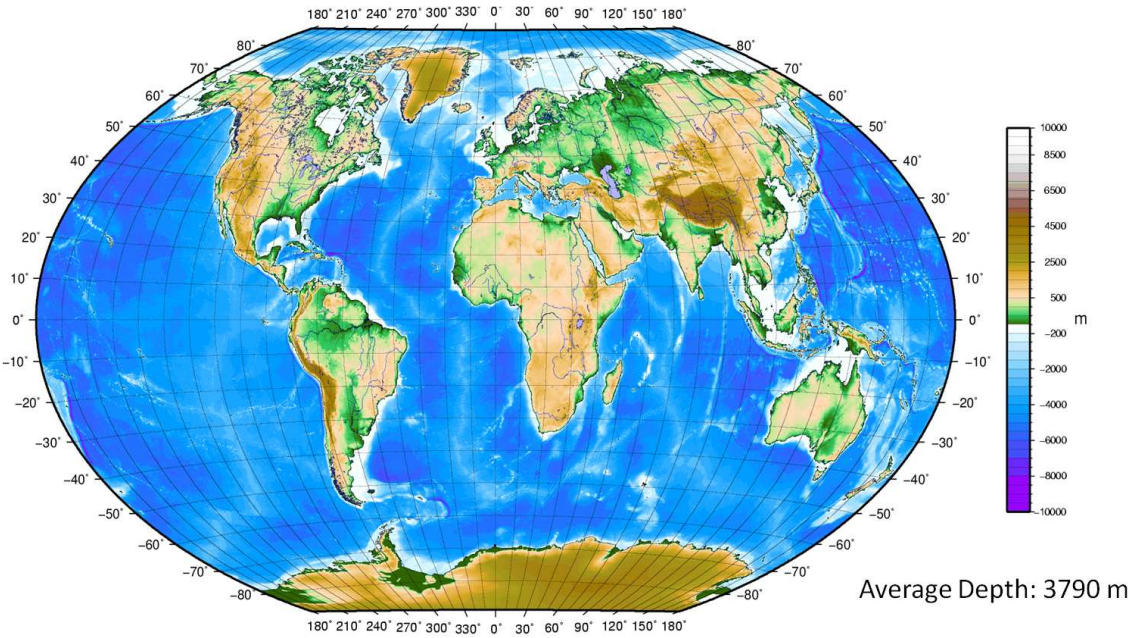

Figure 1.5 – The depth of the Ocean. Adapted from [54].

1.2 Problem Statement

This thesis will explore a solution to the problem of the lack of feasible mid-water localisation options without recourse to acoustic time-of-flight sensors. This method should rely on the vehicle's own measurements in order to improve the range and autonomy of AUV operations. This localisation information can then be fed back into a control algorithm to achieve real-time navigation according to the prescribed mission.

The proposed system should have the potential to work in real-time on board the vehicle with typical sensors to maximise the applicability of this method. It should

also be able to incorporate existing localisation techniques, such as SLAM, LBL or USBL, to increase the accuracy of localisation.

1.3 Principle Contributions

The principle contributions of this thesis include:

- The development, implementation, testing and validation of an isocurrent layer model for the water environment, along with a 3D velocity Acoustic Doppler Current Profiler (ADCP) sensor model to achieve localisation during vertical descent through the water column. The implementation and analysis of the developed models is achieved through the fusion of sensor measurements in an Extended Information Filter (EIF). Simulation and real data are utilised to validate the approach.
- The development, implementation, testing and validation of a gridded Isocurrent Water Volume Element (IWVE) model, along with a beam-directional ADCP sensor model. Spatial correlation in the water current vector field is accounted for in the EIF, through implementing least-squared constraints in the filter between IWVE states. Simulation and real data are utilised to validate the approach.
- The incorporation of IMU measurements and vehicle model constraints to simultaneously aid the localisation. Simulation and real data are utilised to validate the approach.

1.4 Thesis Structure

Chapter 2 outlines and discusses the literature surrounding underwater localisation. The direction for subsequent work is framed to incorporate existing work on the subject, while identifying areas of further work that are possible.

Chapter 3 introduces the ADCP-aided localisation method assuming the water current environment is a series of stacked water current layers, which are assumed to be constant with time in the order of a few minutes. The EIF is proposed as a method to fuse sensor information for localisation, while alternatives are also discussed. The ADCP localisation method is applied to a simple 2D example for illustrative and analytical purposes. Then a 3D example with a simulated AUV illustrates the performance in localisation. A full mission from the *Sirius* AUV is localised with ADCP sensor aiding during the descent and ascent phase of the mission, with view-based SLAM and DVL while within bottom-lock range, validating the approach.

Chapter 4 develops further ADCP sensor and water current environment modelling techniques for more general localisation, particularly in the horizontal direction where a non-constant water current layer may occur. A gridded isocurrent water volume element (IWVE) model is proposed to parameterise the ocean water. The radial velocity measurements of the ADCP sensor along the beam direction are exploited for their lateral looking capability. Neighbourhood correlation models are incorporated to aid the estimation of the water current vector field. Simulation and real data from the *Sirius* AUV are used to evaluate and validate this formulation.

Chapter 5 introduces a novel method to simultaneously incorporate measurements from an IMU and predictions from the vehicle model into the localisation. It exploits the fact that in a delayed-state framework, the inertial and vehicle model can be converted into a delayed-state constraint between poses. Previous methods attempting to do this required tuning a correlation state to model the vehicle constraint; the proposed method does not require such a tuning. Simulations show the applicability of this method, while real data from the *Sirius* AUV is used to validate the method.

Chapter 6 summarises the contributions of this thesis, and suggests avenues for future research.

Chapter 2

Literature Review

2.1 Global Positioning System (GPS)

The Global Positioning System is a satellite-based navigation system. It includes a set of orbiting satellites that are used as active beacons at known locations in space, and provides a measurement of 3D position to the user by providing a measurement of distances (derived from the time delay of a signal) to the satellite. Velocity is also determined by measuring the frequency shift of the signal [48]. The accuracy of these measurements are a function of errors in ephemeris, satellite clock, ionospheric/tropospheric propogation, receiver noise, resolution and multipath [48]. While an AUV can have access to GPS position and velocity measurements while on the sea surface, the signals do not penetrate water, requiring alternatives during submerged missions.

2.2 Doppler Velocity Log (DVL)

The DVL operates by sending out an acoustic pulse, and measuring the return pulse from the sea floor. Using the Doppler effect, the velocity of the sea floor relative to the instrument can be determined in the radial direction, as illustrated in Figure 2.1. By using four differently aligned sensor beams, the 3D velocity of the DVL can be

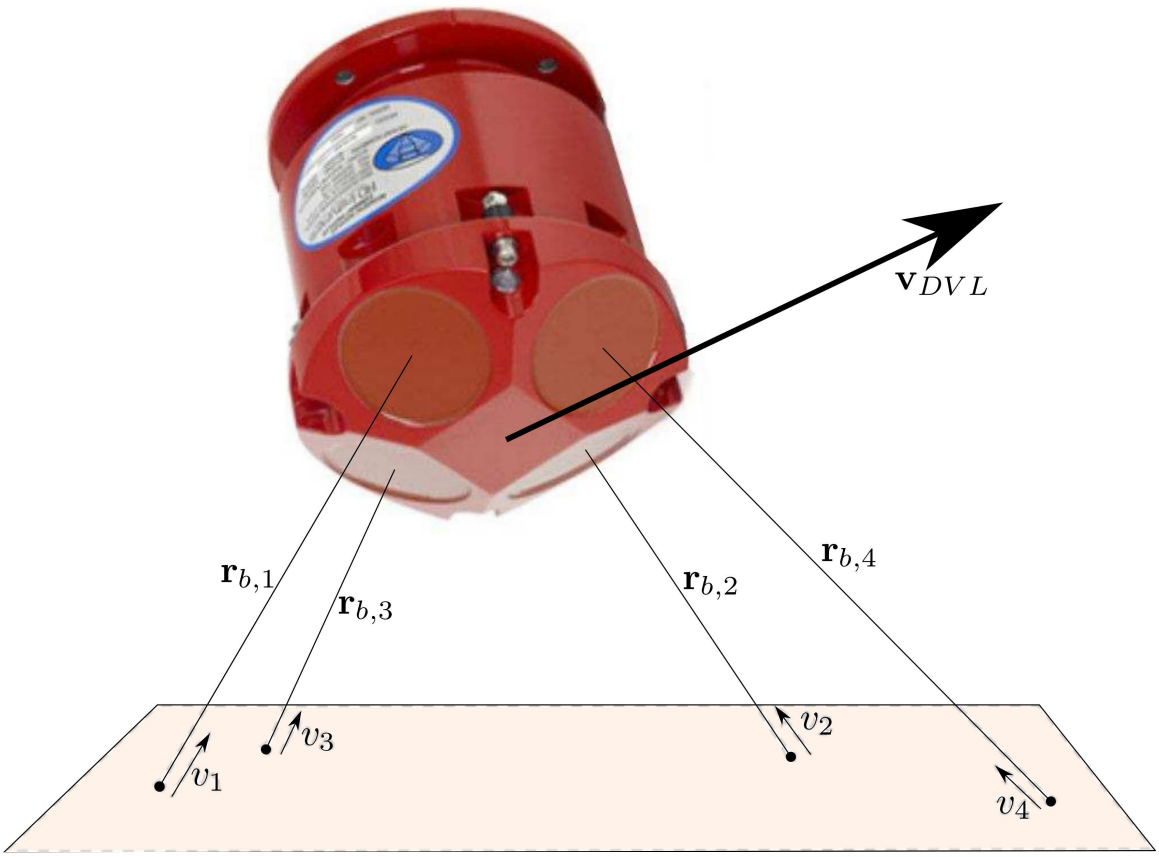

Figure 2.1 – The operation of the DVL sensor relies on measuring the radial velocity along a beam, and processing this information to arrive at the 3D velocity of the DVL sensor

determined. The fourth sensor beam provides redundancy in the estimation of the current profile velocities [11]. The result is a velocity estimate with accuracies typically about 10 mm/s (2σ). The method of combining the beam velocities to attain a 3D velocity as achieved by the RDI DVL is summarised as follows [19].

The beam velocity is the component of the DVL velocity along the beam.

$$v_k = (\mathbf{C}_b^n \hat{\mathbf{r}}_k^b) \cdot (-\mathbf{v}_{DVL}^n) \tag{2.1}$$

Where $\mathbf{v}_{DVL}^n$ is the velocity of the DVL in the navigation frame (such the North

East Down (NED) for a Local Transverse Mercator Projection [12] of the mission area), v_k is the beam velocity measurement of the k^{th} beam, $\mathbf{C}_n^b$ is the coordinate transformation matrix from navigation to body frame and $\hat{\mathbf{r}}_k^b$ is the unit vector along beam k. The four beams, asummed to be mounted at 30 degrees from the vertical in the RDI Navigator DVL, are combined to arrive at a 3D velocity.

$$\mathbf{v}_{beam} = [v_1\ v_2\ v_3\ v_4]^T \tag{2.2}$$

$$\mathbf{T} = \begin{bmatrix} a & -a & 0 & 0 \\ 0 & 0 & -a & a \\ b & b & b & b \\ d & d & -d & -d \end{bmatrix} \tag{2.3}$$

$$a = \frac{1}{2sin(\pi/6)} \tag{2.4}$$

$$b = \frac{1}{4cos(\pi/6)} \tag{2.5}$$

$$d = a/\sqrt{2} \tag{2.6}$$

$$\mathbf{z}_{DVL} = \mathbf{T}\mathbf{v}_{beam} \tag{2.7}$$

The resultant 3D velocity measurement ($\mathbf{z}_{DVL}$) is then modelled as the velocity of the DVL sensor along ground, transformed into body coordinates:

$$\mathbf{v}_{DVL}^b = \mathbf{C}_n^b \mathbf{v}_{DVL}^n \tag{2.8}$$

The redundant measurement allows the calculation of an error velocity term which can be used for error checking. For shallow waters, low-frequency (150kHz) DVL can be in continuous use for depths less than 200m. The DVL sensor provides measurements of the seafloor-relative velocity of the AUV. By combining this information with an appropriate heading reference, the observations can be placed in the global reference frame and integrated to facilitate underwater dead reckoning.

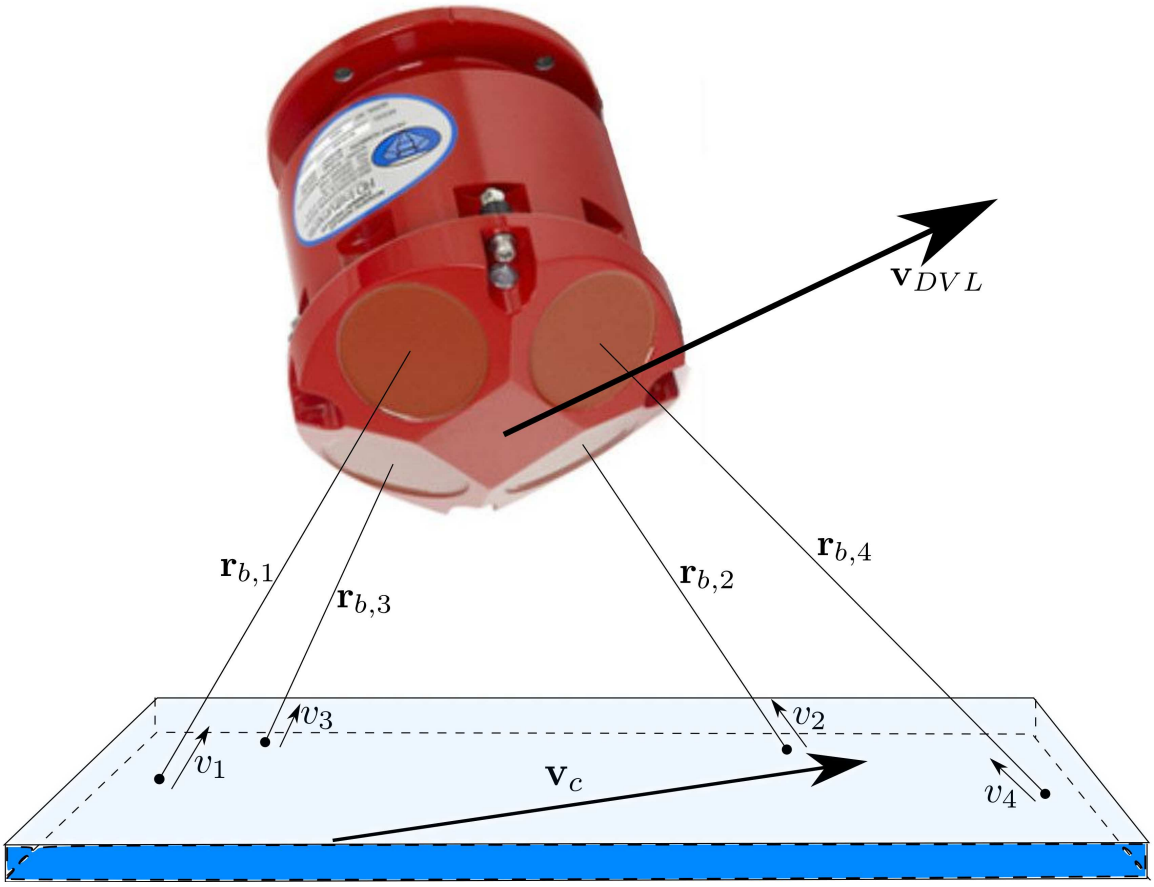

Figure 2.2 – Operation of the DVL sensor in Water track mode

2.2.1 DVL Water-Track Mode

The DVL in water-track mode provides a measurement of the velocity of the AUV relative to a user-programmable water sampling volume that extends away from the instrument. The assumption of horizontally homogenous currents must be applied across a water layer to arrive at a water current estimate [11]. This is portrayed in Figure 2.2.

In addition to the motion of the DVL, the beam velocity will include a component of the water current velocity.

$$v_k = (\mathbf{C}_b^n \hat{\mathbf{r}}_k^b) \cdot (-\mathbf{v}_{DVL}^n + \mathbf{v}_c^n) \tag{2.9}$$

Where $\mathbf{v}_c^n$ is the water current velocity in the navigation frame. In present underwater localisation, currents are typically treated as a single time-varying parameter [36] [16] using observations from the DVL water-track mode. In [16], the water current in the sampled volume is modeled as a first-order Markov process model of the form

$$\dot{\mathbf{v}}_c = -\frac{1}{\tau_c}\mathbf{v}_c + \nu_c \tag{2.10}$$

where τ_c is a time constant which affects the rate at which the bias changes, and ν_c is a random variable with standard deviation [8]

$$\sigma_c = \sqrt{\frac{2f\sigma_{c\,limit}^2}{\tau_c}} \tag{2.11}$$

where $\sigma_{c\,limit}$ is the standard deviation of the bias in the long term, a limit of the magnitude of the water current random walk with time (a manually tuned parameter), f is the frequency at which the process model operates and τ_c is a tuned parameter for the time constant of the expected rate change of the water current.

Thus, since the AUV will also be moving during time periods, spatial and temporal changes in the water currents are coupled.

2.3 Time of Flight Acoustic Localisation methods

In cases where the seafloor depth is greater than the DVL bottom-lock range, transiting from the surface, where GPS is available, to the seafloor presents a localisation problem, since both GPS and DVL are unavailable in the mid-water column. Traditional solutions during this descent include range-limited Long Base Line (LBL) acoustic networks which require additional ship time to deploy and survey (shown in

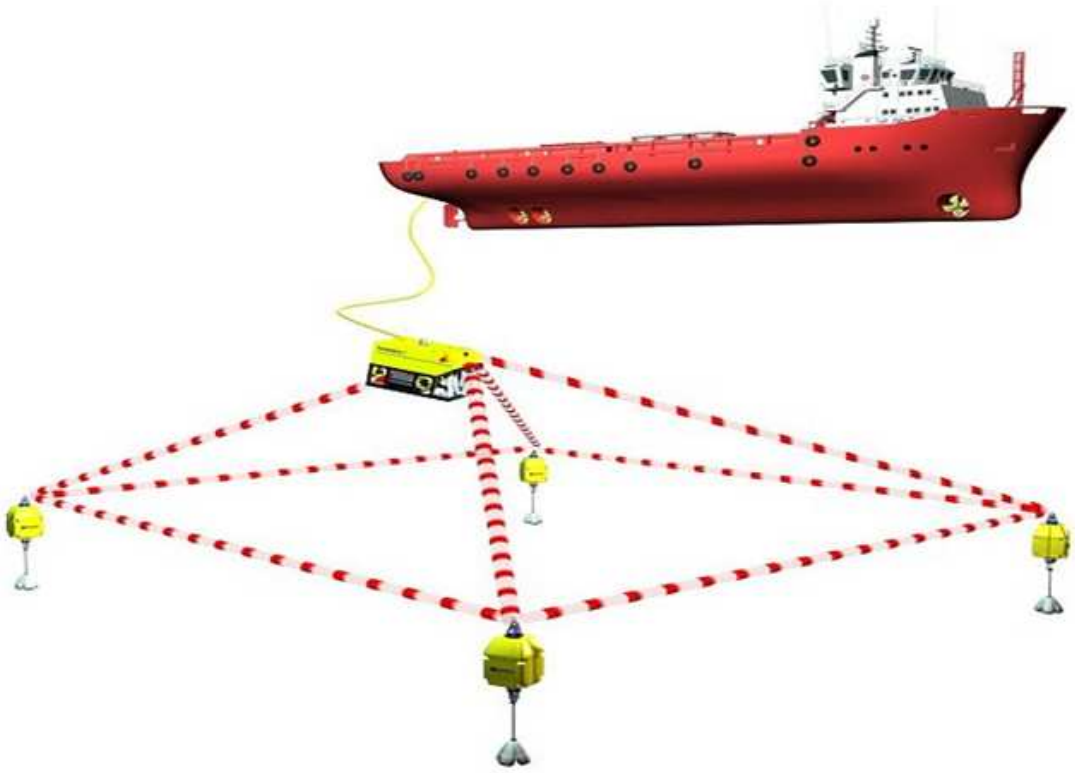

Figure 2.3 – The LBL localisation method relies on surveying in a series of acoustic beacons from a ship, and then navigating the Remotely Operated Vehicle (ROV) or AUV inside the acoustic transponder network. Image courtesy of Sonardyne.

Figure 2.3), along with methods requiring tending, such as ship-based Ultra Short Baseline (USBL) acoustic transceivers (visualised in Figure 2.4). Acoustic positioning may also suffer from multipath returns and the sound speed profile through the water column needs to be accurately known. These acoustic methods typically give $\mathcal{O}(10m)$ accuracy at 1-10 kilometre ranges [24] [33].

2.4 Inertial Measurement Unit (IMU)

IMUs employ accelerometers and gyroscopes to provide body-relative accelerations and rotation rates to constrain the position, velocity and attitude estimates through integration of the outputs. Assuming low velocities as experienced by an AUV, the equations governing this integration are as follows:

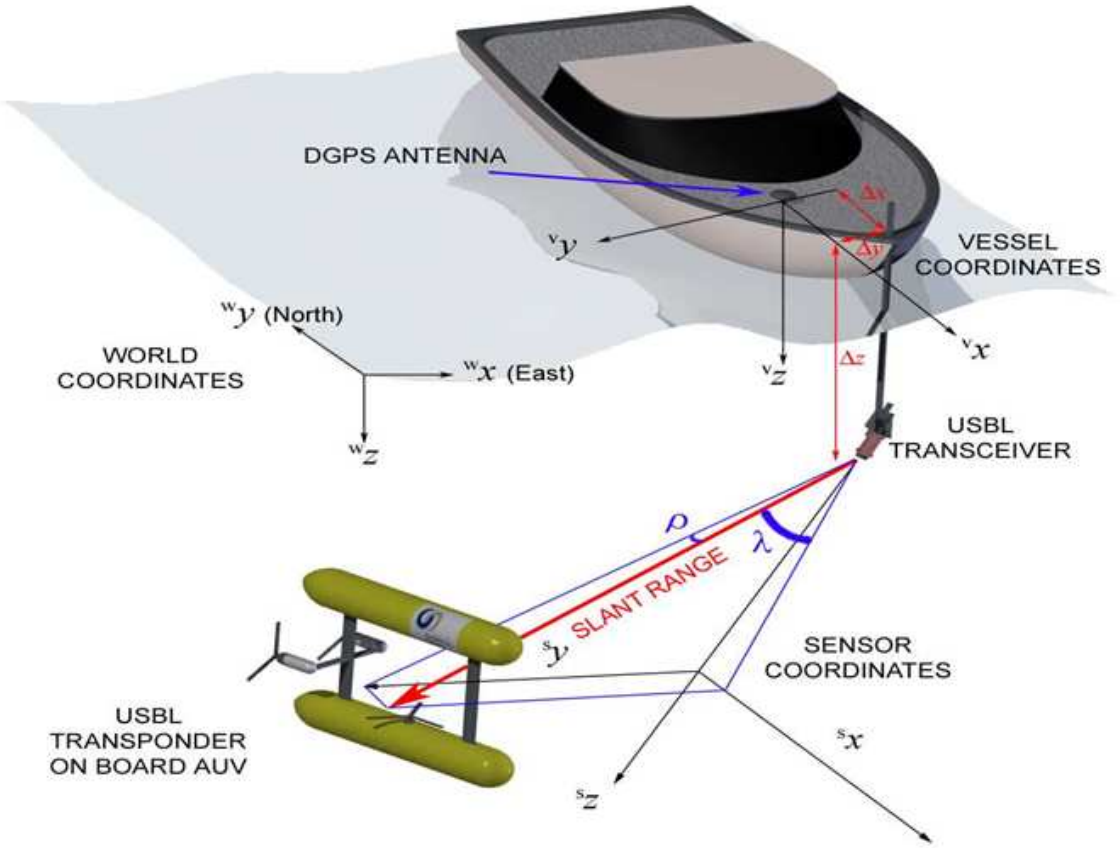

Figure 2.4 – The USBL localisation method requires a ship with GPS to track the relative bearing, tilt and range to the AUV, allowing the AUV to be georeferenced. Image from [45].

$$(2.12)$$

$$\mathbf{v}_{t_2}^n = \mathbf{v}_{t_1}^n + \int_{t_1}^{t_2} (\mathbf{C}_{b,t}^n \mathbf{f}_t^b + \mathbf{g}^n) dt \tag{2.13}$$

$$\mathbf{p}_{t_2}^n = \mathbf{p}_{t_1}^n + \int_{t_1}^{t_2} \mathbf{v}_t^n dt \tag{2.14}$$

$$\boldsymbol{\phi}_{t_2}^n = \boldsymbol{\phi}_{t_1}^n + \int_{t_1}^{t_2} \mathbf{E}_{b,t}^n (\boldsymbol{\omega}_t^b - \mathbf{C}_n^{b,t} \boldsymbol{\Omega}_e^n) dt \tag{2.15}$$

$$(2.16)$$

where:

- $\mathbf{v}_t^n$ is the velocity of the IMU at time t in the navigation frame,
- $\mathbf{C}_{b,t}^n$ is the coordinate transformation matrix from body to navigation frame at time t,
- $\mathbf{f}_t^b$ is the specific force (the IMU accelerometer output) in the body frame at time t,
- $\mathbf{g}^n$ is the gravity vector in the navigation frame,
- $\mathbf{p}_t^n$ is the position of the IMU at time t in the navigation frame,
- $\boldsymbol{\phi}_t^n$ is the attitude of the IMU at time t in the navigation frame,
- $\mathbf{E}_{b,t}^n$ is the rotation rates transformation matrix from body to navigation frame at time t,
- $\boldsymbol{\omega}_t^b$ is the rotation rates (the IMU gyroscope output) in the body frame at time t,
- $\mathbf{C}_n^{b,t}$ is the coordinate transformation matrix from navigation to body frame at time t,
- $\boldsymbol{\Omega}_e^n$ is the rotation rate vector of the Earth in the navigation frame.

Given an IMU capable of gyrocompassing (observing the locally projected 15 deg/hr rotation of the Earth), the position error growth is approximately [52]:

$$\delta p \approx \delta\omega \, \mathbf{R}_0 t \tag{2.17}$$

Where δp is the position drift, $\delta\omega$ is the gyro bias, $\mathbf{R}_0$ is the radius of the Earth, and t is time.

Thus a navigation-grade IMU (often in excess of $100K US [24]) with 0.01°/hr gyro bias, will achieve ∼1 km/hr position drift without aiding. Alternatively, a tactical grade IMU (approximately $16K US) with $1^\circ/hr$ gyro bias will achieve ∼100 km/hr position drift without aiding.

While on the sea surface, the iXSea PHINS IMU (Navigation grade) achieves horizontal localisation with three times better accuracy than the aiding GPS according to specification [20]. The Novatel OEM628 GPS receiver specification [40] quotes a horizontal RMS error with dual frequency (L1/L2) of 1.2 m. Thus the 2σ uncertainty will be 2.4 m. Therefore an iXSea PHINS IMU coupled with the Novatel OEM628 GPS receiver could achieve 0.8 m 2σ position uncertainty on the sea surface.

Once underwater, when the vehicle is within DVL range of the seafloor, $\sim 0.2\%$ distance travelled position error growth (2σ) is possible when DVL is coupled with a navigation-grade IMU [38] [20]. In [53], the position error growth in this case is expected to grow with the square root of time.

2.5 Vehicle Model based Navigation

Using the vehicle dynamics to predict how the vehicle will move given the estimated control action, such as thrusters, allows additional information to be fed into the localisation algorithms.

$$\mathbf{x}(t_{k+1}) = f_{vehicle\,model}(\mathbf{x}(t_k), \mathbf{u}(t_k)) \tag{2.18}$$

Where $\mathbf{x}(t_k)$ is the pose (position, velocity and attitude) of the vehicle at the k^{th} timestep, and $\mathbf{u}(t_k)$ is a vector of control inputs at the k^{th} timestep.

In [17], the vehicle model aids the localisation by modelling the AUV dynamics given control actions and the surrounding water current field. The AUV model parameters must be estimated prior to their usage in the localisation [18]. This is fused with the predicted motion from an IMU in the update stage of an Extended Kalman Filter (EKF), and adding a correlation term to the state vector which has a first-order Markov bias model. This model would require tuning, and may not fully capture the true dynamics of this correlation.

This correlation is modeled as a first-order Markov process model of the form

$$\dot{\Delta\mathbf{v}}_{wb} = -\frac{1}{\tau_{v_{wb}}}\Delta\mathbf{v}_{wb} + \nu_{v_{wb}} \tag{2.19}$$

where $\tau_{v_{wb}}$ is a time constant which affects the rate at which the bias changes, and $\nu_{v_{wb}}$ is a random variable with standard deviation [8]

$$\sigma_{v_{wb}} = \sqrt{\frac{2f\sigma^2_{v_{wb}\,limit}}{\tau_{v_{wb}}}} \tag{2.20}$$

where $\sigma_{v_{wb}\,limit}$ is the standard deviation of the state in the long term, a limit to the magnitude of the vehicle model correlation state random walk with time (a tuned parameter), and f is the frequency at which the process model operates. $\tau_{v_{wb}}$ is a tuned parameter for the time constant of the expected rate change of the vehicle model correlation.

A navigation-grade IMU coupled with a vehicle model and DVL water-track mode estimates of currents can achieve ∼120m per hour (2σ) position uncertainty growth [16], by assuming a time-varying current in the measured water sampling volume, and after acquiring DVL bottom-lock. Prior to DVL bottom-lock, the position uncertainty growth is ∼900m per hour [16].

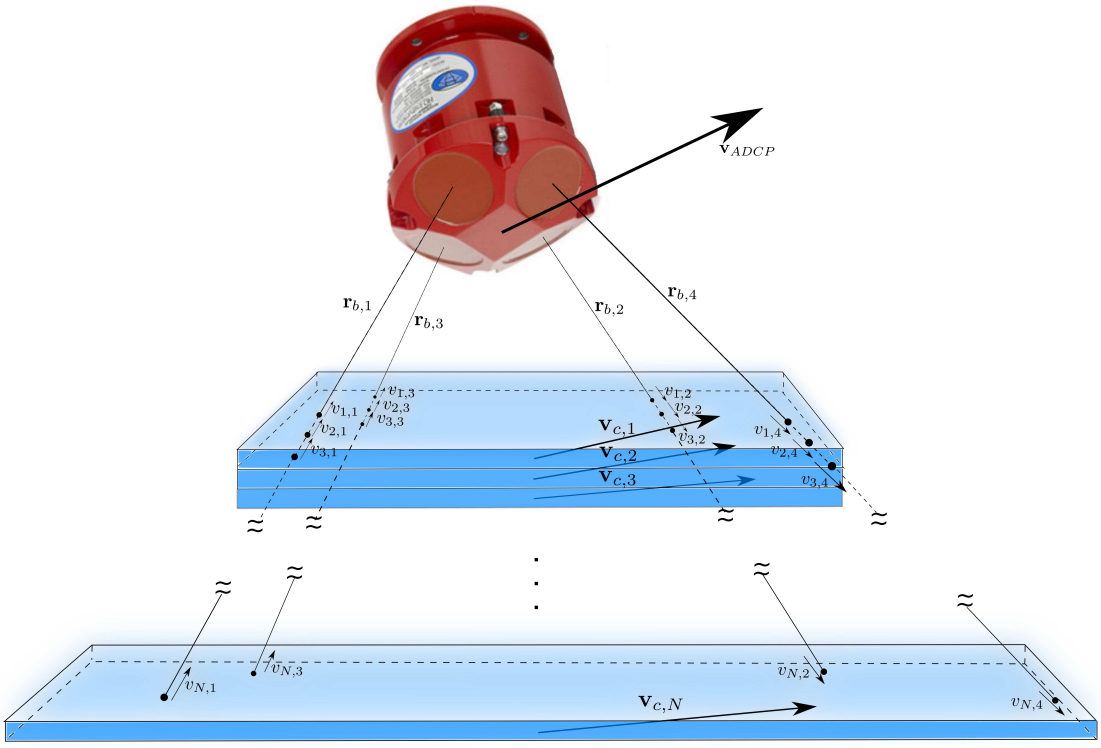

Figure 2.5 – The ADCP mode of the DVL sensor operates by looking at the returns from scatterers in the water column along each of the 4 beams. This information can be combined to arrive at the 3D velocity of the water currents relative to the ADCP sensor in a similar way to the DVL sensor. In this diagram, the measurement cell is set to the same size as the depth cell (because $M = N$), this is optional and need not be the case, although it simplifies modelling.

2.6 Acoustic Doppler Current Profiler (ADCP)

The ADCP is in fact a different mode of the same DVL sensor. It operates by sending out an acoustic pulse, and relying on scatterers, such as plankton, to reflect back the pulse. Using the Doppler effect, the velocity of the scatterers relative to the instrument can be determined in the radial direction. Since it is assumed that the scatterers move with the water currents, the ADCP is measuring the radial velocity of the water column currents relative to the ADCP. By gating the returned signal with time, currents at different ranges from the ADCP sensor can be measured, segmenting the observation into measurement cells. This is illustrated in Figure 2.5.

The radial velocities measured by the ADCP sensor are:

$$v_{i,k} = (\mathbf{C}_b^n \hat{\mathbf{r}}_k^b) \cdot (-\mathbf{v}_{ADCP}^n + \mathbf{v}_{c,j}^n) \tag{2.21}$$

Where $v_{i,k}$ is the radial velocity measurement in the i^{th} measurement cell, along the k^{th} beam and $\mathbf{v}_{c,j}^n$ is the water current velocity in the navigation frame of the j^{th} depth cell.

By using 4 differently aligned sensor beams and assuming horizontally homogeneous currents, the 3D velocity of the current can be determined. This is done in a similar manner to the DVL sensor. The fourth sensor provides redundancy in the estimation of the current profile velocities [11]. Echo intensity can also be used to check if there are anomalies corrupting the returns, such as schools of fish [41]. The result is a current estimate with accuracies typically about 20 mm/s (2σ) observing 2 m/s currents[1].

The focus within the oceanographic community with regard to ADCP use is on estimating water current profiles, such as applying least-squares methods to fuse lowered ADCP and DVL bottom-lock information [57]. Accounting for ADCP sensor biases [11] and sensor uncertainties are not tackled, as the effect on the overall current profile is minimal, however there are implications in the velocity estimates of the ADCP sensor itself during descent or ascent. This is important for localisation as the velocity uncertainty relates to the position uncertainty growth rate.

More recently, in [50], a least-squares approach to the localisation problem focusing on vertical descent and ADCP and DVL measurements is explored, along with optimizing ADCP configuration. This work shows ADCP localisation performance for a well-configured 1 km depth dive can give qualitatively similar results to USBL in this case, with errors of the order of 10m. Fusion with other sensors, such as IMU, bias modelling of the ADCP sensor and generalising to horizontal motion was not explored.

[1]Sourced from email from RD Instruments providing standard deviation of the instrument

Concurrent work

Undertaken concurrently to this thesis is the work of Stanway in [51]. Part of Stanway's work is directly relevant to this thesis as the ADCP is used for localisation. He explores a least squares approach to estimate water currents and vehicle pose. It can be seen as complementary solutions to the same problem in this thesis. In Stanway's work, ADCP sensor configuration and diagnostics are performed, which looks at information such as return strength of the signal, and looks at practical ADCP implementation issues for deep water. In his work, biases are not considered, and an IMU or vehicle model are not incorporated. Additionally, uncertainty bounds are not analysed in Stanway's work. The recursive least squares approach is similar to the compututational complexity of the delayed-state filter (with marginalisation) used in this thesis, for the same sensor usage. Incorporating SLAM or retaining the entire state history of the filter for relinearisation purposes will increase the computational complexity, but Stanway's implementation does not tackle these additions. The accuracy of the method used in this thesis is superior to that of Stanway's, since more sensors will be accommodated. With the same sensors, the incorporation of the ADCP biases in the filter will provide better accuracy than Stanway's work.

2.7 Underwater SLAM

While not directly applicable in the mid-water column, when close to the seafloor, Simultaneous Localisation and Mapping (SLAM) methods allow further navigation improvements [60] by identifying previously explored regions to constrain the localisation solution. This can be achieved by using visual features [32], as shown in Figure 2.6, bathymetric features [2] or a combination of both [26] as shown in Figure 2.7.

SLAM allows more accurate relative localisation when close to the seafloor, as well as enforcing map consistency. To georeference this map, mid-water localisation would need to occur when GPS is unavailable, or USBL/LBL will need to be available the entire mission.

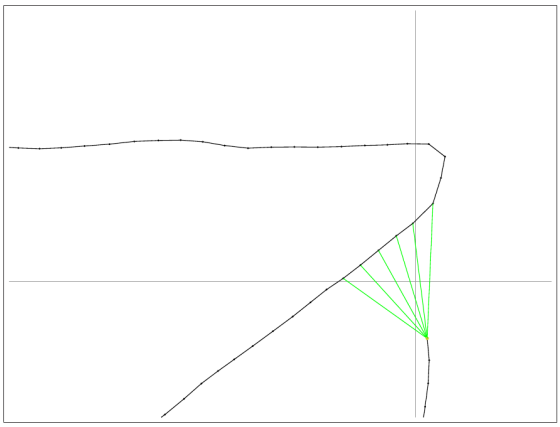

(a) Before loop-closure

(b) After loop-closure

Figure 2.6 – The green lines in (a) represent loop closure hypotheses which could be used to correct the localisation. In (b), a match between the previous image and the current image is made, and a loop closure constraint is applied in red.

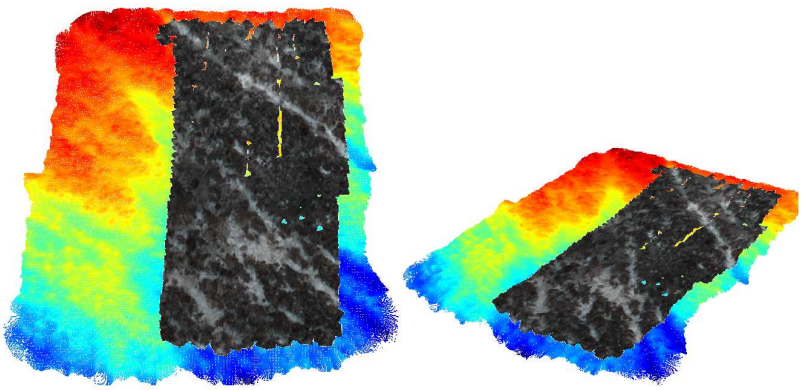

Figure 2.7 – The map created following Visual and Bathymetric SLAM, allowing map consistency to be improved through coupling the mapping with localisation [26].

2.8 Summary

A hypothetical example is used to compare the aforementioned localisation options as typically applied in the current state-of-the-art of underwater localisation. For a one hour descent, which is typically between approximately 700m and 1400m of depth depending on AUV descent rates, Figure 2.8 shows the performance of various options. Without USBL and LBL and relying on an IMU/vehicle model/DVL water track navigation solution will give 120m (2σ) accuracy. Therefore, missions requiring revisit capabilities in depths beyond a few hundred metres must invest in the greater effort of external acoustic methods. LBL is the typical mode of operation for vehicles such as the lost-at-sea Autonomous Benthic Explorer (ABE) AUV when searching for hydrothermal vents [21], where high revisitation accuracy is required for nested surveys (shown in Figure 2.9).

Present methods using on-board sensors to aid localisation in the mid-water column, which do not rely on external acoustics such as LBL or USBL, include IMUs, vehicle model and DVL in water-track mode. Methods using the DVL water-track mode to incorporate observed water currents rely on the assumption that the correlation model is known, and constant, for all time [16]. In reality, the sampled water current is changing due to the vehicle translating and observing a spatially changing water current vector field, along with any temporal change in the water currents.

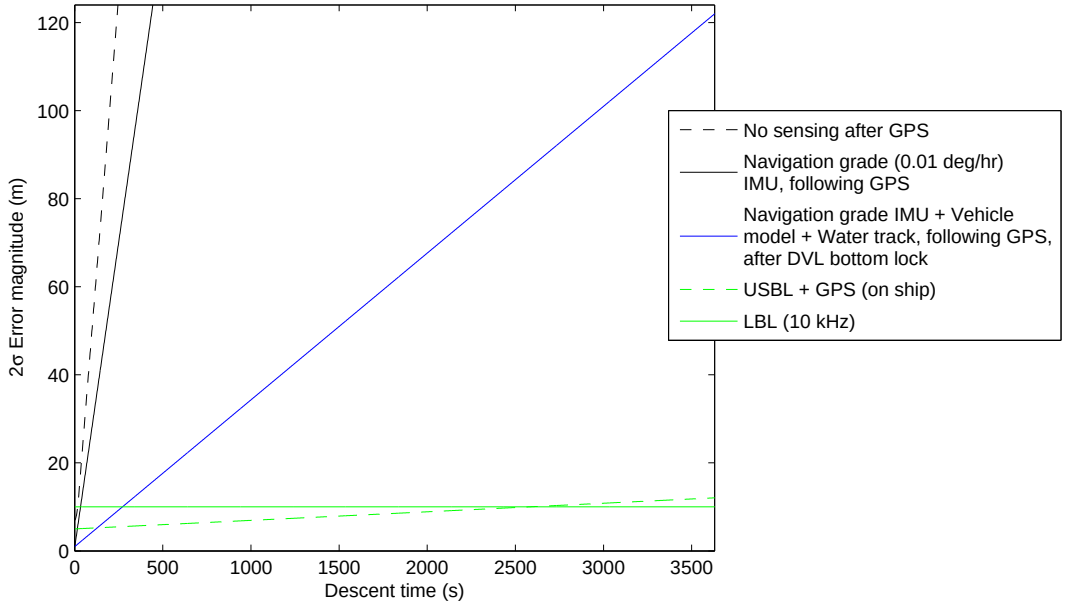

Figure 2.8 – Comparison between different underwater localisation methods where GPS is unavailable for a 1 hour dive, which is typically between approximately 700m and 1400m of depth depending on AUV descent rates. No sensing at all results in errors due to the unestimated water currents.

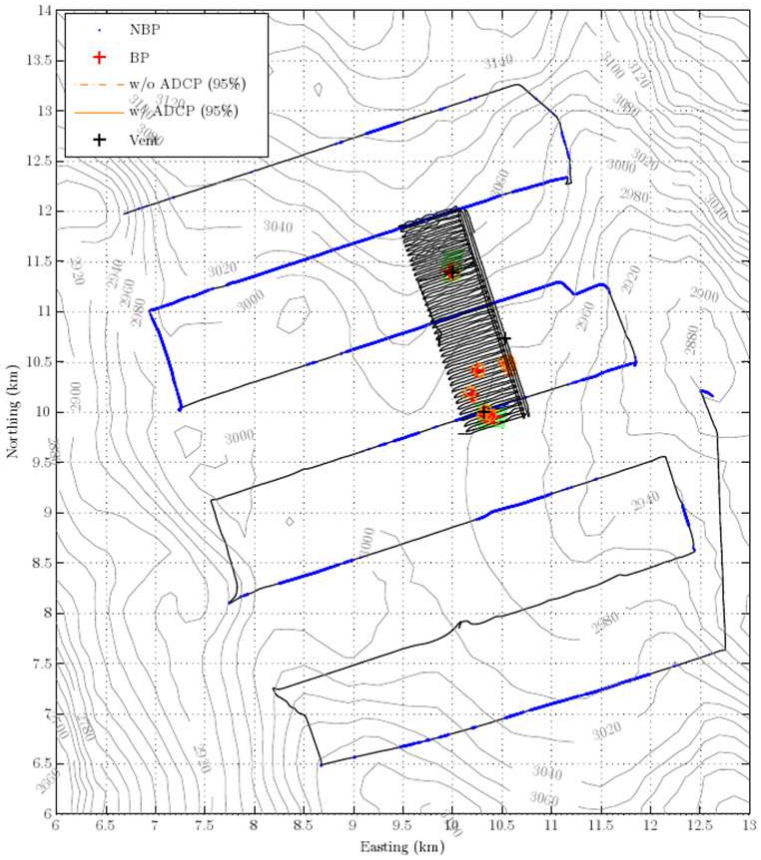

Figure 2.9 – The nested survey strategy used by the ABE AUV to pinpoint the location of a hydrothermal vent [21].

Chapter 3

ADCP Sensor Aiding with Water Layers

An alternative to using the bulk water volume relative velocity from the DVL water-track mode [16], is to use the ADCP mode to provide finer depth resolution current estimation. This opens the possibility of improved vehicle motion estimates, given the observation of fine-scale current structure.

The standard parametrisation of the ocean for Lowered ADCP (LADCP) is to layer the ocean into discrete, isocurrent layers [57], or depth cells. This relies on the assumption of horizontal homogeneity across the water current layer [11]. This chapter applies additional modelling to the ADCP sensor along with further sensor fusion to the standard LADCP formulation, with a focus instead on the vehicle localisation performance instead of the water current profile estimation. As will be shown, accounting for the correlation in the vehicle and water current profile estimates result in improvements in the quality of the estimation of both the vehicle pose and water column current profile.

This chapter explores the performance of the ADCP-aided localisation algorithm as an alternative form of georeferencing for AUV missons for vertical dives. A two degrees-of-freedom simulation allowed the analysis of the error dynamics of the problem. A six degrees-of-freedom simulation is undertaken to explore the possible performance

of the algorithm under typical parameters for the *Sirius* AUV. Finally, a validation of the ADCP localisation algorithm was completed with real data from the Sirius AUV. As a result, this chapter demonstrates the ability to achieve constrained error growth in position by incorporating ADCP measurements into the navigation solution while a vehicle is transitting between the sea surface and the seafloor.

3.1 ADCP estimation and navigation aiding process

In order to illustrate a typical scenario where mid-water localisation is possible with ADCP, a sensing process is outlined. We assume that initially the AUV has position and velocity estimates in the navigation frame at the sea surface from GPS. With the ADCP sensor, body-relative water depth cell velocities below the vehicle are observed with each ADCP measurement cell. These observations can be used to estimate the full current profiles in the navigation frame using the estimated vehicle velocity at the surface. This is illustrated in Figure 3.1(a).

After another ADCP measurement is made, the vehicle reobserves the same depth cells. Given the estimated water current velocity of the reobserved depth cell and the body-relative velocity of these depth cells from the ADCP a filter can be used to simultaneously update the estimate of the vehicle velocity and current profile velocities. This relies on the assumption that the water current velocity in this depth cell remains constant, which is realistic over a reobservation period of minutes. This is a standard assumption in oceanographic water current profiling [57]. This is shown in Figure 3.1(b).

New depth cells can also now be estimated as the vehicle changes depth as shown in Figure 3.1(c). The result is an estimate of the vehicle motion and a water column current profile. When the vehicle is within DVL range of the seafloor, this velocity constraint on the vehicle is also incorporated into the filter. The process is summarised in Algorithm 1.

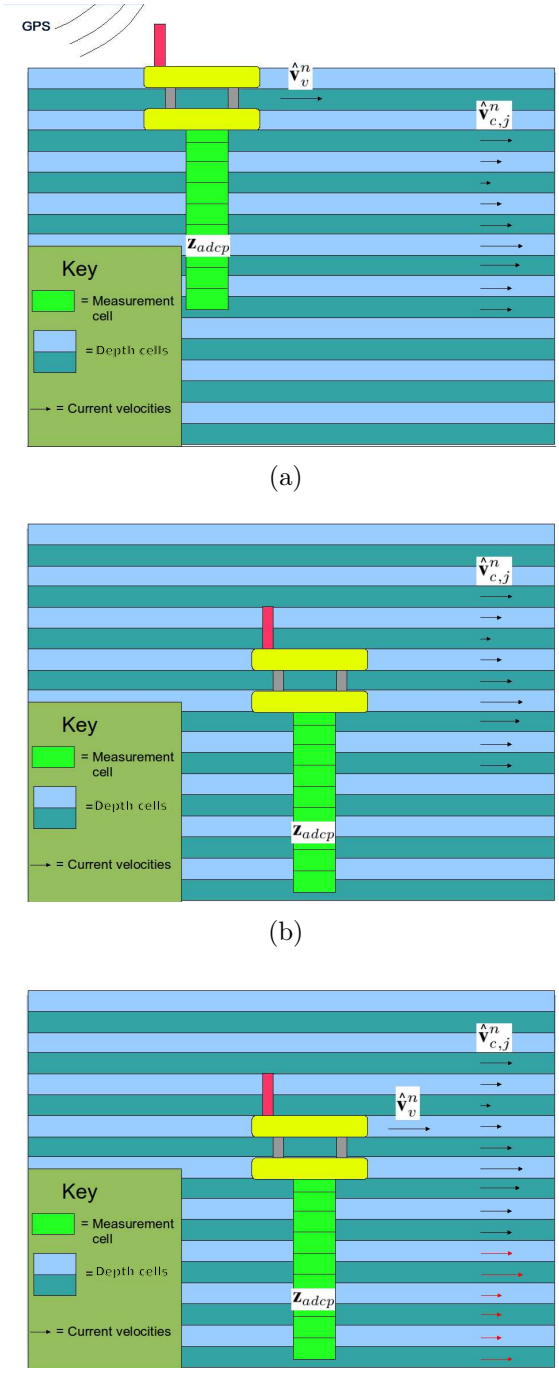

Figure 3.1 – ADCP-aiding method sequence (a) Initial GPS position and velocity are known, and water velocities can be deduced. (b) The AUV moves, and reobserves the same depth cells.(c) The AUV velocity in the world frame can be deduced, along with new depth cells shown in red.

Algorithm 1 ADCP-aided localisation during vertical descent

while On Surface **do**
  $\mathbf{p}_v^n(t_k) = \mathbf{p}_{GPS}$
  $\mathbf{v}_v^n(t_k) = \mathbf{v}_{GPS,Doppler}$
  $\mathbf{v}_{currents}^b = \mathbf{v}_{ADCP}$
  $\mathbf{v}_{currents}^n = \mathbf{v}_v^n(t_k) + \mathbf{v}_{currents}^b$
end while
while Underwater **do**
  $p_v^n, z(t_k) = p_{z,PRESSURE\,DEPTH}$
  $\mathbf{v}_{currents}^b = \mathbf{v}_{ADCP}$
  $\mathbf{v}_v^n(t_k) = \mathbf{v}_{currents}^n - \mathbf{v}_{currents}^b$
  $\mathbf{p}_{v,horizontal}^n(t_k) = \mathbf{p}_{v,horizontal}^n(t_{k-1}) + \mathbf{v}_v^n(t_k)\Delta T$
  if New water current observed with depth **then**
    $\mathbf{v}_{new\,currents}^n = \mathbf{v}_v^n(t_k) + \mathbf{v}_{new\,currents}^b$
  end if
  if Within DVL bottom-lock range **then**
    $\mathbf{v}_v^n(t_k) = \mathbf{v}_{DVL}$
  end if
end while

3.2 Information filter with current profiling

Vehicle pose states, ADCP bias states and water current velocity are all to be simultaneously estimated. The ADCP bias states are estimated as this could lead to corrections in the localisation, and the uncertainty that they introduce can be modelled. Water velocity states are parameterised as isocurrent depth cells, each with an associated velocity vector. If water currents grid cells are assumed approximately constant temporally, their reobservation following their initial observation with an ADCP should be able to constrain the vehicle velocity as illustrated in Figure 3.1(b).

An Extended Information Filter (EIF) can be applied to estimate the states of the vehicle given the various vehicle sensor measurements [58], allowing implementation of the water current layer depth cell states for estimation, along with maintaining the correlations between the states. The EIF also allows relinearisation if required and can incorporate view-based SLAM if applicable. It also enables viewing the entire state history of the vehicle for analysis purposes, as it acts as a delayed state smoother. Further practical usage discussion is contained in Section 3.2.1.

The EIF maintains the correlations between states in addition to a mean estimate of the states. Vehicle pose states such as position, velocity and attitude (IMU bias states are included if IMU bias estimation is incorporated), ADCP bias states and water current velocity states are stored in a state vector (representing the mean estimate of

the states) of the form

$$\hat{\mathbf{x}}^{+}(t_k) = \begin{bmatrix} \hat{\mathbf{x}}^{+}_{P_1}(t_k) \\ \vdots \\ \hat{\mathbf{x}}^{+}_{P_{n_P}}(t_k) \\ \hat{\mathbf{x}}^{+}_{b_{c,1}}(t_k) \\ \vdots \\ \hat{\mathbf{x}}^{+}_{b_{c,n_b}}(t_k) \\ \hat{\mathbf{x}}^{+}_{v_{c,n}}(t_k) \\ \vdots \\ \hat{\mathbf{x}}^{+}_{v_{c,n_v}}(t_k) \end{bmatrix} = \begin{bmatrix} \hat{\mathbf{x}}^{+}_{P}(t_k) \\ \hat{\mathbf{x}}^{+}_{b_c}(t_k) \\ \hat{\mathbf{x}}^{+}_{v_c}(t_k) \end{bmatrix} \tag{3.1}$$

where $\hat{\mathbf{x}}^{+}_{P}(t_k) = \begin{bmatrix} \hat{\mathbf{x}}^{+\mathsf{T}}_{P_1}(t_k), ..., \hat{\mathbf{x}}^{+\mathsf{T}}_{P_{n_P}}(t_k) \end{bmatrix}^{\mathsf{T}}$ is a vector of past and present pose states where n_P is the number of vehicle pose states, $\hat{\mathbf{x}}^{+}_{b_c}(t_k) = \begin{bmatrix} \hat{\mathbf{x}}^{+\mathsf{T}}_{b_{c,1}}(t_k), ..., \hat{\mathbf{x}}^{+\mathsf{T}}_{b_{c,n_b}}(t_k) \end{bmatrix}^{\mathsf{T}}$ is a vector of past and present ADCP bias states where n_b is the number of ADCP bias states and $\hat{\mathbf{x}}^{+}_{v_c}(t_k) = \begin{bmatrix} \hat{\mathbf{x}}^{+\mathsf{T}}_{v_{c,1}}(t_k), ..., \hat{\mathbf{x}}^{+\mathsf{T}}_{v_{c,n_v}}(t_k) \end{bmatrix}^{\mathsf{T}}$ is a vector of past and present ADCP water current velocity states where n_v is the number of water current velocity states. The covariance between the pose states and the water current states are in the form

$$\hat{\mathbf{P}}^{+}(t_k) = \begin{bmatrix} \hat{\mathbf{P}}^{+}_{PP}(t_k) & \hat{\mathbf{P}}^{+}_{Pb_c}(t_k) & \hat{\mathbf{P}}^{+}_{Pv_c}(t_k) \\ \hat{\mathbf{P}}^{+\mathsf{T}}_{Pb_c}(t_k) & \hat{\mathbf{P}}^{+}_{b_cb_c}(t_k) & \hat{\mathbf{P}}^{+}_{b_cv_c}(t_k) \\ \hat{\mathbf{P}}^{+\mathsf{T}}_{Pv_c}(t_k) & \hat{\mathbf{P}}^{+\mathsf{T}}_{b_cb_c}(t_k) & \hat{\mathbf{P}}^{+}_{v_cv_c}(t_k) \end{bmatrix} \tag{3.2}$$

In the information form, the filter maintains the matrix $\mathbf{Y}$, which is the inverse of the covariance matrix, also known as the information matrix

$$\hat{\mathbf{Y}}^{+}(t_k) = [\hat{\mathbf{P}}^{+}(t_k)]^{-1} \tag{3.3}$$

and the information vector $\mathbf{y}$, which is related to the state estimate by

$$\hat{\mathbf{y}}^{+}(t_k) = \hat{\mathbf{Y}}^{+}(t_k)\hat{\mathbf{x}}^{+}(t_k) \tag{3.4}$$

The information vector has the form

$$\hat{\mathbf{y}}^{+}(t_k) = \begin{bmatrix} \hat{\mathbf{y}}^{+}_{P}(t_k) \\ \hat{\mathbf{y}}^{+}_{b_c}(t_k) \\ \hat{\mathbf{y}}^{+}_{v_c}(t_k) \end{bmatrix} \tag{3.5}$$

and the information matrix has the form

$$\hat{\mathbf{Y}}^{+}(t_k) = \begin{bmatrix} \hat{\mathbf{Y}}^{+}_{PP}(t_k) & \hat{\mathbf{Y}}^{+}_{Pb_c}(t_k) & \hat{\mathbf{Y}}^{+}_{Pv_c}(t_k) \\ \hat{\mathbf{Y}}^{+\mathsf{T}}_{Pb_c}(t_k) & \hat{\mathbf{Y}}^{+}_{b_cb_c}(t_k) & \hat{\mathbf{Y}}^{+}_{b_cv_c}(t_k) \\ \hat{\mathbf{Y}}^{+\mathsf{T}}_{Pv_c}(t_k) & \hat{\mathbf{Y}}^{+\mathsf{T}}_{b_cb_c}(t_k) & \hat{\mathbf{Y}}^{+}_{v_cv_c}(t_k) \end{bmatrix} \tag{3.6}$$

Observations, which include ADCP measurements, are assumed to be made according to

$$\mathbf{z}(t_k) = \mathbf{h}[\mathbf{x}(t_k)] + \nu(t_k) \tag{3.7}$$

in which $\mathbf{z}(t_k)$ is an observation vector, $\mathbf{h}[\mathbf{x}(t_k)]$ is the sensor model relating states to observations, and $\nu(t_k)$ is a vector of observation errors with covariance $\mathbf{R}(t_k)$. New information from sensor measurements are incorporated into the information vector and matrix

$$\hat{\mathbf{y}}^{+}(t_k) = \hat{\mathbf{y}}^{-}(t_k) + \mathbf{i}(t_k) \tag{3.8}$$

$$\hat{\mathbf{Y}}^{+}(t_k) = \hat{\mathbf{Y}}^{-}(t_k) + \mathbf{I}(t_k) \tag{3.9}$$

in which

$$\begin{aligned} \mathbf{i}(t_k) \;=\; & \nabla_x^{\mathsf{T}}\mathbf{h}(t_k)\mathbf{R}^{-1}(t_k)(\mathbf{z}(t_k)\ldots \\ & -\mathbf{h}[\hat{\mathbf{x}}^{-}(t_k)] + \nabla_x\mathbf{h}(t_k)\hat{\mathbf{x}}^{-}(t_k)) \end{aligned} \tag{3.10}$$

$$\mathbf{I}(t_k) = \nabla_x^{\mathsf{T}}\mathbf{h}(t_k)\mathbf{R}^{-1}(t_k)\nabla_x\mathbf{h}(t_k) \tag{3.11}$$

where $\hat{\mathbf{x}}^{-}(t_k)$ is the *a priori* state estimate and $\nabla_x\mathbf{h}(t_k)$ is the Jacobian of the observation with respect to the state. Using this framework, the recursive non-linear weighted least squares solution to the states can be estimated.

Joint $p(\boldsymbol{\alpha}, \boldsymbol{\beta})$	Marginal $p(\boldsymbol{\alpha}) = \int p(\boldsymbol{\alpha}, \boldsymbol{\beta}) d\boldsymbol{\beta}$	Conditional $p(\boldsymbol{\alpha}\|\boldsymbol{\beta}) = p(\boldsymbol{\alpha}, \boldsymbol{\beta})/p(\boldsymbol{\beta})$
$\hat{\mathbf{y}} = \begin{bmatrix} \hat{\mathbf{y}_\alpha} \\ \hat{\mathbf{y}_\beta} \end{bmatrix}$	$\hat{\mathbf{y}} = \hat{\mathbf{y}}_\alpha - \hat{\mathbf{Y}}_{\alpha\beta}\hat{\mathbf{Y}}_{\beta\beta}^{-1}\hat{\mathbf{y}_\beta}$	$\hat{\mathbf{y}} = \hat{\mathbf{y}}_\alpha - \hat{\mathbf{Y}}_{\alpha\beta}\hat{\mathbf{x}_\beta}$
$\hat{\mathbf{Y}} = \begin{bmatrix} \hat{\mathbf{Y}}_{\alpha\alpha} & \hat{\mathbf{Y}}_{\alpha\beta} \\ \hat{\mathbf{Y}}_{\beta\alpha} & \hat{\mathbf{Y}}_{\beta\beta} \end{bmatrix}$	$\hat{\mathbf{Y}} = \hat{\mathbf{Y}}_{\alpha\alpha} - \hat{\mathbf{Y}}_{\alpha\beta}\hat{\mathbf{Y}}_{\beta\beta}^{-1}\hat{\mathbf{Y}}_{\beta\alpha}$	$\hat{\mathbf{Y}} = \hat{\mathbf{Y}}_{\alpha\alpha}$

Table 3.1 – Marginalisation and Conditioning operations in the Information Filter. Adapted from [6].

3.2.1 Practical Filter Usage

To implement the Extended Information Filter, a variety of strategies exist to maintain computational efficiency. Given n_p and n_b are the number of states in the pose and bias states respectively and if n_v is the number of water current velocity states, let $n = n_p + n_b + n_v$. Then the naïve Information Filter solve step for the filter states $\hat{\mathbf{x}}^+(t_k)$ in Equation 3.4 will be $\mathcal{O}(n^3)$. The cubic complexity is due to the inversion of $\hat{\mathbf{Y}}^+$ which would be required in order to solve for $\hat{\mathbf{x}}^+(t_k)$.

Thus if the entire pose, bias and water current history are kept, for revisitation or pose-based SLAM, then the solve time will increase cubicly if implemented naïvely. If real-time performance is required and no form of SLAM loop-closure is attempted, then all unrequired poses and water current states (those which will no longer be part of the observations) can be marginalised out by taking the marginal with respect to the remaining states of the filter, and the Information matrix will be of bounded size. Marginalisation still allows the correlations in the states to be maintained, but removes the states from the estimation, disabling relinearisation and smoothing of this state with future information. If the mission plan is known, and there will be no re-observation of a water current velocity state in the time frame for the constant water current assumption to hold, this water current velocity state can be marginalised out of the filter. Thus the filter will run in constant time in this case.

Since the Jacobians in Equations 3.10 and 3.11 are evaluated at the present state estimate, the linearisations of these Jacobians will have an error dependent on the error in the estimate. Stabilizing noise, which is an increase in the estimated covariance

of the measurement to account for this linearisation error, is required in order ensure the filter does not become inconsistent.

The vehicle sensors could identify previously visited regions, with this information constraining the pose estimate. This is known as loop-closure in SLAM. If loop-closure is desired to be incorporated into the filter, strategies for conditioning and marginalising poses, and sparsification of the Information matrix in order to keep the filter sparse and constant-time are discussed in [58] and [56]. Graphical based methods such as those discussed in [26] and [23] could also be applied, depending on the application. If the states are not marginalised away and the previous poses are kept as part of the estimation, then once corrected estimates for previous states exist, these Jacobians can be made more accurate. This is known as relinearisation.

3.2.2 ADCP observation equation

Given the 3D velocities output from the ADCP, the observation function for each ADCP measurement is

$$\mathbf{z}_{ADCP,i} = \mathbf{C}_n^b(-\mathbf{v}_v^n + \sum \mathbf{W}_j \mathbf{v}_{c,j}^n) + \mathbf{b}_{c,i} + \nu_{ADCP} \tag{3.12}$$

Figure 3.2 illustrates the observation function.

where:

- $\mathbf{z}_{ADCP,i}$ = ADCP measured current vector in the ith measurement cell
- $\mathbf{C}_n^b$ = Coordinate transform from navigation/world frame to ADCP/body frame
- $\mathbf{v}_v^n$ = Vehicle velocity in the world/navigation frame
- $\mathbf{W}_j$ = Weighting function for each water current velocity from depth cell j, outlined in [11]
- $\mathbf{v}_{c,j}^n$ = water current velocity from depth cell j. Each depth cell contains a current velocity state in the X and Y direction, which represents the average velocity of the current through that layer

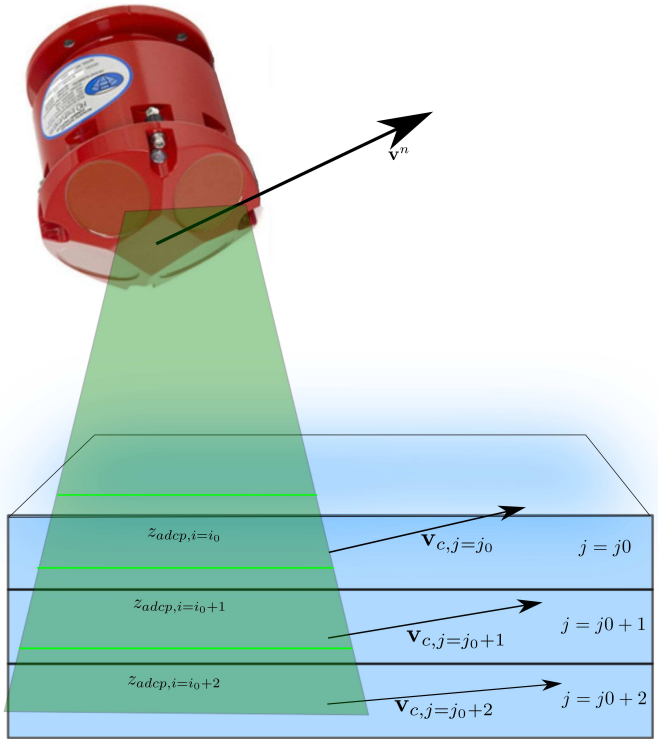

Figure 3.2 – ADCP observation model for 3D velocities. Measurement cells are the $z_{ADCP,i}$ values. Depth cells are represented by j.

- $\mathbf{b}_{c,i}$ = Bias in the ith measurement cell in the body frame
- ν_{ADCP} = Random noise in the ADCP measurement, with standard deviation given by the sensor manufacturer

3.2.3 ADCP biases

Sources of ADCP biases [11] [1] include measurement cell dependent biases, such as beam and sensor misalignment, beam geometry and signal/noise ratio and biases dependent on changing depth, including temperature, pressure, scatterers and sound speed estimate error. These ADCP biases are estimated as the summed effect on the measurement cell observation in the body frame. In order to improve the observability of the ADCP sensor relative biases ($\mathbf{b}_{c,i}$) and allow disambiguation from the true currents ($\mathbf{v}^n_{c,j}$), rotation about heading is required, due to the transformation $\mathbf{C}^b_n$ in Equation 3.12.

A process can be described by a first order Markov process model to simulate bounded random walk. For example, given a state b undergoing bounded random walk, the following model can be applied:

$$\dot{\mathbf{b}_{c,i}} = -\frac{1}{\tau}\mathbf{b}_{c,i} + \nu \tag{3.13}$$

where τ is a time or scale constant which affects the rate at which the state changes, and ν is a normally distributed random variable with standard deviation:

$$\sigma = \sqrt{\frac{2f\sigma^2_{state\,limit}}{\tau}} \tag{3.14}$$

where $\sigma_{state\,limit}$ is the bound on the long term state. This bound is set such that the state sampled at a random point in its evolution will be normally distributed with standard deviation $\sigma_{state\,limit}$ [8].

Thus, the ADCP bias with time can be modeled as a first order Markov process model

of the form

$$\dot{\mathbf{b}}_{c,i} = -\frac{1}{\tau_{bias}}\mathbf{b}_{c,i} + \nu_{bias} \tag{3.15}$$

where τ_{bias} is the expected rate change of the ADCP sensor, which is a tuned parameter and ν_{bias} is a normally distributed random variable with

$$\sigma_{bias} = \sqrt{\frac{2f\sigma^2_{bias\,drift}}{\tau_{bias}}} \tag{3.16}$$

where $\sigma_{bias\,drift}$ is the standard deviation of the bias in the long term, and a limit to the magnitude of the bias (a tuned parameter), f is the frequency at which the process model operates and τ is a tuned parameter that can be be determined through accounting for the expected bias drift rate, which may depend and change on a number of factors as described previously. In a discrete form appropriate to be used in the information filter, the observation equation which links the previous bias state to the present bias state is

$$\mathbf{h}_{bias\,model}(\hat{\mathbf{x}}(t_k)) = \mathbf{b}_{c,i}(t_k) - (1 - \frac{\Delta t}{\tau})\mathbf{b}_{c,i}(t_{k-1}) \tag{3.17}$$

$$\mathbf{z}_{bias\,model} = 0 \tag{3.18}$$

$$R_{bias\,model} = \sigma^2_{bias}\Delta t^2 \tag{3.19}$$

where $\mathbf{b}_{c,i}(t_k)$ is the present bias state, $\mathbf{b}_{c,i}(t_{k-1})$ is the previous bias state, and Δt is the time between new bias states ($= 1/f$).

3.2.4 ADCP measurement weighting function

The ADCP sensor measures velocities in depth cells with a triangular weight function in the case of the Teledyne RDI ADCP, with 15% overlap with adjacent depth cells as described in the RDI ADCP primer [11], shown in Figure 3.3. This is due to currents at the centre of the measurement cell contributing more to the measurement value than those at the edge of the measurement cell. Between 2 and 3 depth cells affect each measurement, depending on the depth where the measurement was taken

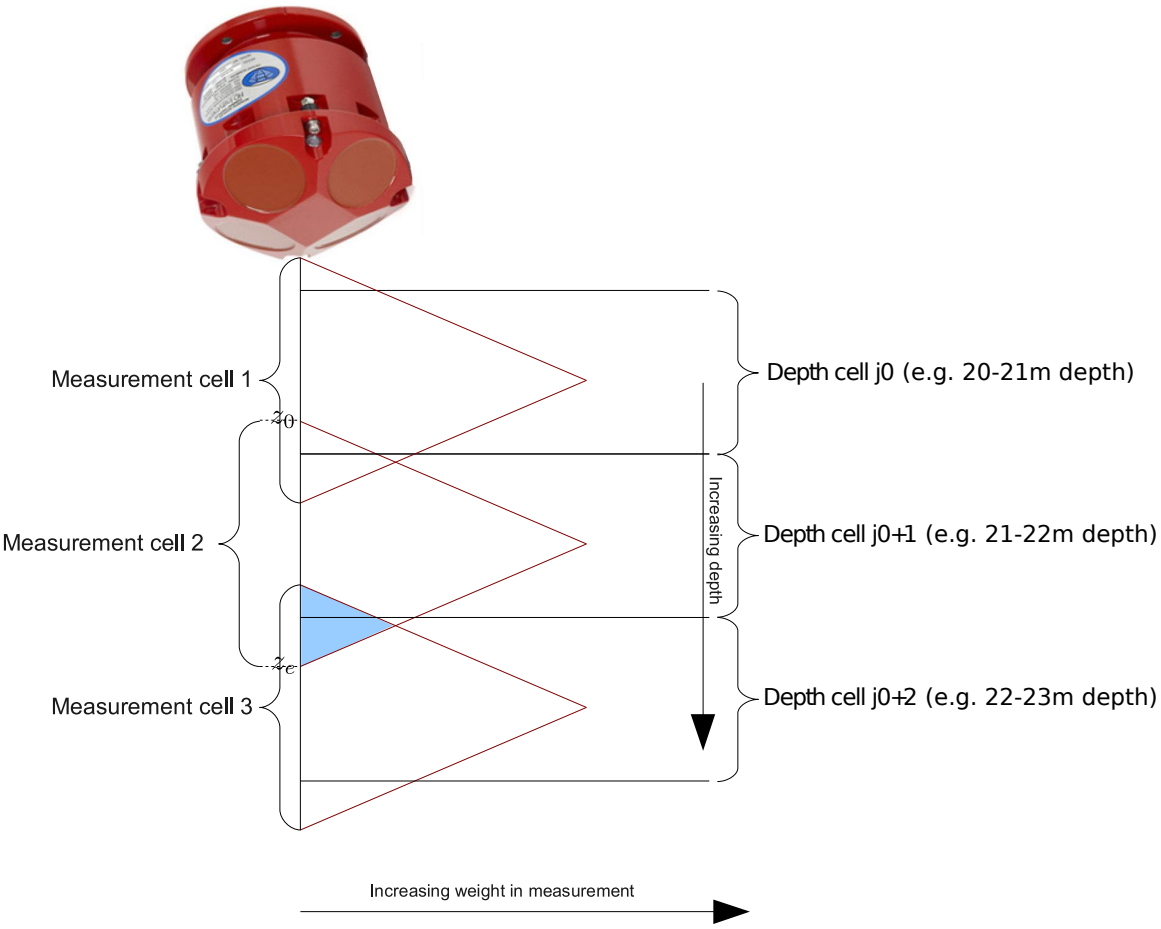

Figure 3.3 – Depth cell weight functions: depth cells are more sensitive to currents at the center of the cell than at the edges. The area in blue is approximately 15% of the total area of one measurement cell triangle. [11]

relative to the depth cell. The weighting for each depth cell depends on the area of the triangle of the measurement cell in that depth cell, and determines the $\mathbf{W}_j$ term in Equation 3.12.

The ADCP measurement for measurement cell 2 is assumed to have a weighting function according to:

$$M_{z_0}^{z_e} = \int_{z_0}^{z_e} w(z) v_c^b(z)\, dz \tag{3.20}$$

where $v_c^b(z)$ is the velocity of the water currents in the ADCP body-frame as a function

of depth, and for a triangular weighting function such as that described in Figure 3.3 for ADCPs, the term $w(z)$ is described as:

$$w(z) = \begin{cases} 4(z - z_0)/(z_e - z_0) & \text{when} \quad (z - z_0)/(z_e - z_0) \leq \frac{1}{2} \\ 4 - 4(z - z_0)/(z_e - z_0) & \text{when} \quad (z - z_0)/(z_e - z_0) > \frac{1}{2} \end{cases} \tag{3.21}$$

3.2.5 ADCP observation equation Jacobians

The predicted observation from the ADCP sensor is given by:

$$\mathbf{h}_{ADCP}[\hat{\mathbf{x}}(t_k)] = \hat{\mathbf{C}}_n^b(-\hat{\mathbf{v}}^n + \sum \hat{\mathbf{W}}_j \hat{\mathbf{v}}_{c,j}^n) + \hat{\mathbf{b}}_{c,i} \tag{3.22}$$

The Jacobian of this predicted observation with respect to position, velocity and attitude is given by:

$$\frac{\partial \mathbf{h}_{ADCP}[\hat{\mathbf{x}}(t_k)]}{\partial \hat{\mathbf{p}}_v^n} = \begin{bmatrix} \mathbf{0}_{2\times 1} \\ \frac{\partial \sum \hat{\mathbf{W}}_j \hat{\mathbf{v}}_{c,j}^n}{\partial \hat{p}_{v,z}} \end{bmatrix} \tag{3.23}$$

$$\frac{\partial \mathbf{h}_{ADCP}[\hat{\mathbf{x}}(t_k)]}{\partial \hat{\mathbf{v}}_v^n} = -\hat{\mathbf{C}}_n^b \tag{3.24}$$

$$\frac{\partial \mathbf{h}_{ADCP}[\hat{\mathbf{x}}(t_k)]}{\partial \hat{\mathbf{v}}_{c,j}^n} = -\hat{\mathbf{C}}_n^b \sum \hat{\mathbf{W}}_j \tag{3.25}$$

$$\frac{\partial \mathbf{h}_{ADCP}[\hat{\mathbf{x}}(t_k)]}{\partial \hat{\boldsymbol{\phi}}^n} = \frac{\partial \hat{\mathbf{C}}_n^b}{\partial \hat{\boldsymbol{\phi}}_v^n}(-\hat{\mathbf{v}}_v^n + \sum \hat{\mathbf{W}}_j \hat{\mathbf{v}}_{c,j}^n) \tag{3.26}$$

As can be seen in Equation 3.23, the predicted observation will not change given translation in the north and east directions since it would merely be sliding across the water layer, with no change. In the down direction, the observation changes due to the weighting function changing with depth, although this will have minimal localisation estimation impact as the pressure depth sensor will be providing accurate absolute depth estimation.

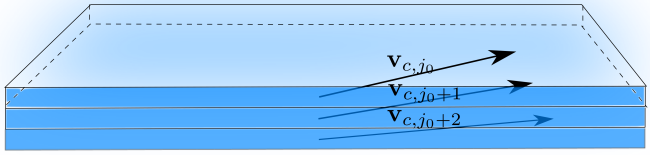

Figure 3.4 – There exists some correlation between vertically adjacent water current depth cells due to shear in the water column. Thus the water current velocities are not randomly distributed with respect to each other, but instead have some dependence on water currents above and below.

In Equation 3.24 and 3.25, the predicted observation will change depending on the orientation of the vehicle. The vehicle velocity states will be constrained by the water current velocity estimates according to this correlation. As a result of Equation 3.26, the predicted observation will change depending on attitude, vehicle velocity and the weighted water current measurements, resulting in any attitude misalignment causing localisation errors. A more thorough sensitivity analysis remains as future work.

3.2.6 Vertical Correlation Model

Vertically adjacent water current depth cells should have some correlation, due to shear in the water column. This is often applied as a smoothing function to the current profile [57]. This is visualised in Figure 3.4, where the water current velocities are not randomly distributed, but instead have some dependence on water currents above and below. Thus, an update with the following measurement model is applied between water current depth cells which are part of the state vector:

$$h_{vertical\ correlation}(\hat{\mathbf{x}}(t_k)) = \mathbf{v}^n_{c,j_0} - \mathbf{v}^n_{c,j_0+1} \tag{3.27}$$

$$\mathbf{z}_{vertical\ correlation} = 0 \tag{3.28}$$

$$R_{vertical\ correlation} = \sigma^2_{vertical\ correlation} \tag{3.29}$$

where $\mathbf{v}^n_{c,j_0}$ is the vertically higher water current depth cell, $\mathbf{v}^n_{c,j_0+1}$ is the verti-

cally lower water current depth cell. The standard deviation of this constraint $\sigma_{vertical\,correlation}$ is set according to the expected rate of current change between the current grids, similar to a smoothing term in LADCP implementations [57]. This standard oceanographic assumption will be applied to vertically adjacent water current velocity states. The sensitivity of the localisation performance on this additional information depends on the frequency of ADCP measurements. The higher the rate of ADCP measurements per depth cell, the less reliance there is on the vertical correlation information to aid the estimation of the water currents. Incorporating physical constraints, even very coarsely, will help the filter decide initialisation values and uncertainties for the unestimated water currents.

3.3 Vertical descent simulations

This section explores the performance of the ADCP localisation algorithm given vertical descent in simulation.

3.3.1 Simulated Vertical Water Currents

The current field is generated as a first order Markov process, to simulate correlated and randomly walking currents with depth, but with a bound on the random walk. The targeted behaviour of the water currents with depth is illustrated in Figure 3.5 [42]. A simulated current field is shown in Figure 3.6.

3.3.2 Two degrees-of-freedom simulation

The example illustrated in Section 3.1 and Figures 3.1(a) to 3.1(c) can be simulated to examine how the errors evolve in the states. A 1-dimensional current field is simulated in which the vehicle is travelling vertically down, and free to move left or right (but not into and out of the page of the figures).

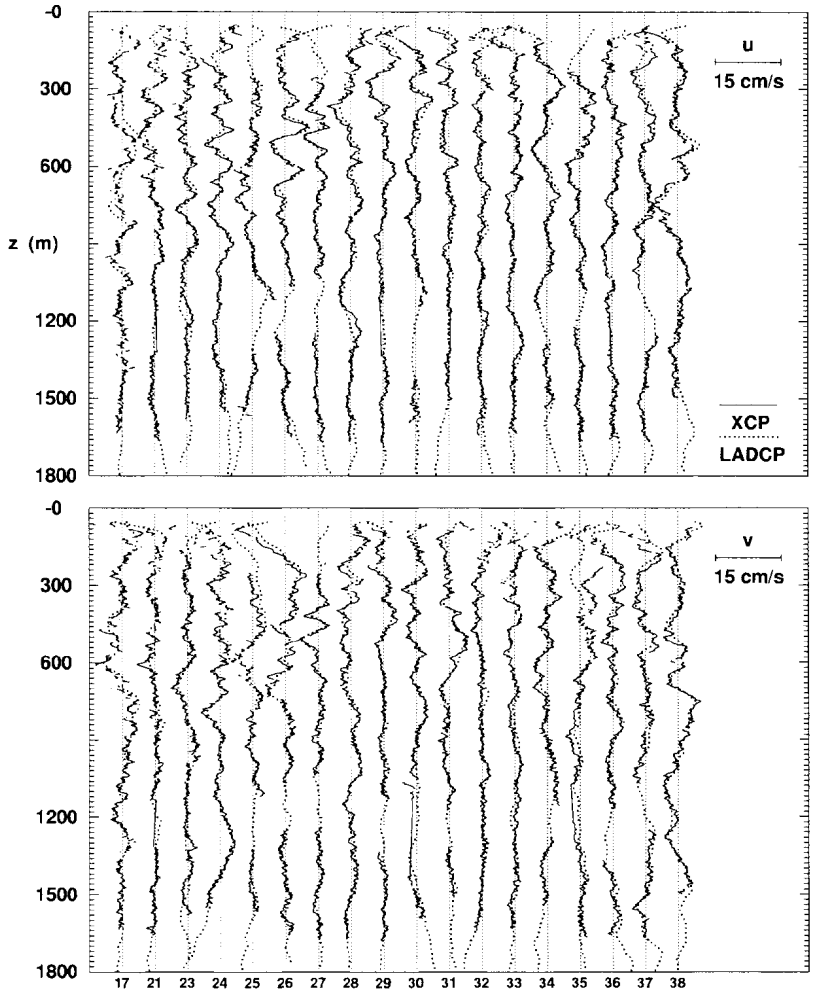

Figure 3.5 – Results for Lowered acoustic Doppler current profiler (LADCP) velocity profiles (dotted lines) and higher-resolution expendable current profiler (XCP) measurements (solid lines) in u (north) and v (east) directions. The y-axis represents depth, and the x-axis represents separate current profiling missions [42].

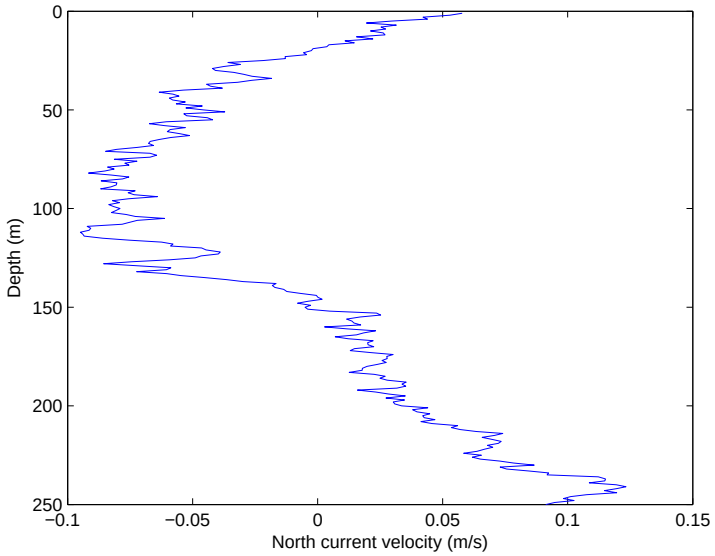

(a)

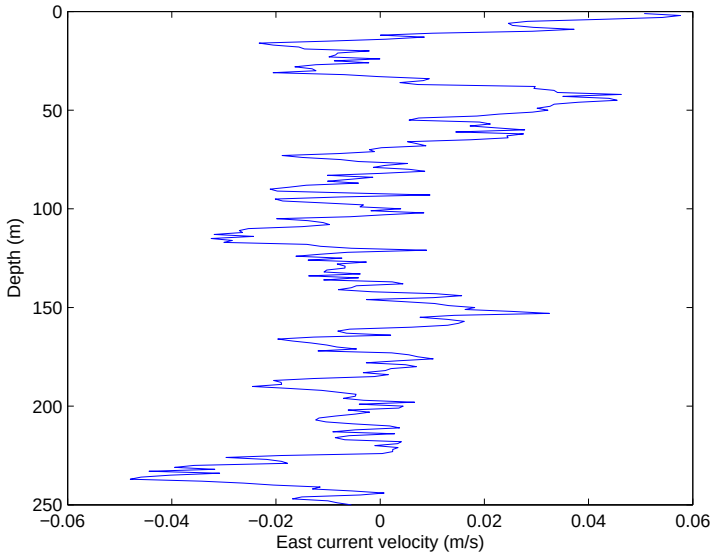

(b)

Figure 3.6 – A simulated current profile for the (a) north and (b) east velocity.

Table 3.2 – Parameter values used in the 2DOF simulation

GPS receiver	Lassen iQ GPS receiver
Initial GPS position fix accuracy	10 m ($2\sigma_p$)
Initial GPS velocity accuracy	0.04 m/s ($2\sigma_v$)
AUV descent rate	0.2 m/s
ADCP make and model	RDI 1200 kHz
ADCP measurement uncertainty	0.02 m/s ($2\sigma_a$)
ADCP range	30 m
Water current depth cell size	1 m
Simulation time	1000 seconds
Simulated depth	240 m
DVL accuracy	0.006 m/s ($2\sigma_{DVL}$)
DVL range	40 m
DVL acquisition time	1000 seconds
ADCP and DVL update rate	3 Hz
Maximum currents	20 cm/s

The vehicle experiences unmodelled (in the localisation filter) drag which causes it to move with the currents. The vehicle is also assumed not to pitch in this simulation, resulting in two degrees-of-freedom (2DOF) in translation. To further simplify the analysis of this example, the bias states are not simulated. The ADCP and DVL operate at approximately 3 Hz in practice for the 1200 kHz sensor, and this is used in the simulation.

Table 3.2 lists parameter values used for the 2DOF simulation. Figure 3.7 outlines the localisation architecture for this simulation.

To facilitate analysis, the full state history, or smoothed solution, of the information filter is used. All poses are kept in the state estimator. The state estimates (x) and uncertainties ($p(x)$) are defined as:

$$x = \hat{\mathbf{x}}(t_0) : \hat{\mathbf{x}}(t_k) | \mathbf{z}(t_0) : \mathbf{z}(t_k) \tag{3.30}$$

$$p(x) = p(\hat{\mathbf{x}}(t_0) : \hat{\mathbf{x}}(t_k) | \mathbf{z}(t_0) : \mathbf{z}(t_k)) \tag{3.31}$$

Figures 3.8(a) and 3.8(c) show the position estimate with a constant velocity (CV)

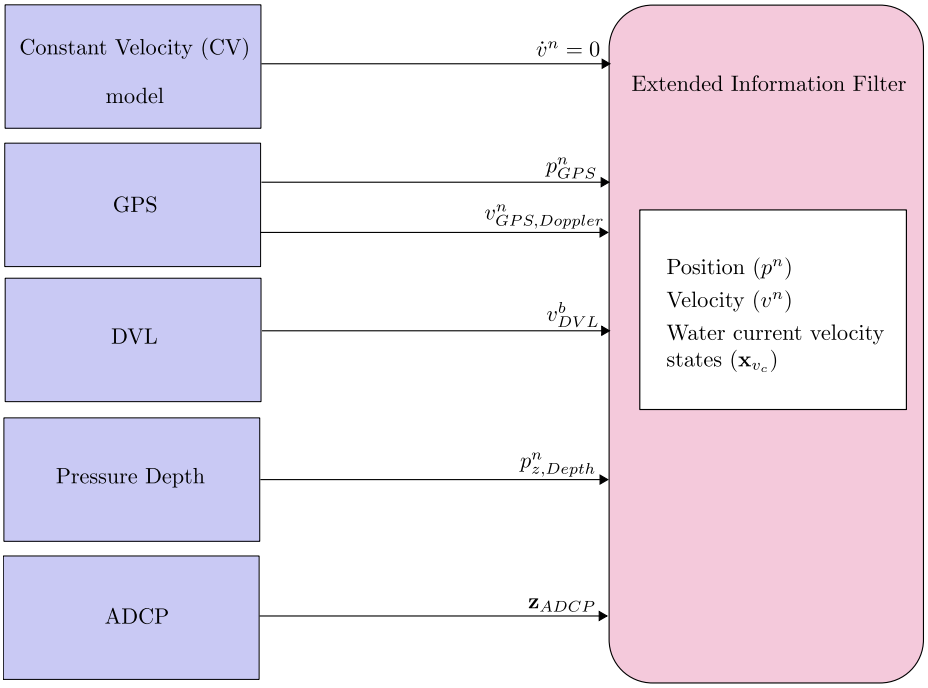

Figure 3.7 – The localisation architecture for the 2DOF simulation.

model and ADCP-aiding respectively before DVL bottom-lock. The CV model assumes currents are approximately 20 cm/s at maximum, therefore it is assumed that the vehicle will experience unknown drift due to this water current uncertainty as it descends. No sensor information other than depth observations are available. The position uncertainty growth for the CV model is approximately 150m (2σ) over the 1000 second dive, while the ADCP-aiding filter position uncertainty growth is approximately 40m (2σ).

Figures 3.8(b) and 3.8(d) show the position estimate for the entire state history with a CV model and ADCP-aiding respectively after DVL bottom-lock. The DVL bottom-lock has constrained some of the velocity history of the dive for the CV model. The position error growth for the CV model is now approximately 90m (2σ) over the 1000 second dive. The DVL bottom-lock in the case of the ADCP-aiding filter allows the entire velocity history to be constrained due to the correlations of vehicle velocity with water current velocity states. The observation of DVL body-relative velocity is back-propagated to the entire descent because these correlations are accounted for in the Information Filter through the corrected water current estimates. The ADCP-aiding filter position uncertainty growth is now approximately 6m (2σ).

Figures 3.10(a) and 3.10(c) show the velocity errors for the entire state history for the CV model and ADCP-aiding filter respectively before DVL bottom-lock. The CV model velocity uncertainty deteriorates to the 20 cm/s water current uncertainty. For the ADCP-aiding filter, the velocity uncertainty slightly increases with time because of information loss from a finite number of uncertain measurements from the ADCP during the descent. Information loss is defined as the increase in velocity uncertainty as velocity estimates are extracted through reobserving the water currents with the ADCP, which translates into position uncertainty due to the position being the integral of velocity with time. This increase in velocity uncertainty is negligible because of the number of reobservations of the current velocity bins (750 times at most in this case). The concept of information loss is examined in more detail is Section 3.3.3. The error in velocity is primarily from the initial GPS velocity error, at 0.04m/s (2σ).

While undergoing descent prior to DVL bottom-lock, the velocity error is seen to

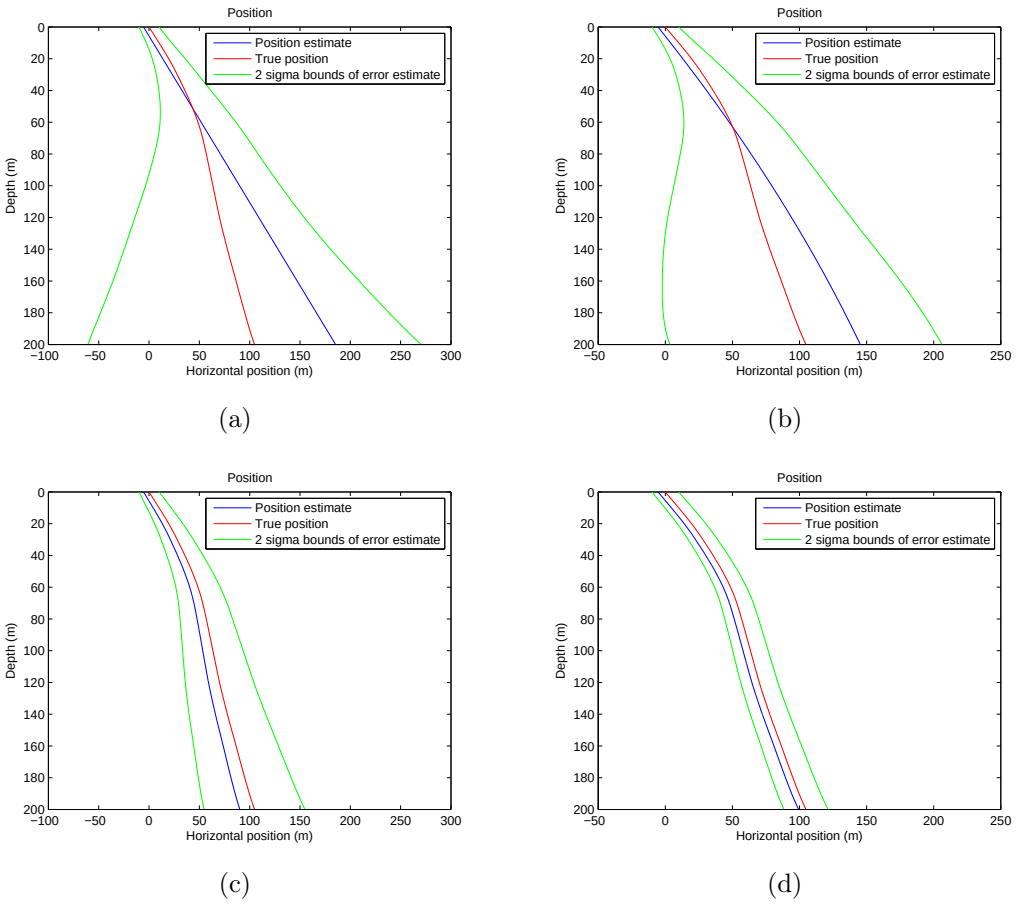

Figure 3.8 – 2DOF simulation position estimates for the entire state history for the constant velocity model (a) before DVL bottom-lock and (b) after DVL bottom-lock, and ADCP-aiding filter (c) before DVL bottom-lock and (d) after DVL bottom-lock.

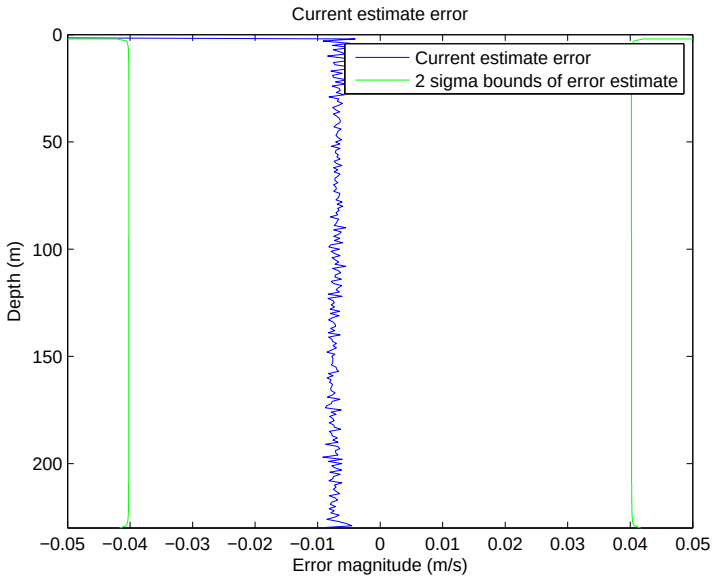

Figure 3.9 – The error in the water current estimate from the 2DOF simulation prior to DVL bottom-lock.

have a Markov nature, the initial velocity error remains like a bias in the vehicle velocity estimate. It acts like a bias because the error in velocity which the vehicle has while on the surface, behaves as a bias in the initial measured water currents. Thus, no matter how many subsequent measurements of the water currents are made while underwater without GPS, this initial velocity bias in the water currents can never be overcome without another georeferenced velocity measurement. Figure 3.11 shows the the ADCP aided velocity uncertainty during the descent, showing a slight increase in velocity uncertainty following GPS loss, and then a slowly increasing velocity uncertainty with time. The bias in all the water currents, except the water currents at the surface which are only observed with the ADCP a limited amount of times during descent, can be seen in Figure 3.9.

In [3], it is proven that the relative map which can be constructed in SLAM has an uncertainty which has a lower bound defined only by the initial vehicle position uncertainty. The same concept applies in this case, except initial vehicle position uncertainty in SLAM is the equivalent of initial vehicle velocity uncertainty in the ADCP localisation scenario. The problems are equivalent due to this initial condition

dependence. This lower bound in the velocity uncertainty is set by the initial velocity uncertainty of the vehicle. Just as the initial velocity uncertainty will strongly determine the position uncertainty growth rate, once DVL bottom-lock is achieved, a georeferenced velocity measurement will be available to the filter.

Figures 3.10(b) and 3.10(d) show the velocity errors for the entire state history for the CV model and ADCP-aiding filter respectively after DVL bottom-lock. The CV model velocity estimates are improved in the time near DVL bottom-lock. For the ADCP-aiding filter, the entire velocity history estimate error is just above 0.006 m/s (2σ), which is similar to the DVL accuracy, but for the entire descent. It is slightly higher than the DVL velocity uncertainty as a result of the small information loss, due to a finite number of uncertain measurements from the ADCP during the descent. Figure 3.12 shows the ADCP aided velocity uncertainty that is smoothed for the entire state history, following DVL bottom lock. The velocity uncertainty is about 8 mm/s for the entire dive. It shows an increasing velocity uncertainty backwards in time from DVL bottom lock acquisition. It is similar to the descent behaviour except in reverse. It shows the slight information loss due to noisy measurements through the water column. This absolute velocity measurement allows the bias in all of the water current measurements from the initial GPS velocity to be reduced in magnitude according to the uncertainty of the DVL. This correction in all the water currents in turn reduces the previous uncertainty in the vehicle velocity.

Figure 3.13 shows the estimated water currents from the filter post-DVL compared to the truth, showing the reduction in uncertainty for all the water column current velocities, while the errors and uncertainty bounds for this estimate are shown to be consistent in Figure 3.14.

3.3.3 Two degrees-of-freedom simulation with varying parameters

The position uncertainty growth, as established in the previous chapter, is closely related to the initial velocity uncertainty of the vehicle. The reliance on other variable

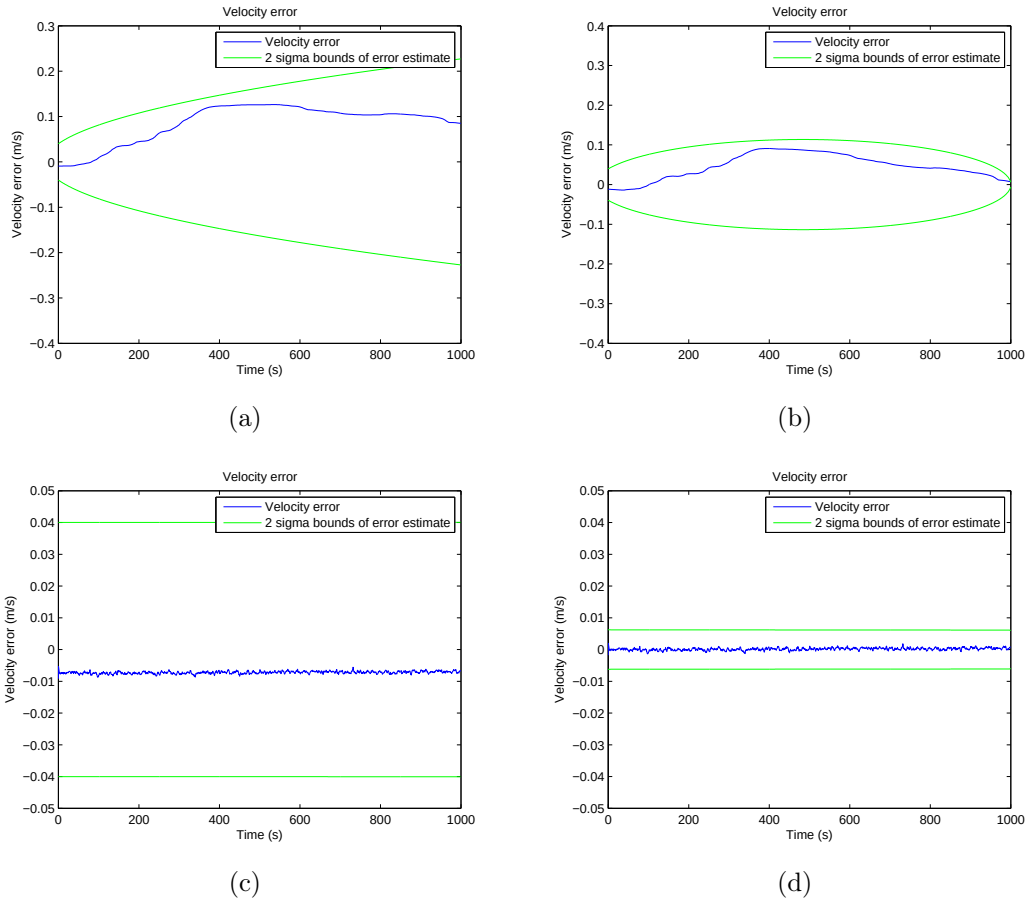

Figure 3.10 – 2DOF simulation velocity errors for the entire state history for the constant velocity model (a) before DVL bottom-lock and (b) after DVL bottom-lock, and ADCP-aiding filter (c) before DVL bottom-lock and (d) after DVL bottom-lock. The Y axis scale above is significantly different comparing (a) and (b) to (c) and (d). Note that the velocity uncertainty for the ADCP-aiding filter is significantly lower than the constant velocity model.

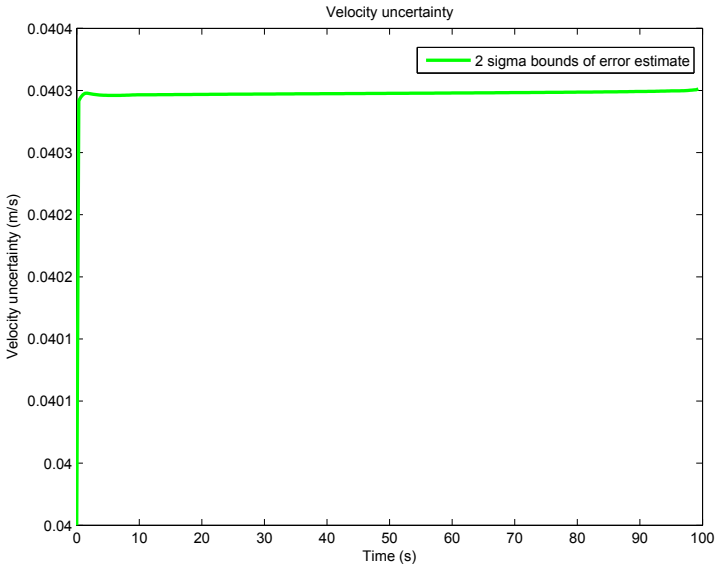

Figure 3.11 – The ADCP aided velocity during the descent, showing a slight increase in velocity uncertainty, and then a slowly increasing velocity uncertainty with time

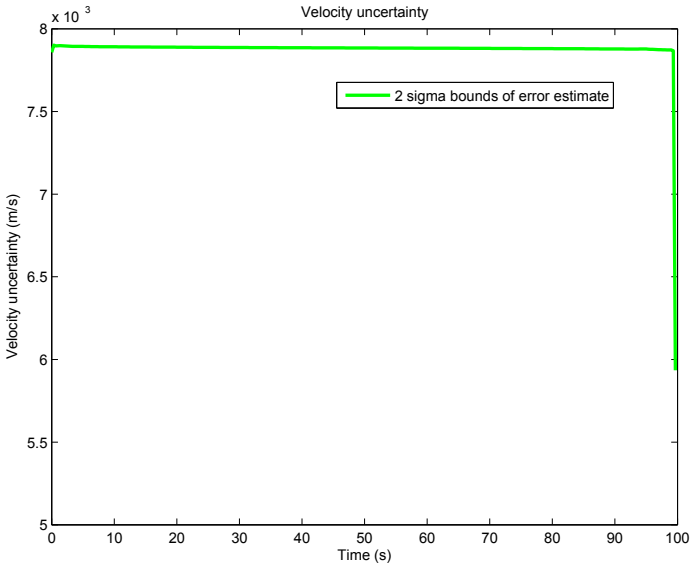

Figure 3.12 – The ADCP aided velocity uncertainty that is smoothed for the entire state history, following DVL bottom lock. It shows an increasing velocity uncertainty backwards in time from DVL bottom lock acquisition.

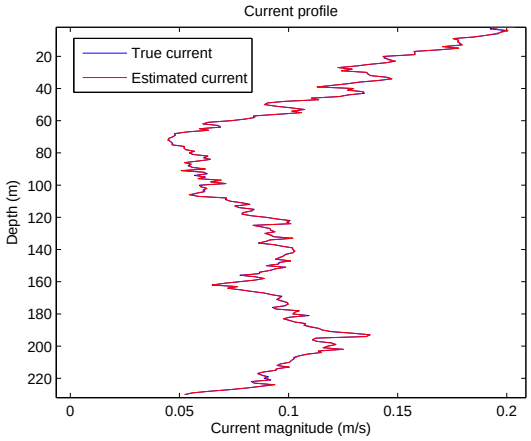

Figure 3.13 – Current profile derived from the 2DOF simulation

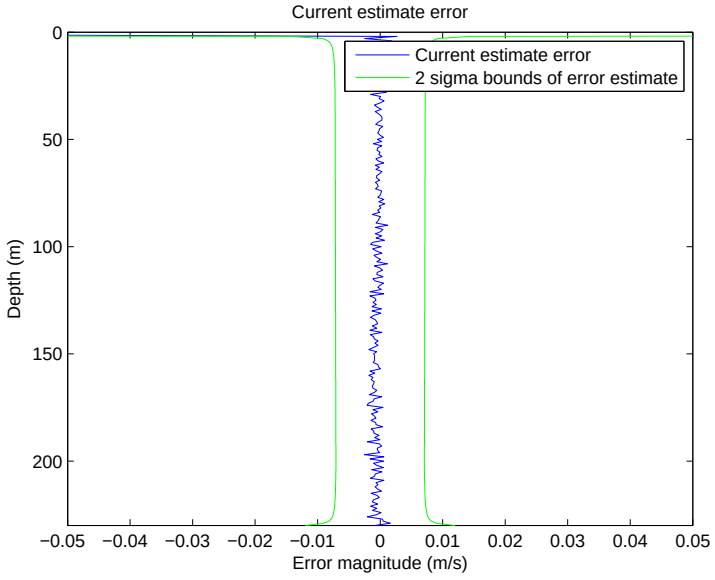

Figure 3.14 – The error in the water current estimate from the 2DOF simulation following DVL bottom-lock.

parameters is yet to be determined. A two degrees-of-freedom simulation, similar to the previous section but with 20 m of descent in 60 m of water, is simulated between GPS blackout and DVL bottom-lock. The following parameters are adjusted to compare the filter uncertainty estimates:

1. AUV descent rate
2. ADCP measurement rate
3. ADCP measurement standard deviation (σ_a)
4. Initial velocity standard deviation (σ_v) whether from GPS or other sources (such as GPS/IMU)

Appendix A contains the details of this analysis. In summary, for a given mission depth:

- The faster the descent rate, the lower the position error. There is a near linear relationship between the mission time and the position uncertainty growth. The increase in velocity uncertainty during faster descents is negligible compared to the reduced mission time.
- The initial velocity standard deviation has a near linear relationship with the position uncertainty error growth prior to DVL bottom-lock. Following DVL bottom-lock, the initial velocity standard deviation will have a negligible impact on the final position uncertainty growth. The exception is if the initial velocity standard deviation (e.g. GPS) is close to the final DVL bottom-lock standard deviation, and if the information loss is not significant. The information loss increases due to a low ADCP measurement rate or high ADCP measurement uncertainty. In this case, further accuracy in the position uncertainty growth is achieved.
- The ADCP measurement rate only improves the position error significantly if the ADCP measurement uncertainty is relatively high. Even with low ADCP

measurement rates, there is often enough reobservation of previously observed water currents to limit information loss and position uncertainty growth.

- The ADCP measurement standard deviation becomes important as the AUV descent rate increases and/or if the ADCP measurement rate is reduced prior to DVL bottom-lock. Once DVL bottom-lock occurs, the ADCP measurement uncertainty itself becomes important as the information loss results in the DVL bottom-lock velocity uncertainty not being able to reduce the uncertainty of the earlier water current velocities. This feeds back into the vehicle velocity estimates and hence the position uncertainty growth. This effect can be mitigated by having a low initial velocity standard deviation to reduce the uncertainty growth during the earlier portion of the descent.

Given this simulation is a simplified representation of the true dynamics of the ADCP localisation filter, a more realistic simulation is undertaken in the following section.

3.3.4 Six degrees-of-freedom simulation

A six degrees-of-freedom (6DOF) simulation of a typical AUV dive was also completed with the following characteristics:

1. An initialisation phase for the GPS/IMU is first simulated, using real IMU/GPS output from a Novatel GPS system to give a realistic initialisation. This allows heading resolution.

2. A vertical dive phase, where no GPS or DVL bottom-lock is possible. The AUV rotates due to hydrodynamic forces or through direct control of thrusters, and allows sensor biases to be estimated.

3. After 1000 seconds, the vehicle reaches within 40m of the seafloor, and acquires bottom-lock to resolve velocity over ground.

4. Following DVL bottom-lock, 30 seconds of DVL measurements are undertaken to allow velocity over ground to be estimated in combination with the IMU.

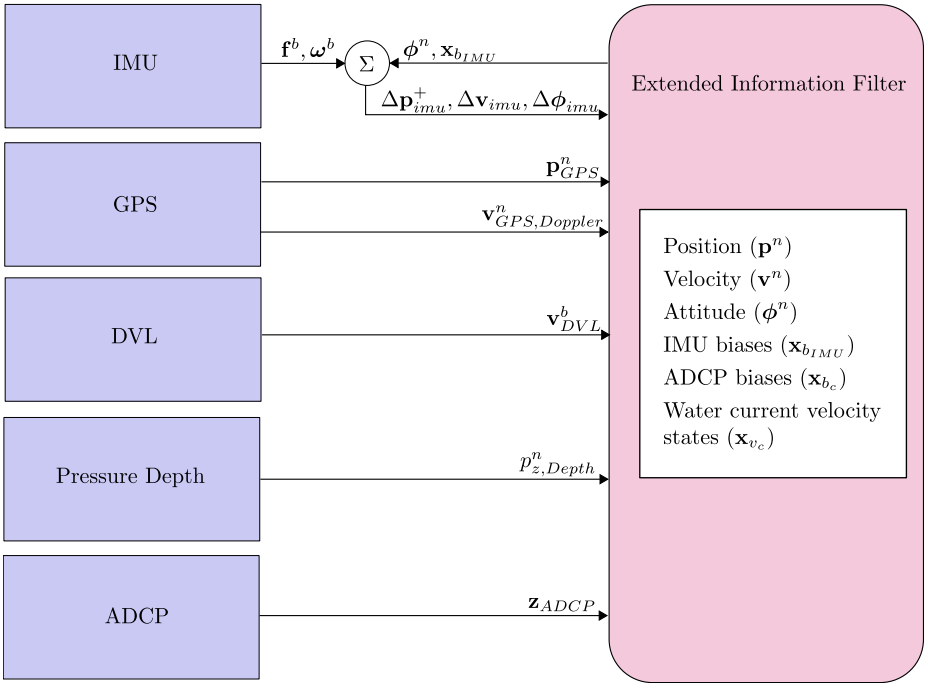

Figure 3.15 – The localisation architecture for the 6DOF simulation.

5. The water current velocities are correlated with depth, with a maximum current around 15 cm/s. This is indicative of a typical current profile [57].

The filter architecture is outlined in Figure 3.15.

AUV vehicle modelling

To model the vehicle motion through the water current environment, it is assumed that the vehicle has differential thrust to control heading and forward velocity. The differential equation defining a 3DOF AUV model [9] with differential thrust such as the *Sirius* AUV [60] is:

$$\mathbf{M}\dot{\mathbf{v}} + \mathbf{C}(\mathbf{v})\mathbf{v} + \mathbf{D}(\mathbf{v})\mathbf{v} + \mathbf{C}^b_n(m\mathbf{g}^n + \mathbf{b}^n) = \boldsymbol{\tau} \tag{3.32}$$

$$\mathbf{v} = \begin{bmatrix} \dot{x_b} \\ \dot{y_b} \\ \dot{z_b} \\ \dot{\psi} \end{bmatrix} \tag{3.33}$$

$$\boldsymbol{\tau} = \begin{bmatrix} F_1 + F_2 \\ 0 \\ F_3 \\ F_1 r - F_2 r \end{bmatrix} \tag{3.34}$$

$$\mathbf{M} = diag\{M_x, M_y, M_z, I_z\} \tag{3.35}$$

$$\mathbf{C}(\mathbf{v}) = \begin{bmatrix} 0 & 0 & 0 & -M_y \dot{y_b} \\ 0 & 0 & 0 & M_x \dot{x_b} \\ 0 & 0 & 0 & 0 \\ M_y \dot{y_b} & -M_x \dot{x_b} & 0 & 0 \end{bmatrix} \tag{3.36}$$

$$\mathbf{D}(\mathbf{v}) = -diag\{D_{\dot{x}}|\dot{x_b}|, D_{\dot{y}}|\dot{y_b}|, D_{\dot{z}}|\dot{z_b}|, D_{\dot{\psi}}|\dot{\psi}|\} \tag{3.37}$$

where

- $\dot{x_b}$, $\dot{y_b}$ and $\dot{z_b}$ are the water relative velocities of the vehicle in the body frame in the forward, starboard and down directions respectively.
- $\dot{\psi}$ is the yaw rotational velocity of the vehicle
- $\mathbf{M}$ is the inertia matrix (including added mass)
- $\mathbf{C}(\mathbf{v})$ is the matrix of Coriolis and centripetal terms (including added mass)
- $\mathbf{D}(\mathbf{v})$ is the damping matrix
- $\boldsymbol{\tau}$ is the vector of control inputs
- F_1, F_2 and F_3 are the thrusts from the port, starboard and vertical thruster respectively
- m is the true mass of the vehicle

- $\mathbf{g}^n$ is the gravity vector in the navigation frame
- $\mathbf{b}^n$ is the buoyancy force in the navigation frame

Due to the lack of previously accurately derived vehicle parameters for the *Sirius* AUV, they are estimated using [35] as a baseline, to represent a hypothetical AUV in simulation, although the model itself is generic. The parameters of the vehicle model used in the simulation are:

Symbol	True value
M_x	500 kg
M_y	500 kg
M_z	225 kg
I_z	179.049 kg m^2
$D_{\dot{x}}$	500 kg m^{-1}
$D_{\dot{y}}$	800 kg m^{-1}
r	0.2 m

Additionally, a thruster model according to [15] and [9] is utilised:

$$F = 0.4\rho d^4|n|n - \frac{1}{3}v_T\rho d^3|n| \tag{3.38}$$

where

- ρ is the density of water
- d is the diameter of the propellor
- n is the revolution speed of the thruster
- v_T is the velocity of the water going into the propellor

This information is used to generate the true motion of the vehicle given vertical thrust through the water column, but for the subsequent ADCP localisation, this information has not been fused into the filter.

Table 3.3 – Parameter values used in the 6DOF simulation which are in addition or different to the 2DOF simulation.

IMU	Honeywell HG1700A58
IMU bias stability	1 degree/hour
AUV rotation rate	8 degrees/second
Bias magnitude ($\sigma_{bias\,drift}$)	0.01 m/s (2σ)
Time constant of bias change (τ_{bias})	500 seconds

IMU integration method

A tactical-grade Honeywell HG1700A58 IMU was simulated, providing position, velocity and attitude constraints through the integration of the body rotation rates and accelerations. The method used to incorporate the inertial measurements into the filter are similar to [30]. A global reference frame is used, and initial attitude is assumed accurate for linearisation purposes, and an addition to account for Earth rotation (∼15 degrees/hour is significant in this case) as calculated in [52]:

$$\Delta\phi_{t+1} = \Delta\phi_t + E_t^{t1}(\omega_t^b - bias_w^{obs} - C_n^k\Omega_e^n)\Delta t \tag{3.39}$$

where $-C_n^k\Omega_e^n$ is the apparent Earth rotation in the body frame.

Further details on the incorporation of inertial measurements are available in Section 5.2. The latitude that the simulation occurs is at approximately 34 degrees South, the same latitude as Sydney, Australia. This information is required for the apparent rotation-rate of the Earth vector.

Results

The simulation mission is illustrated in Figure 3.16.

Table 3.3 summarises the parameter values used in the 6DOF simulation which are in addition or different to the 2DOF simulation. In the subsequent simulation, the measurement cell bias magnitudes are constrained to zero within 0.01 m/s (2σ), in alignment with the RDI specification [11] and the calibration report on the RDI ADCP

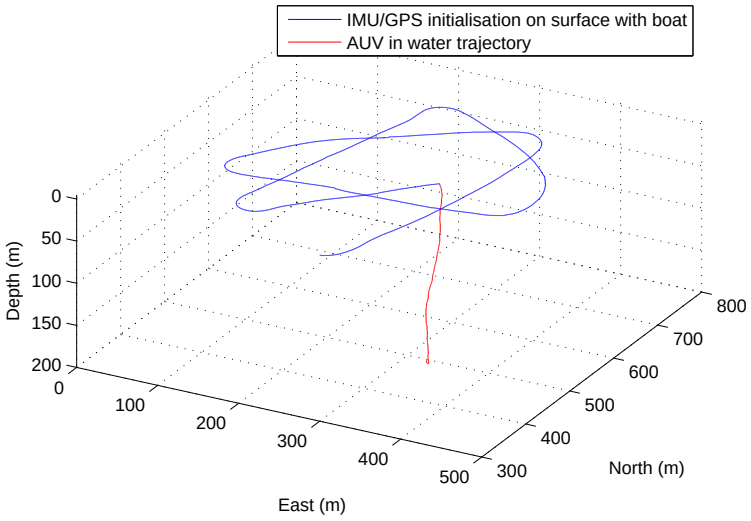

Figure 3.16 – The simulated mission trajectory.

[46], which contains biases of around 0.01 m/s total at most. The biases change with time in a correlated fashion (which accounts for changing depth during descent), simulating the bias effects described in section 3.2.2. A value for τ_{bias} in equation 3.15 of 500 seconds is used to simulate drifting biases over this time scale, although controlled experiments of the ADCP sensor in real environments are required to tune a true value for this parameter.

As can be seen in Figure 3.17, the run-time filter uncertainty estimate of velocity is constrained to about 0.011 m/s (2σ) in the north and east directions. This uncertainty in velocity during the dive phase is from the initial velocity uncertainty after GPS/IMU initialisation and ADCP estimation on the surface. Given a better initial velocity estimate, the error in velocity will be further reduced during the dive, as mentioned in Section 3.3.3. The velocity uncertainty is also not deteriorating noticeably within the 1000 second time, as there are a large number (at most 750 in this case) of reobservations of the same water current depth cells. Since the water current depth cells are continually reobserved, the primary source of error in their estimate is from the initial velocity uncertainty. The errors in the estimates are consistent with the uncertainty bounds.

As illustrated in to Figure 3.18, after 1000 seconds, just prior to DVL bottom-lock, the position uncertainty estimate is 9.5 m (2σ) in the north and east directions. Since the initial position uncertainty was 1 m (2σ) on the surface, the uncertainty growth is 8.5 m. Figure 3.19(a) shows the error plot with time. Figure 3.19(b) shows a zoom-in of the effect of DVL bottom-lock on the position estimates, with the 2σ position estimate uncertainty reaching approximately 2 m, and uncertainty growth of 1 m. The velocity uncertainty does not necessarily equal the position uncertainty growth rate, as a result of the non-linear IMU integration resulting in non-trivial correlation between the position and velocity estimates.

Figure 3.20 shows the north and east velocity state history for the entire dive after DVL bottom-lock. Due to the back-propogation of the DVL body-relative velocity after bottom-lock, the velocity uncertainty is on average about 3.8 mm/s (2σ). This is better than the DVL velocity estimate alone (6 mm/s 2σ) as there is also a tactical-

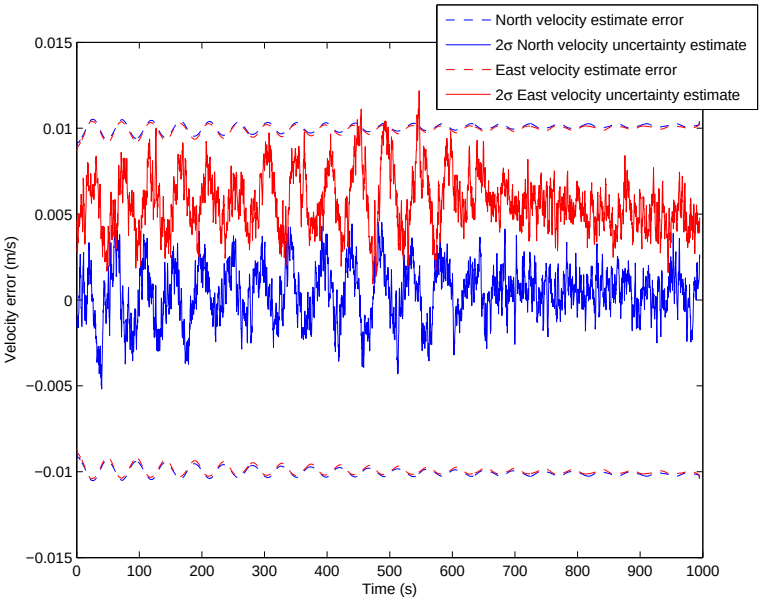

Figure 3.17 – In the 6DOF 1000 second simulation prior to DVL bottom-lock, the north and east run-time vehicle velocity uncertainty is approximately constant as the reobservation of the depth cells allows the error to be maintained at the surface velocity error.

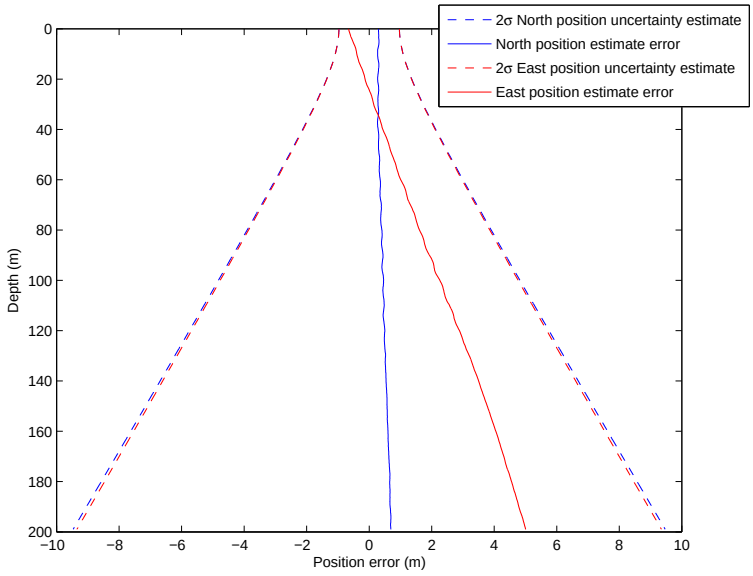

Figure 3.18 – In the 6DOF 1000 second simulation, the vehicle position 2σ uncertainty grows linearly given the velocity estimates have constant error, prior to DVL bottom-lock.

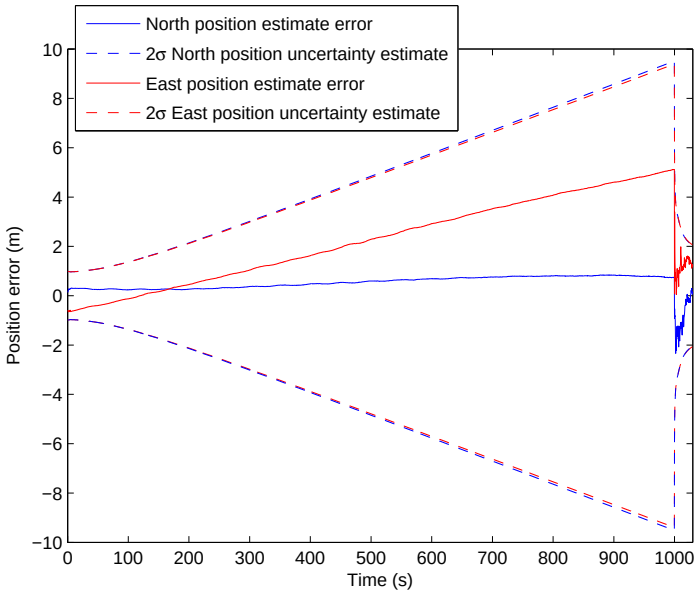

(a)

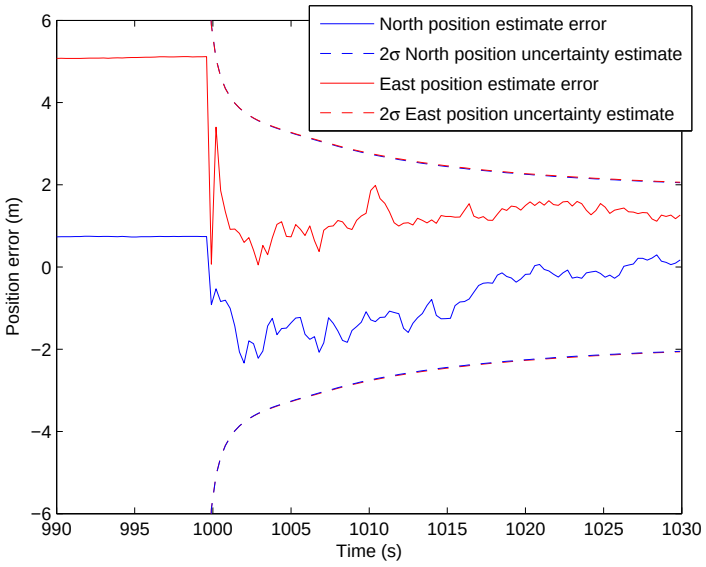

(b)

Figure 3.19 – 6DOF 1000 second simulation (a) The run-time filter position 2σ uncertainty with time. (a) A zoom in on the effect of the DVL bottom-lock occuring at 1000 seconds on the position uncertainty estimate.

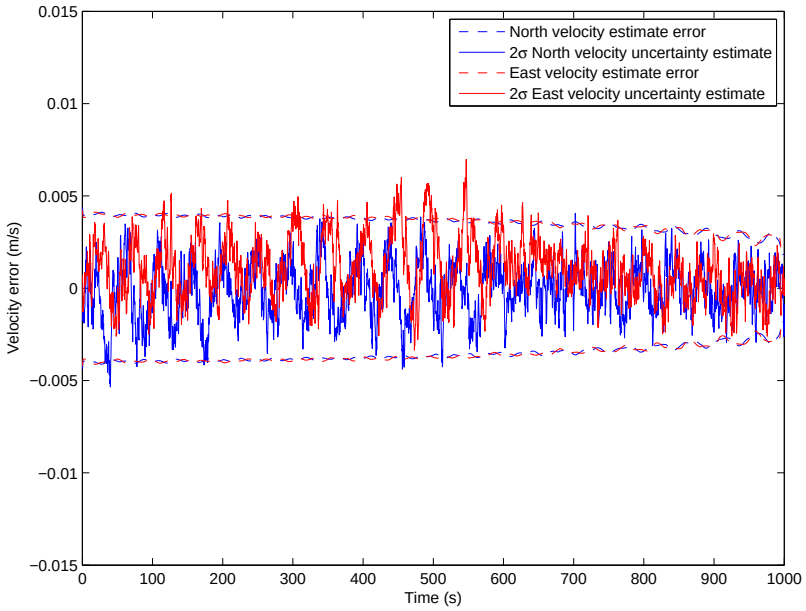

Figure 3.20 – In the 6DOF 1000 second simulation smoothed velocity history in the north and east directions shows that the velocity of the vehicle for the whole descent has been corrected.

grade IMU providing observations.

Figure 3.21 shows the position error for the entire state history after bottom-lock, with a final uncertainty of 2 m (2σ) after 1000 seconds, with uncertainty error growth of 1 m (2σ). The entire smoothed position history has been corrected due to the acquisition of DVL bottom-lock.

To illustrate the ADCP bias estimation, Figure 3.22 illustrates the 10^{th} measurement cell bias error with time after DVL bottom-lock. The measurement cell bias estimates and uncertainties are consistent within the filter. They are estimated to within 2.5 mm/s (2σ) compared to their initial uncertainty of 1 cm/s (2σ), implying the rotation has allowed observability of the bias.

Figure 3.23 shows the simulated current in the north and east directions, and the estimated current with this filter following DVL bottom-lock. Figure 3.24 illustrates the water current errors and uncertainty estimates following DVL bottom-lock. The water current estimation is consistent with the uncertainty bounds.

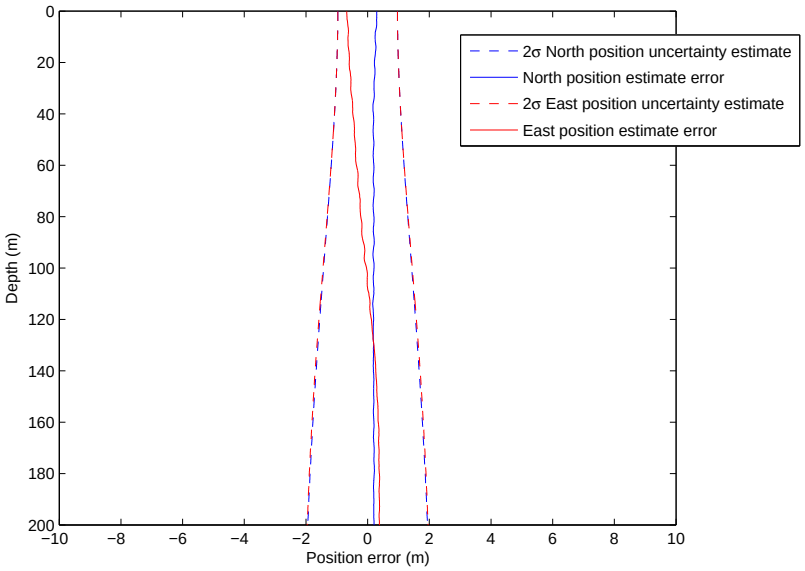

Figure 3.21 – 6DOF 1000 second simulation position full state history after DVL bottom-lock.

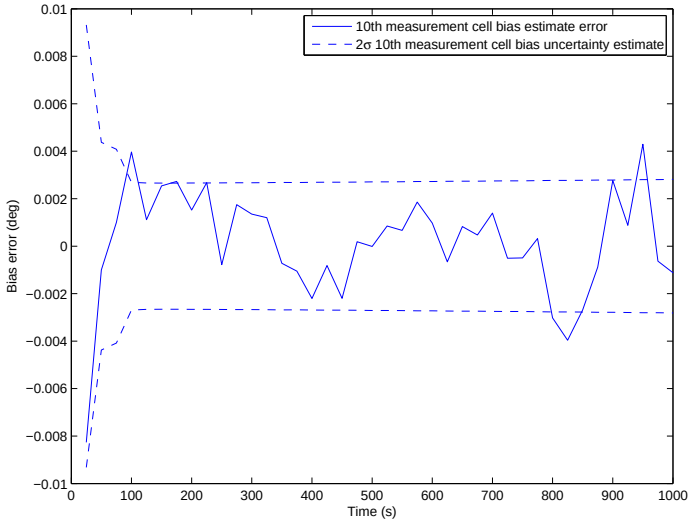

Figure 3.22 – 6DOF 1000 second simulation 10^{th} measurement cell bias error history after DVL bottom-lock.

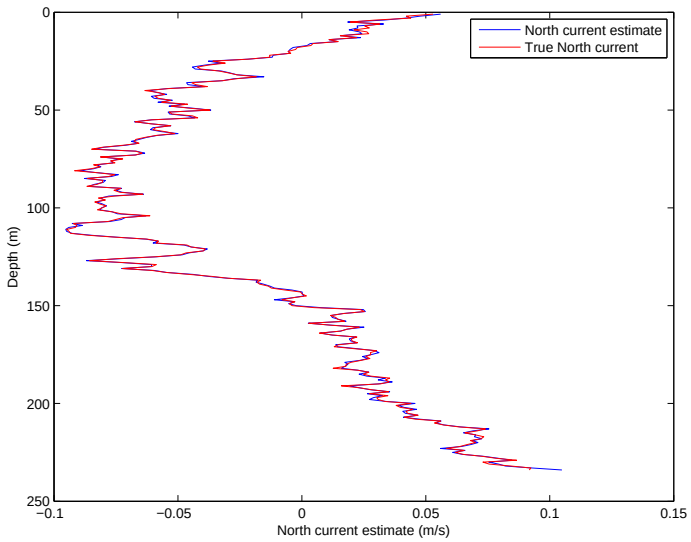

(a)

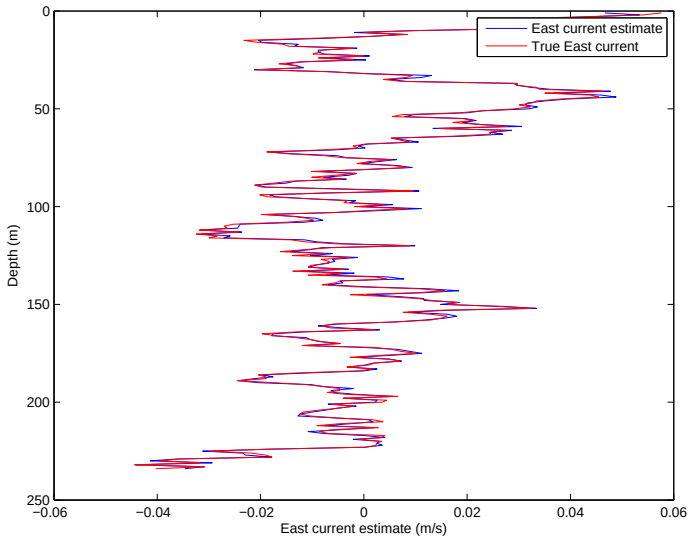

(b)

Figure 3.23 – 6DOF 1000 second simulation current profile estimate and truth from simulation in the (a) north and (b) east directions

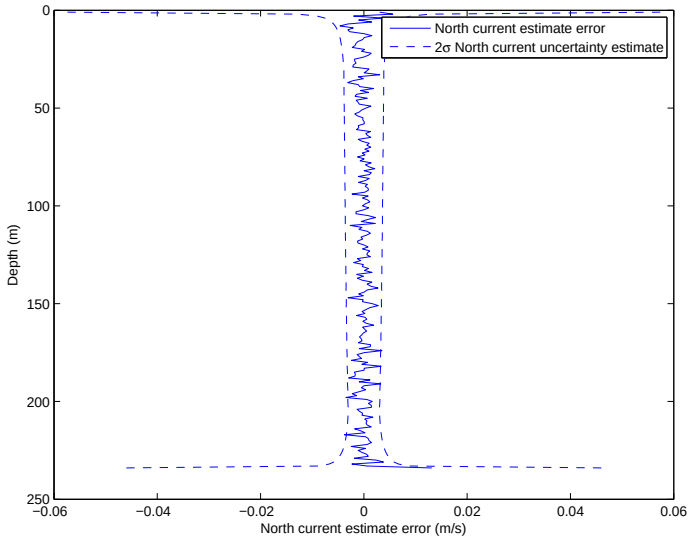

(a)

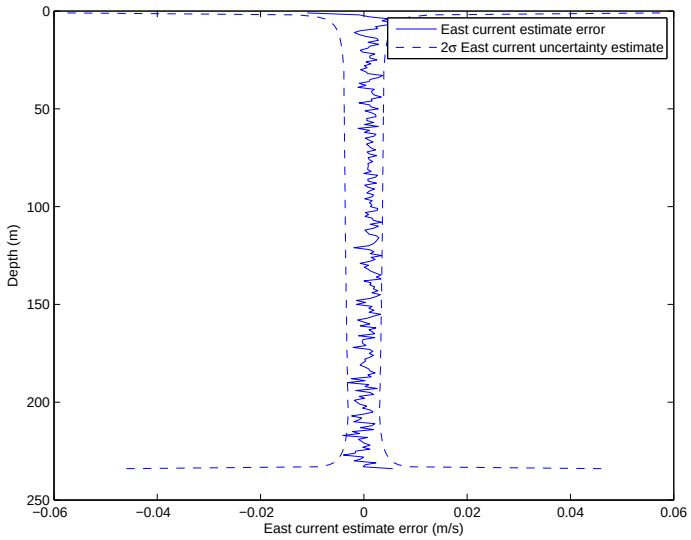

(b)

Figure 3.24 – 6DOF 1000 second simulation current profile estimate error and uncertainty from simulation in the (a) north and (b) east directions

3.3.5 Six degrees-of-freedom simulation with TDCP GPS

As can be seen in the results so far the error growth in position before bottom-lock is dependent on the intial velocity uncertainty. According to van Graas [55], 4-8 mm/s velocity error (2σ) in the horizontal directions is possible with standard GPS by exploiting the carrier phase on the GPS receiver. This is in constrast to the 4 cm/s (2σ) GPS velocity error used in the previous simulations for the Lassen iQ. This means that initial velocity error and thus descent position error growth can also be constrained to the 4-8 mm/s (2σ) range, which is similar to DVL velocity uncertainty.

Time Differenced Carrier Phase (TDCP) [49] is a particular implementation of carrier phase processing. It can be approximately modelled as tracking the change in position of the vehicle.

$$h_{TDCP}(\hat{\mathbf{x}}(t_k)) = \mathbf{p}^n(t_k) - \mathbf{p}^n(t_{k-1}) \tag{3.40}$$

$$R_{TDCP} = \sigma^2_{TDCP} \tag{3.41}$$

The TDCP observation is dissimilar to the DVL observation, as it is a change in position measurement rather than an instantaneous velocity measurement. The delayed state structure of the EIF allows this observation to be correctly accounted for, as modelling it instead as an instantaneous velocity measurement to be input into a naïve EKF implementation could result in modelling errors. The same simulation in the previous section is undertaken with the addition of TDCP GPS on the surface for comparison. The TDCP measurement is assumed to have an uncertainty of 10 mm/s (2σ).

To illustrate the performance improvement possible, Table 3.4 shows the position uncertainty growth can be reduced by incorporating TDCP in the following simulations, especially during the dive phase. Once DVL bottom-lock is obtained, the

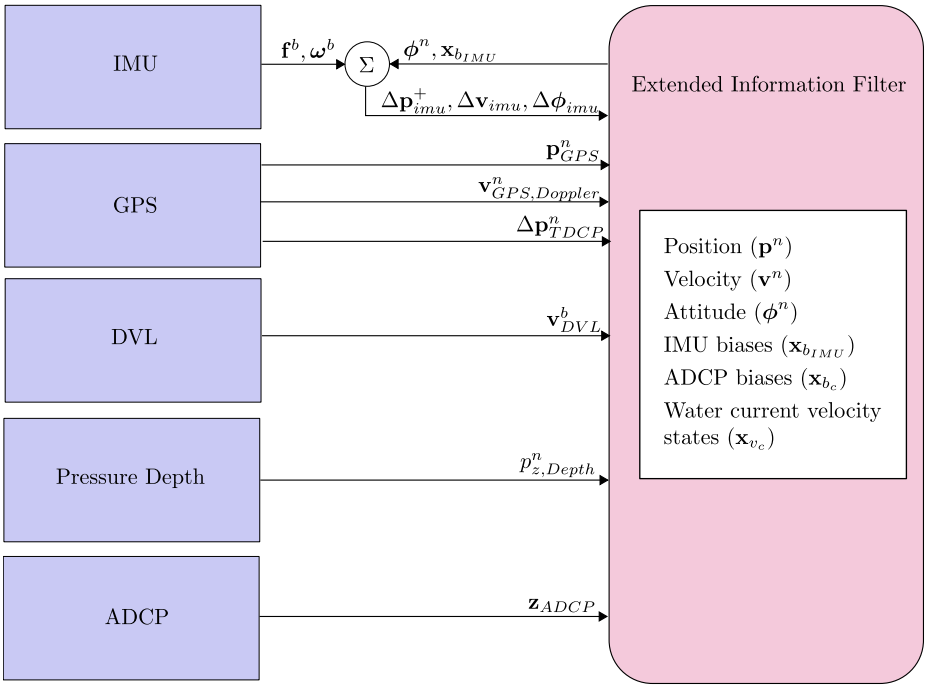

Figure 3.25 – The localisation architecture for the 6DOF simulation with TDCP.

Table 3.4 – Position uncertainty growth rates compared to the initial uncertainty at the sea surface with and without TDCP.

	Position uncertainty growth 2σ	
	Without TDCP	With TDCP
Prior to DVL bottom-lock	∼8.5 m/1000 seconds (∼30.6 m/hour)	∼3 m/1000 seconds (∼10.8m/hour)
Following 30 seconds of DVL bottom-lock	∼1 m/1000 seconds (∼3.6 m/hour)	∼0.9 m/1000 seconds (∼3.2 m/hour)

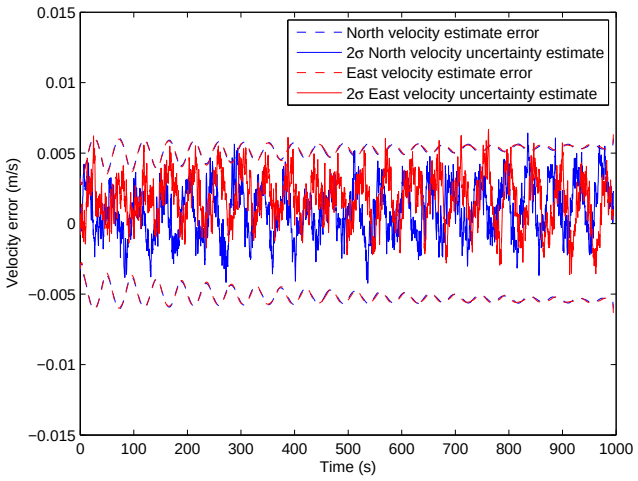

Figure 3.26 – In the 6DOF with TDCP 1000 second simulation, the filter vehicle velocity uncertainty is approximately constant as the reobservation of the depth cells allows the uncertainty to be maintained at the initial surface velocity uncertainty.

difference in localisation performance compared to TDCP being absent is minor. In the 1000 second simulations, the position uncertainty growth is almost linear, with the per-hour uncertainty listed in the table above.

As can be seen in Figure 3.26, the run-time filter uncertainty estimate of velocity is constrained to about 0.007 m/s (2σ) in the north and east directions. This uncertainty in velocity during the dive phase is from the initial velocity uncertainty after GPS/IMU initialisation and ADCP estimation on the surface, including TDCP. Similarly to the TDCP-absent case, the velocity uncertainty is also not deteriorating noticeably within the 1000 second time frame.

As illustrated in Figure 3.27, after 1000 seconds, just prior to DVL bottom-lock, the position error is 4 m (2σ) in the north and east directions, or 3 m uncertainty growth compared to the surface position uncertainty of 1 m (2σ). Figure 3.28(a) shows the error plot with time. Figure 3.28(b) shows a zoom-in of the effect of DVL bottom-lock on the position estimates, with the 2σ position estimate uncertainty reaching approximately 1.9 m, or 0.9 m uncertainty growth compared to the surface uncertainty. The post-DVL uncertainty growth is only slightly lower compared to the no TDCP

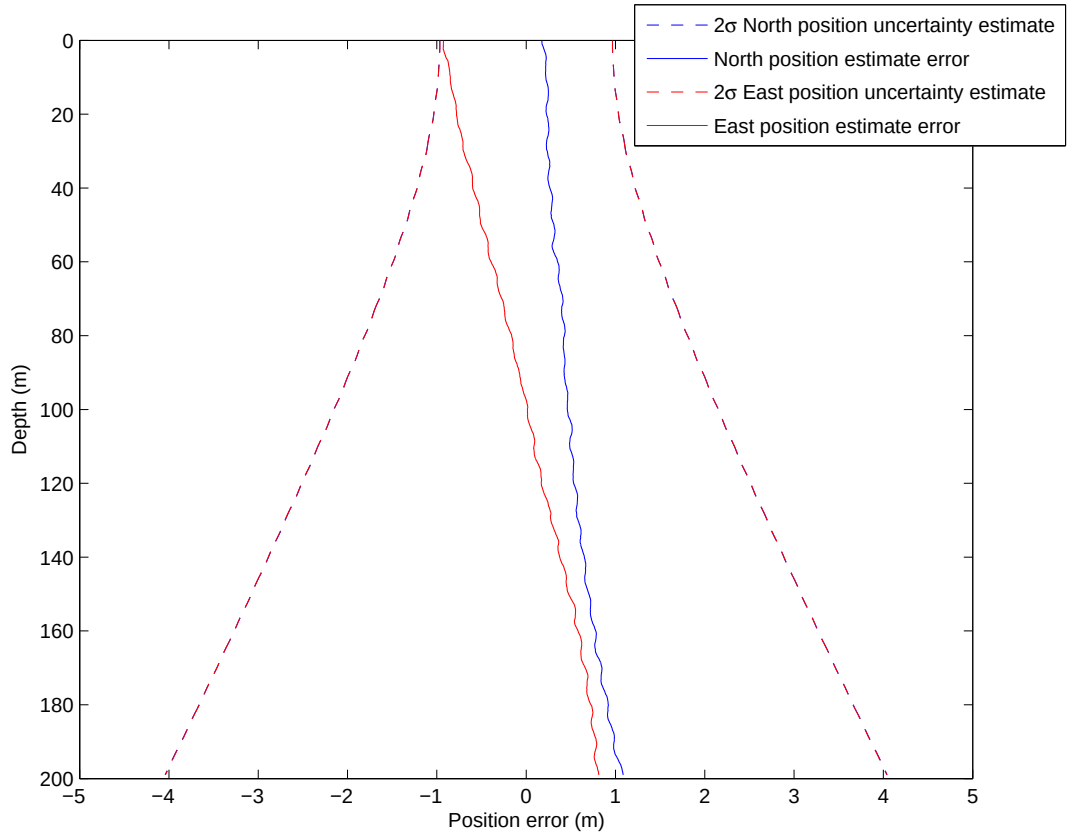

Figure 3.27 – In the 6DOF with TDCP 1000 second simulation, the vehicle position 2σ uncertainty grows linearly given that the velocity estimates have constant error.

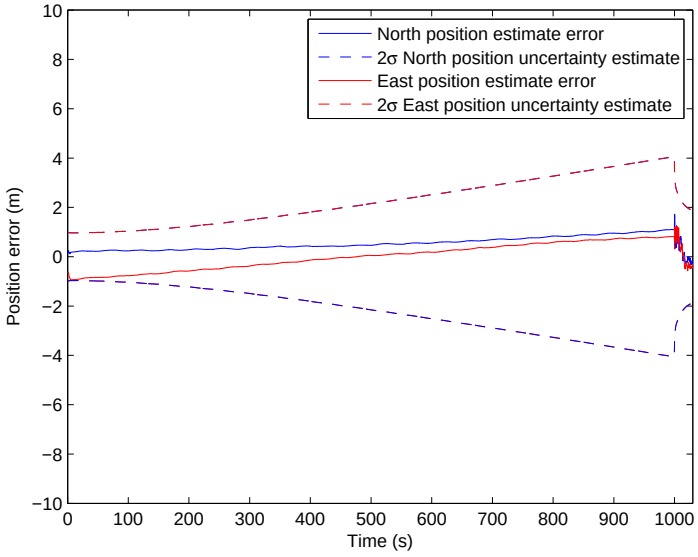

(a)

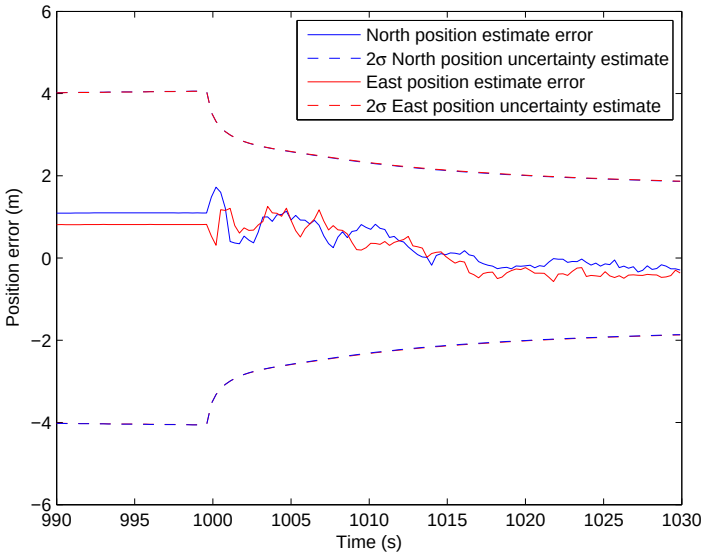

(b)

Figure 3.28 – 6DOF with TDCP 1000 second simulation (a) The run-time filter position 2σ uncertainty with time. (b) A zoom in on the effect of the DVL bottom-lock on the position estimate at 1000 seconds.

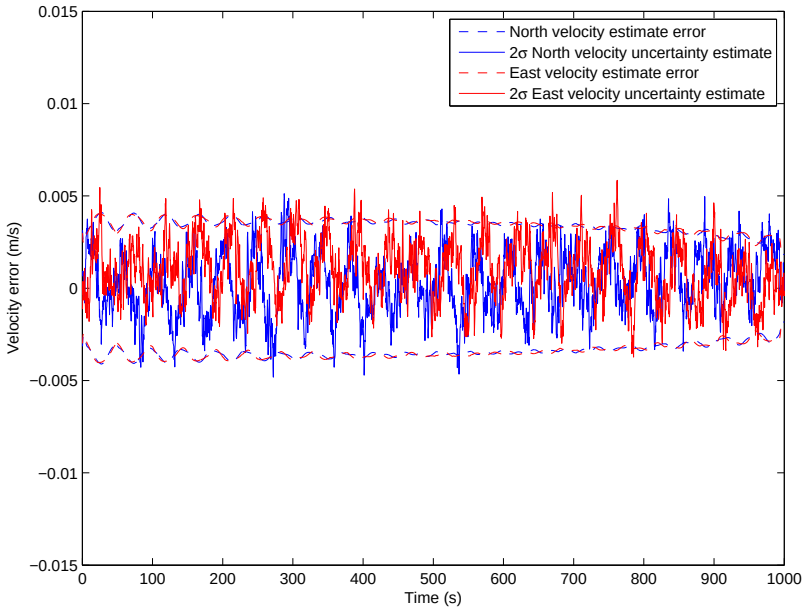

Figure 3.29 – 6DOF with TDCP 1000 second simulation smoothed velocity history in the north and east directions shows that the velocity of the velocity for the whole descent has been corrected.

case. This implies that while the TDCP is aiding the position estimation during descent, the post-descent position uncertainty primarily depends on the DVL/IMU observations.

Figure 3.29 shows the north and east velocity state history for the entire dive after DVL bottom-lock. Similarly to the TDCP-absent case, the velocity uncertainty is on average about 3.4 mm/s (2σ).

Figure 3.30 shows the north and east position error for the entire state history after bottom-lock, with a final uncertainty of 1.9 m (2σ) after 1000 seconds.

Figure 3.31 illustrates the 10^{th} measurement cell bias error with time after DVL bottom-lock. The measurement cell bias estimates are consistent with the filter.

Figure 3.32 shows the simulated current and the estimated current with this filter following DVL bottom-lock. The water current estimation is consistent with the uncertainty bounds, as evident in Figure 3.33.

A simulation in deeper water is undertaken to validate the uncertainty growth rates

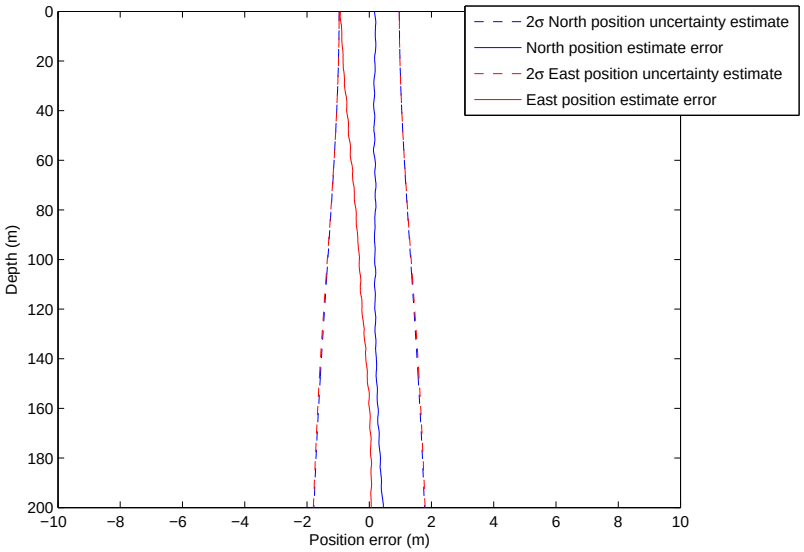

Figure 3.30 – 6DOF with TDCP 1000 second simulation position full state history after DVL bottom-lock.

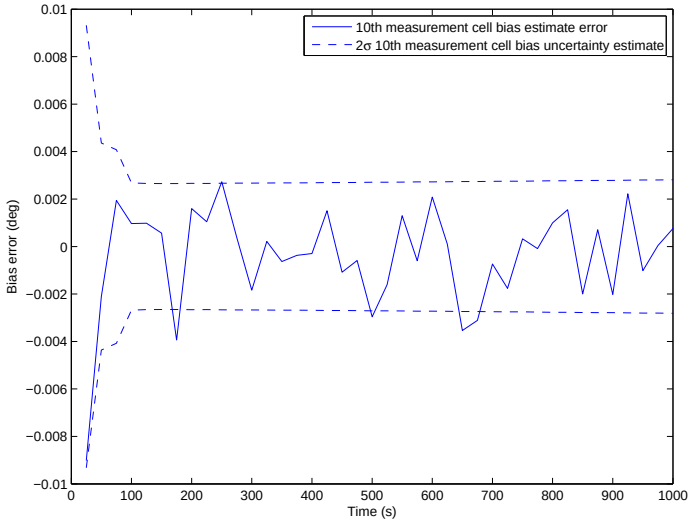

Figure 3.31 – 6DOF with TDCP 1000 second simulation 10^{th} measurement cell bias error history after DVL bottom-lock.

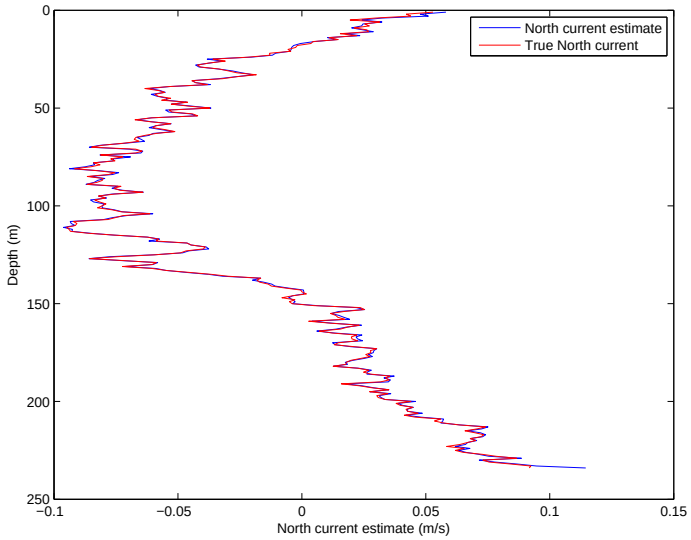

(a)

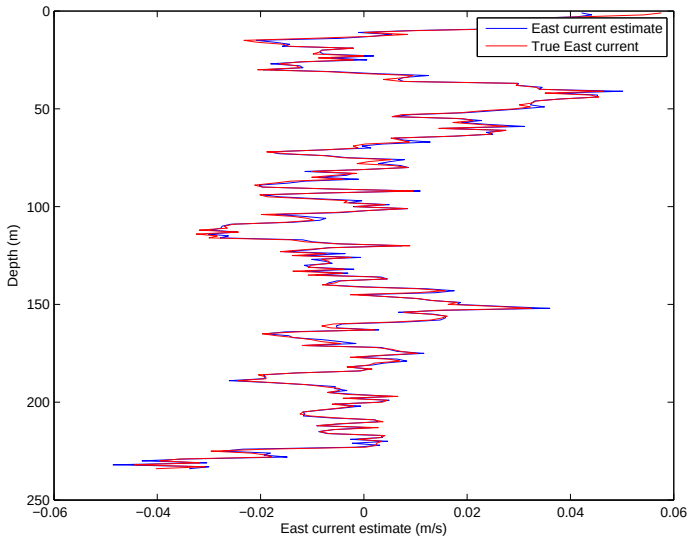

(b)

Figure 3.32 – 6DOF with TDCP 1000 second simulation current profile estimate and truth from simulation in the (a) north and (b) east directions

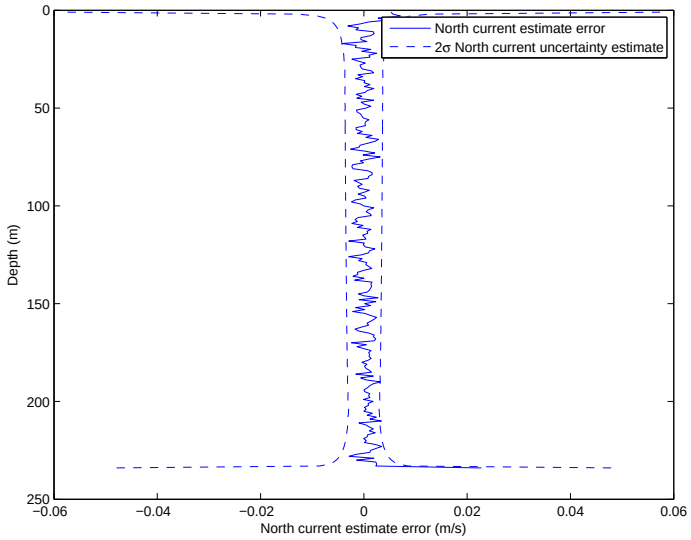

(a)

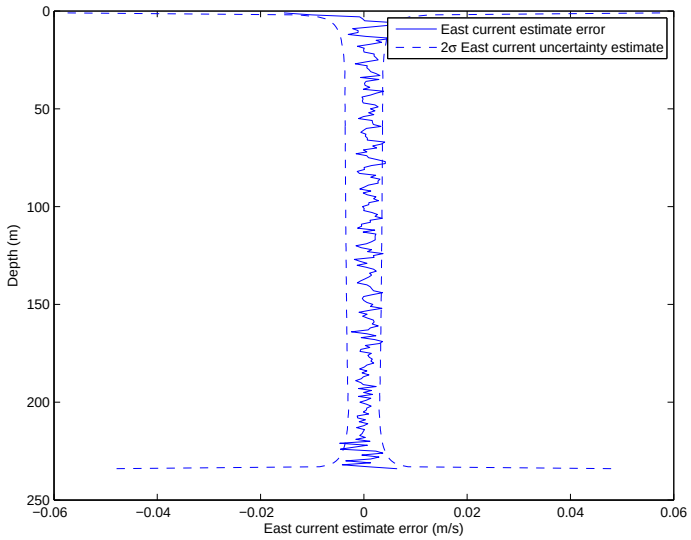

(b)

Figure 3.33 – 6DOF with TDCP 1000 second simulation current profile estimate error and uncertainty from simulation in the (a) north and (b) east directions

over longer periods of time. The following simulation possesses a one hour period of mid-water localisation, without DVL or GPS. With a descent rate of 0.2 m/s, the simulated dive is 760m of water depth. Since it is prohibitive computationally to perform smoothing and maintain the full pose history for this time period, the marginalised filter as described in Section 3.2.2 was applied to provide run-time pose estimates and uncertainties. The run-time filter is the maximum likelihood estimate of the state of the vehicle at the present time, and not for past states, unlike the smoothed solution. The state estimates (x) and uncertainties ($p(x)$) are defined as:

$$x = \hat{\mathbf{x}}(t_k)|\mathbf{z}(t_0) : \mathbf{z}(t_k) \tag{3.42}$$

$$p(x) = p(\hat{\mathbf{x}}(t_k)|\mathbf{z}(t_0) : \mathbf{z}(t_k)) \tag{3.43}$$

As can be seen in Figure 3.34, the run-time filter uncertainty estimate of velocity is constrained to about 0.007 m/s (2σ) in the north and east directions. This uncertainty in velocity during the dive phase is from the initial velocity uncertainty after GPS/IMU initialisation and ADCP estimation on the surface, including TDCP. The actual error in the north velocity is exceeding the upper 2σ bounds regularly. The initial velocity estimate in the north direction on the surface was near the boundary of the 2σ uncertainty estimate. Thus, it will continue to be on the boundary, and this is normal behaviour for the filter, as outlined in Section 3.3.2. In this case, over the 3600 second time span, the velocity uncertainty is slightly increasing, implying some information loss from the continual initialisation of new water current depth cells.

As shown in Figure 3.35, after 1000 seconds, just prior to DVL bottom-lock, the position uncertainty estimate is approximately 16 m (2σ) in the north and east directions, or 15 m uncertainty growth compared to the surface uncertainty. Figure 3.36(a) shows the error plot with time. Figure 3.36(b) shows a zoom-in of the effect of DVL bottom-lock on the position estimates, with the 2σ position estimate uncertainty reaching approximately 7.5 m, or 6.5 m uncertainty growth compared to the surface uncertainty of 1 m. The position estimates show a correlated, but consistent error

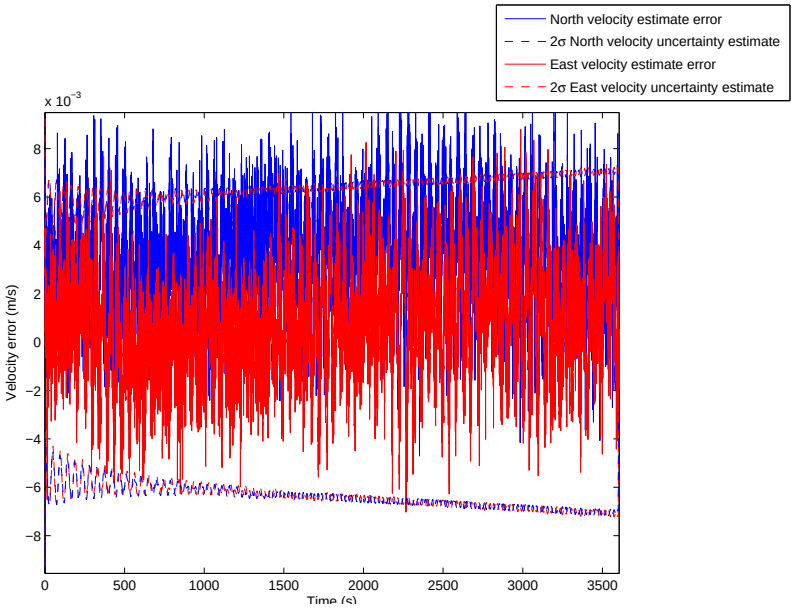

(a)

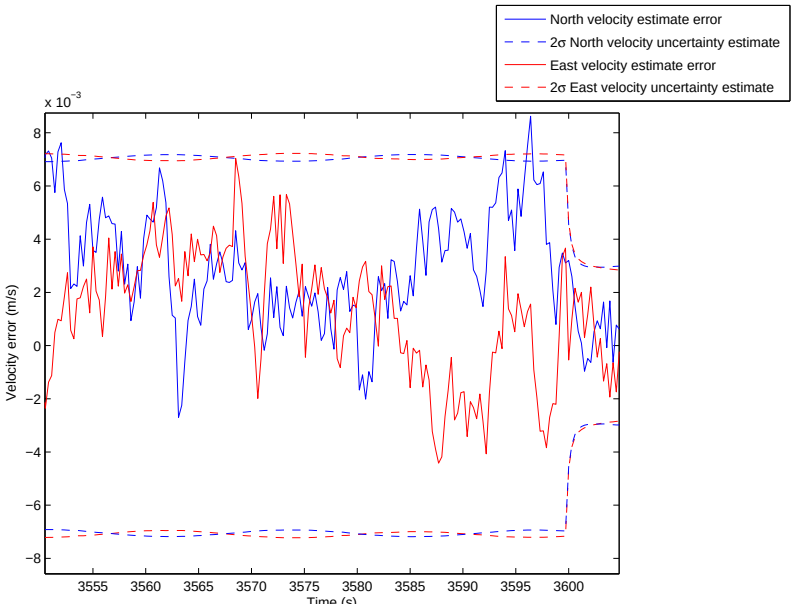

(b)

Figure 3.34 – 6DOF with TDCP 1 hour simulation (a) The run-time filter velocity 2σ uncertainty with time. (b) A zoom in on the effect of the DVL bottom-lock on the velocity estimate at 1000 seconds.

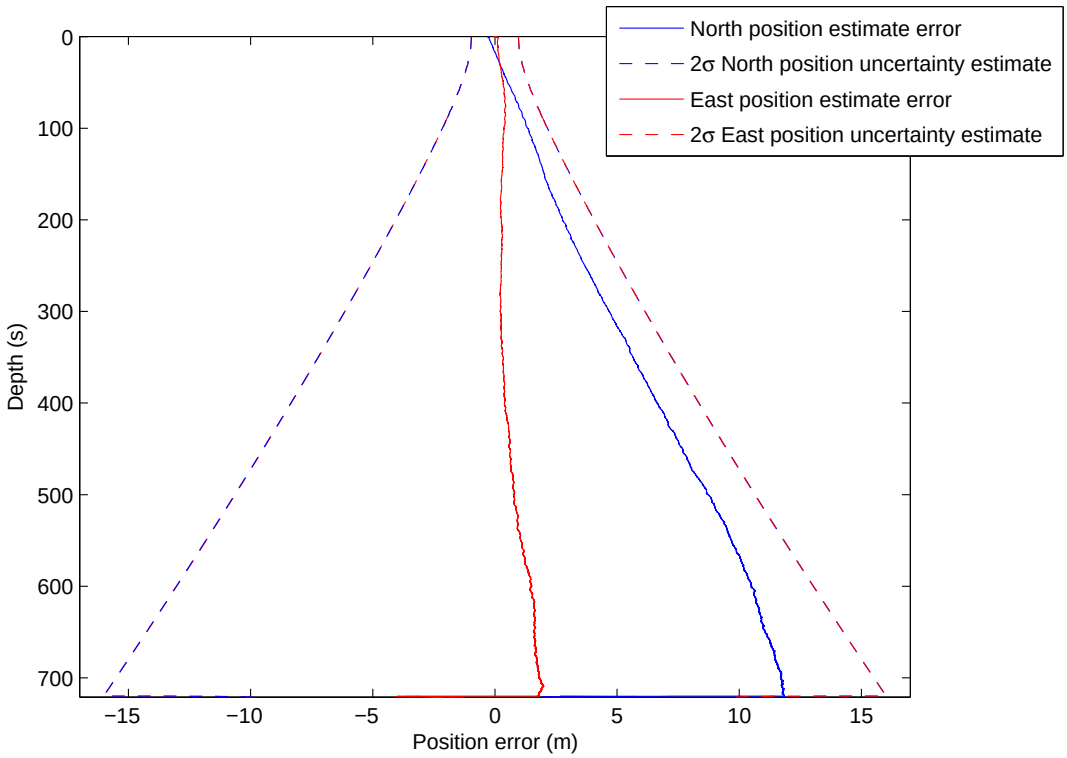

Figure 3.35 – In the 6DOF with TDCP 1 hour simulation, the run-time filter vehicle position 2σ uncertainty grows near-linearly given the velocity estimates have constant error. Following DVL bottom-lock, the error reduces markedly. Figure 3.28(b) shows this effect in detail.

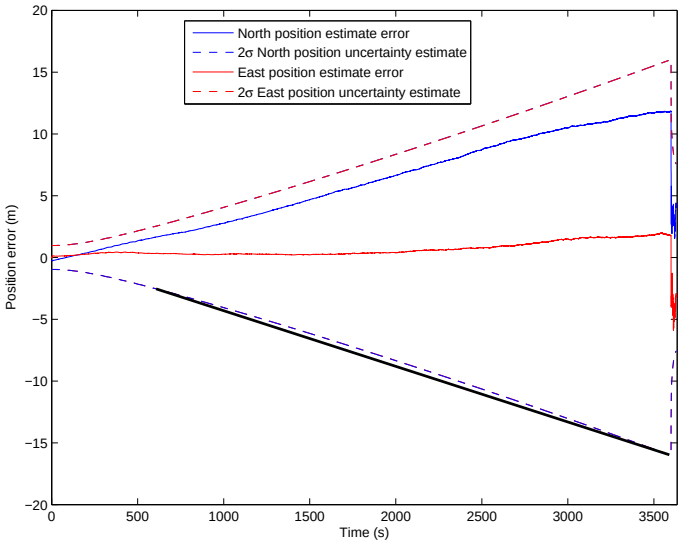

(a)

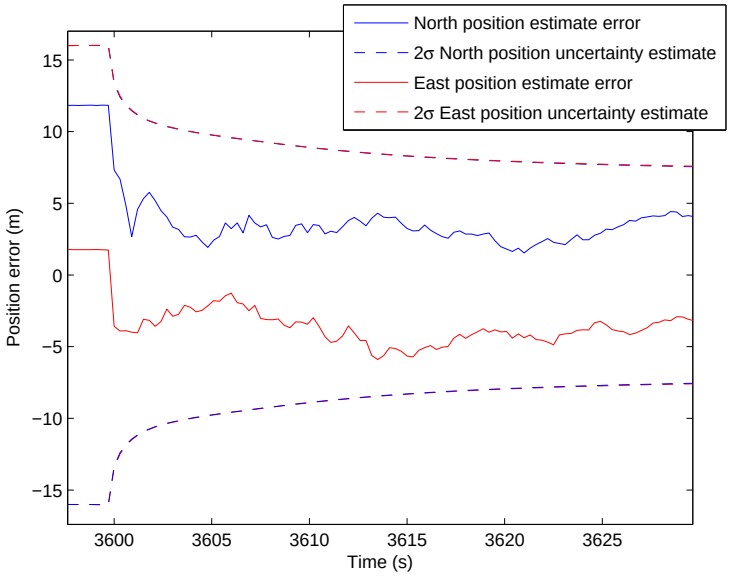

(b)

Figure 3.36 – 6DOF with TDCP 1 hour simulation (a) The run-time filter position 2σ uncertainty with time. A black line is drawn for a portion of the position uncertainty bounds to illustrate the slight non-linearity of the uncertainty growth. (b) A zoom in on the effect of the DVL bottom-lock on the position estimate.

Table 3.5 – Position uncertainty growth rates compared to the initial uncertainty at the sea surface with TDCP over 1000 and 3600 seconds.

	Position uncertainty growth 2σ	
	Over 1000 seconds	Over 3600 seconds
Prior to DVL bottom-lock	∼3 m/1000 seconds (∼10.8m/hour)	∼15 m/hour
Following 30 seconds of DVL bottom-lock	∼0.9 m/1000 seconds (∼3.2 m/hour)	∼6.5 m/hour

with respect to the 2σ uncertainty bounds. This shows that the north velocity estimates, with errors exceeding their 2σ uncertainty bounds, once integrated through the IMU model produce the expected, consistent result for position uncertainty. Table 3.5 outlines the performance over one hour compared to 1000 seconds. The increased uncertainty growth rate over one hour can be attributed to information loss and velocity uncertainty increase during descent.

The one hour descent uncertainty with TDCP is compared to present localisation methods in Figure 3.37, showing similar performance to acoustic beacon methods and significantly improved performance in comparison to the previous state-of-the-art in self-contained localisation.

3.4 Sirius AUV results and View-based SLAM

In order to validate the ADCP-aided localisation algorithm, the following results are obtained through the use of *Sirius* [60], the University of Sydney's Australian Centre for Field Robotics (ACFR) oceangoing AUV. It is a modified version of the mid-sized SeaBED robotic vehicle from Woods Hole Oceanographic Institution [47]. This class of AUV is designed for relatively low-velocity, high-resolution imaging and is passively stable in roll and pitch. The *Sirius* AUV is pictured in Figure 3.38 performing a mission. It is equipped with a suite of oceanographic sensors.

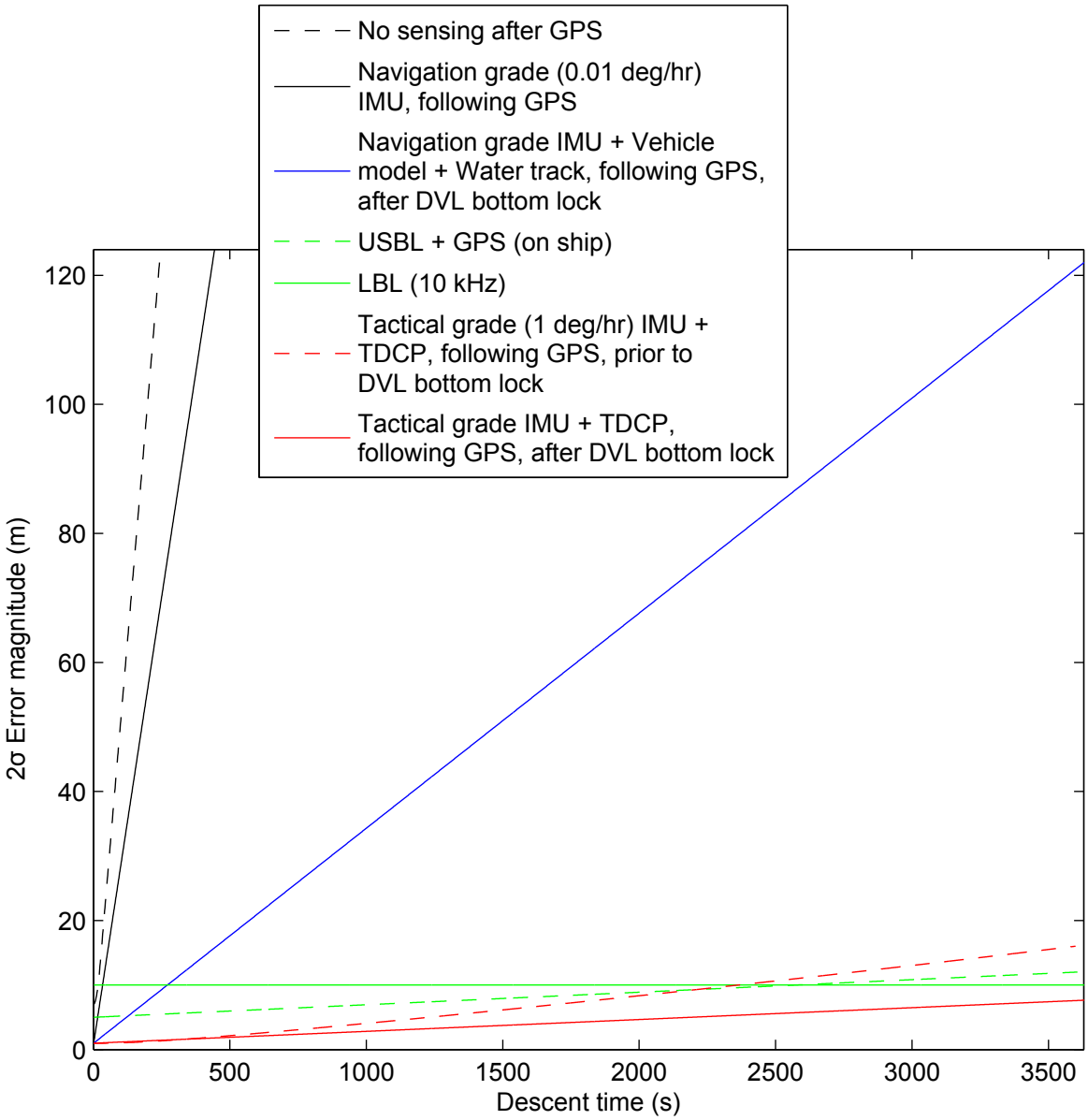

Figure 3.37 – Comparison between different underwater localisation methods and their approximate accuracy where GPS is unavailable for a 1 hour dive, which is typically between approximately 700m and 1400m of depth depending on AUV descent rates. The new localisation method compares favourably in this case with acoustic localisation methods, and outperforms existing self-contained techniques.

Navigation sensors onboard include a 1200 kHz RDI DVL/ADCP, Tracklink 1500 HA USBL and a Lassen iQ GPS receiver, along with a stereo imaging platform, which allows for view-based loop closures [32] [62]. The parameters used in the *Sirius* AUV experiments are outlined in Table 3.6. Images to allow view-based loop closure are available to the *Sirius* AUV when it is at 2 m altitude. The process model used for the vehicle is a constant velocity model. The process noise is tuned according to the worst case dynamics possible by the vehicle, as no thruster model is incorporated in this experiment.

Attitude information is supplied by the in-built magnetic compass and accelerometers in the RDI DVL/ADCP. The 1200 kHz RDI DVL/ADCP uses less power and is more accurate than the 150 kHz version, and can be used at a lower minimum range, which is important for localisation during image acquisition which occurs at 2m altitude. This comes at the cost of the maximum range for bottom-lock, which is 40m in practice for the 1200 kHz compared to 200m for the 150 kHz. The USBL is only utilised for ground truth in the following experiments, and is not fused into the filter. The vehicle USBL position estimate accuracy is a function of the position and attitude uncertainty from the ship (from a Novatel INS/GPS system), in addition to the USBL uncertainty. USBL errors can occur due to multipath, as well as sound speed estimate errors (including variation through the water column) and signal receive strength and noise. The result is an uncertainty of approximately 10m (2σ) in typical conditions. If the USBL was to be fused into the filter, the uncertainty estimates will be further reduced, although the focus of this chapter is to be able to use it as a ground truth for validating the performance without relying on USBL in the filter. Additionally, it is difficult to verify the performance of fusing the USBL into the localisation without a separate ground truth, such as that from LBL. Verifying the performance of utilising all of these sensors simultaneously remains as future work.

Loop-closure observations are created using a six degree-of freedom stereovision relative pose estimation algorithm [32] [62]. The SIFT algorithm is used to extract and associate visual features, and epipolar geometry is used to reject inconsistent feature observations within each stereo image pair. Triangulation is performed to calculate

Table 3.6 – Parameters for the following experiments involving the *Sirius* AUV.

INS/GPS on ship	Novatel (including Honeywell HG1700A58 IMU)
USBL	Tracklink 1500 HA
USBL total uncertainty	10m (2σ) in typical conditions
GPS receiver	Lassen iQ GPS receiver
GPS position uncertainty	10 m (2σ)
GPS velocity uncertainty	0.04 m/s (2σ)
DVL/ADCP sensor	RDI 1200 kHz
DVL velocity uncertainty	0.006 m/s (2σ)
ADCP velocity uncertainty	0.01 m/s (2σ)
Heading sensor	RDI internal fluxgate compass
Heading uncertainty	4 degrees (2σ)
Constant velocity model process noise (2σ)	0.5 m/s^2(surface) 0.1 m/s^2(submerged)

initial estimates of the feature positions relative to the stereo rig, and a redescending M-estimator [31], is used to calculate a relative pose hypothesis that minimises a robustified registration error cost function. Any remaining outliers with observations inconsistent with the motion hypothesis are then rejected. Finally, the maximum likelihood relative vehicle pose estimate and covariance are calculated from the remaining inlier features. The following pose constraints are added to the EIF following this process:

$$h_{Visual\,SLAM}(\hat{\mathbf{x}}(t_k)) = \begin{bmatrix} \hat{\mathbf{p}}^n(t_k) - \hat{\mathbf{p}}^n(t_{k-1}) \\ MatrixToEuler(\hat{\mathbf{C}}_{k_1}^{k_2}) \end{bmatrix} \tag{3.44}$$

$$R_{Visual\,SLAM} = \mathbf{P}_{relative\,transformation} \tag{3.45}$$

3.4.1 Results

Data from two missions completed in 2010 by the vehicle in Tasmania are used to illustrate the performance of the proposed ADCP-aided navigation filter. The first mission is shorter, in relatively shallow water such that DVL lock was available throughout the dive. The second mission was completed in deeper water and relies on USBL observations to validate the positioning accuracy. The filter architecture being verified is outlined in Figure 3.39.

Shallow water dive

The *Sirius* vehicle was used in a mission which involved descending in water which was just within DVL bottom-lock range (about 40m depth for the 1200 kHz DVL), completing some subsurface manoeuvres with visual loop closures for SLAM, and then ascending. The total dive time was approximately 1000 seconds. This mission's position estimates are shown in Figure 3.40. In order to compare the ADCP-aided method with the ground truth from DVL, the DVL measurements were not fused into the filter during the descent and ascent phase for 150 seconds each. This simulates a greater depth where DVL bottom-lock would not be possible, while providing a

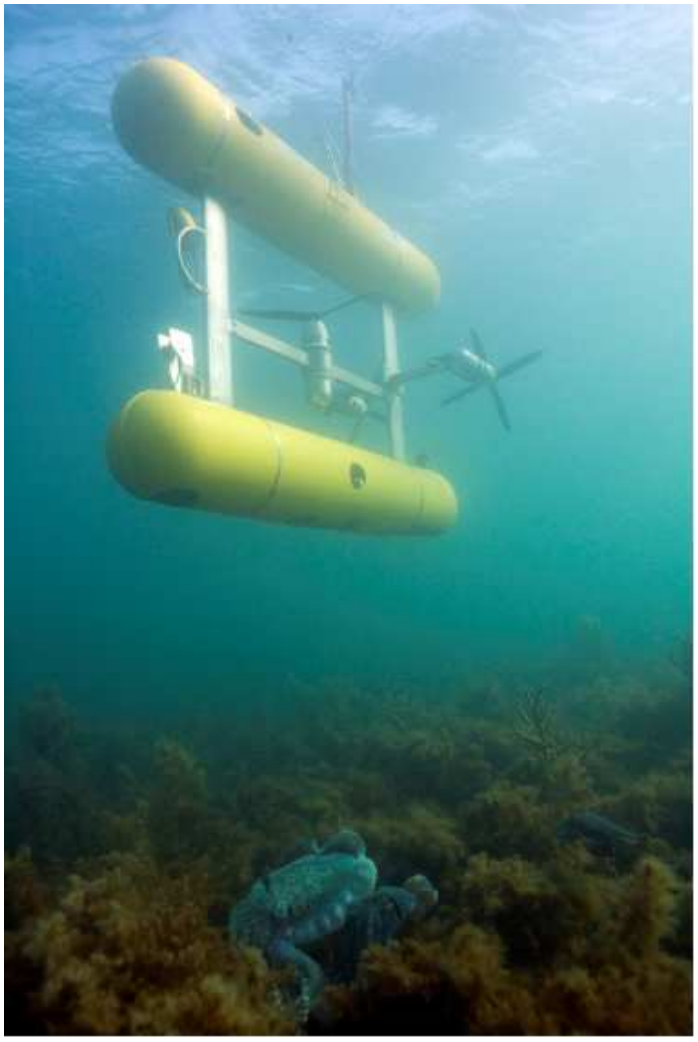

Figure 3.38 – The *Sirius* AUV imaging cuttlefish populations.

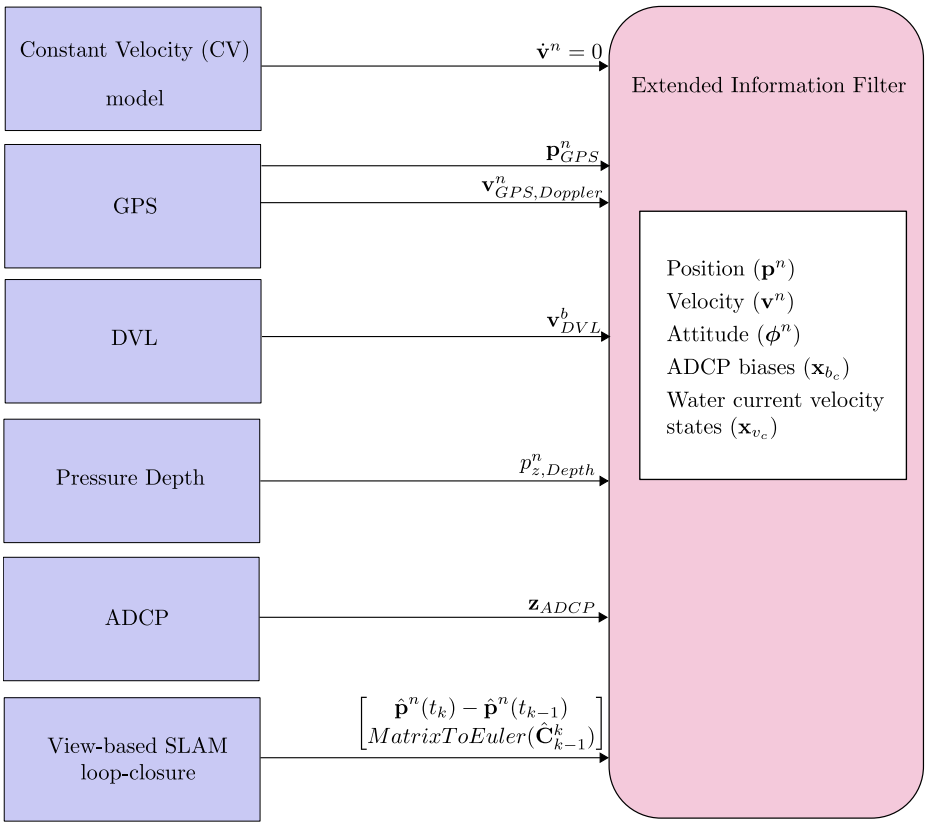

Figure 3.39 – The tested localisation architecture for the *Sirius* AUV.

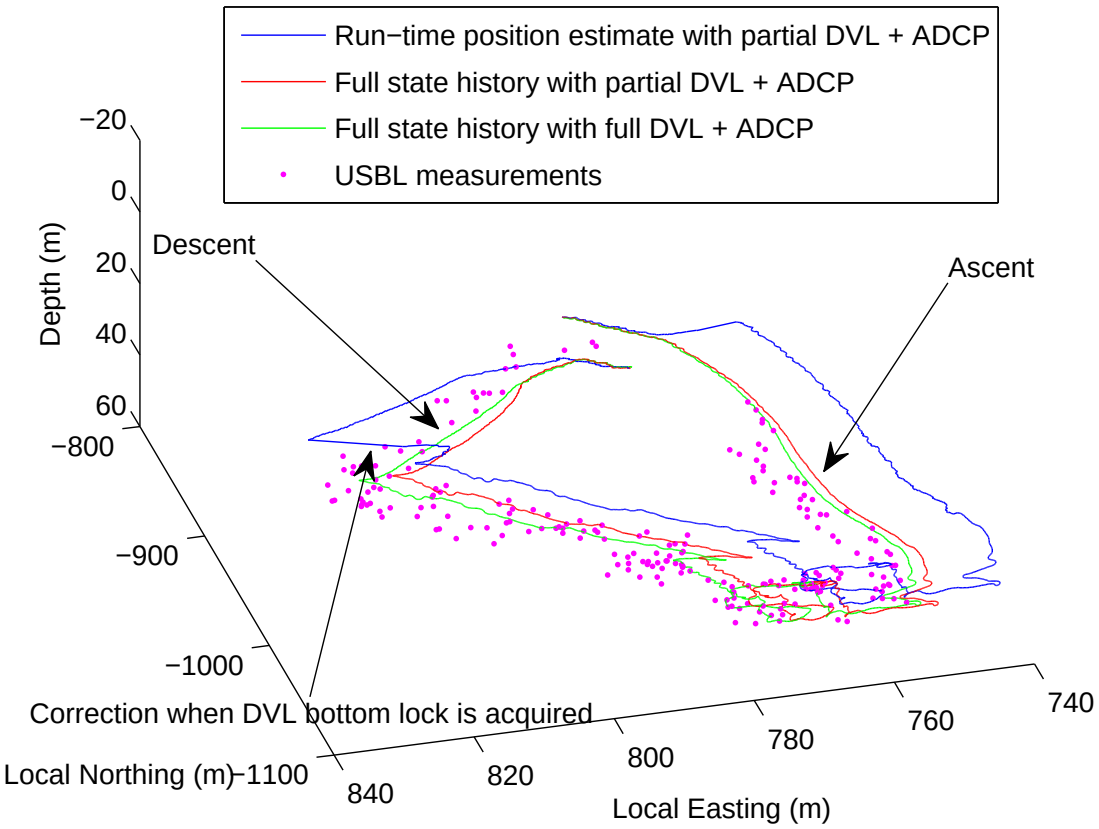

Figure 3.40 – Trajectory of the 40m depth short mission, where DVL bottom-lock is available the entire dive. A simulated partial DVL blackout for 150 seconds during ascent and descent results in only ADCP measurements for this time. The correction following the DVL acquisition is a step change.

comparison with ground truth. Comparisons can illustrate how the ADCP-only case compares to the DVL while descending and ascending. The ADCP was interleaved with the DVL in a 1:1 ratio, with an ADCP reading occuring at approximately 1 Hz. USBL allows ship-based tracking of the vehicle, which allows independent verification of the localisation.

The full state history, or smoothed solution, of the filter is defined as the output of the Information Filter at the end of the mission, with all poses kept in the estimation. The run-time filter is the maximum-likelihood estimate of pose of the vehicle at that time during the mission. As shown in Figure 3.41(a), during descent for the online run-time filter, the error in position grows quickly because there is an error in the

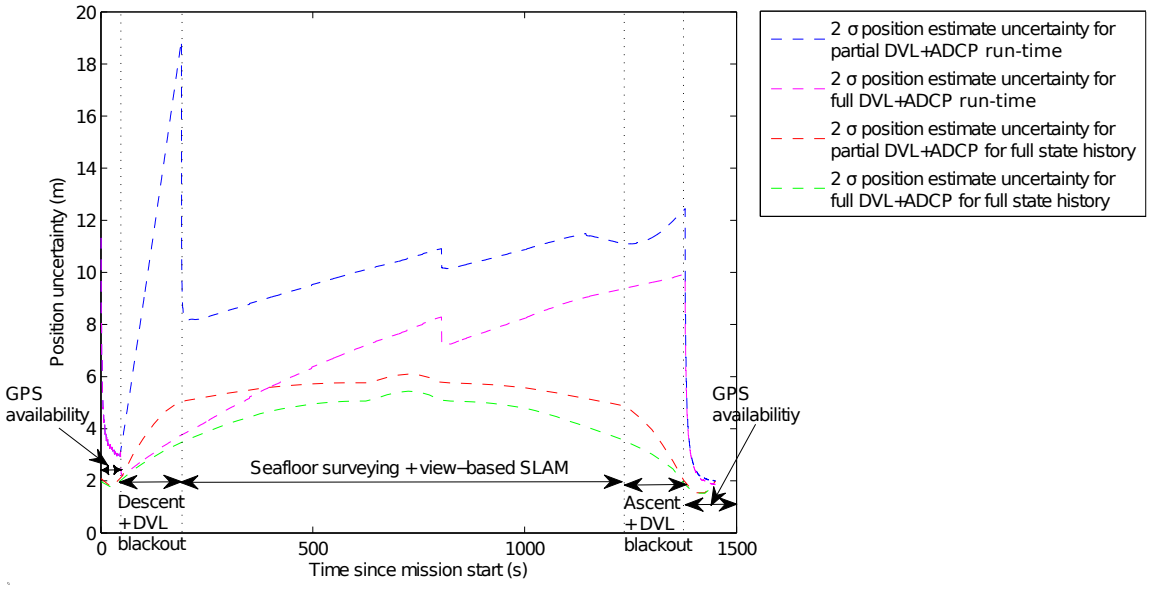

(a)

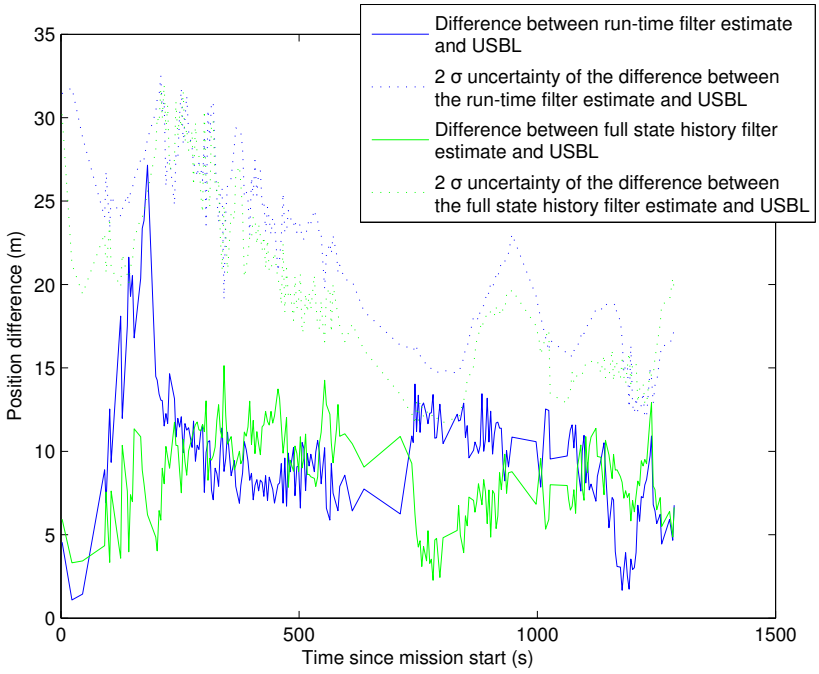

(b)

Figure 3.41 – (a) Shallow water dive position uncertainty estimates for filters with partial and full DVL, in-run and for the full state history (b) Differences between filter results and USBL measurements for the shallow water dive, along with 2 σ uncertainties of this difference, showing that the filter is consistent. The error has a constant offset factor during the bottom phase due to the georeferencing position uncertainty linking the GPS position from the surface, to the ADCP-aided descent and ascent, which the relative SLAM corrections cannot adjust.

estimate of velocity, at about 10 cm/s (2σ). The uncertainty in GPS velocity is inflated as the antenna is attached to a flexible shaft pointing upwards, while the vehicle is undergoing roll and pitch in swell, affecting the ability of the GPS Doppler velocity to estimate the velocity at the DVL sensor. When DVL bottom lock was available, the DVL velocity was used as a ground truth to arrive at an estimate of the GPS velocity uncertainty of 20 cm/s (2σ). Once DVL bottom-lock is acquired, the position uncertainty during the descent is reduced. The reason for this is that once DVL bottom-lock is acquired after descent, the velocity estimates of the water currents in the entire water column are improved. By maintaining correlations between states during the descent, the filter propagates the accurate velocity information attained upon reacquiring bottom-lock back through the entire state history.

During run-time, the position uncertainty of the mission is 12m (2σ) just prior to post-ascent GPS acquisition, and after it is within 6m (2σ) for the full state history. This compares with the error estimate of at most 5m (2σ) for the full state history when using DVL the entire time. So even with only 1 Hz ADCP measurements for 150 seconds during the ascent and descent, the uncertainty associated with the estimates of the entire mission approaches the full DVL localisation case.

This correction is accurate to almost the DVL velocity accuracy. It does not have the same accuracy to the equivalent DVL during this time because only a finite number of measurements with the noisy ADCP sensor are used to observe the water column currents. Thus, there is a slight information loss as expected from the analysis in Section 3.3.3.

The action of a view-based SLAM loop closure is seen at about 800 seconds of mission time, evident from the sudden decrease in uncertainty for the filter while in-run, where the AUV has detected a revisit to a previous site in the mission through image feature matching. This and subsequent loop closure observations act to limit the position uncertainty during the seafloor mapping portion of the dive as the vehicle undertakes its mission. Additionally, a greater improvement in the localisation solution following the post-ascent GPS acquisition is possible, as there exists stronger correlations throughout the dive to link the prior-descent GPS positioning to the

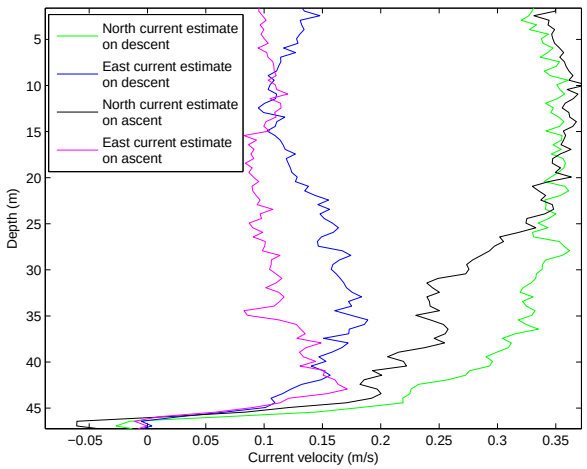

Figure 3.42 – Current estimates for 40m-depth short mission, with ascent and descent occuring approximately 1000 seconds apart with a separation of approximately 200m in the horizontal direction. There is a small change in the water currents over this distance and period of time.

post-ascent GPS positioning.

Figure 3.41(b) compares the filter result with the independently observed USBL observations. It can be seen that the ADCP filter is consistent with the USBL observations, validating that the filter operates as expected with real data, and that the assumptions made throughout the filter formulation are sound.

Figure 3.42 shows the final estimated current for the mission, illustrating the water profile current structure which the ADCP-aided method measures in order to navigate against. Ground truth of the current profile was not available in this instance, however the estimate of the ascent and descent portions of the dive appear consistent over the period of the dive suggesting that the structure of the current profile has not changed significantly over this period.

Deeper water dive

The vehicle also completed a longer dive in 100m of water in which DVL bottom-lock was not available through the descent and ascent. The entire mission time is over 3

hours. The position estimates are shown in Figure 3.43. Ground truth in this case is more reliant on the USBL, as DVL bottom-lock is not available until approximately 40m altitude.

Results in Figure 3.44(a) show how the ADCP method, without the USBL, results in georeferencing for the subsequent seafloor view-based SLAM-aided mission. Georeferencing uncertainty is within 20m (2σ) position accuracy while the mission is underway on the seafloor, and after post-ascent GPS acquisition, the accuracy of the seafloor portion is within 11m (2σ). Due to the mission configuration, the ADCP was interleaved with the DVL in a ratio of 1:5, with the ADCP operating at approximately 0.5 Hz. The interleaving occurs as the DVL and ADCP are in fact the same sensor, and must operate alternately. Even with such a low rate of ADCP measurements, it is possible to localise without an external acoustic source such as USBL, although the localisation uncertainty is higher than the equivalent of having DVL bottom-lock the entire time due to information loss, which could be attained with higher rate ADCP measurements.

The action of a view-based SLAM loop closure is seen at about 3500 seconds of mission time in Figure 3.44(a), and subsequent loop closures limit the uncertainty in position for the mission. The advantages of this coupled with the ADCP-aided descent and ascent are the same as in Section 3.4.1 for the shallow dive mission, even with a 3 hour long seafloor portion of the dive. A further advantage of view-based SLAM is a significantly improved localisation for the seafloor portion of the mission after the post-ascent GPS acquisition due to the increased correlation of temporally distant poses, as seen in Figure 3.44(a).

Figure 3.44(b) compares the filter result with the independent USBL observations. Prior to DVL bottom-lock during the descent using the in-run filter estimate, there is accumulating linearisation error due to the inaccurate velocity estimates and the non-linear rotation in the ADCP sensor model, and the filter becomes inconsistent. Once DVL bottom-lock is acquired, relinearisation can occur with the EIF and the linearisation error is reduced, providing some evidence that the inconsistency observed previously was due to linearisation error. Subsequently, it can be seen that the ADCP

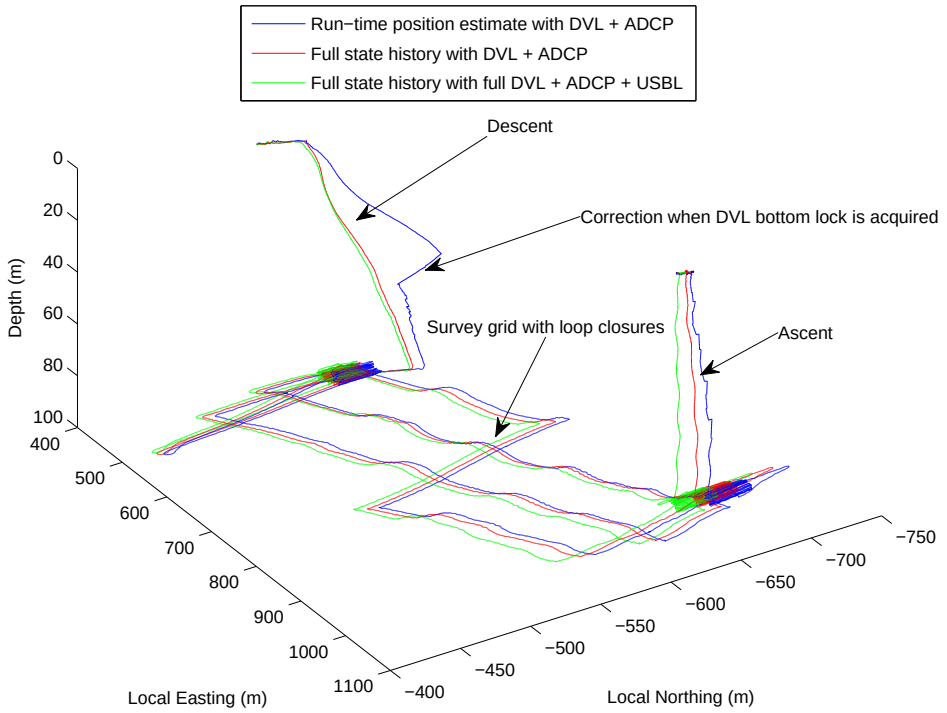

(a)

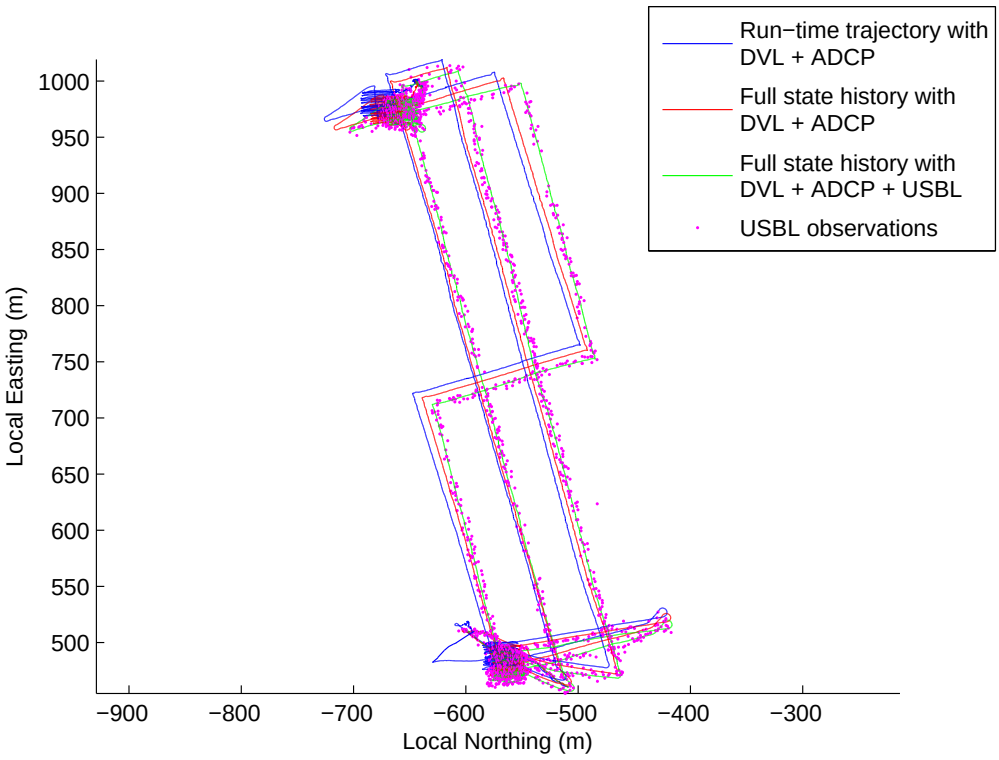

(b)

Figure 3.43 – (a) Oblique and (b) Bird's eye view of the trajectory for 100m depth deeper water mission, where DVL bottom-lock is only available at 40m altitude.

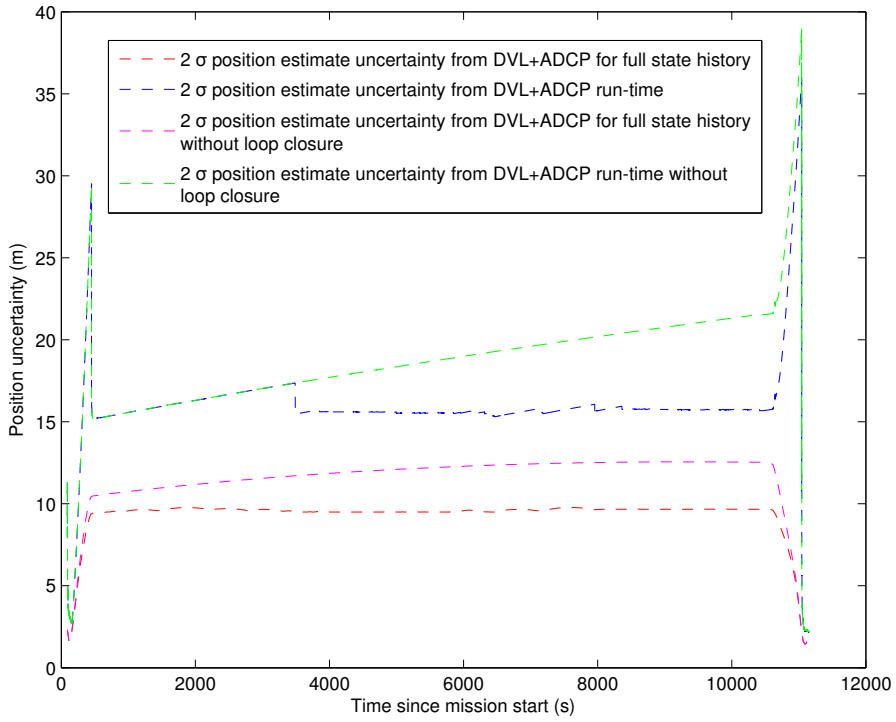

(a)

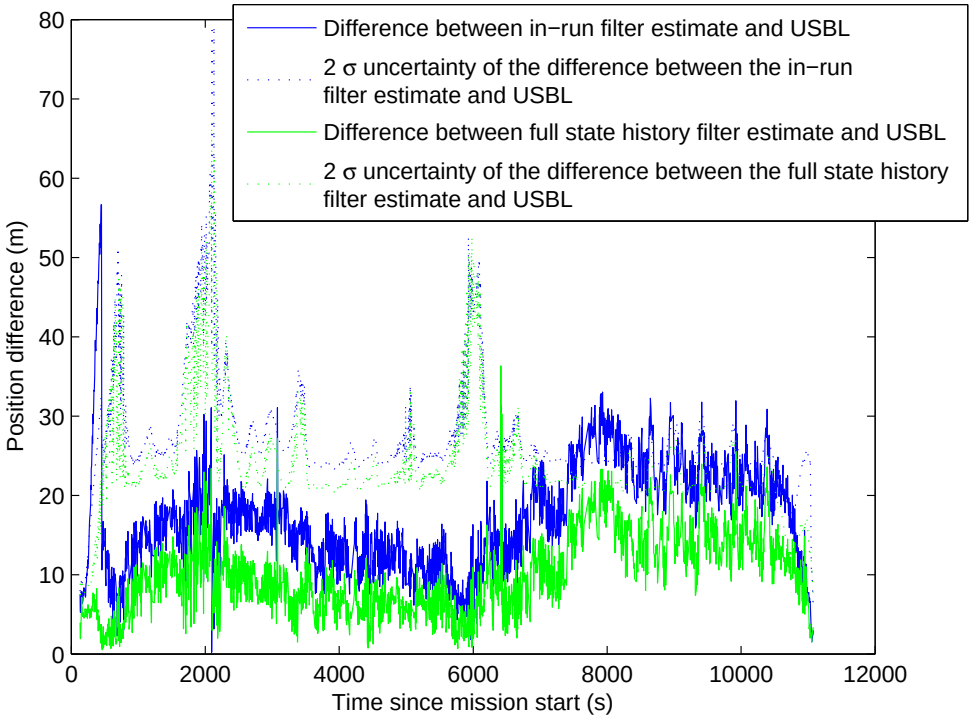

(b)

Figure 3.44 – (a) Deeper water dive position uncertainty estimates for filter in-run and for the full state history, with and without loop closures (b) Differences between filter results and USBL measurements, along with 2 σ uncertainties of this difference, showing that the filter is consistent after DVL bottom-lock

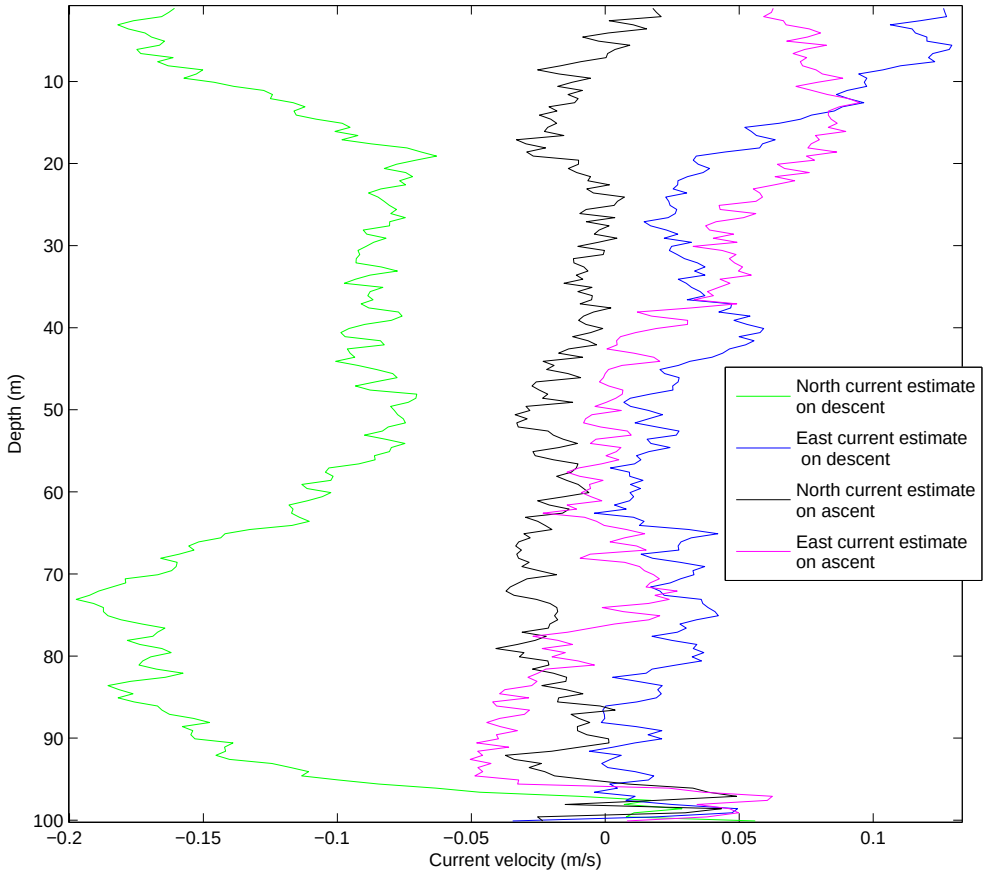

Figure 3.45 – Current estimates for 100m deep water dive, with ascent and descent occuring approximately 3 hours and 600 m apart.

filter is consistent with the USBL observations, validating the performance of the ADCP-aiding method.

The resultant water column current profile is shown in Figure 3.45. It can be seen that a noticeable change in the water current profile has occured over the 3 hours, and translation of approximately 600m in the horizontal direction, between the ascent and descent.

The above results show how ADCP-aided navigation during the descent and ascent of a mission, coupled with view-based SLAM on the seafloor, allows georeferencing

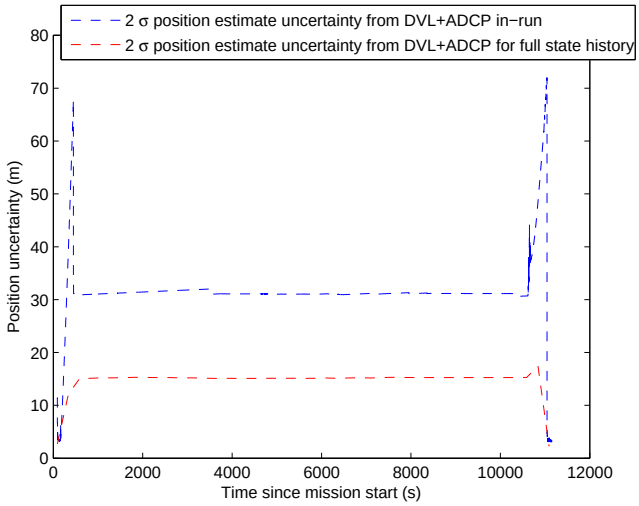

Figure 3.46 – The uncertainty estimates when the ADCP operates at 0.1 Hz

even with infrequent ADCP measurements. Figure 3.46 show the mission uncertainty estimates, combining view-based SLAM, and an ADCP operating at only 0.1 Hz (approximately 30 times less frequent than the full frequency ADCP). The result is 30m (2σ) uncertainty in position during the mission, and 15m (2σ) uncertainty in position following smoothing. The mission errors in Figure 3.47 show that the filter becomes inconsistent during the descent and ascent stages, as a results of the low rate of ADCP measurements. This is due to the accumulation of linearisation error due to the heading non-linearities. Once DVL bottom lock is available following descent, or GPS is available following the ascent, relinearisation allows the filter to become more consistent.

In the case of untended long-term monitoring and exploration AUVs or underwater gliders, tighter constraints on power consumption are imposed. This requires operating sensors sparingly. As shown by the results in this section, even infrequent ADCP measurements provide information which permits localisation. This represents a viable solution for untended and beaconless autonomous underwater navigation. Additionally, an accurate water current vector field estimate is output, which is a useful data product.

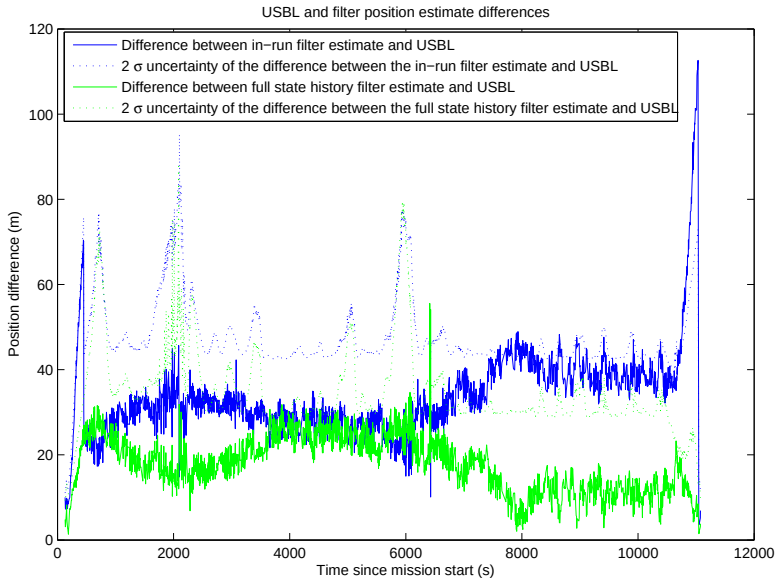

Figure 3.47 – The difference between the filter localisation and the USBL, and the uncertainty estimates in this difference when the ADCP operates at 0.1 Hz

3.5 Summary

This chapter explored the performance of the ADCP-aided localisation algorithm as an alternative form of georeferencing for AUV missons for vertical dives. A two degrees-of-freedom simulation allowed the analysis of the error dynamics of the problem, and showed that a lower initial uncertainty of the velocity on the sea surface and the faster descent rate have the greatest impact in reducing the vehicle position uncertainty growth, and hence georeferencing accuracy prior to reaching DVL bottom-lock range. Given faster descent rates, the uncertainty growth in velocity as a consequence of less measurements of the water column is negligible compared to the reduced time spent in the water column and hence integrating velocity error with time to determine position. The effect of the ADCP measurement rate and standard deviation was also seen to have effects on the localisation, although not as significant.

Once DVL bottom-lock was acquired, the primary driver for the position uncertainty growth was again descent rate and the initial velocity uncertainty. If the initial velocity uncertainty is similar to the DVL bottom-lock velocity uncertainty, and typical ADCP measurement rates and standard deviations are experienced, the position error growth rate will be reduced compared to a higher initial velocity uncertainty. Given low ADCP measurement rates and/or higher standard deviations, a lower initial velocity uncertainty reduces the position uncertainty growth, since information loss has limited the ability of the DVL to reduce the velocity uncertainty for the entire dive.

A six degrees-of-freedom simulation reflected the possible performance of the algorithm under typical parameters for the *Sirius* AUV. Given this more realistic simulation, the impact of the initial velocity uncertainty on the vehicle was shown to still be significant prior to DVL bottom-lock, but with only minor corrections once DVL bottom-lock is acquired. A deeper descent over one hour was simulated, with information loss being evident due to the non-linear increase in position uncertainty with time, as a result of the increase in velocity uncertainty with time. The performance of the algorithm for this one hour simulation was shown to be competitive with acoustic localisation methods.

Finally, a validation of the ADCP localisation algorithm was completed with real data from the Sirius AUV. The scenario of low ADCP measurement rates in the ascent and descent of the vehicle was shown to provide accurate localisation performance compared to USBL ground truth, with the filter framework also allowing the incorporation of loop-closures from view-based SLAM.

As a result, this chapter has demonstrated the ability to achieve constrained error growth in position by incorporating ADCP measurements into the navigation solution while a vehicle is transitting between the sea surface and the seafloor. This makes it appropriate for long-term, accurate navigation of an AUV which dives and resurfaces, and requires underwater position accuracy close to the seafloor, without DVL bottom-lock the entire mission. This alleviates the requirement for a tending vessel or setup of an acoustic network to achieve precise navigation, although including USBL or LBL will only further improve the localisation accuracy.

The limitation of the approach so far is that the isocurrent water layer model does not have the fidelity to account for changing horizontal water currents. The following chapter will explore this problem.

Chapter 4

ADCP Sensor Aiding with Water Grids

In Chapter 3, the assumption of water currents being arranged in isocurrent layers was assumed. This is valid as long as the vehicle does not translate significantly in the horizontal direction. If this was the case, then the assumption of water currents being constant inside the layer will be violated as the water current field can exhibit spatial change in the lateral direction. For example, the problem of navigating in a turbulent water vector field in the horizontal direction, using a horizontally pointed ADCP, was tackled in [10]. Thus it is clear that if horizontal transits occur while in the water column, a new model must be applied. In order to achieve this, the water current layer approach is generalised, with the water current field composing of gridded isocurrent water volume elements (IWVEs), allowing spatial variation in the horizontal direction. This allows general motion within the water column to be accommodated in the localisation algorithm. Additionally, to exploit the lateral looking beams of the ADCP, the raw beam coordinate velocities are utilised instead, accounting for where they travel through the water column. The geometry of the beams are outlined in Figure 4.1.

This chapter explores the extension of the ADCP-aided localisation by generalising the water current layer model to isocurrent water volume elements. Additionally, real

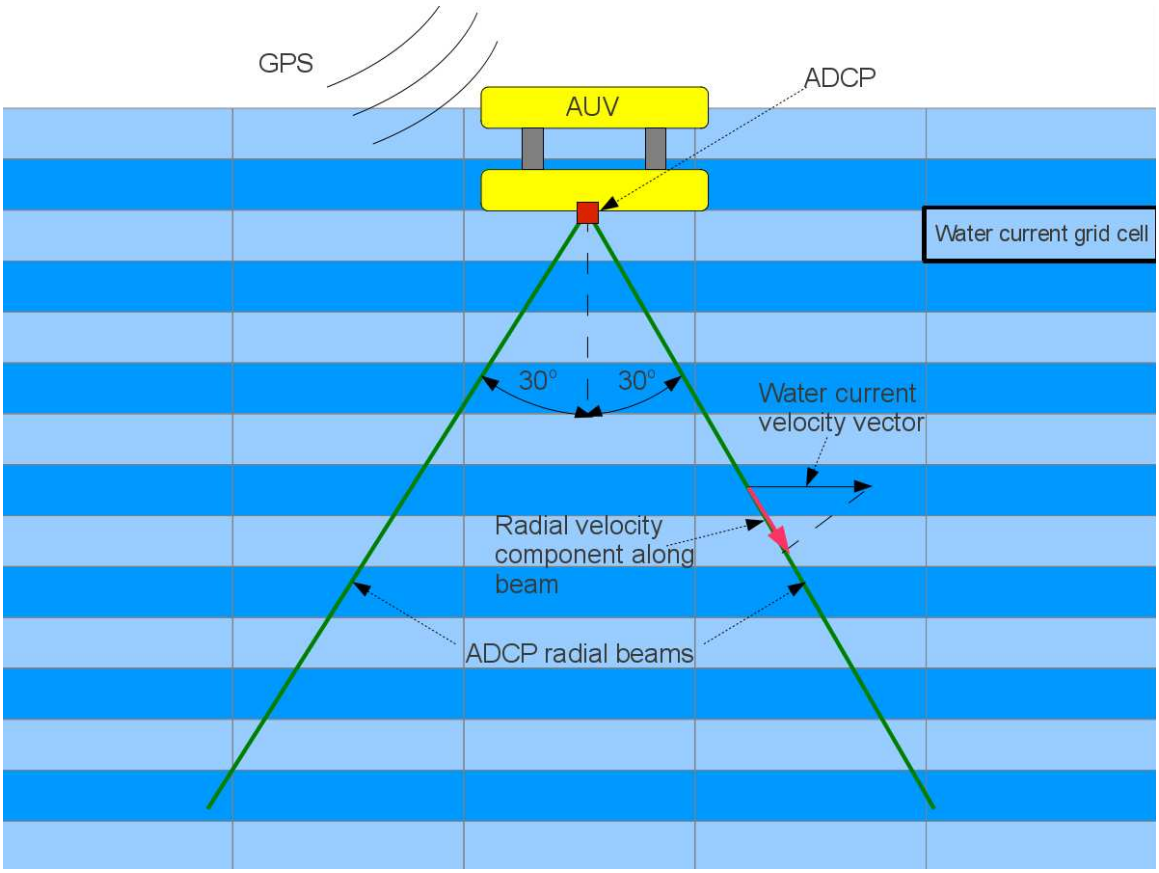

Figure 4.1 – The slanted beam arrangement for the ADCP allows lateral looking capabilities. The beams are arranged in a Janus configuration, with 4 beams angled 30 degrees from the vertical on standard models.

data from the *Sirius* AUV is obtained with GPS ground truth. This was compared to the ADCP-aided localisation while on the sea surface. Thus, this chapter has demonstrates the ability to achieve constrained error growth in position by incorporating ADCP measurements into the navigation solution while a vehicle is undergoing a significant horizontal underwater trajectory when GPS and DVL bottom-lock are unavailable.

4.1 ADCP estimation and navigation aiding process

Initially, the AUV has position and velocity estimates in the navigation frame at the sea surface from GPS. With the ADCP sensor, body-relative radial velocities along the beams of the ADCP are observed, and can be placed in the navigation frame due to the velocity at the sea surface being initially observed. The slanted beam characteristics of the ADCP sensor allow fore, aft, port and starboard direction sensing, and thus allows future reobservation along these dimensions. The fore and aft looking ability is illustrated in Figure 4.2(a).

Once the vehicle has submerged, it no longer can receive GPS. Once an ADCP measurement is made, it reobserves the same IWVEs, as shown in Figure 4.2(b). Since it is reobserving a cell, with its velocity resolved in the navigation frame, along with the body-relative radial velocity of these cells from the ADCP, the vehicle velocity in the navigation frame can be derived using a filter. New current cells can also now be estimated as the vehicle changes position, as the vehicle velocity in the navigation frame is known. This is outlined in Figure 4.2(c). The result is an estimate of vehicle motion and a gridded water current estimate.

The observation function for each ADCP measurement when using the raw beam coordinates is:

$$z_{adcp,i,k} = (\mathbf{C}_b^n \hat{\mathbf{r}_{b,k}}) \cdot (-\mathbf{v}_v^n + \sum \mathbf{W}_j \mathbf{v}_{c,j}^n) + \mathbf{b}_{c,i,k} + \nu_{adcp} \tag{4.1}$$

where:

- $z_{adcp,i,k}$ is the ADCP measured radial current velocity in measurement cell i for beam k. In Figure 4.3 the measurements $z_{adcp,i,k}$ are the radial velocities $v_{i,k}$ without biases and noise
- $\mathbf{C}_b^n$ is the coordinate transform from adcp/body frame to navigation/world frame
- $\hat{\mathbf{r}_{b,k}}$ is the unit vector for beam k in the body frame

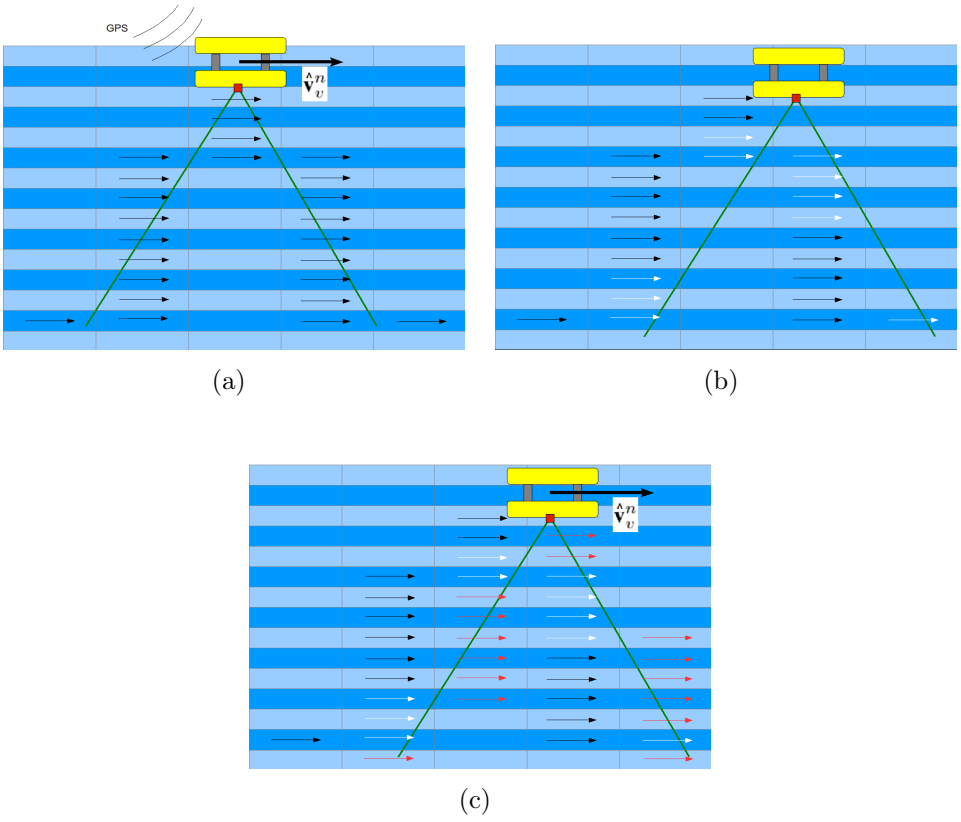

Figure 4.2 – ADCP-aiding method sequence (a) Initial GPS position and velocity are known, and water velocities with black arrows can be deduced. (b) The AUV moves, and reobserves the same IWVEs, shown as white arrows.(c) The AUV velocity in the world frame can be deduced, along with new current bins shown in red.

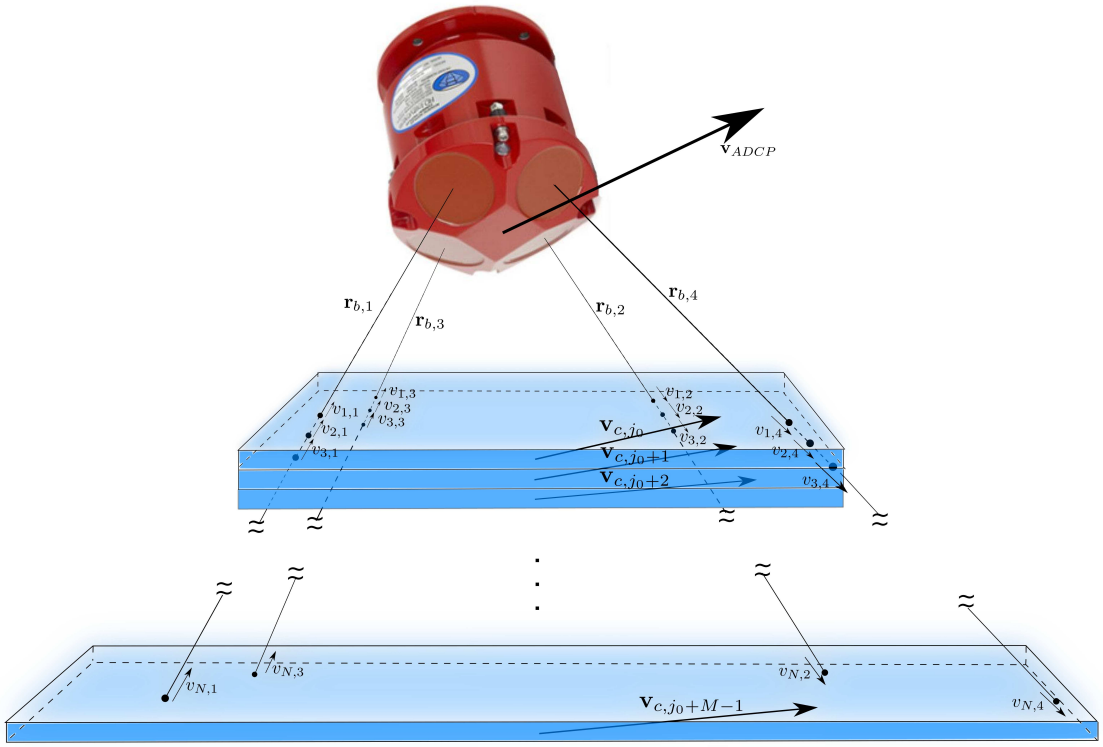

Figure 4.3 – The ADCP sensor possesses 4 beams in a Janus configuration, 30 degrees from the vertical. This allows fore, aft, port and starboard direction sensing capability.

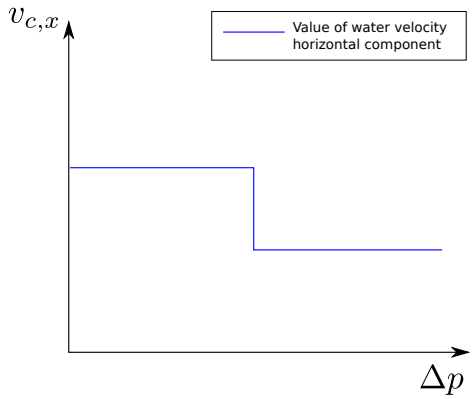

Figure 4.4 – IWVE velocity changes with position, horizontal or vertical translation.

- $\mathbf{v}_v^n$ is the vehicle velocity in the world/navigation frame
- $\mathbf{W}_j$ is a weighting function for each water current velocity from grid cell j
- $\mathbf{v}_{c,j}^n$ is the water current velocity from IWVE j. Each IWVE contains a current velocity vector, which represents the average velocity of the current in that cell
- $\mathbf{b}_{c,i,k}$ is the bias in the measurement cell i for beam k
- ν_{adcp} is the random noise in the ADCP measurement, with the standard deviation given by the sensor manufacturer

Figure 4.4 shows how the velocity of the modelled isocurrents would change across an isocurrent water volume element boundary. Eliminating this quantization error of the water current environment remains as future work. The impact of this assumption will be explored in later sections.

The ADCP measurement is assumed to be from a 1 dimensional line with a weighting function:

$$M_{l_0}^{l_e} = \int_{l_0}^{l_e} w(l) V_{xyz}^b(l)\, dl \tag{4.2}$$

Where $V_{xyz}^b(l)$ is the velocity of the water currents in the body-frame as a function of the line segment through space, illustrated in Figure 4.5.

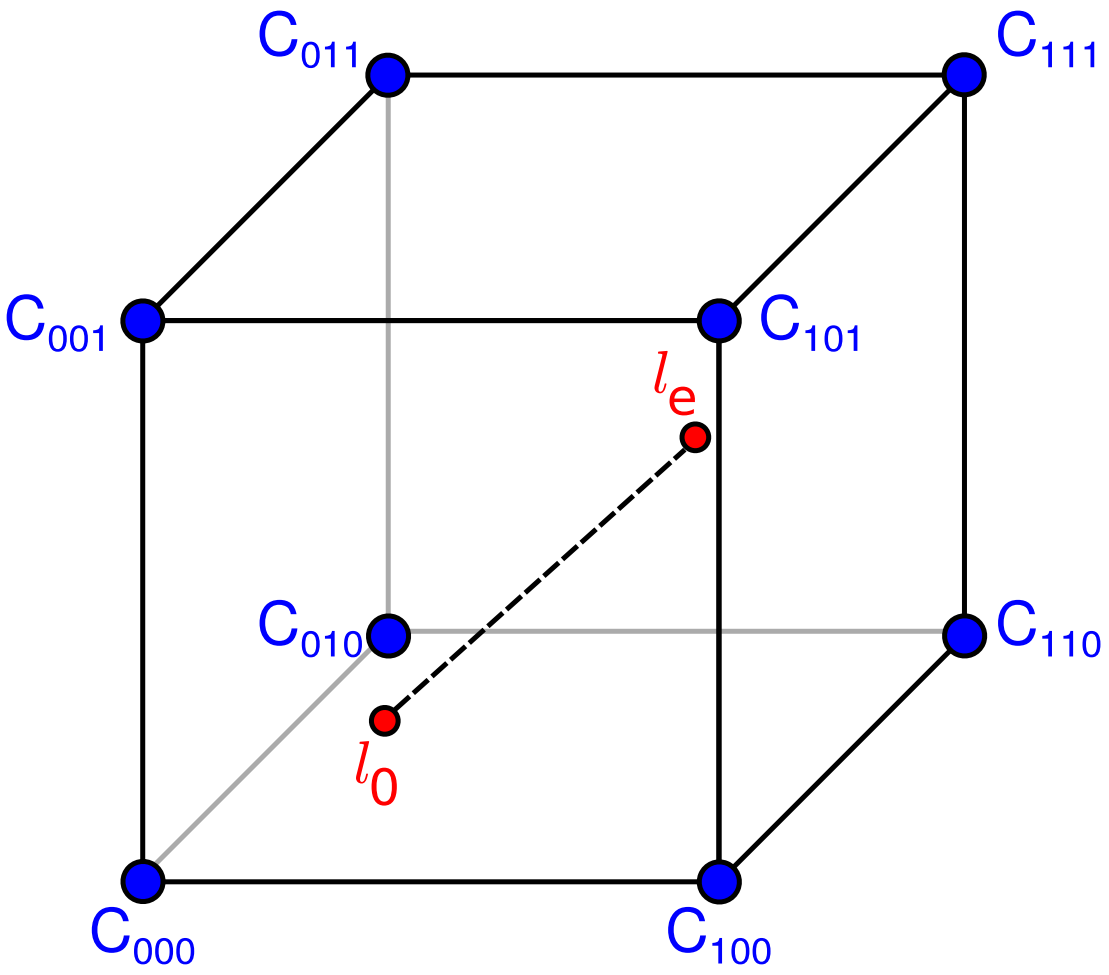

Figure 4.5 – Diagram illustrating a 1 dimensional line in a unit cube. Adapted from [5]

Given:

$$l_0 = \{x_0, y_0, z_0\} \tag{4.3}$$

$$l_e = \{x_e, y_e, z_e\} \tag{4.4}$$

$$l = \frac{x - x_0}{(x_e - x_0)} = \frac{y - y_0}{(y_e - y_0)} = \frac{z - z_0}{(z_e - z_0)} \tag{4.5}$$

then:

$$x = x_0 + l(x_e - x_0) \tag{4.6}$$

$$y = y_0 + l(y_e - y_0) \tag{4.7}$$

$$z = z_0 + l(z_e - z_0) \tag{4.8}$$

Also, for a triangular weighting function such as that described in Figure 3.3 for ADCPs, the term $w(l)$ is described as:

$$w(l) = \begin{cases} 4l & \text{when} \quad l \leq \frac{1}{2} \\ 4 - 4l & \text{when} \quad l > \frac{1}{2} \end{cases} \tag{4.9}$$

4.2 Spatially correlated horizontal water current grid

Given the nature of water mass transport, and the standard representation of the horizontal currents as a vector field, there is an assumption of continuity [39]. In [34], the spatial scale of the flow is considered about 50 m assuming homogenous conditions, and standard practice in oceanography is to smooth the water currents spatially to exploit this correlation. To apply some correlation into the horizontal vector field that is being estimated, an update with the following measurement model is applied

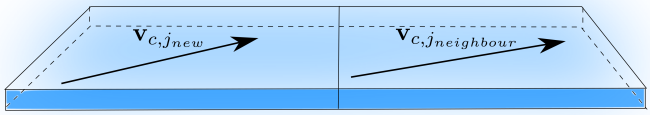

Figure 4.6 – Horizontally adjacent water current grid cells are expected to have similar water current velocities due to continuity [39].

if newly initialised water current grids have pre-existing neighbouring grids:

$$h_{correlation}(\hat{\mathbf{x}}(t_k)) = \mathbf{v}^n_{c,j_{new}} - \mathbf{v}^n_{c,j_{neighbour}} \tag{4.10}$$

$$\mathbf{z}_{correlation} = 0 \tag{4.11}$$

$$R_{correlation} = \sigma^2_{correlation} \tag{4.12}$$

where $\mathbf{v}^n_{c,j_{new}}$ is the new current grid, $\mathbf{v}^n_{c,j_{neighbour}}$ is the old neighbouring current grid. The standard deviation $\sigma_{correlation}$ is set according to the expected rate of current change between the current grids.

4.3 Horizontal trajectory simulations

This section will explore the performance in simulation of the ADCP localisation algorithm given the new beam-coordinate ADCP model, the IWVE representation of the water current velocity environment and the spatial correlation modelling.

4.3.1 Simulated Water Current Environment

To simulate the three-dimensional water current velocity vector field, the following assumptions are made:

1. The ocean flow is assumed to be bi-dimensional in the north and east directions,

resulting in strong vertical strafication. This assumption is due to the rapid rotation of the Earth, resulting in strong stratification and horizontal scales much larger than the vertical [43].

2. With this assumption, ocean dynamics are described by the two-dimensional Navier-Stokes equation [10]:

$$\frac{\partial \omega}{\partial t} + (\vec{V}\nabla)\omega = \nu_f \triangle \omega \tag{4.13}$$

where $\vec{V} = (V_x, V_y)$ is the velocity field in the water current layer, ν_f is the viscosity of the fluid, $\omega = \frac{\partial V_y}{\partial x} - \frac{\partial V_x}{\partial y}$ is the vorticity ,∇ is the gradient operator and $\triangle$ is the Laplacian operator. An approximate solution to Equation 4.13 can be constructed as a superposition of one-point vortex solutions called viscous Lamb vortices [27]:

$$V_x(\vec{r}) = -\Gamma \frac{y - y_0}{2\pi(\vec{r} - \vec{r_0})^2}[1 - e^{\frac{r^2}{\delta^2}}] \tag{4.14}$$

$$V_y(\vec{r}) = \Gamma \frac{x - x_0}{2\pi(\vec{r} - \vec{r_0})^2}[1 - e^{\frac{r^2}{\delta^2}}] \tag{4.15}$$

where x_0, y_0 is the coordinate of the centre of the vortex, $\vec{r} = \sqrt{(x - x_0)^2 + (y - y_0)^2}$ δ is the radius scale of the vortex and Γ is the strength of the vortex. A number of large scale Lamb vortices are simulated acting on each depth layer of water current.

3. The water current velocity fields should be correlated across depth, due to shear effects. This should result in vertical water current profiles given vertical descent as in Chapter 3. To simulate this effect, the centres of the vortices x_0, y_0 undergo a random walk with depth. Additionally, the parameters δ and Γ undergo a constrained random walk through a first order Markov process as in Equation 3.13. The resulting simulated water current environment is outlined in Figures 4.7 and 4.8. This environment grids the water current velocity field

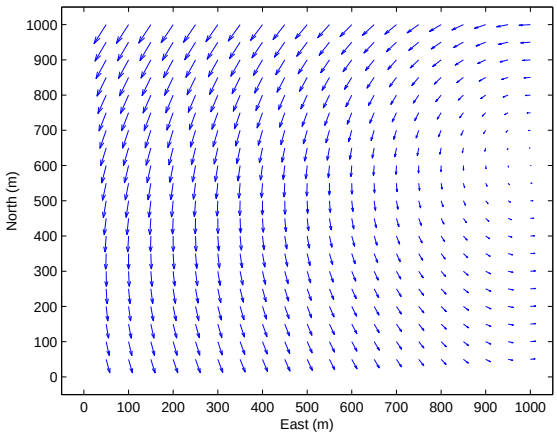

(a)

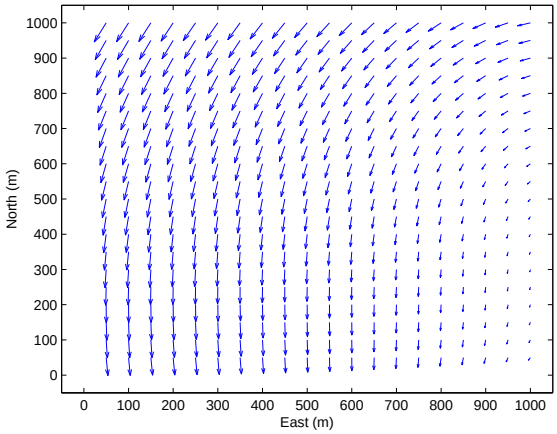

(b)

Figure 4.7 – The simulated water current vector field at (a) 1 m depth and (b) 20 m depth. The water currents in the horizontal are dictated by Lamb vortices, while the vertical direction allows a random drift in the Lamb vortex parameters.

at 1 m depth resolution and 50 m horizontal resolution.

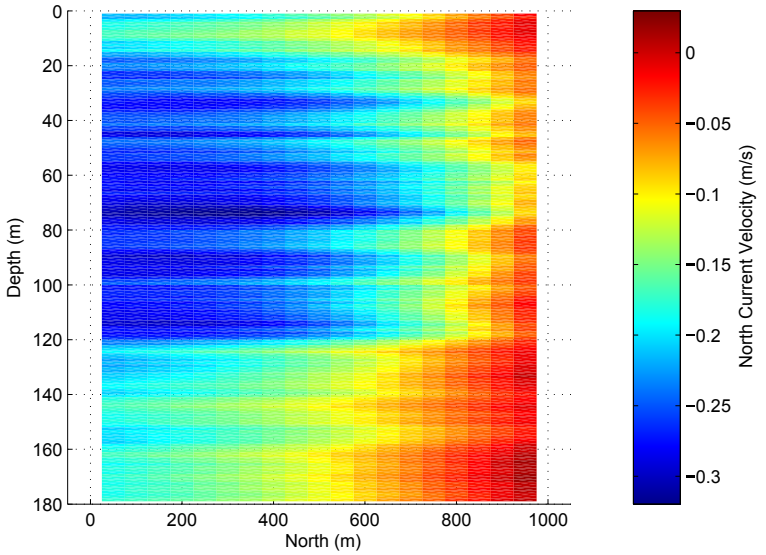

(a)

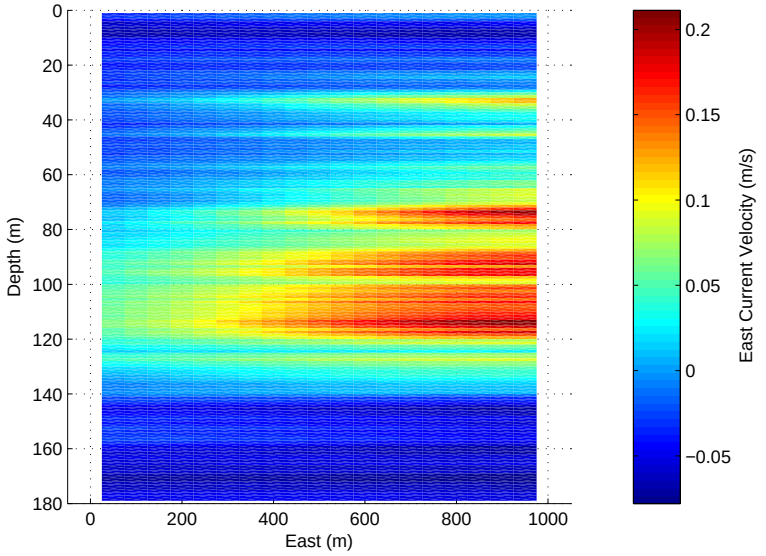

(b)

Figure 4.8 – The (a) north and (b) east water current magnitude slices given constant north at 500m. The vertical slice should have some correlation with depth due to shear constraints.

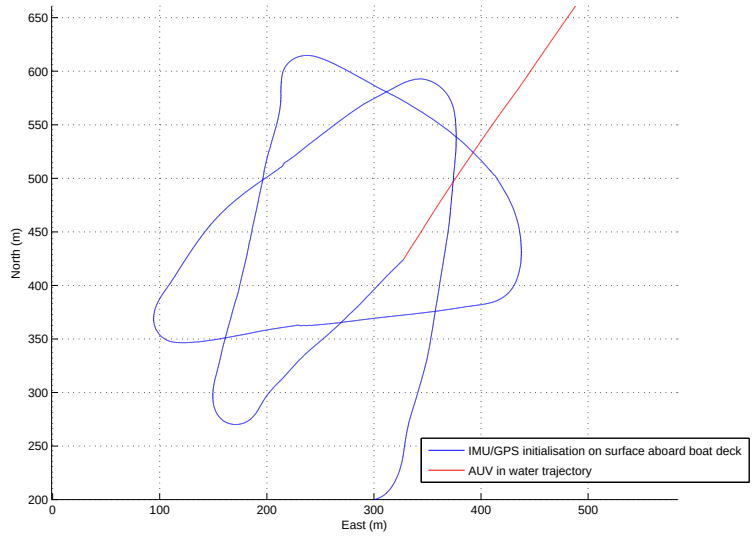

(a)

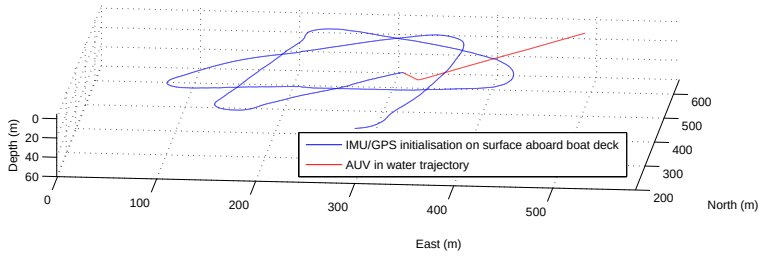

(b)

Figure 4.9 – Horizontal motion simulation trajectory from (a) above and (b) obliquely.

4.3.2 Horizontal motion simulation

The *Sirius* AUV [60] is simulated with access to GPS position, GPS Doppler velocity and Time Differenced Carrier Phase (TDCP) [49] on the sea surface. The vehicle then enables its lateral thrusters at maximum, achieving approximately 0.5 m/s relative to the surrounding water. The vehicle dives to 10 m, losing GPS access, and then continues for 700 seconds, and DVL bottom-lock is unavailable for the entire mission. The mission trajectory is shown in Figure 4.9.

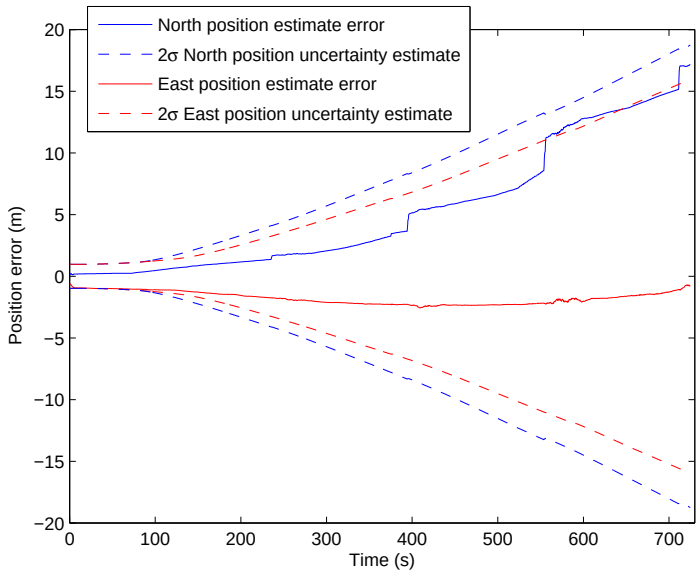

Figure 4.10 – The horizontal motion simulation position uncertainty estimate is growing non-linearly with time as a result of the increasing velocity uncertainty.

Figure 4.10 shows the filter position estimate uncertainty increasing from the start of the mission, with the non-linear increase in position uncertainty apparent as the velocity uncertainty increases. The position uncertainty has grown from the initial 1 m 2σ to approximately 14 m and 16 m 2σ in the north and east directions respectively, after 700 seconds of localisation.

The choice of grid size depends on scale of the water currents changing. In [34], the spatial scale of the flow is considered about 50 m assuming homogenous conditions, hence a grid size of 50 m was chosen. As seen in Figure 4.11, the velocity uncertainty jumps as old water current velocity IWVEs are no longer observed and new IWVEs are initialised. The result is increasing velocity uncertainty with time. The information loss rate in the water currents and vehicle velocity for the horizontal case are greater than for vertical descents. This occurs because the geometry of the ADCP beams pointing primarily downward, a lack of absolute positioning among the water current field as was the case with pressure depth and vertical descent, and the horizontal homogeneity assumption being violated as beams intersect with different IWVEs. The assumption of horizontal homogeneity which allowed all 4 beams of the ADCP

to observe the same water current depth cell simultaneously is assumed to no longer hold, resulting in limited observability of water currents and information loss. The trend of increasing uncertainty in the water current velocity estimates are shown in Figure 4.12. The large spikes in the water current velocity uncertainty estimates exist if certain IWVEs are only observed from very limited geometry, for example one beam makes a few measurements into the IWVE. The horizontal correlation in the filter for this simulation is assumed to be pessimistic.

The localisation algorithm must discriminate between a changing ADCP bias, the current velocity which changes spatially, and the changing velocity of the vehicle itself. The ADCP bias is assumed to change slowly (in the order of 500 seconds), while the currents are allowed to change according to spatial change, assuming velocity of a current in an IWVE stays the same during the reobservation period. The vehicle itself has access to IMU measurements. Thus, there exists some observability and ability to discriminate between these factors.

Figure 4.13 shows the estimated vehicle trajectory and ground truth, along with the estimated water current field surrounding the vehicle during its mission. This figure also shows how the filter estimates the spatial water current field variation in the horizontal and vertical direction, as there are different magnitudes in the vectors across space.

This result illustrates that the purely horizontal localisation can be achieved by parameterising the water current velocity field into IWVEs. Errors due to the IWVE formulation, such as step changes in the velocity uncertainty, indicate limitations in this water current modelling method. Coupling horizontal and vertical motion will be explored in the next section.

4.3.3 Spiral descent simulation

The *Sirius* AUV [60] is simulated with access to GPS position, GPS Doppler velocity and Time Differenced Carrier Phase (TDCP) [49] on the sea surface. The vehicle then enables it's lateral and vertical thrusters to spiral descend, achieving approximately

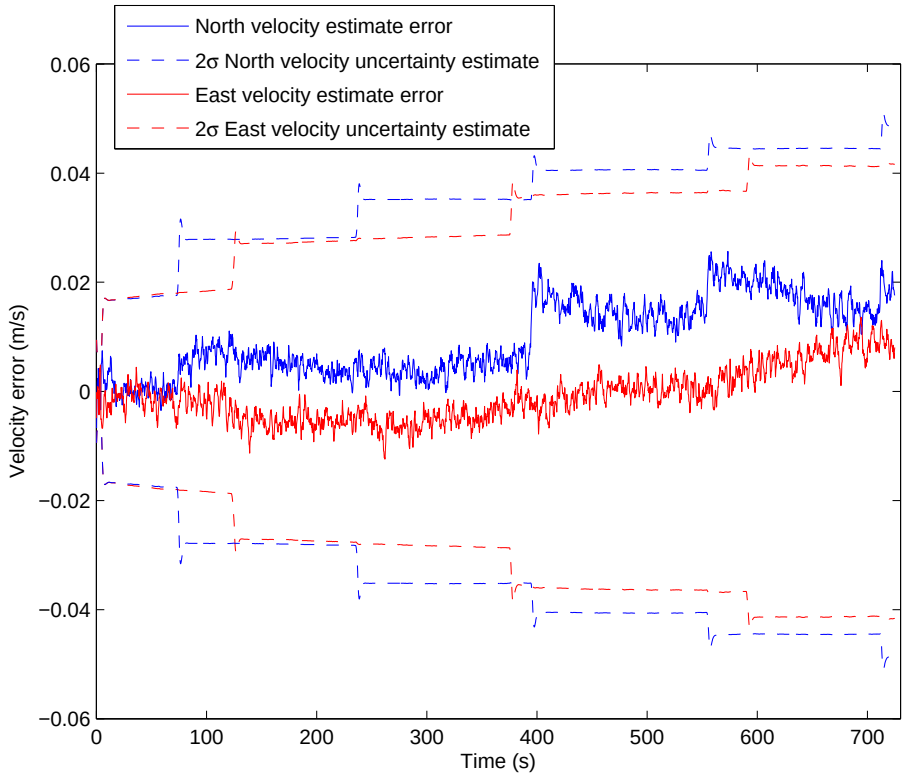

Figure 4.11 – The horizontal motion simulation velocity estimate uncertainty of the vehicle is increasing with time as new IWVEs are encountered in the horizontal direction.

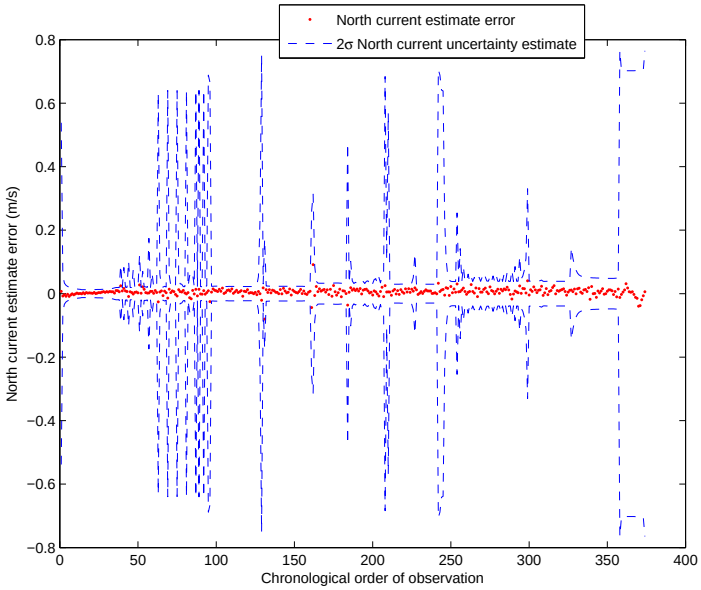

(a)

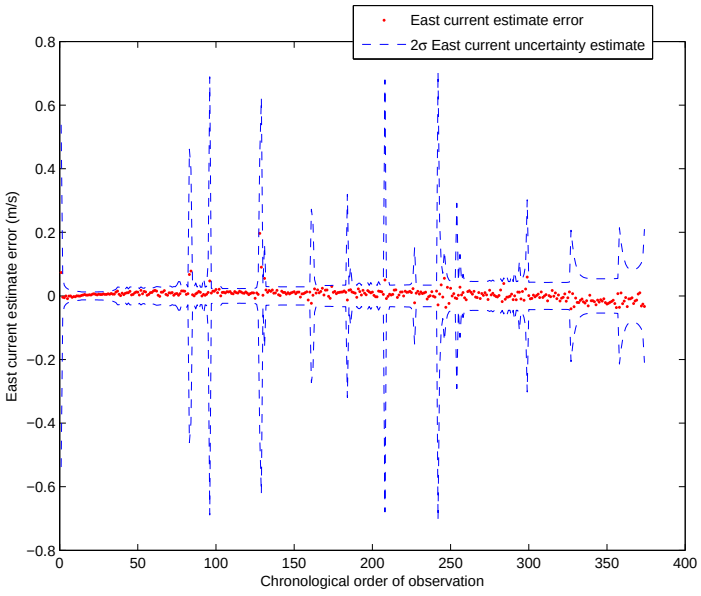

(b)

Figure 4.12 – The horizontal motion simulation water current velocity estimate errors and uncertainty in the (a) north and (b) east in the order in which they are observed and initialised. The spikes in uncertainty are due to poorly observed IWVEs.

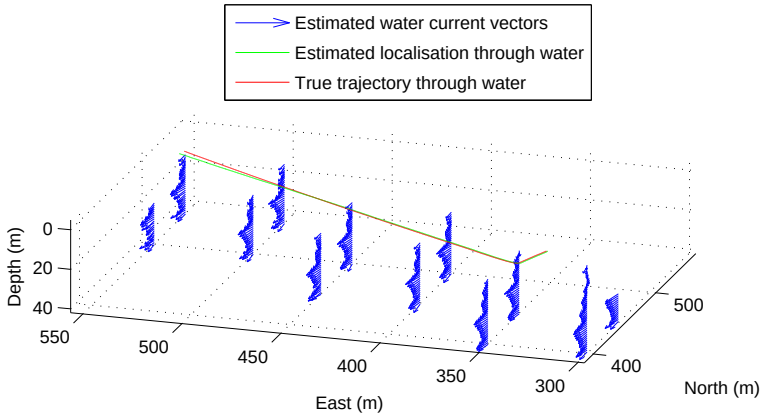

(a)

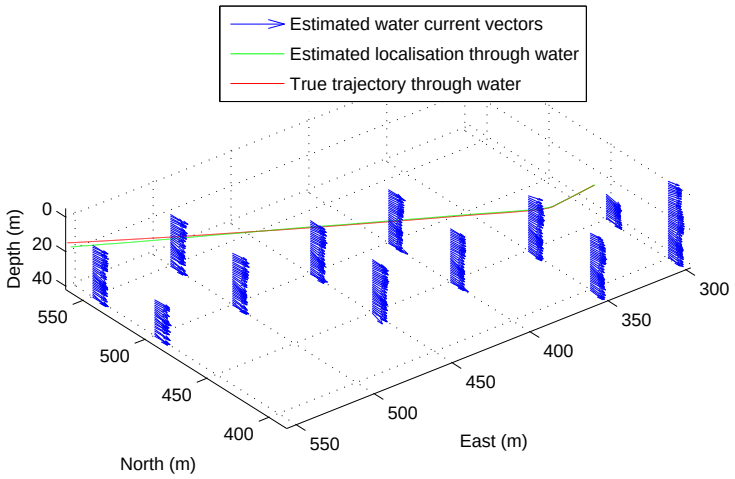

(b)

Figure 4.13 – The horizontal motion simulation estimated mission trajectory and ground truth, along with the estimated water current field from two different views.

0.5 m/s relative to the surrounding water. The spiralling movement occurs for AUVs such as the Autosub6000 [37] and ABE [7]. The vehicle dives to 140 m over 700 seconds without GPS access, and then DVL bottom-lock is acquired. The mission trajectory is shown in Figure 4.14.

As seen in Figure 4.15, the velocity uncertainty increases as old water current velocity volume elements are no longer observed and new IWVEs are initialised. The rate of velocity uncertainty increase is reduced compared to the purely horizontal motion case as in the previous simulation. The velocity uncertainty increase is mitigated by rotation, allowing the same IWVEs to be observed for a longer period of time. Additionally, rotation allows better observability of the IWVEs velocity from different beam angle orientations, improving the water current estimate and the subsequent vehicle velocity estimate.

Figure 4.16 shows the filter position estimate uncertainty increasing from the start of the mission, with the non-linear increase in position uncertainty apparent as the velocity uncertainty increases. The position uncertainty has grown from the initial 1 m (2σ) to approximately 11.5 m (2σ) in the 700 seconds prior to DVL bottom-lock. Following DVL bottom-lock, the position uncertainty estimate is reduced to approximately 7 m (2σ), with the position uncertainty growth approximately 6 m (2σ).

Figure 4.17 shows the estimated vehicle trajectory and ground truth, along with the estimated water current field surrounding the vehicle during its mission. Note how the filter estimates the water current field changes spatially in the horizontal and vertical direction.

The water current velocity estimates are shown in Figure 4.18 following DVL bottom-lock, with improved estimates throughout the mission where possible.

This result shows approximatley 9 mm/s (2σ) position uncertainty growth, compared to the DVL velocity uncertainty of 6 mm/s (2σ). In this scenario, by utilising radial-velocity beam coordinates and thus the lateral looking capability of the ADCP, accurate horizontal localisation is possible during the mid-water column portion of

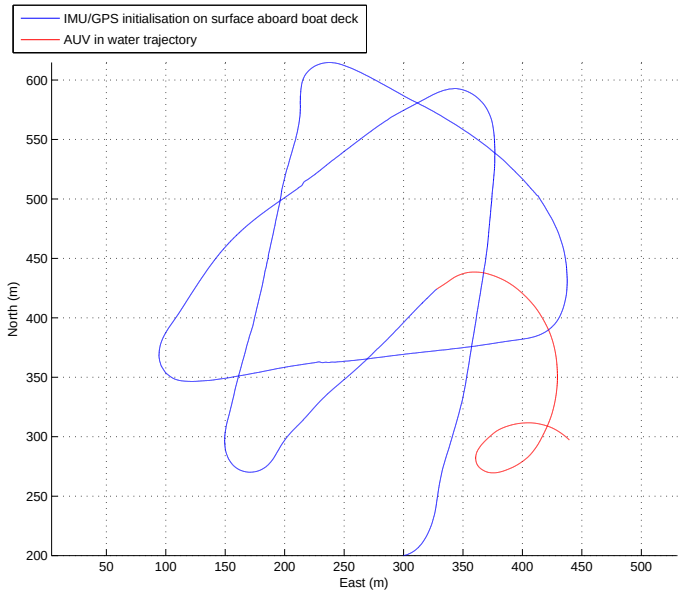

(a)

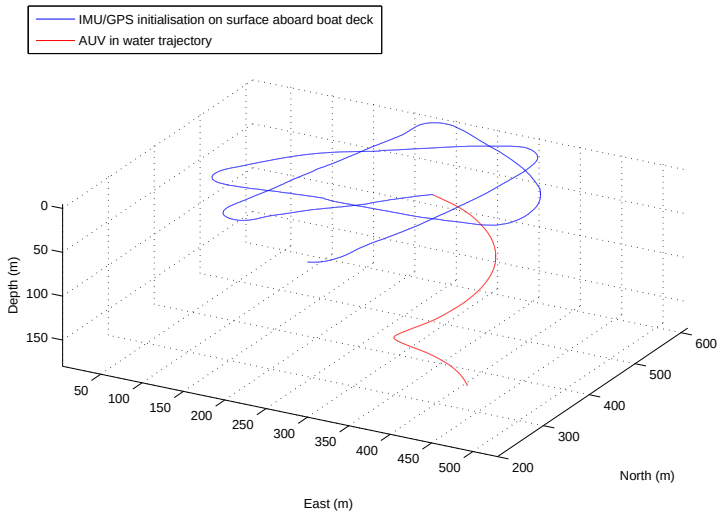

(b)

Figure 4.14 – The spiral descent simulation mission trajectory from (a) above and (b) obliquely.

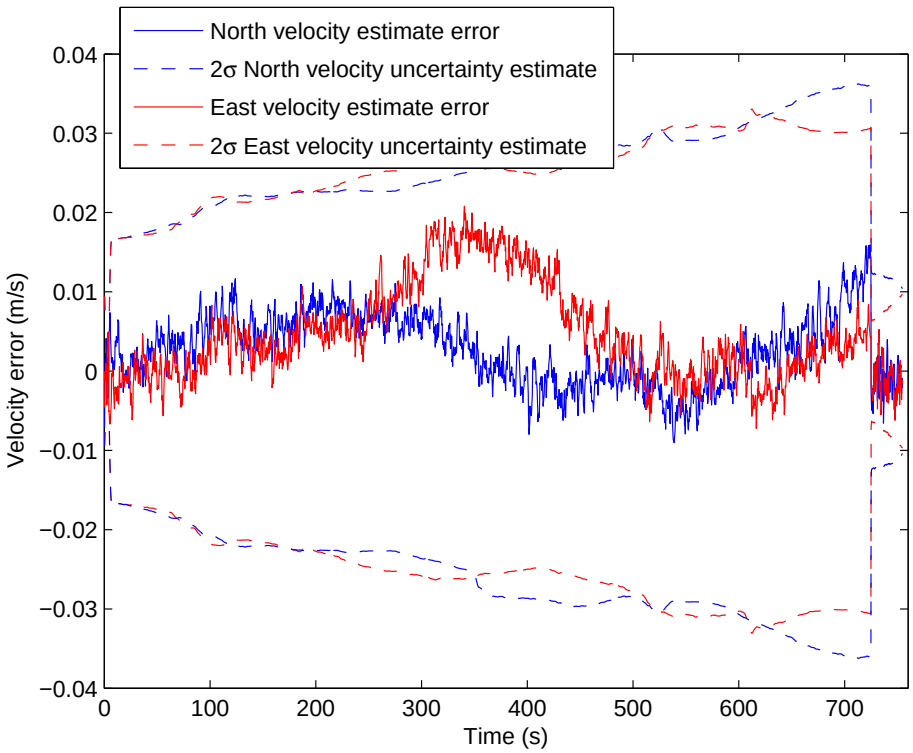

Figure 4.15 – The spiral descent simulation velocity estimate uncertainty of the vehicle is increasing with time as new IWVEs are encountered in the horizontal direction.

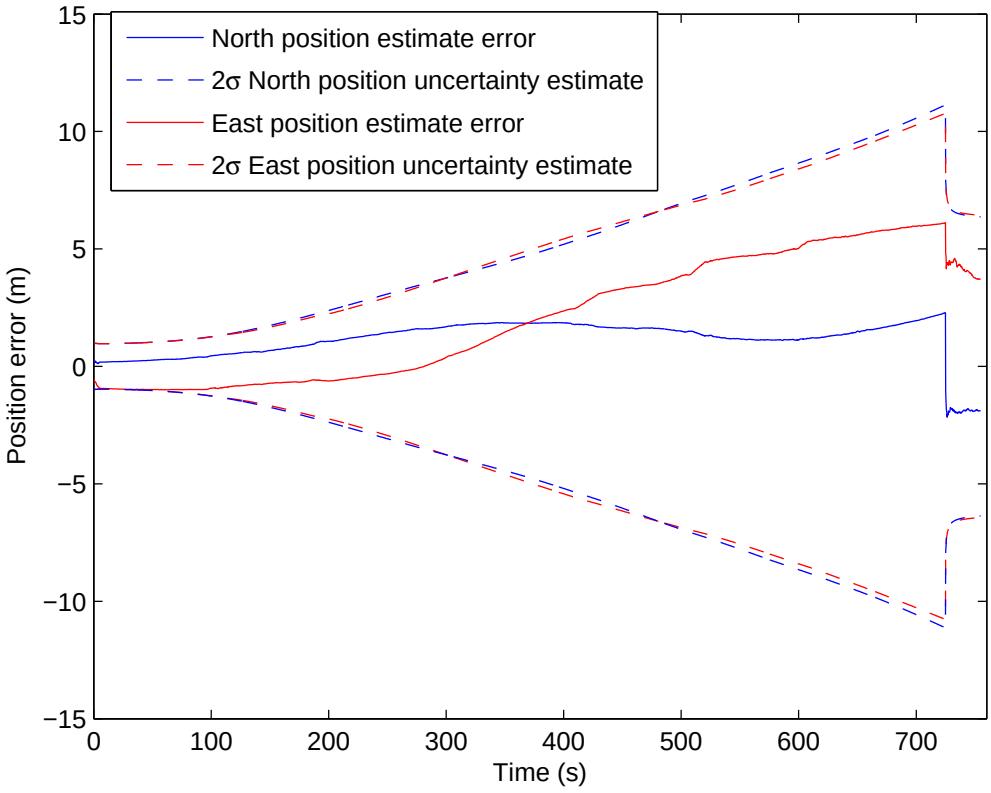

Figure 4.16 – The position uncertainty estimate is growing non-linearly with time as a consequence of the increasing velocity uncertainty, although at a reduced rate compared to a purely horizontal trajectory.

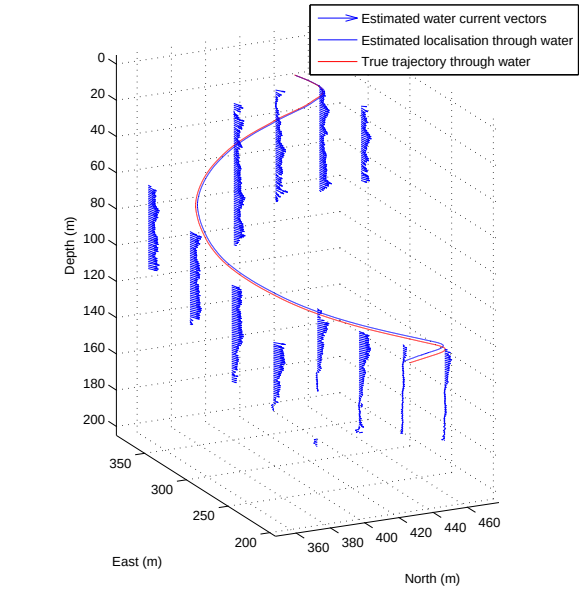

(a)

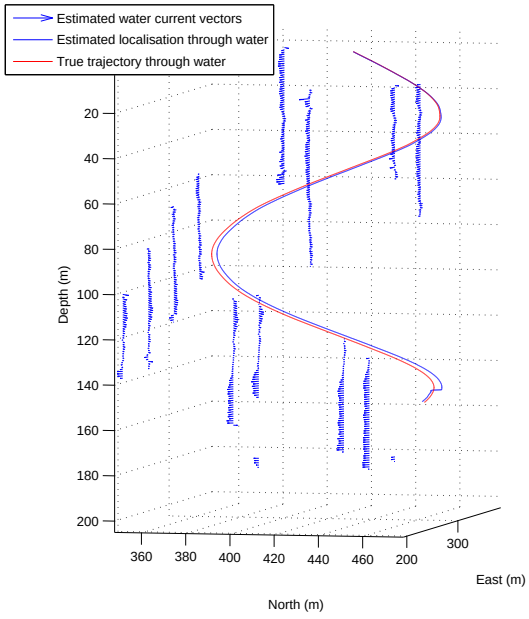

(b)

Figure 4.17 – The spiral descent simulation estimated mission trajectory and ground truth, along with the estimated water current field from two different views.

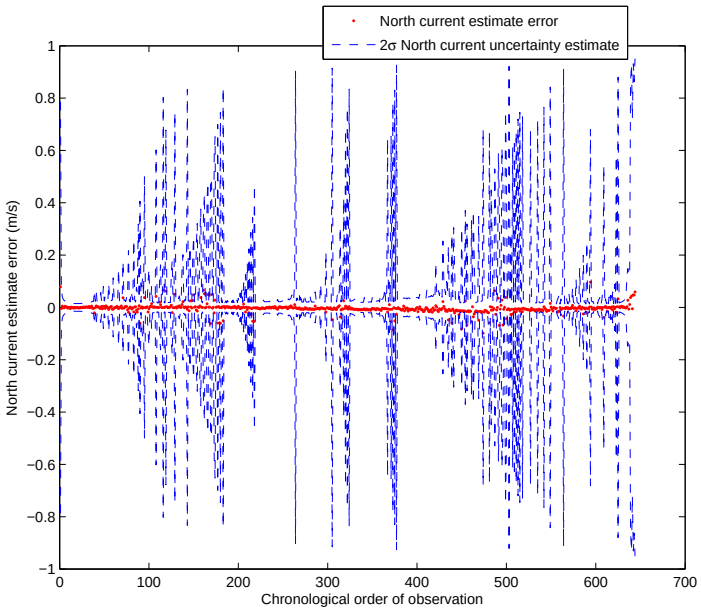

(a)

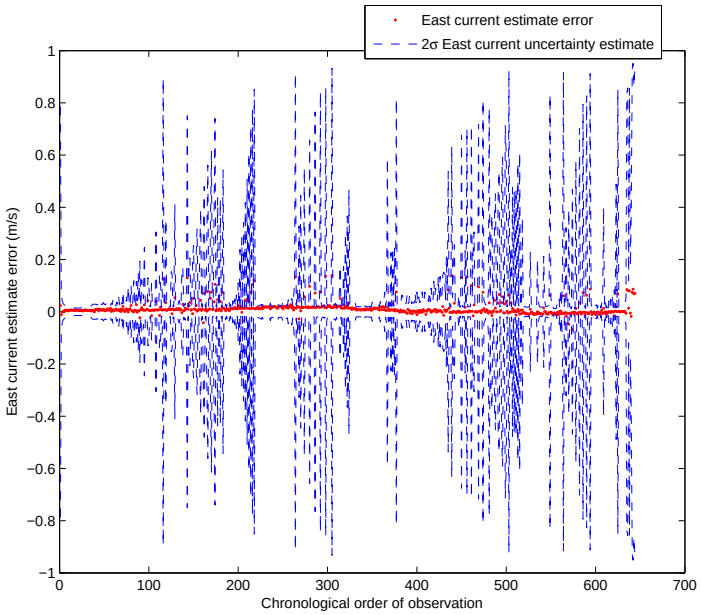

(b)

Figure 4.18 – The spiral descent simulation water current velocity estimate errors and uncertainty in the (a) north and (b) east in the order in which they are observed and initialised. The spikes in uncertainty are due to poorly observed IWVEs.

the dive and is comparable to the equivalent of having DVL bottom-lock for the entire mid-water column trajectory once DVL bottom-lock is acquired. This is despite no GPS or DVL bottom-lock being available in this mid-water column.

4.4 Sirius Horizontal motion results

The following results are obtained through the use of *Sirius* [60]. The vehicle is drifting on the sea surface with GPS available. In order to test the horizontal localisation using the ADCP sensor, the experiment consists of 500 seconds of simulated GPS blackout, while the Sirius AUV is travelling laterally across the sea surface. The vehicle travels 40m in this time. The environment is gridded at 20 m to model spatially varying currents during this short transit.

The water column aided localisation is compared to the GPS aided solution which is considered ground truth. The mission is done while sea surface effects like swell is affecting the vehicle, and due to the GPS antenna being attached to a flexible shaft pointing upwards, the GPS Doppler velocity is considered inaccurate, leading to an initial velocity uncertainty of 20cm/s (2σ) by observing previous missions where DVL bottom-lock is available for comparison.

Figure 4.19 shows the filter position uncertainty and estimate error compared to the ground truth prior to GPS reacquisition. The position error growth rate is higher than in the simulation in Section 4.3.2 due to the initial velocity uncertainty from GPS being much higher. As a result, the global reference for velocities are inaccurate, and the entire water current map will have this error, since the ADCP can only supply velocities in a relative frame of reference.

Figure 4.20 shows the filter position uncertainty and estimate error compared to the ground truth after GPS reacquisition, demonstrating the improvement in the position estimate for the entire state history during the GPS blackout once GPS is reacquired.

Figure 4.21 shows the estimated vehicle trajectory and ground truth, along with the estimated water current field surrounding the vehicle during its mission. A grid re-

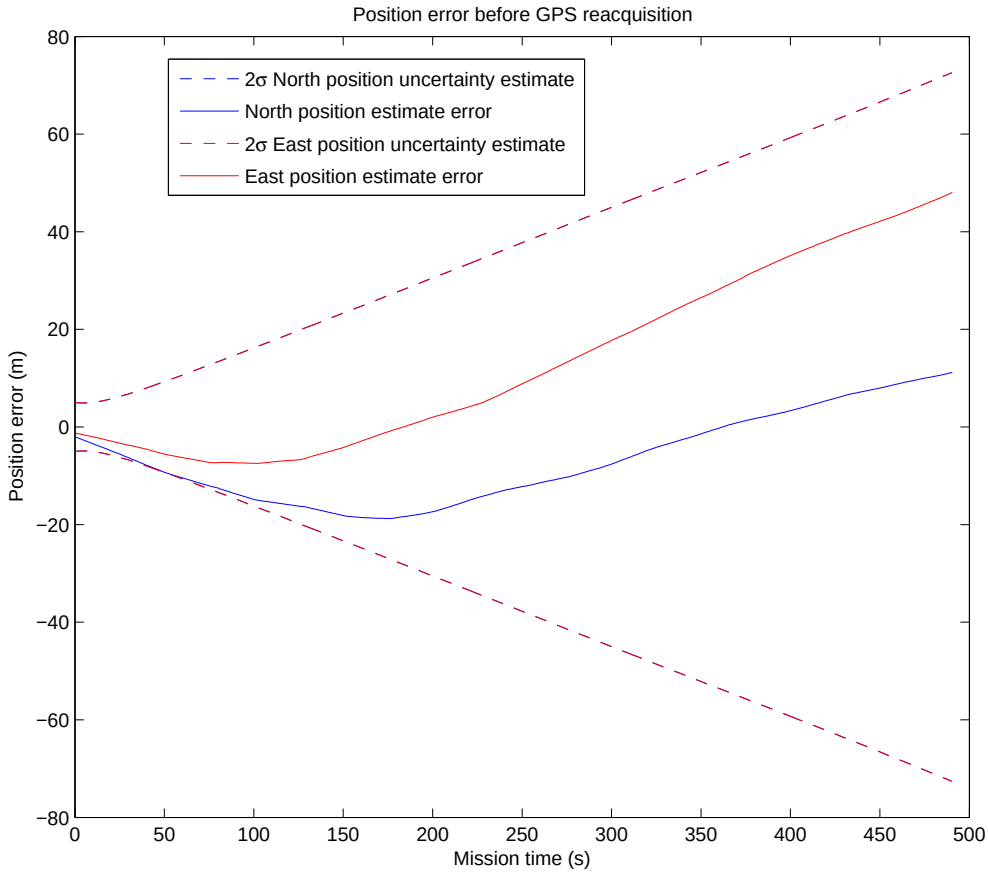

Figure 4.19 – GPS simulated blackout experiment: Position estimate uncertainty and error compared to the GPS aided ground truth prior to GPS reacquisition.

localisation step was completed by using the new smoothed solution of past poses following GPS reacquisition to place the previously incorrectly localised ADCP measurements in the correct water current grids. This grid-relocalisation step is similar to a relinearisation of the past Jacobians. This allows inaccurate linearisations and data associations, in this case the incorrectly localised water current velocity states, to be repositioned given the new knowledge of the past poses. Although the position drifts markedly in this plot, this is due to the vehicle being close to stationary in the ground truth, and as a result of the velocity error, the position drift grows. Given a more accurate initial velocity, the position drift will be reduced to approximately this accuracy. The important result from this experiment is that new horizontal IWVEs have been initialised, while still maintaining a velocity estimate of the vehicle.

Although this result results in position uncertainty growth of approximately 65 m (2σ) over 500 seconds, this still compares favourably to other self-contained localisation methods. Given no other form of aiding, a navigation-grade IMU will have an error of $\sim$140 m over 500 seconds, and the combination of navigation-grade IMU, DVL water-track and vehicle model [16], prior to DVL bottom-lock, gives 125 m (2σ) uncertainty. If a constant position model is assumed, there would be an uncertainty associated with the assumption of the unmodelled water currents. The surface water currents in areas such as Kurishio off Japan, or the Gulf Stream, can attain velocities of 0.4-1.3 m/s [13]. Thus, if the water current is not observed or estimated, the worst case in this scenario would be assumed, leading to between 200 m and 650 m in position uncertainty given the AUV will drift with the currents. Thus, even with poor initial velocity uncertainty, and without an IMU, the localisation performance in this experiment gives promising results. Experiments with accurate GPS and IMU would give performance which reflects the results in simulation to a greater degree, and remains as future research.

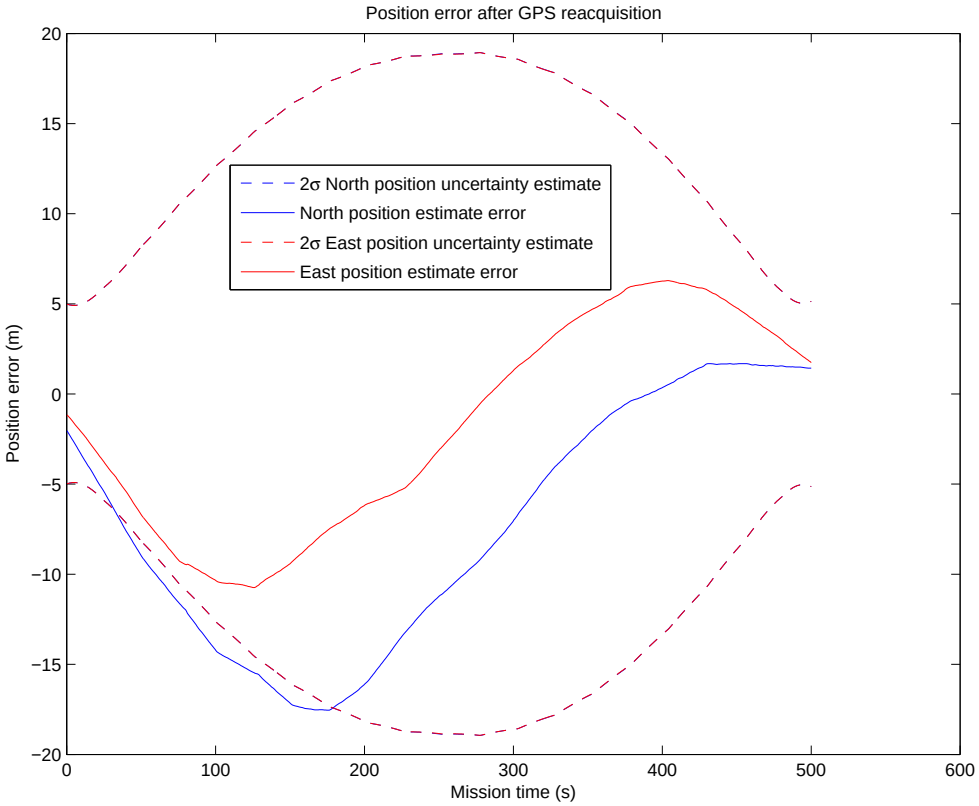

Figure 4.20 – GPS simulated blackout experiment: Position estimate uncertainty and error compared to the GPS aided ground truth following to GPS reacquisition.

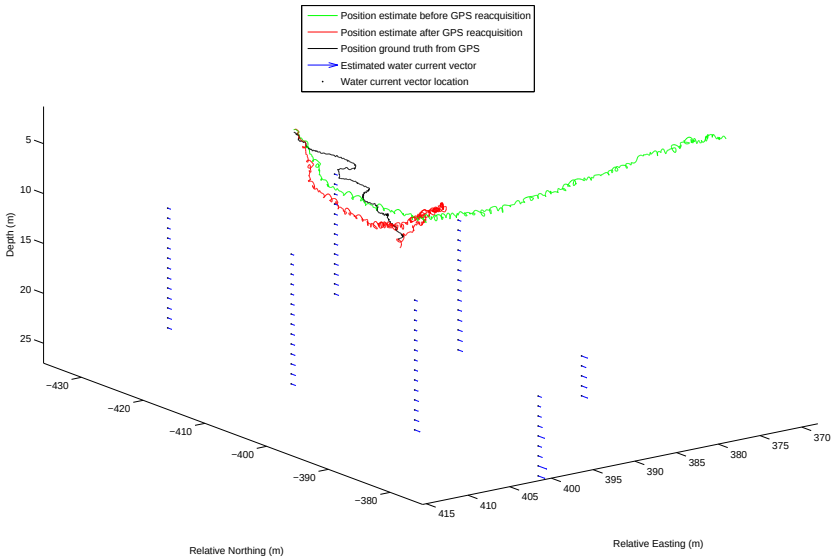

Figure 4.21 – GPS simulated blackout experiment: Estimated trajectory of the vehicle before and after GPS, along with ground truth with full GPS and the estimated water current field. The observed position drift of the vehicle before GPS reacquisition is due to the vehicle being close to stationary in the ground truth, but due to the velocity error, the position drift grows.

4.5 Summary

This chapter has explored the extension of the ADCP-aided localisation by generalising the water current layer model to isocurrent water volume elements. A simulation of the *Sirius* AUV was undertaken with purely horizontal motion once the vehicle had surmerged away from GPS. The information loss rates in the vehicle uncertainty are significantly greater than the vertical descent case. The assumption of horizontal homogeneity which allowed all four beams of the ADCP to observe the same water current depth cell simultaneously is assumed to no longer hold, resulting in limited observability and information loss. A spiralling descent simulation was undertaken, which showed some mitigation of this information loss rate, as the rotation around the water currents allowed greater observability and hence reduced the information loss rate.

Additionally, real data from the *Sirius* AUV was obtained with GPS ground truth. This was compared to the ADCP-aided localisation while on the sea surface. Although the GPS accuracy is sub-optimal, the results showed that localisation by estimating the horizontal water current vector field with IVWEs gives less position uncertainty growth than alternative self-contained localisation methods. Future work will attempt to obtain real data which further validates that the simulation results are in fact attainable in real ocean conditions.

Thus, this chapter has demonstrated the ability to achieve constrained error growth in position by incorporating ADCP measurements into the navigation solution while a vehicle is undergoing a significant horizontal underwater trajectory when GPS and DVL bottom-lock are unavailable. This makes it appropriate for long-term, accurate navigation of an AUV which undertakes missions with horizontal translations in the mid-water column. This alleviates the requirement for a tending vessel or setup of an acoustic network to achieve precise navigation, which may not scale given horizontal transit beyond the horizon. In order to further improve the localisation of the vehicle, given the estimated water current environment surrounding the vehicle, knowledge of the vehicle model could be utilised. The following chapter explores this possibility.

Chapter 5

Combined Inertial and Vehicle Model aiding

From the results in Chapter 3 and 4, results show improved localisation by incorporating the ADCP aiding. The uncertainty bounds in position will still grow unbounded with time, especially in the horizontal localisation case, without the aid of acoustic localisation. Information about the vehicle dynamics could be used to improve the localisation, with less reliance on USBL or LBL. Additionally, utilising the IMU and vehicle model at the same time could improve the localisation better than using either by itself. In Section 3.3.4, a differential thrust model for an AUV was outlined. A method to incorporate a vehicle model simultaneously with an IMU without the need to model or tune a correlation state as in [17] would ensure a more consistent filter.

Previous work on AUV localisation using an IMU and Vehicle model, whether drag based or constant velocity model, tends to use either of them them as the prediction stage of a Extended Kalman Filter, as the control actions into the control input model, to evolve the state from a previous time to the present time [25] [17]. Then, the other one is used as an update. But by doing this, the independent observation assumption is violated, as the vehicle model or IMU is a constraint between the previous state and the present state. With the prediction stage of an EKF, the previous state has been marginalised away. Thus, this will lead to an inconsistent filter due to violation

of this assumption.

Thus, there remains the open problem of achieving the use of an IMU and vehicle model simultaneously, in a consistent manner. An IMU and a drag based vehicle model are proposed to be incorporated into the navigation. A novel method for incorporating the vehicle model and IMU simultaneously as the process models for the EIF is now outlined.

This chapter formulates a novel method to incorporate measurements from an IMU and predictions from the vehicle model at the same time into the localisation. It exploits the fact that in a delayed state framework, the inertial and vehicle model could be converted into a delayed state constraint between poses. Simulations show that localisation improvements depend on the undertaken mission trajectory. For a vertical descent with little horizontal motion, the improvement in localisation accuracy is minimal. For purely horizontal motion, localisation improvements are evident given the introduction of the vehicle model. Finally, real data from the *Sirius* AUV is processed, which compares the incorporation and absence of the vehicle model. Improvements in the localisation are shown as a result of the vehicle model compared to combined GPS and DVL position ground truth, validating the approach for this data.

5.1 Integration concept

In [29], numerically integrating the IMU measurements as constraints between low rate poses, for example at 5 Hz compared to the 100 Hz IMU output, was used to allow an inertial SLAM formulation without initialisation. The contribution that this chapter makes, is that the IMU and vehicle model can be numerically integrated to be used as constraints between poses. The IMU integration is also modified from [29] to be used in a global reference frame. Then, these constraints between poses can then be applied in a delayed state framework. The idea is graphically represented in Figure 5.1. The following equations now outline how this framework operates for a simple 1-dimensional case.

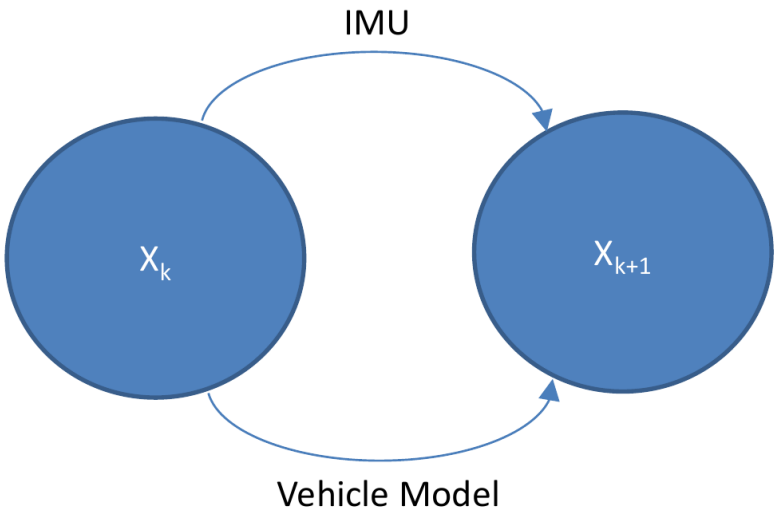

Figure 5.1 – The IMU and the vehicle model act as delayed state constraints between poses X_k and X_{k+1}

Equation 5.1 begins with a constant acceleration (a) assumption and applying an Euler integration for velocity (v). Δt is the time step. For example, $\Delta t = 0.01$ seconds for 100 Hz acceleration inputs. Equation 5.2 applies an Euler integration for position (p). Equation 5.3 represents the change in velocity between pose states. This constraint can be incorporated into the EIF. Given v_N is the velocity at a certain pose state, say 1 second after the initial velocity v_1, the change in velocity will be the sum of the accelerations times delta T, with 100 acceleration measurements used in the integration if the rate of inputs is 100 Hz. The right hand side (RHS) of Equation 5.3 represents the constraint, while the left hand side (LHS) of the equation represents the integrated measurement. If position is also part of the pose state, then the constraint in Equation 5.4, which is the correction for non-zero acceleration compared to the constant velocity assumption, is equal to the double integration of the acceleration times delta T for the 100 acceleration measurements. The RHS of Equation 5.4 represents the constraints, while the LHS represents the integrated measurement.

The acceleration measurement from the IMU (z_{IMU}) is the addition of the true acceleration at the IMU (a_{IMU}) and noise (ϵ_{IMU}). Additionally, the acceleration measurement from the vehicle model (z_{VM}) is the addition of the true acceleration according

to the vehicle model (a_{VM}) and noise (ϵ_{VM}). These constraints can be incorporated in parallel into a delayed state framework, and if they are non-linear and are linearised, they can be re-linearised at an arbitrary time in the future if a better linearisation is available [22]. This process would be more difficult if the standard prediction stage used by an EIF was implemented instead.

$$v_2 = v_1 + a_1 \Delta t \tag{5.1}$$

$$p_2 = p_1 + v_1 \Delta t \tag{5.2}$$

$$v_N - v_1 = \sum_{n=1}^{N-1} a_n \Delta t \tag{5.3}$$

$$p_N - p_1 - v_1(T_N - T_1) = \sum_{n=1}^{N-1} \sum_{n=1}^{N-1} a_n \Delta t \tag{5.4}$$

$$z_{IMU} = a_{IMU} + \varepsilon_{IMU} \tag{5.5}$$

$$z_{VM} = a_{VM} + \varepsilon_{VM} \tag{5.6}$$

The purpose of the numerical integration of multiple IMU or vehicle model "control actions" is the allow them to be represented as full rank constraints between poses. This must be done in a way to be independent to previous observations, and thus can be used as a delayed state update between two consecutive poses, which can be achieved with this approach. The ADCP aiding method provides the water current estimates, providing the water relative velocities of the vehicle, and thus feeds back into the vehicle model localisation estimation.

Additionally, the uncertainty in the parameter estimates, such as drag coefficients of the vehicle, from a previous system identification, can be input into the filter, since the parameter can be treated as a state. So regardless of the accuracy of the previous system identification, if the parameter uncertainty is specified, then the filter can determine the amount of impact the vehicle model will have.

5.2 Derivation of the integration framework

In order to apply both an inertial model and a vehicle model, the delayed state structure of the Information Filter is exploited. In a similar way to inertial integration [29], a thruster and drag vehicle model is integrated, as described in Section 3.3.4. This form of constraint makes the integrated inertial and vehicle model suitable for pose based SLAM applications where vision and bathymetric based SLAM is applied [26], since this constraint can be used in a least-squares optimization and be relinearised later. The following formulation also has the advantage of not requiring the explicit modelling of the correlation between each vehicle model update as in [17].

The algorithm used to construct the constraints between poses is outlined in Algorithm 2. Algorithm 3 presents the Jacobians and covariances of these constraints. The integration theory as derived from [29] relies on the following equations describing the evolution of position, velocity and attitude as a function of body-relative accelerations and rotation rates:

$$\mathbf{p}^n_{t_2} = \mathbf{p}^n_{t_1} + \int_{t_1}^{t_2} \mathbf{v}^n_t dt \tag{5.7}$$

$$\mathbf{v}^n_{t_2} = \mathbf{v}^n_{t_1} + \int_{t_1}^{t_2} (C^n_{b,t}\mathbf{f}^b_t + \mathbf{g}^n) dt \tag{5.8}$$

$$\boldsymbol{\phi}^n_{t_2} = \boldsymbol{\phi}^n_{t_1} + \int_{t_1}^{t_2} E^n_{b,t}\boldsymbol{\omega}^b_t dt \tag{5.9}$$

where:

- $\mathbf{v}^n_t$ is the velocity of the IMU at time t in the navigation frame,
- $\mathbf{C}^n_{b,t}$ is the coordinate transformation matrix from body to navigation frame at time t,
- $\mathbf{f}^b_t$ is the specific force (the IMU accelerometer output) in the body frame at time t,
- $\mathbf{g}^n$ is the gravity vector in the navigation frame,

- $\mathbf{p}_t^n$ is the position of the IMU at time t in the navigation frame,
- $\boldsymbol{\phi}_t^n$ is the attitude of the IMU at time t in the navigation frame,
- $\mathbf{E}_{b,t}^n$ is the rotation rates transformation matrix from body to navigation frame at time t,
- $\boldsymbol{\omega}_t^b$ is the rotation rates in the body frame at time t,
- $\mathbf{C}_n^{b,t}$ is the coordinate transformation matrix from navigation to body frame at time t,

Given the following identities:

$$\Delta\mathbf{p}_{t_2}^{+t_1} = \iint_{t_1}^{t} C_{b,t}^n \mathbf{f}_t^b dt^2 \tag{5.10}$$

$$\Delta\mathbf{v}_{t_2}^{t_1} = \int_{t_1}^{t} C_{b,t}^n \mathbf{f}_t^b dt \tag{5.11}$$

$$\Delta\boldsymbol{\phi}_{t_2}^{t_1} = \int_{t_1}^{t} E_{b,t}^n \boldsymbol{\omega}_t^b dt \tag{5.12}$$

The term $\Delta\mathbf{p}_{t_2}^{+t_1}$ represents the correction in the position estimate compared to constant velocity. Then Equations 5.7, 5.8 and 5.9 become:

$$\mathbf{p}_{t_2}^n = \mathbf{p}_{t_1}^n + \mathbf{v}_{t_1}^n(t_2 - t_1) + C_{t_1}^n \Delta\mathbf{p}_{t_2}^{+t_1} + \frac{1}{2}(t_2 - t_1)^2 \mathbf{g}^n \tag{5.13}$$

$$\mathbf{v}_{t_2}^n = \mathbf{v}_{t_1}^n + C_{t_1}^n \Delta\mathbf{v}_{t_2}^{t_1} + (t_2 - t_1)\mathbf{g}^n \tag{5.14}$$

$$\boldsymbol{\phi}_{t_2}^n = EulerFromRotationMatrix(\mathbf{C}_{t_1}^n \Delta\mathbf{C}_{t_2}^{t_1}) \tag{5.15}$$

The form for $\mathbf{f}_t^b$ and $\mathbf{w}_t^b$ depends on the inertial model, or the vehicle model. For the inertial model, they can be solved by Euler integration with the following equations:

$$\Delta \mathbf{v}_{imu,k+1} = \Delta \mathbf{v}_{imu,k} + \mathbf{C}_{b,k}^{b,0}(\mathbf{f}_k^b - \mathbf{bias}_a^{obs})\Delta t \tag{5.16}$$

$$\Delta \mathbf{p}_{imu,k+1}^{+} = \Delta \mathbf{p}_{imu,k}^{+} + \mathbf{v}_{imu,k+1}\Delta t \tag{5.17}$$

$$\Delta \boldsymbol{\phi}_{imu,k+1} = \Delta \boldsymbol{\phi}_{imu,k} + \mathbf{E}_{b,k}^{b,0}(\boldsymbol{\omega}_k^b - \mathbf{bias}_\omega^{obs} - \mathbf{C}_n^k \boldsymbol{\Omega}_e^n)\Delta t \tag{5.18}$$

where $\boldsymbol{\Omega}_e^n$ is the rotation rate vector of the Earth in the navigation frame, $\mathbf{bias}_a^{obs}$ is the estimated bias in the accelerometer, and $\mathbf{bias}_\omega^{obs}$ is the estimated bias in the gyroscope.

For the vehicle model, the Euler integration is derived as follows:

$$\begin{bmatrix} \ddot{x}_{b,k} \\ \ddot{y}_{b,k} \\ \ddot{\psi}_k \end{bmatrix} = \begin{bmatrix} (F_{1,k} + F_{2,k} - D_{\dot{x}}\dot{x}_{b,k}\left|\dot{x}_{b,k}\right| + M_y\dot{y}_b\omega_{vm,k})/M_x \\ (-D_{\dot{y}}\dot{y}_{b,k}\left|\dot{y}_{b,k}\right| + M_x\dot{x}_{b,k}\omega_{vm,t})/M_y \\ (F_{1,k}r - F_{2,k}r - D_{\dot{\psi}}\omega_{vm,k}\left|\omega_{vm,k}\right| - M_y\dot{x}_{b,k}\dot{y}_{b,k} + M_x\dot{x}_{b,k}\dot{y}_{b,k})/I_z \end{bmatrix} \tag{5.19}$$

$$\Delta \mathbf{v}_{vm,k+1} = \Delta \mathbf{v}_{vm,k} + \mathbf{R}_{b,k}^{b,0} \begin{bmatrix} \ddot{x}_{b,k} \\ \ddot{y}_{b,k} \end{bmatrix} \Delta t \tag{5.20}$$

$$\Delta \mathbf{p}_{vm,k+1}^{+} = \Delta \mathbf{p}_{vm,k}^{+} + \Delta \mathbf{v}_{vm,k+1}\Delta t \tag{5.21}$$

$$\omega_{vm,k+1} = \omega_{vm,k} + \ddot{\psi}_k \Delta t \tag{5.22}$$

$$\Delta \psi_{k+1} = \Delta \psi_k + \omega_{vm,k+1}\Delta t \tag{5.23}$$

$$\begin{bmatrix} \dot{x}_{b,k+1} \\ \dot{y}_{b,k+1} \end{bmatrix} = \begin{bmatrix} \dot{x}_{b,k} \\ \dot{y}_{b,k} \end{bmatrix} + \mathbf{R}_{b,k}^{b,0} \begin{bmatrix} \ddot{x}_{b,k} \\ \ddot{y}_{b,k} \end{bmatrix} \Delta t \tag{5.24}$$

The vehicle model constraint is initialised with a rotation rate estimate from the IMU. Therefore the correlation between the IMU constraint and the vehicle model constraint must be accounted for. The vehicle model is only applied for the North and East directions for localisation purposes, as the Down velocity component is already well estimated with the IMU, ADCP and pressure depth sensor, and the roll and pitch acting on the vehicle is assumed small. Attitude estimation occurs due to an

interaction between the GPS, IMU and vehicle model. The process noise for the IMU model is from the IMU measurement uncertainty itself. The process noise for the vehicle model is from the uncertainty in the thruster action. Additionally, the vehicle model used in this case is the generic model derived from [9], but any vehicle model can be utilised in this framework.

Algorithm 2 solves the Equations 5.10, 5.11 and 5.12 through Euler integration for both the inertial and vehicle model. Higher order integration could be used for more precision, but Euler integration is used because of its relative simplicity and easier to calculate analytical Jacobians. The Jacobians for the filter are solved using Algorithm 3. The state ordering for the Jacobian F in Algorithm 2 is: $[\Delta\mathbf{p}^{+}_{imu,k},\ \Delta\mathbf{v}_{imu,k},\ \Delta\boldsymbol{\phi}_{imu,k},\ \mathbf{bias}^{obs}_{a},\ \mathbf{bias}^{obs}_{w},\ \Delta\mathbf{p}^{+}_{vm,k},\ \Delta\mathbf{v}_{vm,k},\ \Delta\psi_k,\ \omega_{vm,k},\ D_{\dot{x}},\ D_{\dot{y}},\ D_{\dot{\psi}},\ M_x,\ M_y,\ I_z,\ r,\ X_i]$

The form of the Noise Injection Covariance Q in Algorithm 2 is:

$Q = diag\{Q_{IMU}, \sigma^2_{F_1}, \sigma^2_{F_2}\}$

While determining the partial derivatives for the F_{VM} Jacobian, the following identities also need to be applied:

$$\mathbf{v}_i = \begin{bmatrix} \dot{x_{b,0}} \\ \dot{y_{b,0}} \end{bmatrix} \tag{5.25}$$

$$\phi_i = \phi^n_{k=0} \tag{5.26}$$

$$\mathbf{X}_i = \begin{bmatrix} v_i \\ \phi_i \end{bmatrix} \tag{5.27}$$

$$\begin{bmatrix} \dot{x_{b,k}} \\ \dot{y_{b,k}} \end{bmatrix} = \mathbf{v}_i + \Delta\mathbf{v}_{vm,k} \tag{5.28}$$

The $\mathbf{X}_i$ and $\mathbf{v}_c$ states exist in the Jacobian calculations to allow the extraction of the derivatives of the vehicle model deltas with respect to the initial states of vehicle and water current velocity in the body frame, and global heading. The vehicle and water current velocities impact on the rate changes in $\ddot{x}_{b,k}$ and $\ddot{y}_{b,k}$, while the global heading affects the Earth rotation correction for $\omega_{vm,0}$ and $\Delta\boldsymbol{\phi}_{imu,k+1}$.

Algorithm 2 Inertial and Vehicle Model Constraint

N = Number of Inertial Measurements to be Integrated
$k = 0$
$\Delta\mathbf{v}_{imu,0} = 0$
$\Delta\mathbf{p}^{+}_{imu,0} = 0$
$\Delta\boldsymbol{\phi}_{imu,0} = 0$
$\Delta\mathbf{v}_{vm,0} = 0$
$\Delta\mathbf{p}^{+}_{vm,0} = 0$
$\begin{bmatrix}\dot{x}_{b,0}\\ \dot{y}_{b,0}\end{bmatrix} = \mathbf{R}^{b,k}_{n,k}\begin{bmatrix}\dot{x}_{n,0} - v^{n}_{c,x}\\ \dot{y}_{n,0} - v^{n}_{c,y}\end{bmatrix}$
$\omega_{vm,0} = (\omega^{b}_{1} - bias^{obs}_{w} - C^{0}_{n}\Omega^{n}_{e})_{3,1}$
$\Delta\psi_0 = 0$
while $k < N$ **do**
$k = k + 1$
$\Delta t = t_{k+1} - t_k$
$\Delta\mathbf{v}_{imu,k+1} = \Delta\mathbf{v}_{imu,k} + \mathbf{C}^{b,0}_{b,k}(\mathbf{f}^{b}_{k} - \mathbf{bias}^{obs}_{a})\Delta t$
$\Delta\mathbf{p}^{+}_{imu,k+1} = \Delta\mathbf{p}^{+}_{imu,k} + \mathbf{v}_{imu,k+1}\Delta t$
$\Delta\boldsymbol{\phi}_{imu,k+1} = \Delta\boldsymbol{\phi}_{imu,k} + \mathbf{E}^{b,0}_{b,k}(\boldsymbol{\omega}^{b}_{k} - \mathbf{bias}^{obs}_{w} - \mathbf{C}^{k}_{n}\boldsymbol{\Omega}^{n}_{e})\Delta t$
$\begin{bmatrix}v_{T1}\\ v_{T2}\end{bmatrix} = \begin{bmatrix}\dot{x}_{b,k} + r\omega_{vm,k}\\ \dot{x}_{b,k} - r\omega_{vm,k}\end{bmatrix}$

$\begin{bmatrix}F_1\\ F_2\end{bmatrix} = \begin{bmatrix}0.4\rho d^4|n_1|n_1 - \frac{1}{3}v_{T1}\rho d^3|n_1|\\ 0.4\rho d^4|n_2|n_2 - \frac{1}{3}v_{T2}\rho d^3|n_2|\end{bmatrix}$

$\begin{bmatrix}\ddot{x}_{b,k}\\ \ddot{y}_{b,k}\\ \ddot{\psi}_{k}\end{bmatrix} = \begin{bmatrix}(F_{1,k} + F_{2,k} - D_{\dot{x}}\dot{x}_{b,k}\,|\dot{x}_{b,k}| + M_y\dot{y}_b\omega_{vm,k})/M_x\\ (-D_{\dot{y}}\dot{y}_{b,k}\,|\dot{y}_{b,k}| + M_x\dot{x}_{b,k}\omega_{vm,t})/M_y\\ (F_{1,k}r - F_{2,k}r - D_{\dot{\psi}}\omega_{vm,k}\,|\omega_{vm,k}| - M_y\dot{x}_{b,k}\dot{y}_{b,k} + M_x\dot{x}_{b,k}\dot{y}_{b,k})/I_z\end{bmatrix}$
$\Delta\mathbf{v}_{vm,k+1} = \Delta\mathbf{v}_{vm,k} + \mathbf{R}^{b,0}_{b,k}\begin{bmatrix}\ddot{x}_{b,k}\\ \ddot{y}_{b,k}\end{bmatrix}\Delta t$

$\Delta\mathbf{p}^{+}_{vm,k+1} = \Delta\mathbf{p}^{+}_{vm,k} + \Delta\mathbf{v}_{vm,k+1}\Delta t$
$\omega_{vm,k+1} = \omega_{vm,k} + \ddot{\psi}_{k}\Delta t$
$\Delta\psi_{k+1} = \Delta\psi_{k} + \omega_{vm,k+1}\Delta t$
$\begin{bmatrix}\dot{x}_{b,k+1}\\ \dot{y}_{b,k+1}\end{bmatrix} = \begin{bmatrix}\dot{x}_{b,k}\\ \dot{y}_{b,k}\end{bmatrix} + \mathbf{R}^{b,0}_{b,k}\begin{bmatrix}\ddot{x}_{b,k}\\ \ddot{y}_{b,k}\end{bmatrix}\Delta t$

end while
$\Delta\mathbf{v}_{imu} = \Delta\mathbf{v}_{imu,k+1}$
$\Delta\mathbf{p}^{+}_{imu} = \Delta\mathbf{p}^{+}_{imu,k+1}$
$\Delta\boldsymbol{\phi}_{imu} = \Delta\boldsymbol{\phi}_{imu,k+1}$
$\Delta\mathbf{v}_{vm} = \Delta\mathbf{v}_{vm,k+1}$
$\Delta\mathbf{p}^{+}_{vm} = \Delta\mathbf{p}^{+}_{vm,k+1}$
$\Delta\psi_{vm} = \psi_{k+1}$

Algorithm 3 Inertial and Vehicle Model Jacobian and Covariance Creation

N = Number of Inertial Measurements to be Integrated
$k = 0$
$\mathbf{P} = \mathbf{0}_{32\times32}$
$\mathbf{J} = \mathbf{I}_{32\times32}$
$\mathbf{J}_{21,21} = 0$
$\mathbf{J}_{21,9} = 1/\Delta t$
$\mathbf{J}_{21,15} = -1$
while $k < N$ **do**
$k = k + 1\mathrm{D}$

$$\mathbf{F}_{IMU} = \begin{bmatrix} \mathbf{I}_3 & \mathbf{I}_3\Delta t & \mathbf{0}_{3\times3} & \mathbf{0}_{3\times3} & \mathbf{0}_{3\times3} \\ \mathbf{0}_{3\times3} & \mathbf{I}_3 & \frac{\partial\Delta\mathbf{v}_{imu,k+1}}{\partial\Delta\boldsymbol{\phi}_{imu,k}} & -\mathbf{C}_t^{t_1}\Delta t & \mathbf{0}_{3\times3} \\ \mathbf{0}_{3\times3} & \mathbf{0}_{3\times3} & \frac{\partial\Delta\boldsymbol{\phi}_{imu,k+1}}{\partial\Delta\boldsymbol{\phi}_{imu,k}} & \mathbf{0}_{3\times3} & -\mathbf{E}_t^{t_1}\Delta t \\ \mathbf{0}_{3\times3} & \mathbf{0}_{3\times3} & \mathbf{0}_{3\times3} & \mathbf{I}_3 & \mathbf{0}_{3\times3} \\ \mathbf{0}_{3\times3} & \mathbf{0}_{3\times3} & \mathbf{0}_{3\times3} & \mathbf{0}_{3\times3} & \mathbf{I}_3 \end{bmatrix}$$

$$F_{VM} = \begin{bmatrix} \mathbf{I}_2 & \mathbf{I}_2\Delta t & \frac{\partial\Delta\mathbf{v}_{vm,k+1}}{\partial\Delta\boldsymbol{\phi}_{vm,k}} & \frac{\partial\Delta\mathbf{v}_{vm,k+1}}{\partial\omega_{vm,k}} & \frac{\partial\Delta\mathbf{v}_{vm,k+1}}{\partial\mathbf{v}_c} & \mathbf{0}_{1\times17} & \frac{\partial\Delta\mathbf{v}_{vm,k+1}}{\partial M} & \mathbf{0}_{2\times1} & \frac{\partial\Delta\mathbf{v}_{vm,k+1}}{\partial\mathbf{X}_i} \\ \mathbf{0}_{2\times2} & \frac{\partial\Delta\mathbf{v}_{vm,k+1}}{\partial\Delta\mathbf{v}_{vm,k}} & & & & \frac{\partial\Delta\mathbf{v}_{vm,k+1}}{\partial D} & & & \\ & \mathbf{0}_{1\times4} & 1 & \Delta t & & & \mathbf{0}_{1\times15} & & \\ \mathbf{0}_{1\times2} & \frac{\partial\omega_{vm,k+1}}{\partial\Delta\mathbf{v}_{vm,k}} & 0 & \frac{\partial\omega_{vm,k+1}}{\partial\omega_{vm,k}} & \frac{\partial\omega_{vm,k+1}}{\partial\mathbf{v}_c} & \frac{\partial\omega_{vm,k+1}}{\partial D} & \frac{\partial\omega_{vm,k+1}}{\partial M} & \frac{\partial\omega_{vm,k+1}}{\partial r} & \frac{\partial\omega_{vm,k+1}}{\partial X_i} \\ & & \mathbf{0}_{15\times6} & & & & \mathbf{I}_{15} & & \end{bmatrix}$$

$$\mathbf{F}_{IMU,\phi} = \begin{bmatrix} \mathbf{0}_{6\times18} & \mathbf{0}_{6\times3} \\ \mathbf{0}_{3\times18} & \frac{\partial\Delta\boldsymbol{\phi}_{imu,k+1}}{\partial\phi_i} \\ \mathbf{0}_{6\times18} & \mathbf{0}_{6\times3} \end{bmatrix}$$

$$\mathbf{F} = \begin{bmatrix} \mathbf{F}_{IMU} & \mathbf{F}_{IMU,\phi} \\ \mathbf{0}_{17\times17} & \mathbf{F}_{VM} \end{bmatrix}$$

$$\mathbf{G} = \begin{bmatrix} & & \mathbf{0}_{3\times8} & \\ \mathbf{C}_t^{t_1}\Delta t & & \mathbf{0}_{8\times5} & \\ \mathbf{0}_{3\times3} & \mathbf{E}_t^{t_1}\Delta t & & \mathbf{0}_{3\times2} \\ & & \mathbf{0}_{8\times8} & \\ & \mathbf{0}_{2\times6} & & \mathbf{R}_{b,k}^{b,0}\begin{bmatrix} \frac{\partial\ddot{x}_{b,k}}{\partial n_1} & \frac{\partial\ddot{x}_{b,k}}{\partial n_2} \\ 0 & 0 \end{bmatrix} \\ & & \mathbf{0}_{1\times8} & \\ \mathbf{0}_{1\times5} & \frac{\partial\ddot{\psi}_k}{\partial\mathbf{bias}_w^{obs}}\Delta t & \frac{\partial\ddot{\psi}_k}{\partial n_1} & r\frac{\partial\ddot{\psi}_k}{\partial n_2} \\ & & \mathbf{0}_{12\times8} & \end{bmatrix}$$

$\mathbf{J}_{t+1} = \mathbf{F}\mathbf{J}_t$
$\mathbf{P}_{t+1} = \mathbf{F}\mathbf{P}_t\mathbf{F}^T + \mathbf{G}\mathbf{Q}\mathbf{G}^T$

end while
$\mathbf{J}_{t_1}^{t_2} = \mathbf{J}_{t+1}$
$\mathbf{P}_{t_1}^{t_2} = \mathbf{P}_{t+1}$

The predicted inertial and vehicle model constraints are derived from rearranging Equations 5.7, 5.8 and 5.9. The vehicle model constraints are only for the North and East directions. The predicted constraints for the present state estimate are:

$$\mathbf{h}_{\Delta\mathbf{p}^{+t_1}_{imu,t_2}}(\hat{\mathbf{x}}(t_k)) = \mathbf{C}^{t_1}_n(\mathbf{p}^n_{t_2} - \mathbf{p}^n_{t_1} - \mathbf{v}^n_{t_1}(t_2 - t_1) - \frac{1}{2}(t_2 - t_1)^2\mathbf{g}^n) - \Delta\mathbf{v}_{imu} \tag{5.29}$$

$$\mathbf{h}_{\Delta\mathbf{v}^{+t_1}_{imu,t_2}}(\hat{\mathbf{x}}(t_k)) = \mathbf{C}^{t_1}_n(\mathbf{v}^n_{t_2} - \mathbf{v}^n_{t_1} - (t_2 - t_1)\mathbf{g}^n) - \Delta\mathbf{p}^+_{imu} \tag{5.30}$$

$$\mathbf{h}_{\Delta\boldsymbol{\phi}^{+t_1}_{imu,t_2}}(\hat{\mathbf{x}}(t_k)) = EulerFromRotationMatrix(\mathbf{C}^{t_1}_n\mathbf{C}^n_{t_2}) - \Delta\boldsymbol{\phi}_{imu} \tag{5.31}$$

$$\mathbf{h}_{\Delta\mathbf{p}^{+t_1}_{vm,t_2}}(\hat{\mathbf{x}}(t_k)) = \mathbf{R}^{t_1}_n(\mathbf{p}^n_{t_2} - \mathbf{p}^n_{t_1} - \mathbf{v}^n_{t_1}(t_2 - t_1)) - \Delta\mathbf{v}_{vm} \tag{5.32}$$

$$\mathbf{h}_{\Delta\mathbf{v}^{+t_1}_{vm,t_2}}(\hat{\mathbf{x}}(t_k)) = \mathbf{R}^{t_1}_n(\mathbf{v}^n_{t_2} - \mathbf{v}^n_{t_1} - (t_2 - t_1)\mathbf{g}^n) - \Delta\mathbf{p}^+_{vm} \tag{5.33}$$

$$h_{\Delta\phi^{+t_1}_{vm,t_2}}(\hat{\mathbf{x}}(t_k)) = \phi_{t_2} - \phi_{t_1} - \Delta\psi_{vm} \tag{5.34}$$

Thus the total predicted inertial and vehicle model constraint is:

$$\mathbf{h}_{process}(t_k) = \begin{bmatrix} \mathbf{h}_{\Delta\mathbf{p}^{+t_1}_{imu,t_2}}(\hat{\mathbf{x}}(t_k)) \\ \mathbf{h}_{\Delta\mathbf{v}^{+t_1}_{imu,t_2}}(\hat{\mathbf{x}}(t_k)) \\ \mathbf{h}_{\Delta\boldsymbol{\phi}^{+t_1}_{imu,t_2}}(\hat{\mathbf{x}}(t_k)) \\ \mathbf{h}_{\Delta\mathbf{p}^{+t_1}_{vm,t_2}}(\hat{\mathbf{x}}(t_k)) \\ \mathbf{h}_{\Delta\mathbf{v}^{+t_1}_{vm,t_2}}(\hat{\mathbf{x}}(t_k)) \\ \mathbf{h}_{\Delta\boldsymbol{\phi}^{+t_1}_{vm,t_2}}(\hat{\mathbf{x}}(t_k)) \end{bmatrix} \tag{5.35}$$

$$\mathbf{z}_{process} = \mathbf{0}_{14\times 1} \tag{5.36}$$

The matching elements of $\mathbf{P}^{t_2}_{t_1}$ resulting from Algorithm 3 will be used as the covariance for the measurement update.

The IMU gyro and accelerometer biases are correlated according to the first order Markov process described by Equation 3.13 within the Information Filter.

5.3 Simulation

The following simulations from previous Chapters are repeated, with the same noise seeds, and with the vehicle model added as part of the estimation:

1. Simulation from Section 3.3.5, with vertical descent over 1000 seconds.
2. Simulation from Section 4.3.2, with a horizontal trajectory underwater over 700 seconds.

The localisation results are compared between four separate scenarios:

1. The parameters in the vehicle model are assumed to have had a prior system identification within 1% (3 σ) of their true value. This uncertainty is supplied to the filter, which allows this constant parameter bias to be properly accounted for in the uncertainty estimates of the filter. The applied force control action (F_1 and F_2) is supplied at 100 Hz, and is assumed to be modelled to an accuracy of approximately 0.25 N (3 σ), which arises because of uncertain propellor revolution speed, velocity through water and thrust modelling.
2. The parameters in the vehicle model are assumed to have had a prior system identification within 10% (3 σ) of their true value. This uncertainty is supplied to the filter, which allows this constant parameter bias to be properly accounted for in the uncertainty estimates of the filter. The applied force control action (F_1 and F_2) is supplied at 100 Hz, and is assumed to be modelled to an accuracy of approximately 2.5 N (3 σ), which arises because of uncertain propellor revolution speed, velocity through water and thrust modelling.
3. The parameters in the vehicle model are assumed to have had a prior system identification within 50% (3 σ) of their true value. This uncertainty is supplied to the filter, which allows this constant parameter bias to be properly accounted for in the uncertainty estimates of the filter. The applied force control action (F_1 and F_2) is supplied at 100 Hz, and is assumed to be modelled to an accuracy

of approximately 12.5 N (3 σ), which arises because of uncertain propellor revolution speed, velocity through water and thrust modelling.

4. No vehicle model is incorporated into the localisation.

5.3.1 Vertical descent with vehicle model aiding

Figure 5.2 shows very little difference in the estimate error between the four filters. Figure 5.3 shows the uncertainty estimate prior to DVL bottom-lock goes from 4m (no vehicle model) 3.9m (50% paramater uncertainty) to 3.8m (10% paramater uncertainty) and finally to 3.6m (1% parameter uncertainty). Post DVL bottom-lock gives a nearly identical result. For the vertical descent case, since the no vehicle model case was already low in error relative to it's uncertainty bounds, the addition of a vehicle model does not appreciably improve the error, although the uncertainty bounds have decreased slightly, with 2, 5 and 10 percent improvements with 50%, 10%, 1% uncertainty in the vehicle parameters respectively. In this case, the error has not appreciably reduced, and even increased, while the uncertainty bounds have decreased. This is due to the initial errors also being quite low relative to the uncertainty bounded without the vehicle model in this case, while the addition of the vehicle model has reduced the uncertainty, but increased the error, which is possible given the markov nature of the localisation information from the ADCP-aided method and the vehicle model.

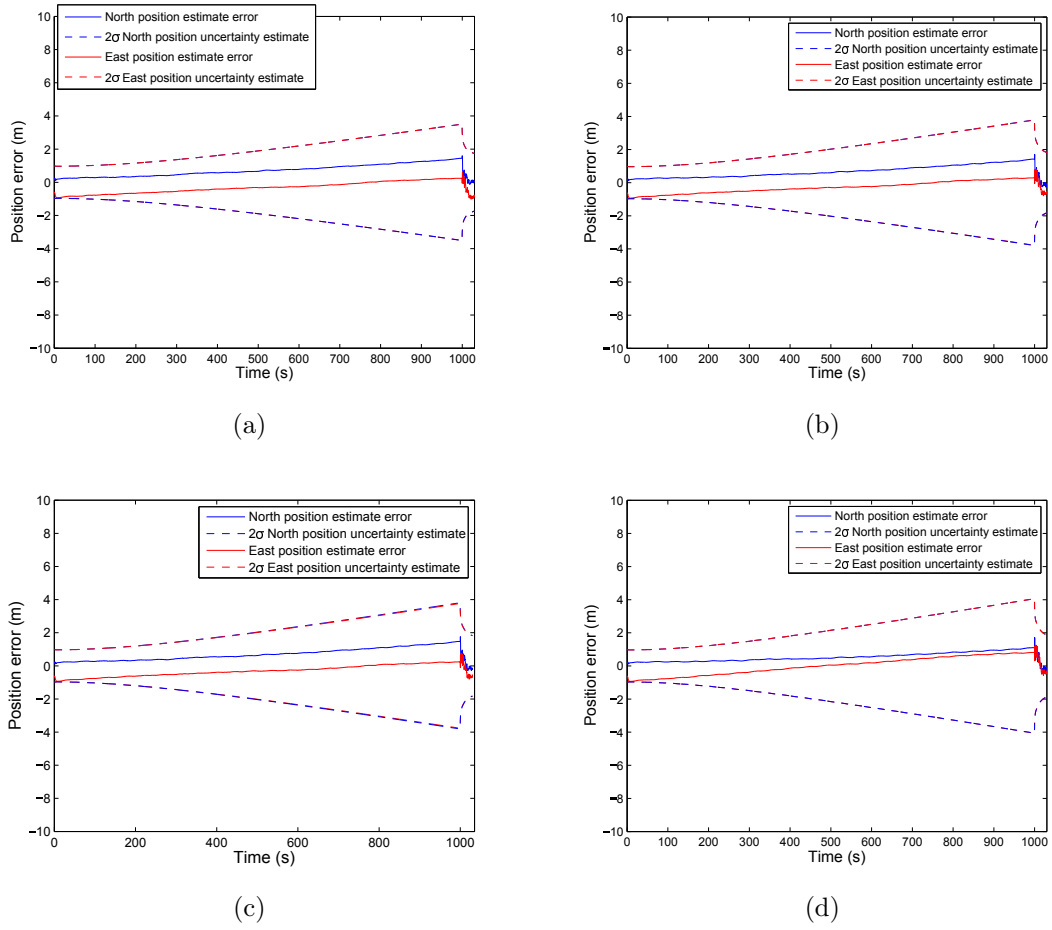

Figure 5.2 – The vertical descent simulation position estimates and uncertainties for (a) 1% (3 σ) vehicle model parameter uncertainty, (b) 10% (3 σ) vehicle model parameter uncertainty and (d) without vehicle model aiding.

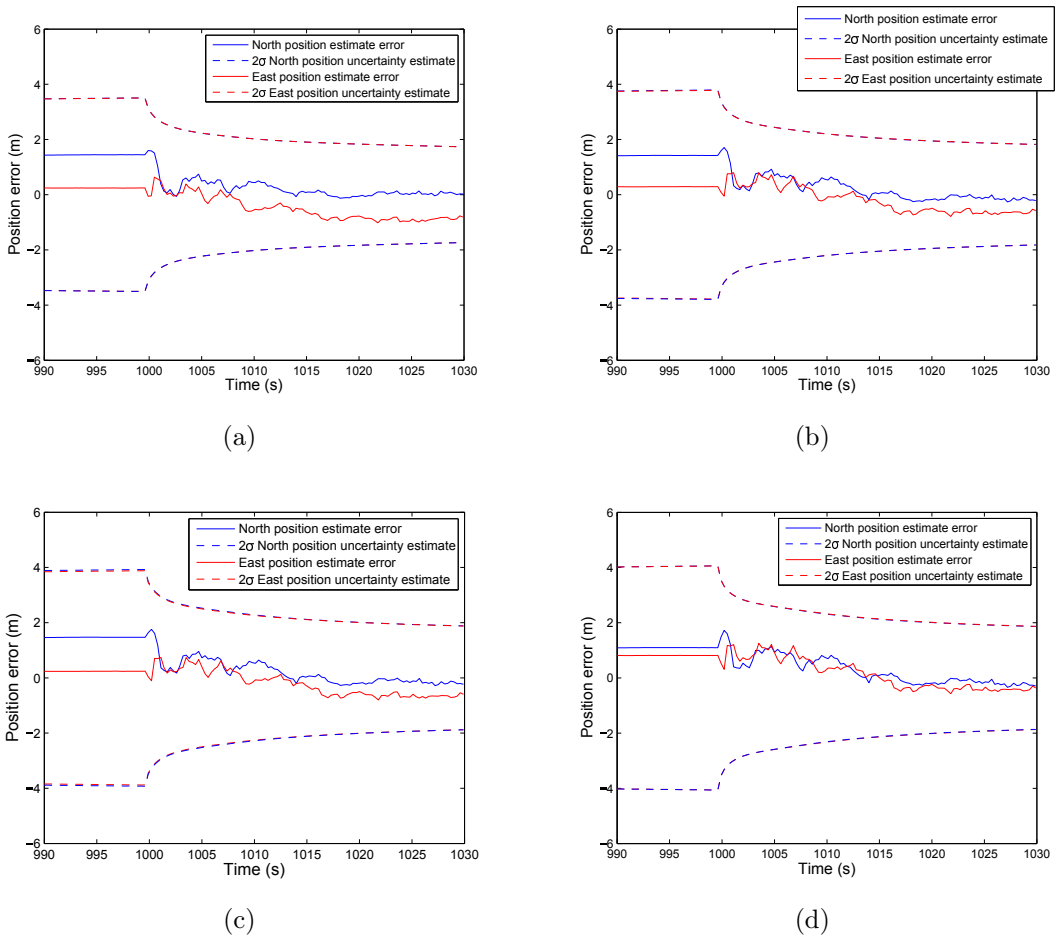

Figure 5.3 – A zoom on the vertical descent simulation position estimates and uncertainties (a) 1% (3 σ) vehicle model parameter uncertainty, (b) 10% (3 σ) vehicle model parameter uncertainty and (d) without vehicle model aiding.

5.3.2 Horizontal motion with vehicle model aiding

Figure 5.4 shows the estimate error and uncertainty estimates given the four filter realisations. It shows the uncertainty reduction after 800 seconds of horizontal transit, compared to no vehicle model is 0.8m (50% paramater uncertainty) to 2m (10% paramater uncertainty) and finally 6m (1% parameter uncertainty). The uncertainty bounds have decreased slightly, with 5, 12 and 37 percent improvements with 50%, 10%, 1% uncertainty in the vehicle parameters respectively. These figures shows a definite trend towards improved accuracy given vehicle model incorporation in the estimate error between the four filter instances. The uncertainty estimate at the end of the 700 seconds of no GPS decreases as the vehicle model accuracy is increased, and the position estimate error reduces accordingly. This result implies incorporating a vehicle model gives some gain in accuracy if the velocity of the vehicle relative to the water stays away from zero, as is the case in this simulation.

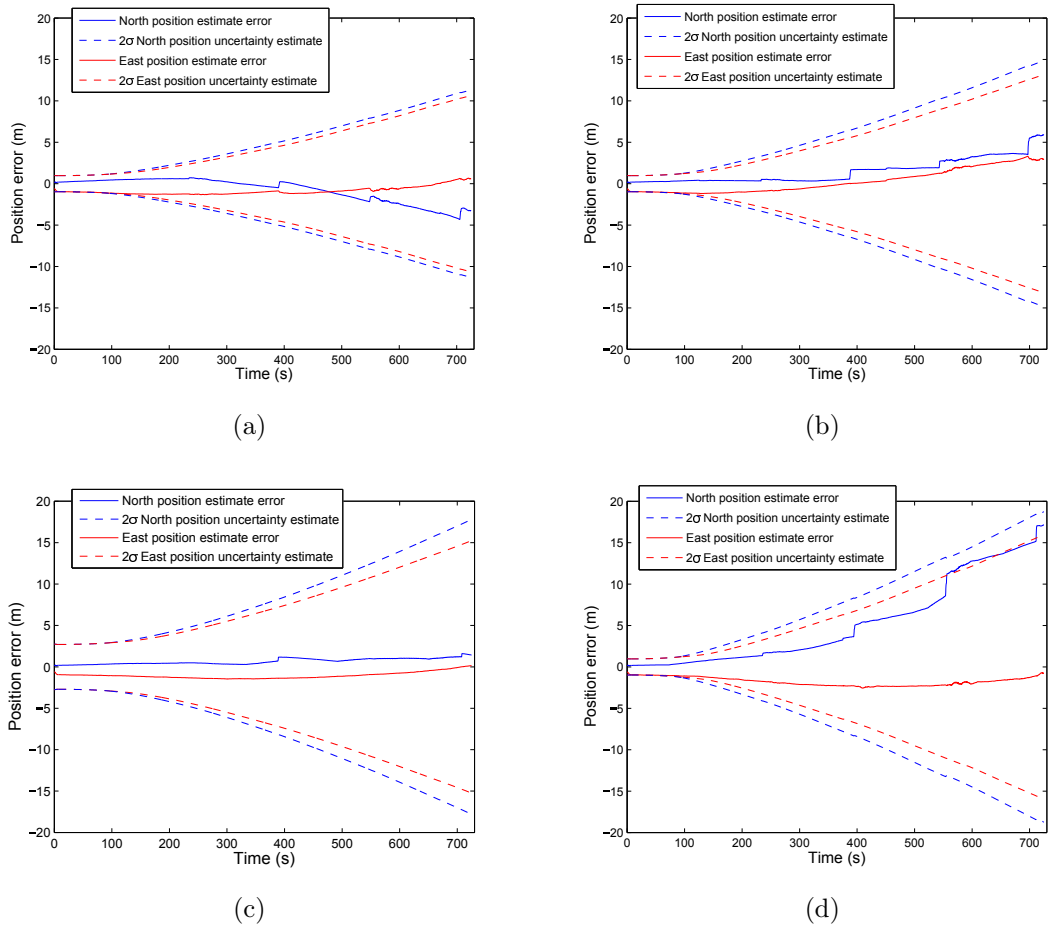

Figure 5.4 – The horizontal motion simulation position estimates and uncertainties for (a) 1% (3 σ) vehicle model parameter uncertainty, (b) 10% (3 σ) vehicle model parameter uncertainty and (d) without vehicle model aiding.

5.4 Sirius AUV vehicle modeling aiding results

In order to validate this application of the vehicle model in coupling with the IMU and ADCP aided localisation, data obtained through the use of *Sirius* is utilised. The vehicle model used is the same as generic model used in Chapter 3, derived from [9], while initial parameters are also used from [35]. The model parameters were assumed to have approximately 30% - 50% uncertainty in their values, due to the lack of previously previous system identification. Even with such a coarse vehicle model, slight improvements in the localisation can be made as will be shown. The experiment consists of 250 seconds of simulated GPS and DVL blackout, while the Sirius AUV is travelling laterally across the sea surface. The vehicle travels 65 m in this time. The water current environment is gridded at 20 m in order to model the spatial change in the currents during this small transit.

The water column aided localisation is compared to the GPS and DVL aided solution which is considered ground truth. The mission is done while sea surface effects like swell is affecting the vehicle, and due to the GPS antenna being attached to a flexible shaft, the GPS Doppler velocity is considered inaccurate, leading to a velocity uncertainty of 20cm/s (2σ) from the GPS derived velocity. This uncertainty is determined by comparing to the more accurate DVL velocity available. To simulate a more accurate GPS velocity sensor, the DVL is also fused to arrive at the initial velocity uncertainty of 1cm/s (2σ). The uncertainty of the DVL is inflated from the standard 6 mm/s (2σ) due to a lever arm between the IMU and DVL sensor frames, introducing velocity uncertainty as a result of misalignment and rotation rate uncertainty. The ADCP data to aid the localisation in this case operates only every 3-4 seconds as the sensor is operating with ten DVL measurements to one ADCP measurement.

With no vehicle model, the position estimate error compared to ground truth is shown in Figure 5.5(a). Given the sparse ADCP measurements, the position uncertainty grows rapidly. The estimated vehicle path, compared to ground truth, along with the estimate water current environment is shown in Figure 5.6. The localisation error has grown to approximately 25 m in the north, and 20 m in the east after 300 seconds,

with an estimated uncertainty of 30 m (2σ).

With the addition of a vehicle model, the localisation performance compared to the ground truth is illustrated in Figure 5.5(b). A localisation error within 20m from the ground truth and with an estimated uncertainty of less than 30 m 2 σ is attained following 300 seconds of simulated GPS and DVL blackout, exhibiting a slight improvement in the localisation accuracy. The uncertainty is reduced by 2m in this case, over more than 200 seconds, or a 7% reduction. The large position uncertainty growth is due to the low rate of ADCP measurements. The estimated vehicle path, compared to ground truth, along with the estimated water current environment is shown in Figure 5.7. Even with an uncertain vehicle model, slight improvements in the localisation is possible.

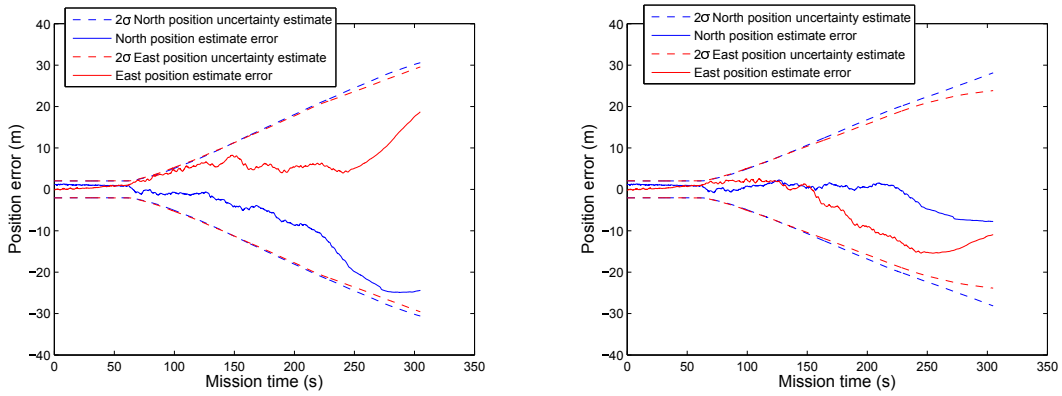

(a) (b)

Figure 5.5 – (a) The ADCP aided localisation with IMU, but without vehicle model, exhibits a high position uncertainty growth rate due to very sparse ADCP measurements. (a) applies a vehicle model, with the localisation slightly improved

5.5 Summary

This chapter formulated a novel method to incorporate measurements from an IMU and predictions from the vehicle model at the same time into the localisation. It exploits the fact that in a delayed state framework, the inertial and vehicle model could be converted into a delayed state constraint between poses. Previous methods

attempting to do this required tuning a correlation state, while this method does not require such a tuning. By adding the vehicle states to the estimation, they are correctly modelled in the estimation as a correlated state. There exists a coupling with estimates of the water current field around the vehicle, which the ADCP localisation method provides, and the water relative velocity of the vehicle which is input into the vehicle model.

Simulations showed that localisation improvements depend on the undertaken mission trajectory. For a vertical descent with little horizontal motion, the improvement in localisation accuracy is minimal. For purely horizontal motion, localisation improvements are evident given the introduction of the vehicle model. This is due to the uncertainty reduction from using a vehicle model having more impact on the higher uncertainty growth rate for the horizontal transit case. Finally, real data from the *Sirius* AUV is processed, which compares the incorporation and absence of the vehicle model. Improvements in the localisation are shown as a result of the vehicle model compared to combined GPS and DVL position ground truth, validating the approach for this data. Future research will include targeted experiments to further validate this approach.

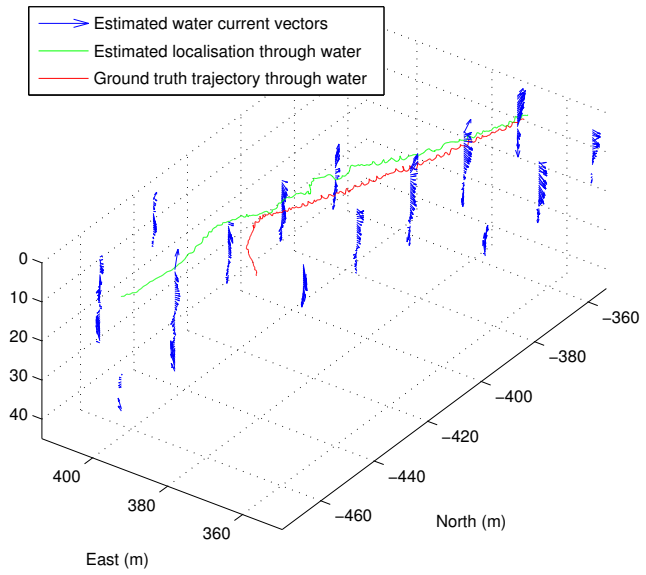

(a)

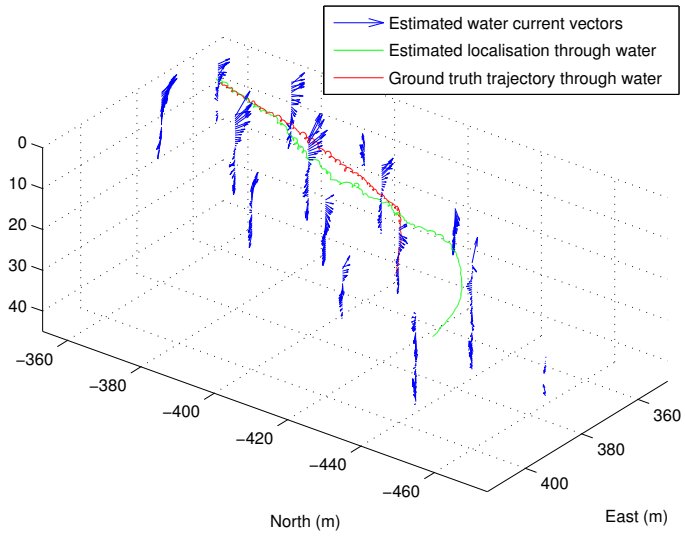

(b)

Figure 5.6 – Two views of the estimated water current environment along with the estimated vehicle localisation without a vehicle model, and the GPS/DVL ground truth for comparison.

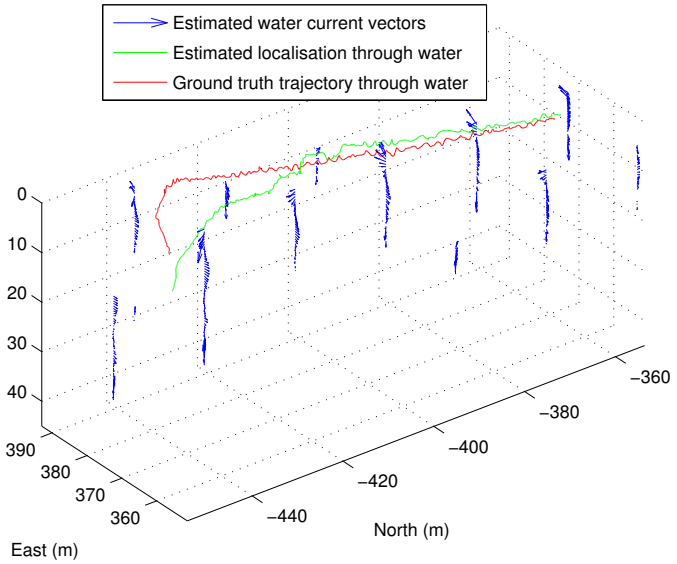

(a)

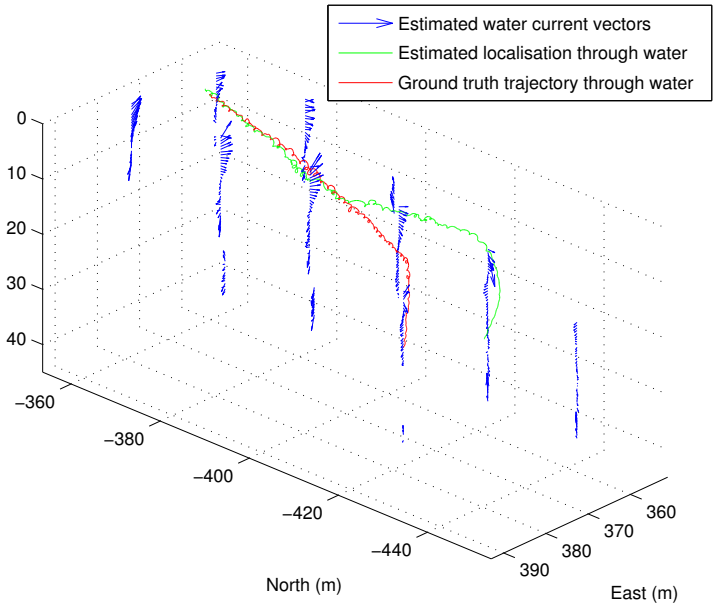

(b)

Figure 5.7 – Two views of the estimated water current environment along with the estimated vehicle localisation following the incorporation of a vehicle model, and the GPS/DVL ground truth for comparison.

Chapter 6

Conclusions and Future Research

6.1 Introduction

This thesis has developed a solution to the problem of the lack of feasible mid-water localisation options without recourse to acoustic time-of-flight sensors. This method relies on the vehicle's own measurements in order to improve the range and autonomy of AUV operations, including ADCP measurements and vehicle modelling. This localisation information can then be fed back into a control algorithm to achieve real-time navigation according to the prescribed mission.

The proposed system has the potential to work in real-time on board an AUV with typical sensors. The developed framework also allows the incorporation of existing localisation techniques, such as SLAM, to increase the accuracy of localisation.

6.2 Summary of Contributions

Specific contributions in detail are as follows:

- The development, implementation, testing and validation of isocurrent layer models for the water environment, along with a 3D velocity ADCP sensor model

to achieve localisation during vertical descent through the water column. The implementation and analysis of the developed models is achieved through the fusion of sensor measurements in an EIF. Simulation and real data are utilised to validate the approach. Specific novel contributions include:

- A two degrees-of-freedom simulation allowed the analysis of the error dynamics of the problem, and showed that a lower initial uncertainty of the velocity on the sea surface and the faster descent rate have the greatest impact in reducing the vehicle position uncertainty growth, and hence georeferencing accuracy prior to reaching DVL bottom-lock range. Given faster descent rates, the uncertainty growth in velocity as a consequence of less measurements of the water column is negligible compared to the reduced time spent in the water column and hence integrating velocity error with time to determine position. The effect of the ADCP measurement rate and standard deviation was also seen to have effects on the localisation, although not as significant. Once DVL bottom-lock was acquired, the primary driver for the position uncertainty growth was again descent rate and the initial velocity uncertainty. If the initial velocity uncertainty is similar to the DVL bottom-lock velocity uncertainty, and typical ADCP measurement rates and standard deviations are experienced, the position error growth rate will be reduced compared to a higher initial velocity uncertainty. Given low ADCP measurement rates and/or higher standard deviations, a lower initial velocity uncertainty reduces the position uncertainty growth, since information loss has limited the ability of the DVL to reduce the velocity uncertainty for the entire dive.
- A six degrees-of-freedom simulation reflected the possible performance of the algorithm under typical parameters for the *Sirius* AUV. Given this more realistic simulation, the impact of the initial velocity uncertainty on the vehicle was shown to still be significant prior to DVL bottom-lock, but with only minor corrections once DVL bottom-lock is acquired. A deeper descent over one hour was simulated, with information loss being evident

due to the non-linear increase in position uncertainty with time, as a result of the increase in velocity uncertainty with time. The performance of the algorithm for this one hour simulation was shown to be competitive with acoustic localisation methods.

- A validation of the ADCP localisation algorithm was completed with real data from the Sirius AUV. The scenario of low ADCP measurement rates in the ascent and descent of the vehicle was shown to provide accurate localisation performance compared to USBL ground truth, with the filter framework also allowing the incorporation of loop-closures from view-based SLAM.

- The development, implementation, testing and validation of a gridded IWVE model, along with a beam-directional ADCP sensor model. Spatial correlation in the water current vector field is accounted for in the EIF, through implementing least-squared constraints in the filter between IWVE states. Simulation and real data are utilised to validate the approach. Specific novel contributions include:

  - The ADCP-aided localisation is extended by generalising the water current layer model to isocurrent water volume elements. A simulation of the *Sirius* AUV was undertaken with purely horizontal motion once the vehicle had surmerged away from GPS. The information loss rates in the vehicle uncertainty are significantly greater than the vertical descent case. The assumption of horizontal homogeneity which allowed all 4 beams of the ADCP to observe the same water current depth cell simultaneously is assumed to no longer hold, resulting in limited observability and information loss. A spiralling descent simulation was undertaken, which showed some mitigation of this information loss rate, as the rotation around the water currents allowed greater observability and hence reduced the information loss rate.

  - Real data from the *Sirius* AUV was obtained with GPS ground truth. This was compared to the ADCP-aided localisation while on the sea surface.

Although the GPS accuracy is sub-optimal, the results showed that localisation by estimating the horizontal water current vector field with IVWEs gives less position uncertainty growth than alternative self-contained localisation methods.

- The incorporation of IMU measurements and vehicle model constraints to simultaneously aid the localisation. Simulation and real data are utilised to validate the approach. Specific novel contributions include:
  - The formulation of a novel method to incorporate measurements from an IMU and predictions from the vehicle model at the same time into the localisation. It exploits the fact that in a delayed state framework, the inertial and vehicle model could be converted into a delayed state constraint between poses. Previous methods attempting to do this required tuning a correlation state, while this method does not require such a tuning. By adding the vehicle states to the estimation, they are correctly modelled in the estimation as a correlated state. There exists a coupling with estimates of the water current field around the vehicle, which the ADCP localisation method provides, and the water relative velocity of the vehicle which is input into the vehicle model.
  - Simulations showed that due to the significant non-linearity of the vehicle model close to zero vehicle velocity relative to the surrounding water currents, localisation improvements depend on the undertaken mission trajectory. For a vertical descent with little horizontal motion, the non-linearity in the vehicle model nullifies the localisation information that the vehicle model provides. For a purely horizontal motion, where the vehicle velocity was away from the highly non-linear zero velocity point, localisation improvements are evident given the introduction of the vehicle model.
  - Real data from the *Sirius* AUV is processed, which compares the incorporation and absence of the vehicle model. Improvements in the localisation are shown as a result of the vehicle model compared to combined GPS and DVL position ground truth, validating the approach for this data.

6.3 Future Work

6.3.1 Further modelling of the water current environment

Since the water current environment can be assumed to be smooth, a parametrisation of the water current vector field which avoids the discretisation errors invoked by the isocurrent water volume element based method could allow more accurate water current modelling and thus localisation. Recent developments in Vector Field SLAM (VFSLAM) [14] show parallels with the AUV localisation problem within a water current vector field. Thus this problem can be categorised into a wider set of problems which try to simultaneously estimate the state of a vector field and localise. The observation of the vector field in the AUV case using an ADCP is dependent on position, attitude as well as velocity through the field.

In [14], two infrared light spots are projected onto the ceiling. The robot measures the bearing to the two lights spots using an optical sensor. This measurement, which depends on multipath, is modelled as a time-invariant vector field over a 2D grid on the ground for the robot to localise within, with equally spaced cell nodes. A bilinear interpolation model is used between equally spaced cell nodes to model the vector field. Extending this parameterisation and method to the underwater domain is a potential area of future research.

Prior information from oceanographic insights could also be input into the water current vector field model, such as well known local water current behaviour based on the position of the vehicle in the ocean. One example includes the seasonal cycles in the East Australian Current [44]. Additionally, physical models of the action of small scale water currents would aid the localisation, potentially involving the mass water transport equations [39].

6.3.2 Further Experimental validation

More targeted experiments to further validate the proposed localisation methods would shed further insights into the performance of the algorithm in real circum-

stances. Validation with real data using higher accuracy GPS velocity, and optimal measurement rate ADCP, will help validate the performance seen in simulation. Real-time implementation of the localisation and navigation procedures in this thesis would present further challenges, and would increase the utility of AUV operations.

6.3.3 Multiple Vehicles

By incorporating multiple vehicles, with selective sharing of their state vector through acoustic communications, a more extended view of the water current vector field could be estimated. This would feed back into the localisation and potential planning algorithms, given that knowledge of the water current vector field allows more accurate forecasting of the vehicle motion.

6.3.4 Incorporating different vector and scalar fields

The paper by Leonard [28] also proposes navigation using Magnetic field sensing as undertaken by aquatic fauna for navigation, or gravimetric sensing. These localisation tasks could potentially use insights from this thesis and the Vector Field SLAM problem.

Chemical sensing, such as that employed by Salmon to return to their natal river to spawn [4], along with other environmental sensing such as salt water and temperature, could be modeled as a Scalar Field, with potential for localisation.

Bibliography

[1] C. Atkinson. *Analysis of shipboard ADCP data from RRS Discovery Cruise D324: RAPID Array Eastern Boundary.* National Oceanography Centre Southampton, 2008.

[2] S. Barkby, S.B. Williams, O. Pizarro, and M.V. Jakuba. A featureless approach to efficient bathymetric SLAM using distributed particle mapping. *Journal of Field Robotics*, 28(1):19–39, 2011.

[3] M.W.M.G. Dissanayake, P. Newman, S. Clark, H.F. Durrant-Whyte, and M. Csorba. A solution to the simultaneous localization and map building (SLAM) problem. *Robotics and Automation, IEEE Transactions on*, 17(3): 229–241, 2001.

[4] A. Dittman and T. Quinn. Homing in Pacific salmon: mechanisms and ecological basis. *Journal of Experimental Biology*, 199(1):83, 1996.

[5] User:Stannered en:User:Skorkmaz. File:Enclosing points.svg - Wikimedia Commons [Public domain]. `http://commons.wikimedia.org/wiki/File:Enclosing_points.svg`. Accessed 18-02-2012.

[6] R.M. Eustice. *Large-area visually augmented navigation for autonomous underwater vehicles.* PhD thesis, Massachusetts Institute of Technology and Woods Hole Oceanographic Institution, 2005.

[7] G. Ferri, M.V. Jakuba, and D.R. Yoerger. A novel method for hydrothermal vents prospecting using an autonomous underwater robot. In *Robotics and Automation, 2008. ICRA 2008. IEEE International Conference on*, pages 1055–1060. IEEE, 2008.

[8] W.S. Flenniken IV. Modeling inertial measurement units and analyzing the effect of their errors in navigation applications. *Auburn University Masters Thesis*, 2005.

[9] T.I. Fossen. Guidance and control of ocean vehicles. *New York*, 1994.

[10] B. Garau, A. Alvarez, and G. Oliver. AUV navigation through turbulent ocean environments supported by onboard H-ADCP. In *Robotics and Automation, 2006. ICRA 2006. Proceedings 2006 IEEE International Conference on*, pages 3556–3561, 2006.

[11] R.L. Gordon and RD Instruments. Principles of Operation a Practical Primer. *RD Instruments, San Diego*, 1996.

[12] E.W. Grafarend and F.W. Krumm. *Map projections*. Springer-Verlag Berlin Heidelberg, 2006.

[13] M.G. Gross. Oceanography. pages 74–75, 1990.

[14] J.S. Gutmann, G. Brisson, E. Eade, P. Fong, and M. Munich. Vector field SLAM. In *Robotics and Automation, 2010. ICRA 2010. Proceedings 2010 IEEE International Conference on*, pages 236–242. IEEE, 2010.

[15] A.J. Healey, SM Rock, S. Cody, D. Miles, and JP Brown. Toward an improved understanding of thruster dynamics for underwater vehicles. *Oceanic Engineering, IEEE Journal of*, 20(4):354–361, 1995.

[16] O. Hegrenaes and E. Berglund. Doppler water-track aided inertial navigation for autonomous underwater vehicle. In *OCEANS 2009-EUROPE, 2009. OCEANS '09.*, pages 1–10, May 2009.

[17] O. Hegrenaes and O. Hallingstad. Model-Aided INS With Sea Current Estimation for Robust Underwater Navigation. *Oceanic Engineering, IEEE Journal of*, 36(2):316–337, 2011.

[18] O. Hegrenses, O. Hallingstad, and B. Jalving. Comparison of mathematical models for the HUGIN 4500 AUV based on experimental data. In *Underwater Technology and Workshop on Scientific Use of Submarine Cables and Related Technologies, 2007. Symposium on*, pages 558–567. IEEE, 2007.

[19] RD Instruments. ADCP coordinate transformation: Formulas and calculations. *RDI Manual*, 1998.

[20] iXSea. PHINS brochure. Accessed 22-03-2012.

[21] M.V. Jakuba. *Stochastic mapping for chemical plume source localization with application to autonomous hydrothermal vent discovery*. PhD thesis, Massachusetts Institute of Technology and Woods Hole Oceanographic Institution, 2007.

[22] M. Kaess, V. Ila, R. Roberts, and F. Dellaert. The Bayes Tree: Enabling Incremental Reordering and Fluid Relinearization for Online Mapping. *Computer Science and Artificial Intelligence Laboratory. MIT technical report MIT-CSAIL-TR-2010-021*, 2010.

[23] M. Kaess, H. Johannsson, R. Roberts, V. Ila, J. Leonard, and F. Dellaert. iSAM2: Incremental smoothing and mapping with fluid relinearization and incremental variable reordering. In *Robotics and Automation (ICRA), 2011 IEEE International Conference on*, pages 3281–3288. IEEE, 2011.

[24] J.C. Kinsey, R.M. Eustice, and L.L. Whitcomb. A survey of underwater vehicle navigation: Recent advances and new challenges. In *Proceedings of the 7th Conference on Maneuvering and Control of Marine Craft (MCMC'2006). IFAC, Lisbon*. Citeseer, 2006.

[25] M. Koifman and IY Bar-Itzhack. Inertial navigation system aided by aircraft dynamics. *Control Systems Technology, IEEE Transactions on*, 7(4):487–493, 1999.

[26] C. Kunz. *AUV Navigation and Mapping in Dynamic, Unstructured Environments*. PhD thesis, Ph. D. dissertation, MIT/WHOI, 2011.

[27] H. Lamb. Hydrodynamics, 738 pp. *Cambridge University Press, New York*, 1932.

[28] J. Leonard, A. Bennett, C. Smith, and H. Feder. Autonomous underwater vehicle navigation. In *IEEE ICRA Workshop on Navigation of Outdoor Autonomous Vehicles*, 1998.

[29] T. Lupton. *Inertial SLAM with Delayed Initialisation*. PhD thesis, University of Sydney, 2010.

[30] Todd Lupton and Salah Sukkarieh. Efficient integration of inertial observations into visual SLAM without initialization. In *Intelligent Robots and Systems, 2009. IROS 2009. IEEE/RSJ International Conference on*, pages 1547–1552, Oct. 2009.

[31] I. Mahon. *Vision-based navigation for autonomous underwater vehicles*. PhD thesis, University of Sydney, 2008.

[32] I. Mahon, S.B. Williams, O. Pizarro, and M. Johnson-Roberson. Efficient View-Based SLAM Using Visual Loop Closures. *Robotics, IEEE Transactions on*, 24(5):1002 –1014, oct. 2008. ISSN 1552-3098.

[33] M. Mandt, K. Gade, and B. Jalving. Integrating DGPS-USBL position measurements with inertial navigation in the HUGIN 3000 AUV. In *Proceedings of the 8th Saint Petersburg International Conference on Integrated Navigation Systems, Saint Petersburg, Russia*, 2001.

[34] G.O. Marmorino, C.L. Trump, and Z.R. Hallock. Near-surface current measurements using a ship-deployed "horizontal" ADCP. *Journal of Atmospheric and Oceanic Technology*, 16(10):1456–1463, 1999.

[35] S.C. Martin and L.L. Whitcomb. Preliminary results in experimental identification of 3-DOF coupled dynamical plant for underwater vehicles. In *OCEANS 2008*, pages 1–9. IEEE, 2008.

[36] R. McEwen, H. Thomas, D. Weber, and F. Psota. Performance of an AUV navigation system at Arctic latitudes. *IEEE Journal of Oceanic Engineering*, 30(2):443–454, 2005.

[37] S. McPhail. Autosub6000: A deep diving long range AUV. *Journal of Bionic Engineering*, 6(1):55–62, 2009.

[38] F. Napolitano, A. Chapelon, A. Urgell, and Y. Paturel. PHINS: The autonomous navigation solution. *Sea Technology*, 45(2):55–58, 2004.

[39] G. Neumann. *Ocean currents*, volume 4. Elsevier, 1968.

[40] Novatel. OEM628 brochure. Accessed 22-03-2012.

[41] P.E. Plimpton, H.P. Freitag, and M.J. McPhaden. ADCP Velocity Errors from Pelagic Fish Schooling around Equatorial Moorings*. *Journal of Atmospheric and Oceanic Technology*, 14(5):1212–1223, 1997.

[42] K. Polzin, E. Kunze, J. Hummon, and E. Firing. The finescale response of lowered ADCP velocity profiles. *Journal of Atmospheric and Oceanic Technology*, 19(2):205–224, 2002.

[43] P.B. Rhines. Geostrophic turbulence. *Annual Review of Fluid Mechanics*, 11 (1):401–441, 1979.

[44] KR Ridgway and JS Godfrey. Seasonal cycle of the East Australian Current. *Journal of Geophysical Research*, 102(C10):22921–22, 1997.

[45] P. Rigby, O. Pizarro, and S.B. Williams. Towards geo-referenced AUV navigation through fusion of USBL and DVL measurements. In *OCEANS 2006*, pages 1–6. IEEE, 2006.

[46] H.H. Shih, C. Payton, J. Sprenke, and T. Mero. Towing basin speed calibration of acoustic Doppler current profiling instruments. In *Proc. 2000 Joint Conference on Water Resources Engineering and Water Resources Planning and Management*, 2000.

[47] H. Singh, A. Can, R. Eustice, S. Lerner, N. McPhee, O. Pizarro, and C. Roman. Seabed AUV offers new platform for high-resolution imaging. *EOS, Transactions of the AGU*, 85(31):289–294, 2004.

[48] B.K.H. Soon. *Robust Relative Navigation in Large-Scale Environments*. PhD thesis, University of Sydney, 2008.

[49] B.K.H. Soon, S. Scheding, H.K. Lee, H.K. Lee, and H. Durrant-Whyte. An approach to aid INS using time-differenced GPS carrier phase (TDCP) measurements. *Gps Solutions*, 12(4):261–271, 2008. ISSN 1080-5370.

[50] M.J. Stanway. Dead reckoning through the water column with an acoustic Doppler current profiler: Field experiences. In *OCEANS 2011*, pages 1–8. IEEE, 2011.

[51] M.J. Stanway. *Contributions to automated realtime underwater navigation.* PhD thesis, Massachusetts Institute of Technology, 2012.

[52] D.H. Titterton and J.L. Weston. *Strapdown inertial navigation technology.* Peter Peregrinus Ltd, 2004.

[53] G. Troni, C.J. McFarland, K.A. Nichols, and L.L. Whitcomb. Experimental evaluation of an inertial navigation system for underwater robotic vehicles. In *Robotics and Automation (ICRA), 2011 IEEE International Conference on*, pages 3064–3071. IEEE, 2011.

[54] User:David.Monniaux. File:World_map.png-Wikimedia Commons [Creative Commons Attribution-Share Alike 2.0 Generic]. `http://commons.wikimedia.org/wiki/File:World_map.png`. Accessed 18-02-2012.

[55] F. van Graas and A. Soloviev. Precise velocity estimation using a stand-alone GPS receiver. *Navigation(Washington, DC)*, 51(4):283–292, 2004.

[56] J. Vial, H. Durrant-Whyte, and T. Bailey. Conservative sparsification for efficient and consistent approximate estimation. In *Intelligent Robots and Systems (IROS), 2011 IEEE/RSJ International Conference on*, pages 886–893. IEEE, 2011.

[57] M. Visbeck. Deep velocity profiling using lowered acoustic Doppler current profilers: Bottom track and inverse solutions. *Journal of Atmospheric and Oceanic Technology*, 19(5):794–807, 2002.

[58] M.R. Walter, R.M. Eustice, and J.J. Leonard. Exactly sparse extended information filters for feature-based SLAM. *The International Journal of Robotics Research*, 26(4):335–359, 2007.

[59] S. Williams, O. Pizarro, M. Jakuba, and N. Barrett. AUV benthic habitat mapping in South Eastern Tasmania. In *Field and Service Robotics*, pages 275–284. Springer, 2010.

[60] S.B. Williams, O. Pizarro, I. Mahon, and M. Johnson-Roberson. Simultaneous Localisation and Mapping and Dense Stereoscopic Seafloor Reconstruction Using an AUV. In *Experimental Robotics*, pages 407–416. Springer, 2009.

[61] S.B. Williams, O. Pizarro, M.V. Jakuba, I. Mahon, S.D. Ling, and C.R. Johnson. Repeated AUV surveying of urchin barrens in North Eastern Tasmania. In *Robotics and Automation (ICRA), 2010 IEEE International Conference on*, pages 293–299. IEEE, 2010.

[62] S.B. Williams, O. Pizarro, J.M. Webster, R.J. Beaman, I. Mahon, M. Johnson-Roberson, and T.C.L. Bridge. Autonomous underwater vehicle–assisted surveying of drowned reefs on the shelf edge of the Great Barrier Reef, Australia. *Journal of Field Robotics*, 27(5):675–697, 2010.

Appendix A

Position error growth for a two degree of freedom simulation with varying parameters

This appendix explores the reliance of the position uncertainty growth with respect to mission parameters, as proposed in Section 3.3.3. The vehicle experiences unmodelled (in the localisation filter) drag which causes it to move with the currents. The vehicle is also assumed not to pitch in this simulation, resulting in 2 degrees of freedom (2DOF) in translation. To further simplify the analysis of this example, the bias states are not simulated. 20 m of descent in 60 m of water is simulated between GPS blackout and DVL bottom-lock. A 1-dimensional current field is simulated in which the vehicle is travelling vertically down, and free to move left or right (but not into and out of the page of the figures). The default values for the parameters are listed in Table A.1 below, and unless otherwise varying, they are kept at these values.

Table A.1 – Parameter values used in the 2DOF simulation

GPS receiver	Lassen iQ GPS receiver
Initial GPS position fix accuracy	10 m (2σ)
Initial GPS velocity accuracy (σ_v)	0.04 m/s (2σ)
AUV descent rate	0.2 m/s
ADCP make and model	RDI 1200 kHz
ADCP measurement uncertainty (σ_a)	0.02 m/s (2σ)
ADCP range	30 m
Current bin size	1 m
Simulation time	1000 seconds
Simulated depth	60 m
DVL accuracy	0.006 m/s (2σ)
DVL range	40 m
DVL acquisition time	1000 seconds
ADCP and DVL measurement rate	3 Hz
Maximum currents	20 cm/s

The following parameters are varied in order to analyse the effect on the filter position uncertainty estimates:

1. AUV descent rate
2. ADCP measurement rate or measurement frequency
3. ADCP measurement standard deviation (σ_a)
4. Initial velocity accuracy (σ_v) whether from GPS or other sources (such as GPS/IMU)

The following sections plot the relationships between these parameters, along with some discussion of the trends. The position uncertainty growth is defined as the 2σ uncertainty of the final position relative to the initial position, and thus is relative to the initial position uncertainty.

A.1 AUV descent rate vs. ADCP measurement rate

As evident from Figure A.1, the descent rate is a primary concern for the position uncertainty growth. Figure A.2 shows that the uncertainty growth is in fact near linear with respect to the time between GPS blackout and DVL bottom-lock. Therefore, there is an inverse relationship between position uncertainty growth and descent rate. Figure A.3 shows that ADCP measurement rate has no effect on position error growth given changes in the descent rate. Once DVL bottom lock is acquired, the relationship between these variables remains unchanged as evident in Figures A.4, A.5 and A.6. This relationship between descent rate and position uncertainty growth is due to faster descent rates having a negligible effect on the velocity uncertainty during the descent, thus a similar velocity uncertainty is being integrated over a longer time for a given mission.

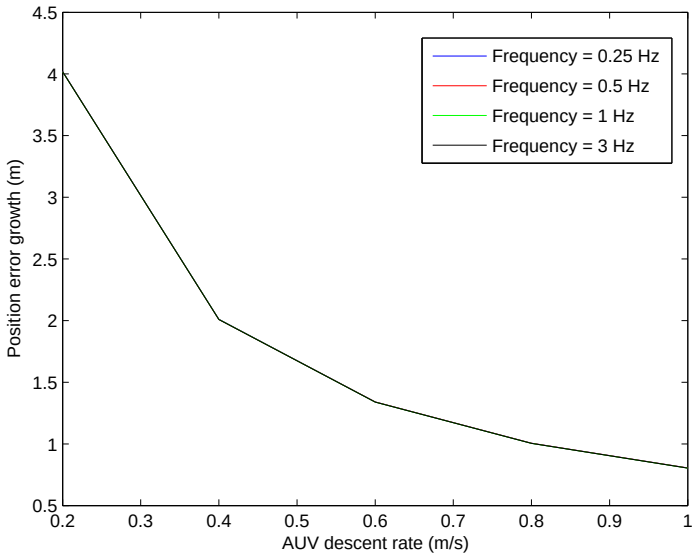

Figure A.1 – AUV descent rate vs. position uncertainty growth for various ADCP measurement rates prior to DVL bottom lock

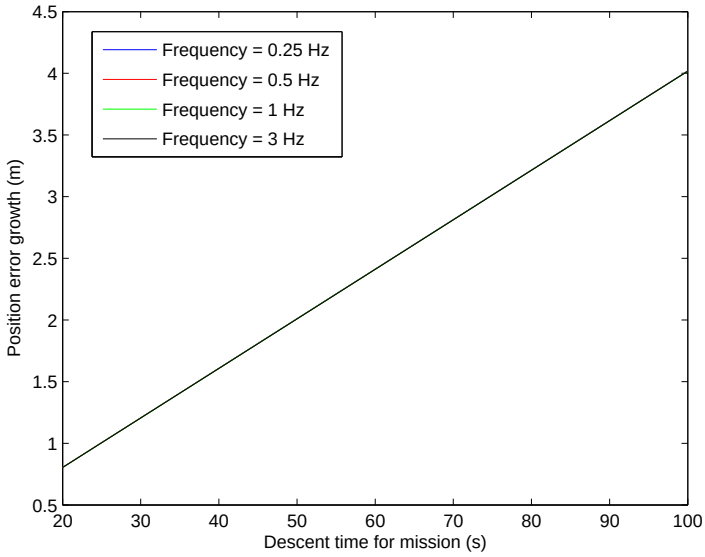

Figure A.2 – Mission descent time vs. position uncertainty growth for various ADCP measurement rates prior to DVL bottom lock

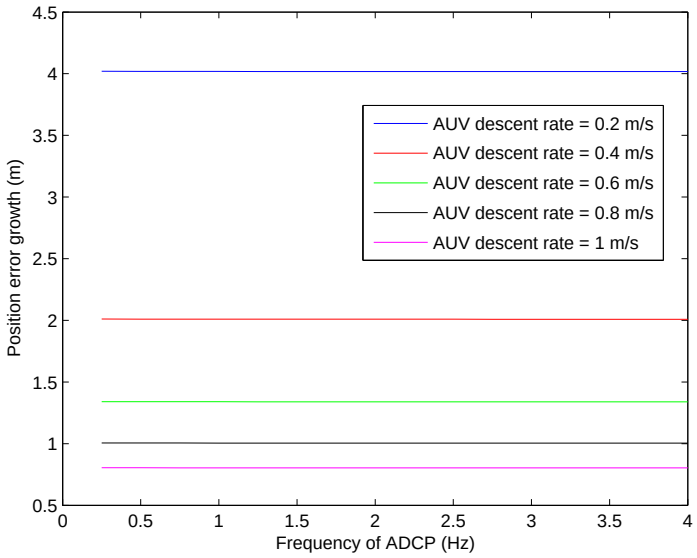

Figure A.3 – ADCP measurement rate vs. position uncertainty growth for various descent rates prior to DVL bottom lock

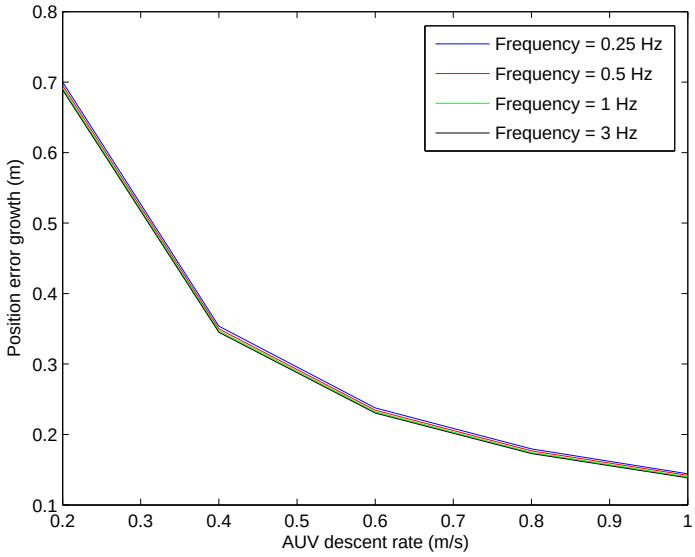

Figure A.4 – AUV descent rate vs. position uncertainty growth for various ADCP measurement rates following DVL bottom lock

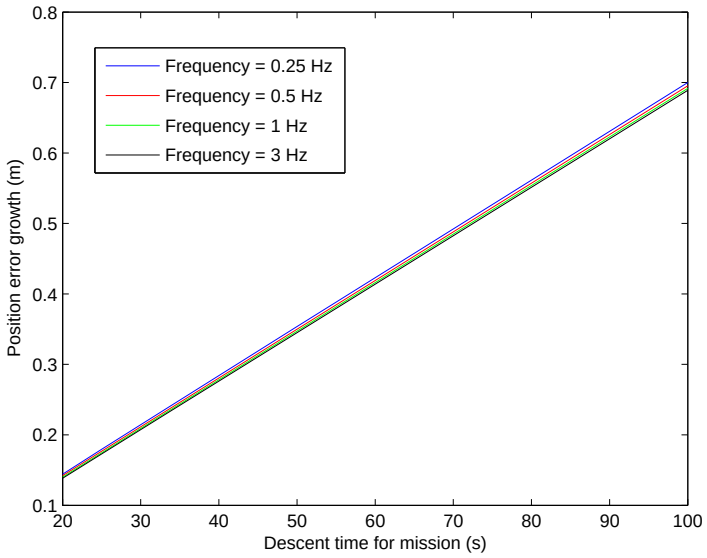

Figure A.5 – Mission descent time vs. position uncertainty growth for various ADCP measurement rates following DVL bottom lock

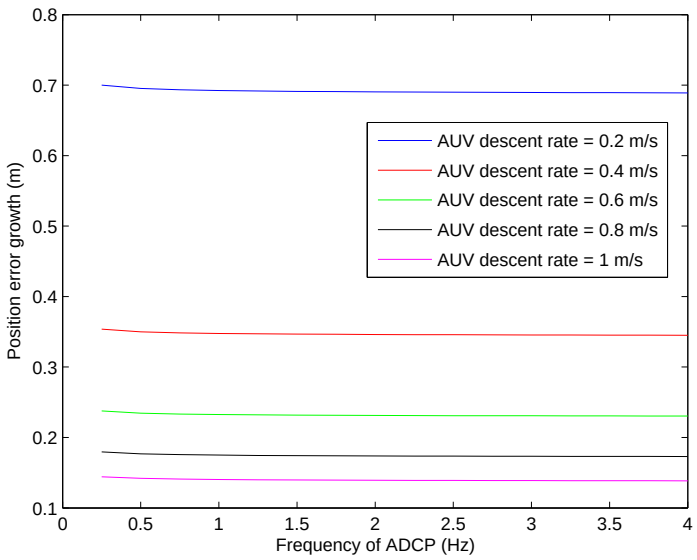

Figure A.6 – ADCP measurement rate vs. position uncertainty growth for various descent rates following DVL bottom lock

A.2 AUV descent rate vs. ADCP measurement standard deviation (σ_a)

As can be seen in Figures A.7, A.8 and A.9, a slow descent rate prior to DVL bottom lock is affected by high ADCP noise magnitudes, compared to the same ADCP noise magnitudes for faster descent rates. Given that the vehicle velocity uncertainty can deteriorate faster given high uncertainty ADCP measurements, this information loss is integrated over a longer period of time with the slow descent rate, and is somewhat mitigated by reaching the seafloor faster. Following DVL bottom lock, A.10, A.11 and A.12 exhibit this same property, implying that the information loss in the water column is irreversible, and can be mitigated by having a faster descent rate.

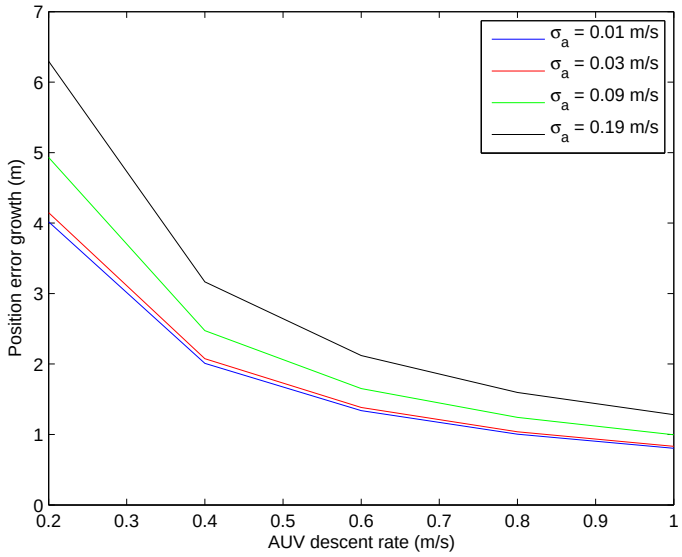

Figure A.7 – AUV descent rate vs. position uncertainty growth for various ADCP measurement standard deviations prior to DVL bottom lock

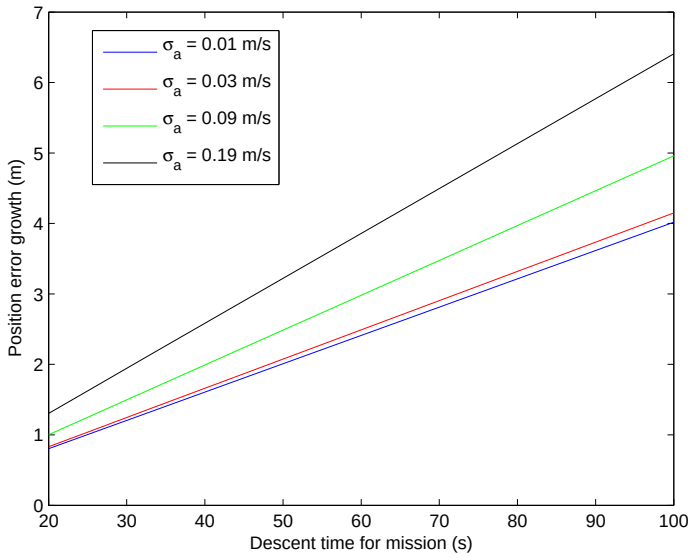

Figure A.8 – Mission descent time vs. position uncertainty growth for various ADCP measurement standard deviations prior to DVL bottom lock

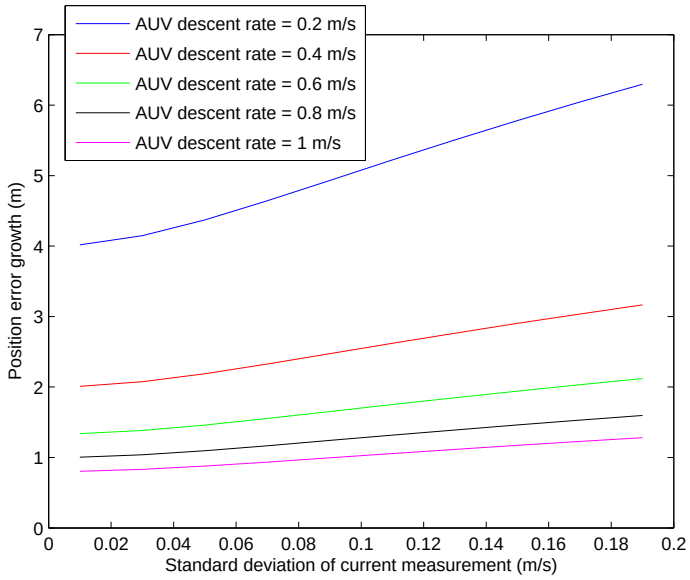

Figure A.9 – ADCP measurement standard deviation vs. position uncertainty growth for various descent rates prior to DVL bottom lock

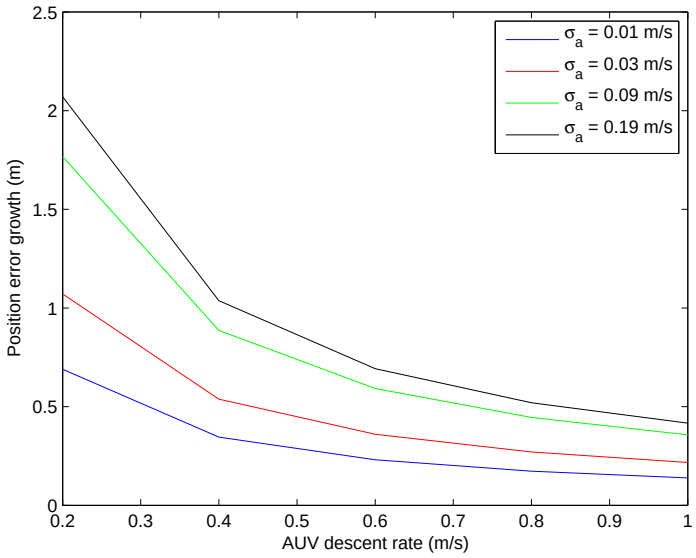

Figure A.10 – AUV descent rate vs. position uncertainty growth for various ADCP measurement standard deviations following DVL bottom lock

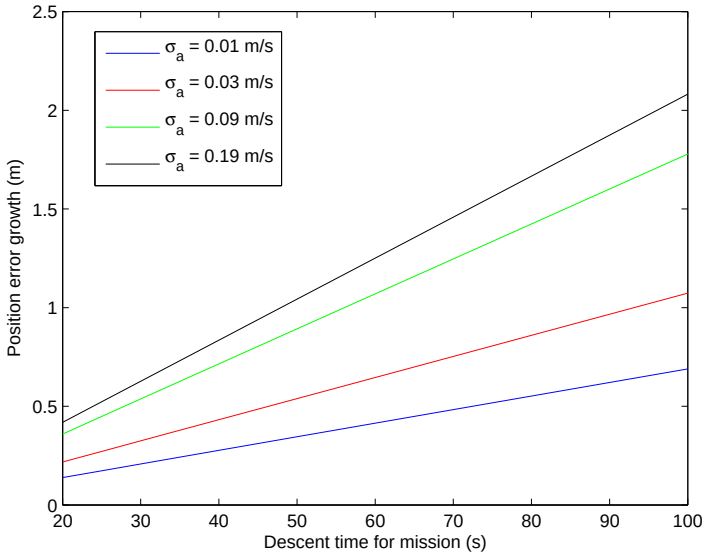

Figure A.11 – Mission descent time vs. position uncertainty growth for various ADCP measurement standard deviations following DVL bottom lock

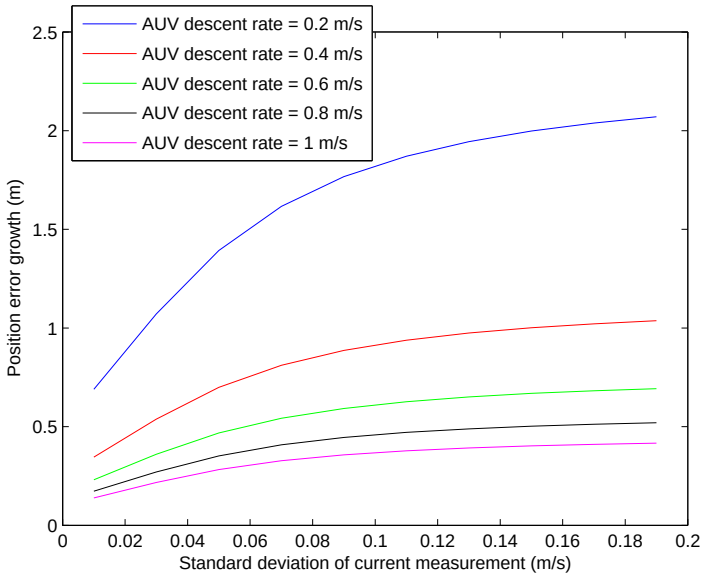

Figure A.12 – ADCP measurement standard deviation vs. position uncertainty growth for various descent rates following DVL bottom lock

A.3 AUV descent rate vs. Initial velocity standard deviation (σ_v)

As can be seen in Figures A.13, A.14 and A.15, the initial velocity standard deviation is another primary driver for the position uncertainty growth in addition to descent rate prior to DVL bottom-lock. There exists a near linear relationship between the initial velocity standard deviation and the position error growth. As descent rates increase, the position uncertainty growth is reduced depending on the magnitude of the initial velocity standard deviation. Figures A.16 and A.17 show that once DVL bottom lock is achieved, the uncertainty in position becomes independent of the initial velocity standard deviation. The exception is when the magnitude of the initial velocity uncertainty is similar to the DVL bottom lock uncertainty, in which case both velocity estimates are combined to reduce the position uncertainty growth. This is evident in Figure A.18.

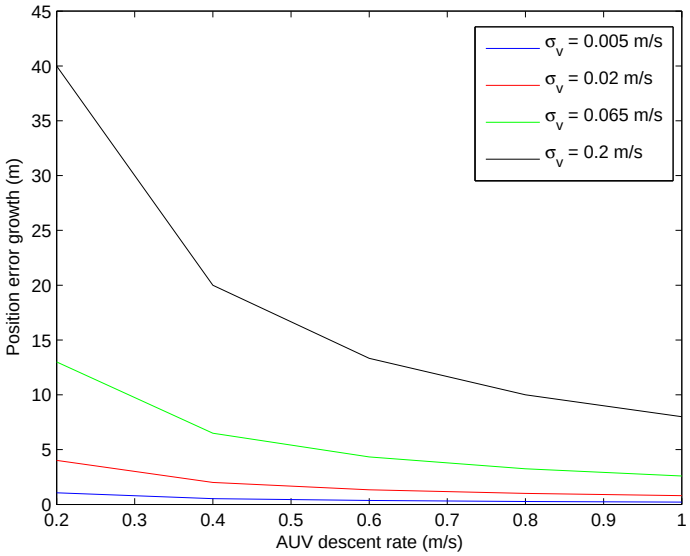

Figure A.13 – AUV descent rate vs. position uncertainty growth for various initial velocity standard deviations prior to DVL bottom lock

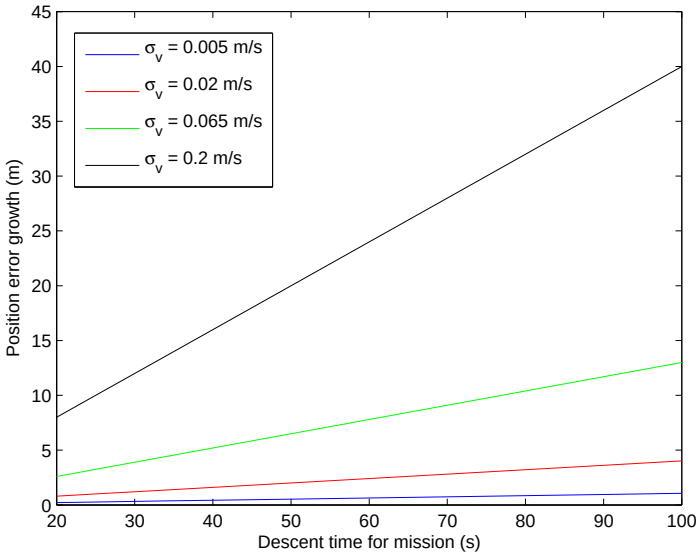

Figure A.14 – Mission descent time vs. position uncertainty growth for various initial velocity standard deviations prior to DVL bottom lock

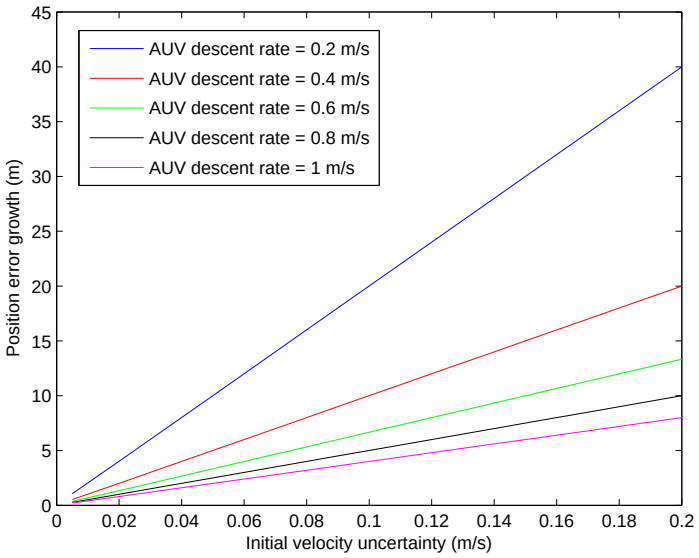

Figure A.15 – Initial velocity standard deviation vs. position uncertainty growth for various descent rates prior to DVL bottom lock

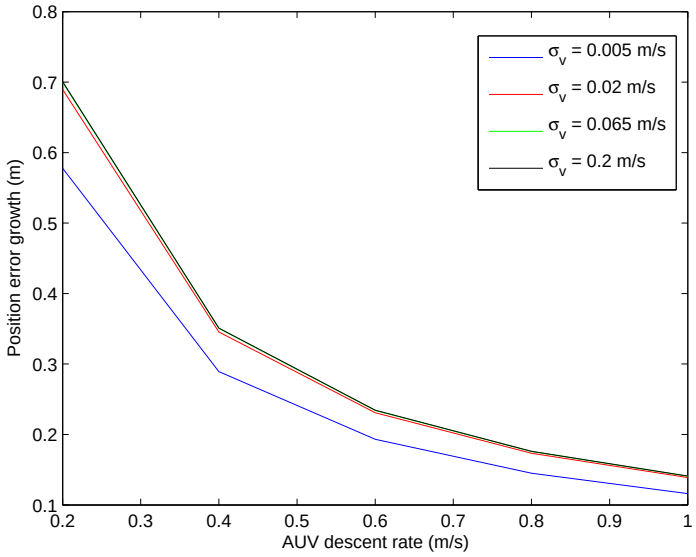

Figure A.16 – AUV descent rate vs. position uncertainty growth for various initial velocity standard deviations following DVL bottom lock

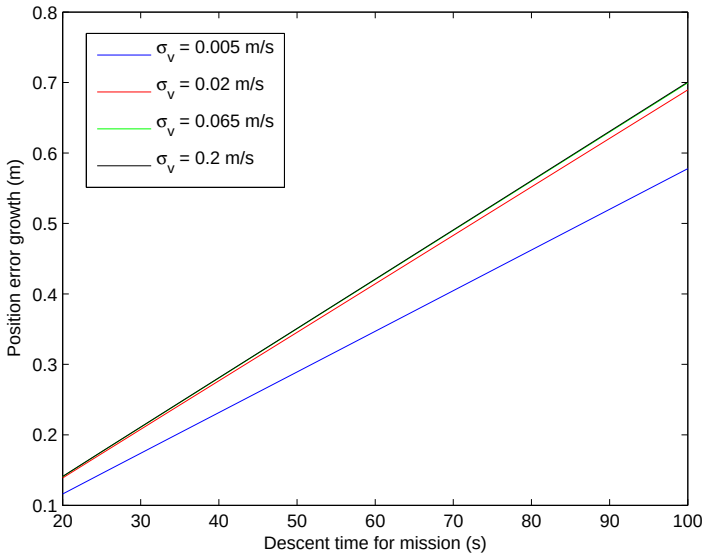

Figure A.17 – Mission descent time vs. position uncertainty growth for various initial velocity standard deviations following DVL bottom lock

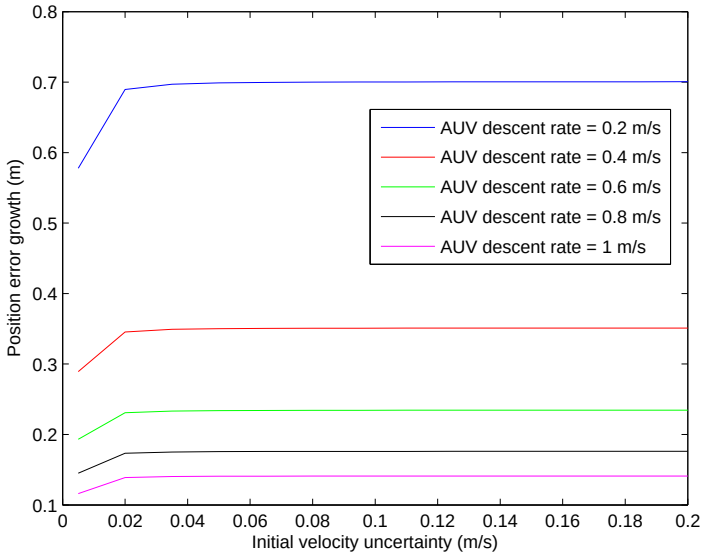

Figure A.18 – Initial velocity standard deviation vs. position uncertainty growth for various descent rates following DVL bottom lock

A.4 ADCP measurement rate vs. ADCP measurement standard deviation (σ_a)

Figures A.19 shows that the position uncertainty growth becomes independent of ADCP measurement rate given low ADCP measurement standard deviation prior to DVL bottom lock. Given higher ADCP measurement standard deviation as in Figure A.20, lower measurement update rates result in higher position uncertainty growth. This is a result of high amounts of information loss as there are few, noisy measurements to estimate velocity as the vehicle travels down the water column, resulting in the growth of water current velocity uncertainty, feeding back into the velocity estimate uncertainty prior to bottom lock. Figure A.20 also has a concave up curve, implying increasing impact on the position uncertainty growth superlinearly with higher ADCP measurement standard deviation. Once DVL bottom is acquired, the effect of information loss has been mitigated with respect to a low ADCP measurement rate as shown in Figures A.21, as the velocity uncertainty of the water currents

can be reduced. Figure A.22 shows that while the position uncertainty growth increases as ADCP measurement standard deviation increases, the curve is concave down, implying a stabilising effect by incorporating DVL bottom lock in this case.

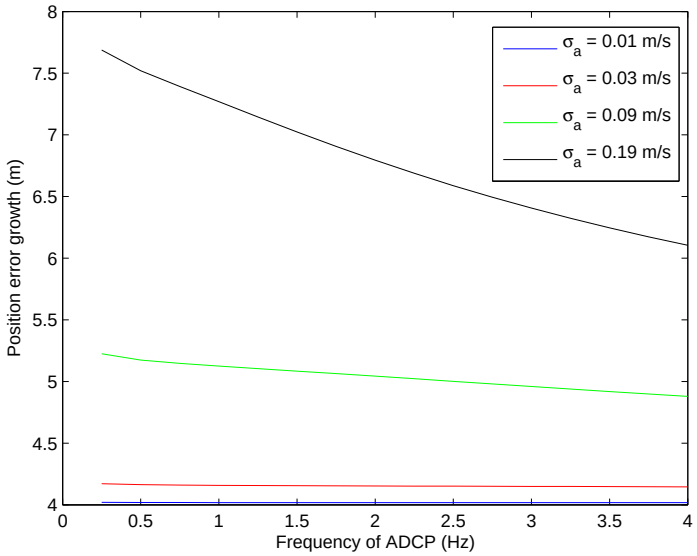

Figure A.19 – ADCP measurement rate vs. position uncertainty growth for various ADCP measurement standard deviations prior to DVL bottom lock

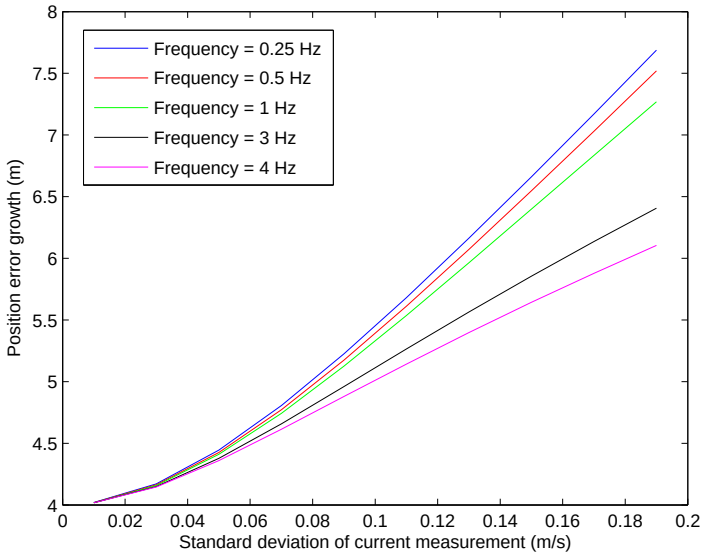

Figure A.20 – ADCP measurement standard deviation vs. position uncertainty growth for various ADCP measurement rates prior to DVL bottom lock

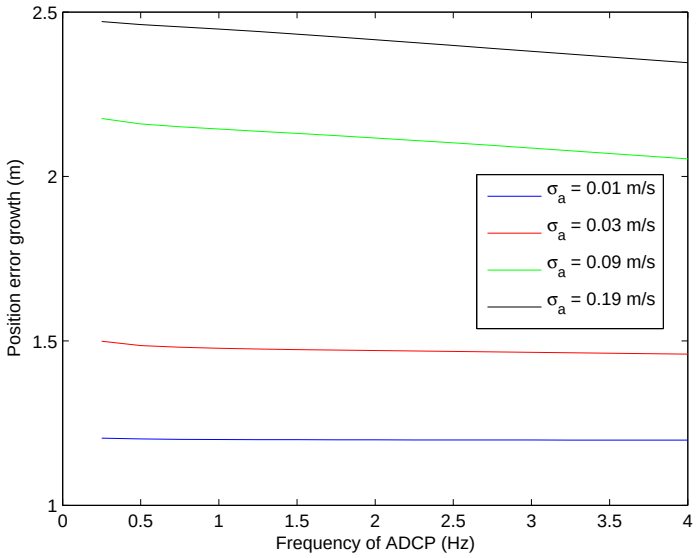

Figure A.21 – ADCP measurement rate vs. position uncertainty growth for various ADCP measurement standard deviations prior to DVL bottom lock

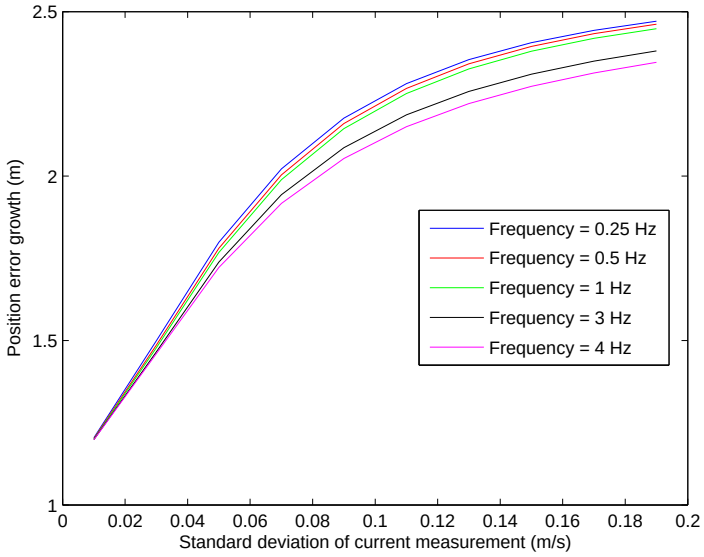

Figure A.22 – ADCP measurement standard deviation vs. position uncertainty growth for various ADCP measurement rates prior to DVL bottom lock

A.5 ADCP measurement rate vs. Initial velocity standard deviation (σ_v)

During descent, prior to DVL bottom-lock, the ADCP measurement rate has negligible impact on the error growth in comparison to the the effect of the initial velocity uncertainy, as illustrated in Figure A.23. The initial velocity uncertainty continues to have a linear impact on the position uncertainty growth, with the uncertainty growth rate almost independent of the ADCP measurement rate, as seen in Figure A.24. Once DVL bottom-lock is acquired, the ADCP measurement rate has a slight effect on the final position uncertainty growth, as evidenced by Figure A.25 and A.26. As the DVL bottom-lock is acquired, any information losses due to a low ADCP measurement rate will have a more pronounced effect on the position error growth as it reduces the impact the low uncertainty velocity measurement can have in reducing previous uncertainty in velocity earlier in the mission.

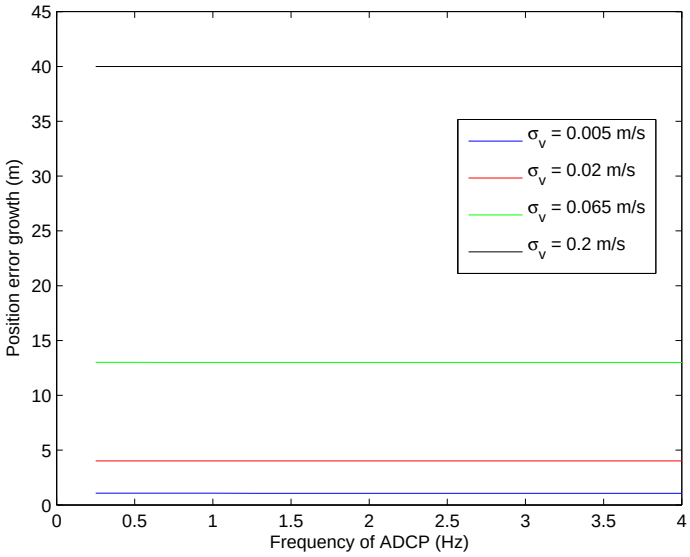

Figure A.23 – ADCP measurement rate vs. position uncertainty growth for various initial velocity standard deviations prior to DVL bottom lock

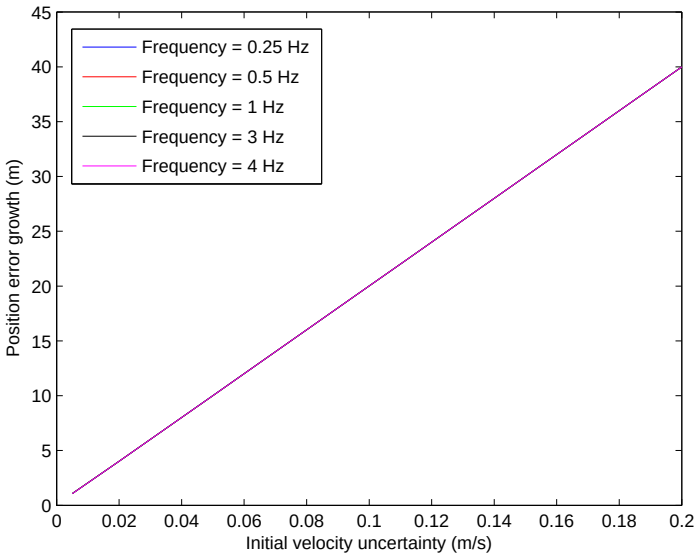

Figure A.24 – Initial velocity standard deviation vs. position uncertainty growth for various ADCP measurement rates prior to DVL bottom lock

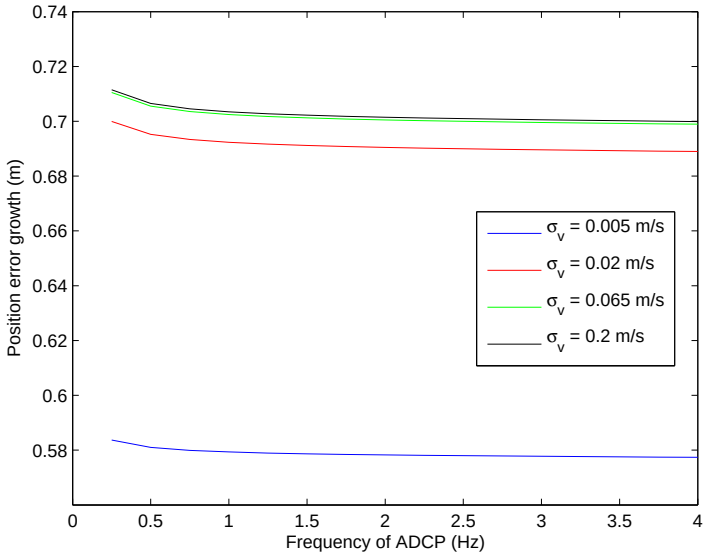

Figure A.25 – ADCP measurement rate vs. position uncertainty growth for various initial velocity standard deviations prior to DVL bottom lock

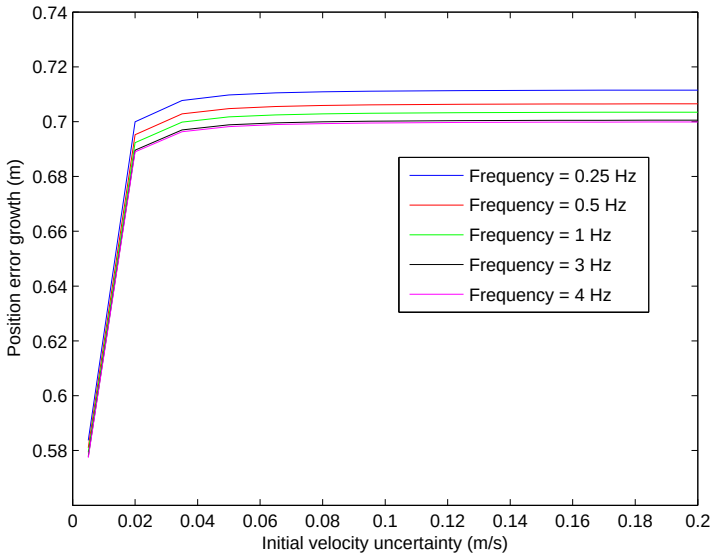

Figure A.26 – Initial velocity standard deviation vs. position uncertainty growth for various ADCP measurement rates prior to DVL bottom lock

A.6 Initial velocity standard deviation (σ_v) vs. ADCP measurement standard deviation (σ_a)

Prior to DVL bottom-lock, the initial velocity uncertainty is the dominant determinant of the position uncertainty growth, as shown in Figure A.27. When the initial velocity standard deviation is small compared to the ADCP measurement standard deviation, a lower ADCP measurement standard deviation will allow position error growth reductions. Figure A.27 illustrates this effect in more detail. Once DVL bottom-lock occurs, due to a large correction possible in the vehicle velocity and water current velocities, the standard deviation in the ADCP measurement becomes important as the information loss rates limit the ability of the DVL bottom-lock velocity to reduce the prior velocity estimates and hence position uncertainty growth. This is illustrated in Figures A.29 and A.30. The ADCP measurement standard deviation becomes more important as the initial velocity uncertainty increases, as the position uncertainty growth rates become more dependent on the DVL bottom-lock velocity estimates to reduce the velocity uncertainty earlier in the mission.

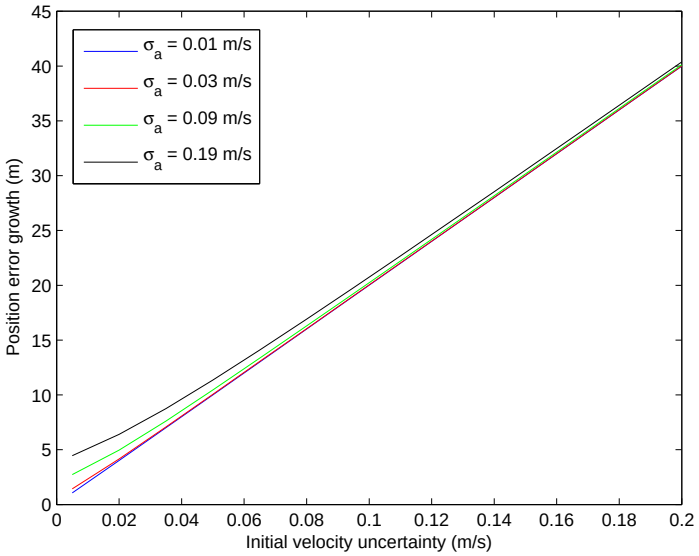

Figure A.27 – Initial velocity standard deviation vs. position uncertainty growth for ADCP measurement standard deviations prior to DVL bottom lock

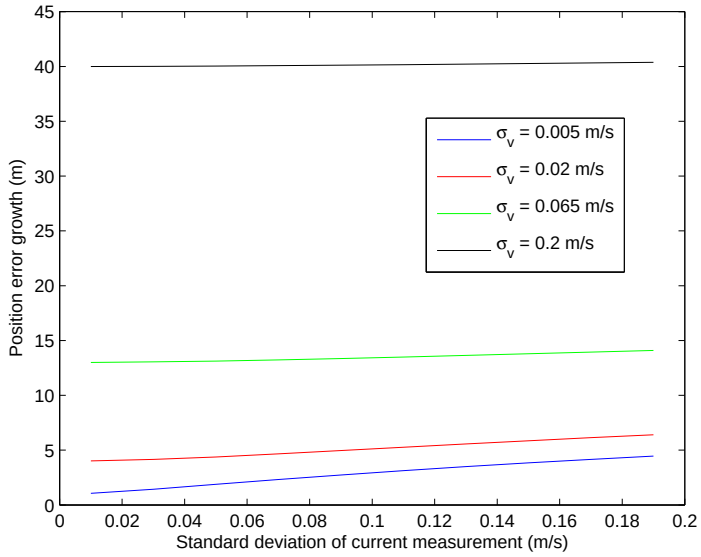

Figure A.28 – ADCP measurement standard deviation vs. position uncertainty growth for various initial velocity standard deviations prior to DVL bottom lock

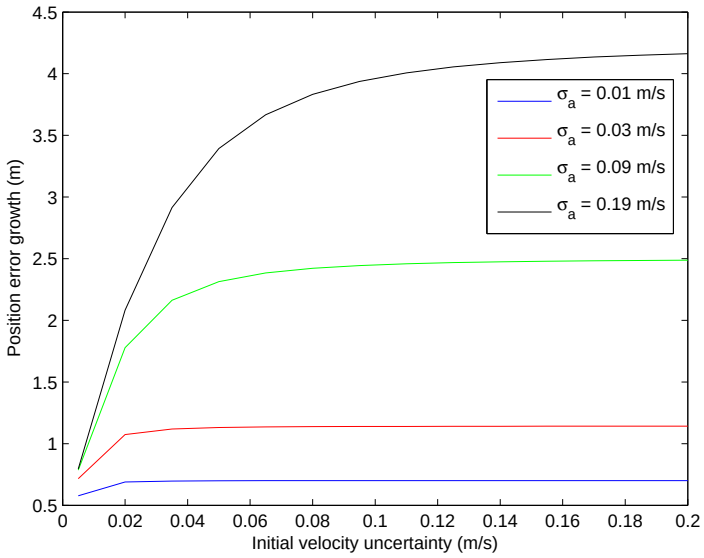

Figure A.29 – Initial velocity standard deviation vs. position uncertainty growth for various ADCP measurement standard deviations prior to DVL bottom lock

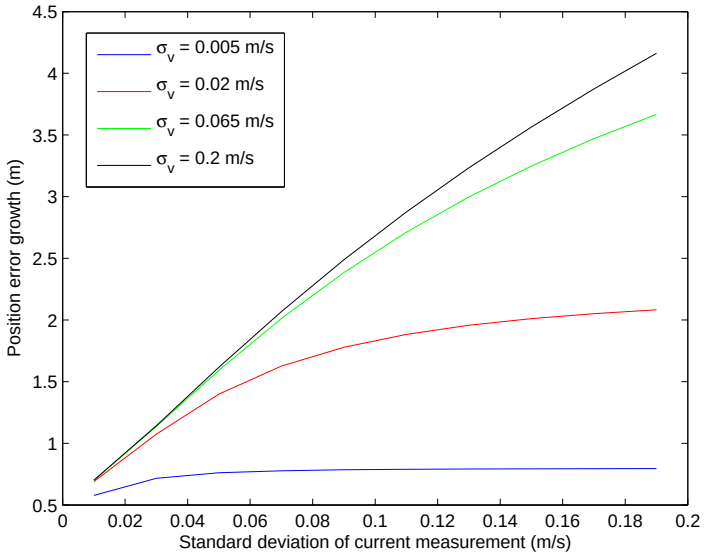

Figure A.30 – ADCP measurement standard deviation vs. position uncertainty growth for various initial velocity standard deviations prior to DVL bottom lock